SEISMIC REFLECTION IMAGING IN CRYSTALLINE TERRAINS

by

Mladen R. Nedimović

Geophysics Laboratory
Department of Physics
University of Toronto

A thesis submitted in conformity with the requirements
for the degree of **Doctor of Philosophy**
at the University of Toronto

To my greatest teachers, geophysicists -
to my parents

SEISMIC REFLECTION IMAGING IN CRYSTALLINE TERRAINS

Doctor of Philosophy, 2000, Mladen R. Nedimović
Geophysics Laboratory, Department of Physics
University of Toronto

Abstract

In the past couple of decades there has been an enormous progress in seismic reflection imaging of both sedimentary and crystalline igneous-metamorphic rock structures. Most of the immense increase in seismic resolving power has been attributed to the development of the 3D seismic method and prestack migration.

In principle, the more complex the geometry of the subsurface structures being explored, the greater the need is for 3D surveying. But, for cost and access reasons, most of seismic reflection data collected in crystalline terrains has been acquired by 2D crooked line profiling. When the survey geometry is significantly crooked and the structures have a cross-profile dip, several standard 2D imaging procedures may severely underperform. Particularly affected are common mid-point (CMP) stacking and profile migration. This is why imaging of 2D crooked line data has always been considered hazardous. While high fold 2D crooked line profiling should not be compared to full 3D surveying, it really is a kind of 3D survey of a swath of terrain around the "slalom" line. Thus, it should be looked upon as an opportunity to learn more about 3D rock structure in the vicinity of the profile rather than a problem.

My research objective has therefore been focused on:

- Exploring and developing processing methods which usefully exploit the 3D character of crooked line data to reveal the true geometry of the reflectors;
- Searching for alternative ways to minimize the deleterious effect of crooked line geometry and 3D structures on the resulting 2D seismic images, when extracting 3D information is not feasible.

To these ends I have designed the following data manipulation processes:

1. *Optimum cross dip analysis and the optimum cross dip stack.* This algorithm first analyzes cross-profile dip of the imaged reflectors and then collapses recorded bands of

reflectivity into single events, making 3D structure meaningful and interpretable on a 2D seismic section.

2. *3D prestack migration of 2D crooked line data.* Bands of reflectivity recorded in 2D crooked line data are preserved and positioned to their true subsurface locations within an output 3D data volume by this specialized prestack migration.

3. *Amplitude stack.* This simple procedure of combining signal amplitudes is used as a measure of last resort when 1. and 2. fail to yield 3D structural information.

To test the developed processes on synthetic data but actual survey geometries, I designed and programmed a ray-Born modeling code, and produced seven models ranging from several point diffractors up to fifteen reflectors. The developed processes were also tested on two actual data sets: one regional crustal and one high resolution mining profile, both acquired in the Archean Superior Province.

From these tests I have found that:

- When 2D crooked line geometry forms a 3D swath of data wider than a few hundred meters, 3D prestack migration will focus the events in space well enough for interpretation. The process is, however, computationally cumbersome. The wider the survey swath, the better the focusing is. Further improvement in focusing may be achieved by prestack migrating amplitude data;
- Although the cross dip stack does not output a 3D volume like prestack migration, and it retains only the stronger of overlapping reflective responses, it provides most of the same interpretative information when superimposed on a cross dip color map;
- Cross dip stack is much faster to obtain and easier to interpret than the 3D prestack migrated volume, and should be routinely applied to 2D crooked line data. Reflective events of a cross dip stack can be 3D poststack migrated by another application process developed by the author;
- Amplitude stacks require very little CPU power and are surprisingly highly informative about the general structural trends imaged.
- Regardless of the technique applied, only those parts of the reflectors that face the survey line produce a strong enough response to be imaged, and they most often represent only a fraction of the full 3D structure in the vicinity of the profile.

In general, it is often possible to recover the 3D geometry of the structure imaged by a 2D crooked line survey.

Acknowledgments

I am most of all grateful to my thesis supervisor, Prof. Gordon F. West for his continuous guidance and support throughout the coarse of this study. The amount of thought, enthusiasm and work invested by him in this dissertation is immeasurable and is felt in its entirety. His understanding when differences of view arose, and even more so his ability to tolerate my various lateral interests is accepted with gratitude. Still, I would particularly like to thank him for the kind way in which he slowly managed to help me build confidence to tackle the most challenging geophysical problems.

Helpful comments and suggestions by my research committee members, Prof. Richard C. Bailey and Prof. Jerry X. Mitrovica are appreciated. Prof. Mitrovica was easy to approach and kept a close eye on my work. Prof. Bailey's questions always provided me with a 3-stage experience: first there was the fear of what he was about to ask; then, there was the fear combined with confusion, when I didn't understand what he had just asked; and finally, once I had solved the problem, there was always (and continues to be) a deep appreciation for the valuable insights that he had provided, often on very important research issues that I had overseen.

I would like to thank my external examiner Prof. R. Gerhard Pratt and my Ph.D. exam committee members Prof. David J. Dunlop and Prof. Russell N. Pysklywec for their improvements to my thesis and for making my external Ph.D. exam a wonderful experience.

The progress of this project, specially at its early stages, was made much smoother by numerous computer programs as well as advice generously provided by Weizhong Wang.

The geophysics graduate students and the time spent together will be cherished in the years to come. I am immensely thankful to them for making my time better, both in work and leisure.

Data used in the thesis was graciously provided by the Lithoprobe Project and, thanks to Larry Petrie and Larry Matthews, by Noranda Inc. Khader Khan and Raul Chuna certainly deserve thanks for their drafting expertise and help.

Financial support in the form of the University of Toronto Doctoral Fellowships, an OGS

scholarship, CSEG scholarships and through an NSERC grant to my thesis supervisor G. F. West is greatly appreciated.

I can't "get away" without acknowledging Sageev for so many things that producing the list would be like writing the "Diary of a Mad Man". Thanks so much.

Finally, I'd like to thank my dearest Jennifer, for not fearing to share our lives in difficult times. It is her love, understanding and unconditional support that gave me the critical energy to complete this work. Thanks also for editing the manuscript, and of course, for Forde and all your tremendous care for him.

Contents

List of Tables

List of Figures

Chapter 1

Introduction

The crust of the Earth is a very heterogeneous rock mass. For economic, scientific and safety reasons, much effort has been put towards exploring its complex structure. Generally, crustal studies require a multidisciplinary approach in which various geological and geophysical disciplines are applied.

Geophysics is a science in which principles of physics are applied to the study of the Earth. It takes an advantage of the fact that "building blocks" of the Earth's crust manifest varying physical properties, and therefore make it possible to build tools to probe it remotely. The major division of geophysical methods is based on the physical property examined. Density, elasticity, electrical conductivity, magnetism and radioactivity are the main physical properties exhibited by the Earth's materials. The corresponding suites of geophysical methods developed are gravitational, seismic, electrical, magnetic and radioactive.

1.1 Seismic Reflection Imaging: Basics

Reflection seismology belongs to the group of seismic methods. This method is founded on:

- *Elastic wave propagation.* Rocks will transmit P and S elastic waves without major attenuation (other than that due to geometrical spreading of wavefronts and reflectivity) as long as the wavelength (λ) of the waves is only 2 to 3 orders of magnitude less than the path length (e.g., if λ is 10 m then the useful propagation distance is $1 - 10$ km);

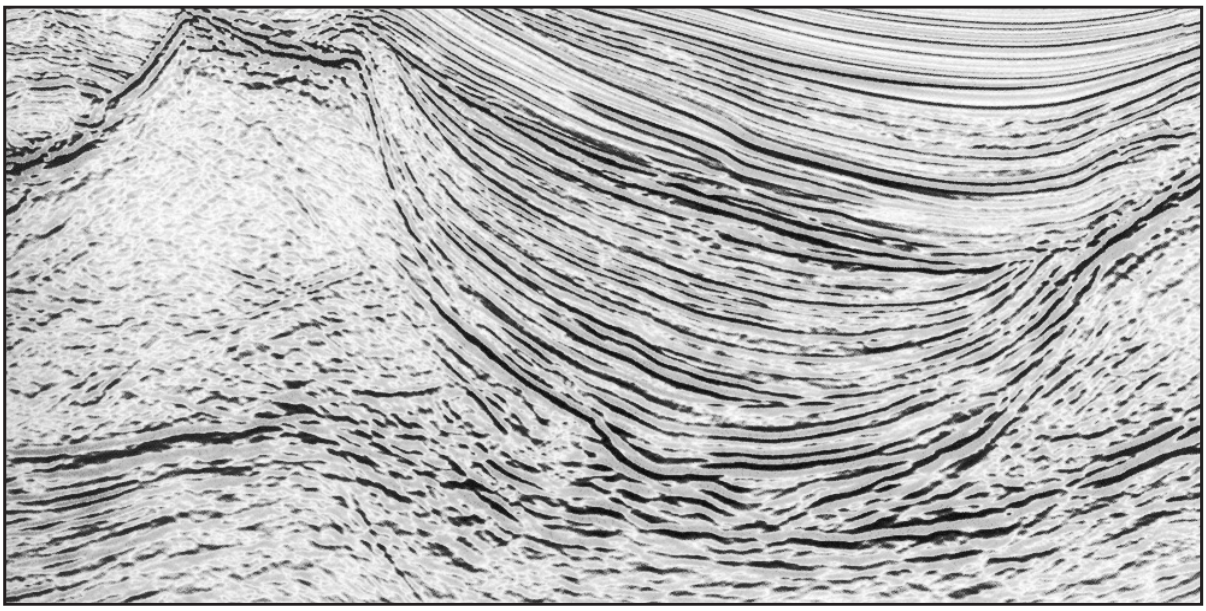

Figure 1.1: An image of salt diapirs in a Brazil sedimentary basin, extracted from The Leading Edge v19(2), page 127 (courtesy of The Society of Exploration Geophysicists, 2000). P waves were used to form this section. The richness of detail is striking. Even the difficult-to-image, steeply dipping sides of the salt diapirs are clearly visible. No labels for the axes were provided.

- *Reflectivity.* Spatial heterogeneity in the local elastic moduli and/or density of the rocks will cause a fraction of the incident elastic energy to reflect or backscatter. The term "reflection" is used when dealing with extended interfaces and incident wavefronts, and the term "scattering" when the geometry of the heterogeneity is less regular.

Reflection seismology attempts to detect and position all the boundaries and zones that mark a change in elastic moduli and/or density within the surveyed rock mass. This is done by recording and analyzing the reflected and backscattered waves generated by the seismic interfaces when sources of elastic waves are applied to the Earth at or near the surface. Importantly, the majority of lithological boundaries are also seismic interfaces allowing seismic reflection imaging to potentially be, if not geologically all encompassing then, very detailed. An excellent example of the resolving power that can sometimes be achieved with seismic reflection imaging is shown if figure 1.1.

Like echo-location systems such as radar and sonar, seismology works with time-domain signals from nearly impulsive sources. A signal's delay from the source instant is a measure of distance traveled. Thus, fundamentally, reflection seismology is a form of distance ranging, except that the velocity of propagation has also to be determined.

Error in ranging arises both from the limited resolution of traveltime determination and from velocity error.

The relatively long wavelength of recordable seismic waves means that a relatively large receiver array is needed to determine the direction of launch or approach of a seismic wave. Also, the effectiveness of a large array may be hindered because of the difficulties in estimating near surface velocities, and/or because of other destructive effects of the ever present local lateral heterogeneity. Furthermore, the heterogeneity of the material along the source-receiver paths tends to distort the wavefield before and after it encounters the target zone. It is therefore not usually practical to determine directions of wavefield propagation with sufficient accuracy to position reflecting points directly by using waves from only one source point. Lateral positioning of reflection points has to be done by different methods than are typical of radar, sonar and optical reflection imaging. The positioning step in creating a seismic reflection image is called migration, and is normally done at a late or as a final stage in data processing.

Two major steps, data acquisition and data processing can be distinguished in seismic reflection imaging. Both steps equally affect the imaging quality. Processing is always a post-acquisition task because it has to be adapted (tuned) to the actual earth surveyed, and its structure is initially unknown.

1.1.1 Seismic Reflection Data Acquisition

Because of near-surface heterogeneity, the need to separate waves of different type, the complexity of the target heterogeneity and the need to determine average velocity structure, a seismic reflection survey essentially consists of a relatively dense grid or line of source points, each recorded by an even more dense array of receiver points. The necessity to separate sources from receivers during data acquisition is a consequence of source-generated noise that can often completely mask reflected/scattered waves, occasionally even for the full length of recording. The reason for having many more observation points than the source points is because recording points are much cheaper. But there are maximum size limits to receiver arrays also, since many of the data processing procedures are based on an assumption that seismic rays have relatively steep dips. Typically, receiver arrays are designed to have a length $< \frac{1}{2}$ of the target depth of exploration.

Each receiver point itself is also an array. From ~10 to ~20 geophones ("listening devices") usually form a single recording (trace). Local geophone arrays are mostly used

to suppress random noise and surface waves.

The large number of sources and receivers used to collect data allow for multiple "illumination" of the target heterogeneities. The measure of data (trace) density is called the fold, which is the number of traces per desired unit surface area. If the image of a volume of interest is thought of as a spatial array N_x, N_y, N_z pixels large, the number of time samples on seismograms should roughly correspond to N_z through the wave velocity, and the desired unit surface area should equal the pixel surface area. The number of seismic recordings (traces) collected by the survey can be expressed as the product of sources and receivers (n_s x n_r). All modern surveys arrange that:

$$\frac{n_s \text{ x } n_r}{N_x \text{ x } N_y} \equiv \text{“FOLD”} \gg 1. \tag{1.1}$$

Typically, the fold is greater than 10 and smaller than 100. The fold of a single survey does not automatically indicate the density of information obtained at depth. For the same survey parameters, as the dip of the studied structures steepens, the area "illuminated" decreases and the information density increases.

The recording time during seismic acquisition is usually set to be significantly longer than the two way reflection time of the deepest zone of interest. This allows diffracted responses that improve focusing during migration to be largely recorded.

In order to facilitate the separation of what is considered as signal (P, or S, or converted wave reflections) from other types of reflections, sources and receiver used to collect the data are made directional. While surveys can be designed to record any type of reflected signal, or even all of it, most investigations are still P waves studies that employ vertical motion geophones.

Two types of surveying are most common: 2D and 3D. 2D surveying is mostly carried out on linear profiles and has as its objective a 2D cross-section of the subsurface along the survey line. 3D surveying is carried out over a desired surface area and results in a data volume that contains information describing the reflectivity of the subsurface region of interest. But before the collected signal can usefully be exploited for interpretation, much work on forming the images has to be carried out.

1.1.2 Seismic Reflection Data Processing

The main goal of seismic processing is to construct high quality reflectivity images of the investigated subsurface. In order to do so, seismic data processing (table 1.1) has to

accomplish many objectives. For example, it has to:

- Allow for the actual topography of studied area and configuration of the survey (geometry);
- Correct for near surface effects including miscellaneous variable time delays and local waveform and amplitude distortions (statics, source-receiver deconvolutions, source-receiver amplitude corrections, etc.);
- Correct for the spherical divergence and anelastic attenuation (amplitude corrections);
- Separate waves of different type, e.g., P and S reflections, P and S direct waves and surface waves of various types (e.g., local slant stack, FK filtering, etc.);
- Attenuate environment-generated waves caused by wind, traffic, running water, electrical leakages, etc. (e.g., 1D, 2D and 3D bandpass filtering);
- Determine average velocity structure down to the deepest zone of interest (velocity analysis);
- Remove the effect of non-coincident sources and receivers on traveltimes (normal moveout (NMO) and dip moveout (DMO) time shifting);
- Create intermediate image products like the synthetic zero-offset seismic time section or volume (CMP stack);
- Position reflected signals both laterally and in depth (migration).

Imaging is typically a "bootstrap" process which proceeds in a few iterations to the final result. Usually, the first image is produced by common mid-point (CMP) stacking and is called, for a 2D case, a "synthetic zero offset seismic time section" (SZOSTS) or a "CMP stacked section". For a 3D case, CMP stack becomes CMP bin stack and the terms used for the obtained output are SZOST data volume or CMP stacked data volume. The goal of a CMP bin stack is to form a single seismic trace of reflected energy (of designated type - usually P reflection of P incident waves) for every surface pixel of the output image. This trace signal should resemble that which might have been recorded with a coincident source and receiver at the surface point under ideal conditions (no surface topography, no effects of local heterogeneity, no interference between wave types).

Table 1.1:

SCHEMATIC DIAGRAM OF TYPICAL SEISMIC DATA PROCESSING		
FIRST PASS **MAY BE REPEATED SEVERAL TIMES TO OPTIMIZE PARAME-TERS**	• PREPROCESSING ➤ Geometry ➤ Statics ➤ Deconvolution ➤ Amplitude corrections ➤ Bandpass filtering ➤ Surface wave/noise removal	• CMP PROCESSING ➤ Binning/CMP gathering ➤ Moveout velocity analysis ➤ Dip moveout partial migration (omit in first pass) ➤ CMP stack to SZOSTS ➤ Poststack time migration ↓
FINAL PASS	• PRESTACK MIGRATION ➤ Construction of final migration velocity model ➤ Prestack depth migration of all preprocessed data traces →	COSMETIC FILTERING - IMAGE PREPARATION

The time traces of the CMP stacked data contain only amplitude and range information. Unless the mapped structures are smooth and nearly horizontal, migration is required to turn stacked data into an image of structure. The migration does this by using the surface locations of the traces of stacked sections/volumes as a giant space array to determine the lateral position of each event.

Both CMP stacking and migration require velocity models of the ground. These are constructed by analyzing how various reflection events correlate from trace-to-trace.

In processing data from geometrically complex terrains, there will be several steps of velocity determination. Then, the final image will usually be prepared by so called prestack depth migration where the (corrected and adjusted) n_s x n_r data traces are combined directly to obtain the reflectivity image of the subsurface, bypassing the preliminary step of CMP stacking.

1.1.3 Important Considerations for Reflectivity Imaging

The quality of seismic imaging depends on factors such as:

1. Spatial relationship between the survey and the reflectors;
2. Vertical resolution;

3. Horizontal resolution;
4. Surface shape of the reflectors; and
5. Signal to noise (S/N) ratio.

1. Reflection signals are the strongest and easiest to interpret when the survey profile/area approximately faces reflectors of interest.

2. Under normal ground conditions, all the available controlled and semi-controlled seismic sources (like vibrators and explosives respectively) generate band limited signals. Therefore, the actual (or computed) transient signal that constitutes an elementary primary or reflected wave event has a waveform of quite finite duration called a wavelet. When the two successive physical boundaries are close to each other, the wavelets reflected from these boundaries interfere with each other. Interference between the signals can become very strong and make it impossible to distinguish if there are two, one, or in some cases any reflecting contacts. The point at which the seismic reflection method fails to separately image two adjacent boundaries (change in elasticity/density) is called the limit of vertical or temporal resolution.

A basic grasp of limits of vertical resolution and constructive/destructive interference can be gained by examining figure 1.2. Parts (a) and (b) show schematic diagrams of the thin layer models used. The first model (a) is one of the thin layer pinched between two different materials with the acoustic impedance increasing with depth. The second model (b) is of a thin layer embedded in a homogeneous material of a different acoustic impedance than the thin layer. Chosen reflection coefficients on the boundaries would cause strong reflections in real data acquisition. Parts (c) and (e) show the generated responses for the model (a) and parts (d) and (f) show the responses generated using model (b). The model was built so that the amplitude fall-off proportional to the distance traveled, and the reduction in amplitude due to each reflection and first order multiples, was taken into account. The waves are impinging normally at the boundary. Layer thickness varies from $2\lambda_d$ to $\lambda_d/16$, where λ_d is the dominant wavelength.

For layer thickness $\geq\lambda_d$, the events corresponding to each layer boundary are well separated in time. As the layer thickness gets smaller the reflections from both boundaries progressively start to interfere. Both boundaries are visible up to a thickness of $\sim(\lambda_d/4)$ for model (a). For thickness less than $\sim(\lambda_d/4)$ two events appear as one, but because of constructive interference its waveform is distorted and the amplitudes stronger than when the wavelets are separated. The amplitude tends to become twice that of one

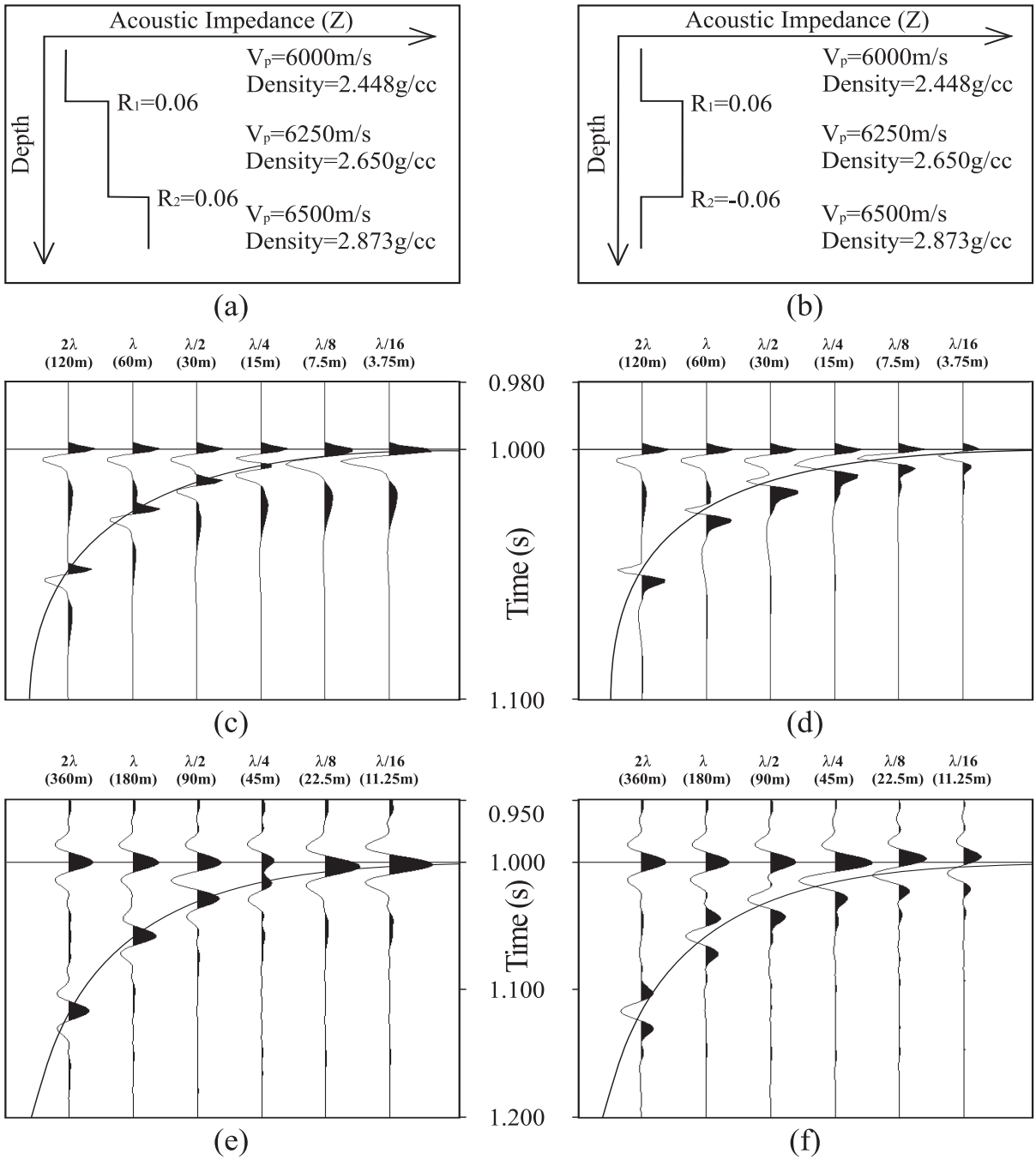

Figure 1.2: Parts (a) and (b) are models used to generate the thin layer seismic reflection response for various layer thicknesses. The layer thickness is expressed as a multiple or a fraction of the dominant wavelet which was calculated using the compressional wave velocity given in the models (a) and (b) and the dominant frequency of ~35 Hz for crustal scale and ~100 Hz for exploration scale seismic surveys. The upper boundary of the thin layer is positioned at an arbitrary depth of 3000 m (1 s). Butterworth minimum-phase wavelet (30-180 Hz) was used for mineral exploration scale modeling (parts (c) and (d)) and Klauder zero-phase wavelet (10-56 Hz) for crustal scale modeling (parts (e) and (f)) of the thin layer response. The discussion on the generated models is given in the text.

boundary alone as the thickness approaches zero. Examples obtained using model (b) show that both events are separately visible up to $\sim(\lambda_d/2)$ after which first constructive interference ($\sim(\lambda_d/4)$) and later ($< (\lambda_d/4)$) destructive interference occurs. From the thickness of ($\sim(\lambda_d/8)$) modeled data looks like a derivative of the input wavelet with steeply diminishing amplitudes as the layer thickness approaches zero.

The two most important insights gained from examining the data in figure 1.2 are:

- The limit of vertical resolution of $\sim (\lambda_d/8)$ as stated in the literature that often references the work of Widess (1973) appears to be exaggerated;
- Constructive and destructive interference can, at its extreme, make weak reflectors appear strong and strong reflectors disappear in seismic sections.

3. Reflection events as observed on individual seismograms do not originate from a point on reflecting surface but rather from a zone on the reflector. The radius of this zone, the *Fresnel Zone*, is defined for P waves as (e.g., Dobrin and Savit, 1988):

$$Fr = \frac{V_P}{4}\sqrt{\frac{t}{f}} \tag{1.2}$$

where V_P is the compressional wave velocity, t is the two-way travel time, and f is the dominant frequency of the reflection. The radius of the Fresnel Zone is governed by the limits of the constructive wave interference and is frequency-dependent. Bodies larger than the Fresnel Zone will generate reflections of full amplitude (table 1.2). A body occupying only 25% of the Fresnel Zone is still imaged but with the amplitude that is about 60% of the one that would have been recorded if the body was larger or equal to the Fresnel Zone. The Fresnel Zone thus does not represent a sharp cut-off threshold in imaging. Smaller bodies can also be successfully imaged. And if reflection signals can be recorded with sufficient accuracy, migration can reduce the lateral resolution from the Fresnel limit to a few times the vertical resolution limit.

4. Reflection amplitude and its relation to the size of the Fresnel Zone is calculated for specular mirrors; surfaces that are smooth to better than $\sim\lambda_d/4$. The contact zones and layer boundaries in igneous and metamorphic terrains are rarely even close to being specular reflectors. These interfaces are often rough and can act as much as scatterers of elastic energy as mirrors, thus adding another factor (surface shape of the reflector) for consideration in seismic imaging.

Table 1.2: Fresnel Zone size in typical crustal scale and mineral exploration scale seismic reflection surveys. Average velocity used to calculate the Fresnel Zone was 7000 m/s and 6000 m/s for crustal scale and mineral scale surveys respectively while the dominant frequencies used were 35 Hz and 100 Hz.

Crustal scale		**Mining scale**	
Time(s)	Fresnel Zone(m)	Time(s)	Fresnel Zone(m)
3.0	≈512	0.5	≈106
6.0	≈725	1.0	≈150
9.0	≈887	1.5	≈184
12.0	≈1025	2.0	≈212
15.0	≈1146	2.5	≈237
18.0	≈1255	3.0	≈260

5. S/N ratio weakens as the examined zone is further away from the source and the receivers, because of geometrical spreading and anelastic attenuation. Furthermore, a part of the source wave energy is returned back at the lithologic boundaries due to reflectivity.

Spatial relationship between the survey and the target reflectors, vertical resolution, horizontal resolution, surface shape of the reflectors and signal to noise (S/N) ratio have a very profound effect on seismic reflection imaging and must be taken into account during acquisition, processing and interpretation of seismic data.

1.2 Reflection Seismology in Sedimentary Basins

Sedimentary rocks cover approximately 75% of the Earth's continental surface and form most of the landscape (Hamblin, 1991). They hold a large amount of mineral wealth, most of the fossil fuels, and store huge amounts of fresh water in their upper parts. The longstanding great effort directed toward the exploration of sedimentary environments comes, therefore, as no surprise. Their lesser structural complexity in comparison to igneous and metamorphic terrains further facilitates the investigations. As a result, the structure of sedimentary basins is, in general, better determined than that of the crystalline crust. Much of that knowledge has been gained through seismic reflectivity studies that work particularly well in stratified environments.

Early History of Reflection Seismology. The earliest experiments with the seismic reflection method were conducted in central Oklahoma (USA) from 1919 to 1921 by J. C. Karcher (Dobrin and Savit, 1988). By the mid 1930's this method not only became a standard exploration tool, it has become the most widely used geophysical technique.

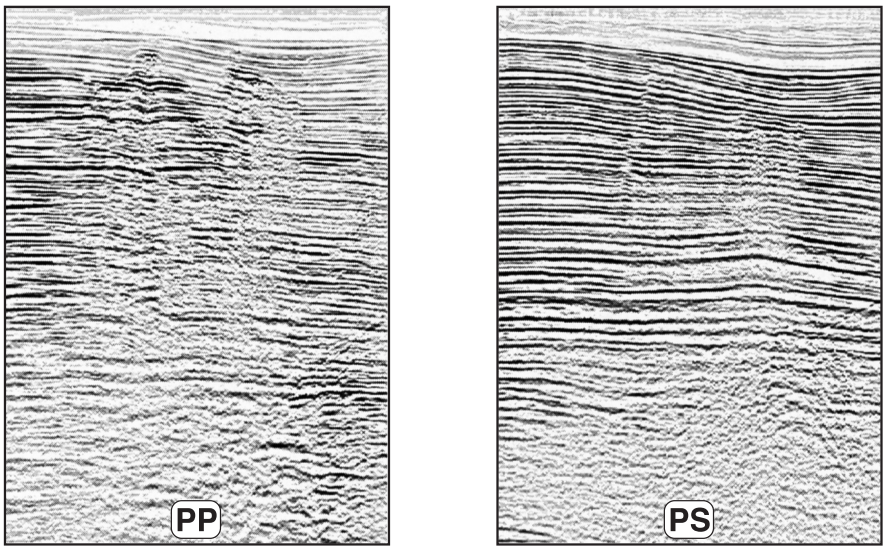

Figure 1.3: Both sections shown are migrated reflectivity images of the same subsurface (form the Far East). The left image is formed using compressional wave (PP) reflectivity and the right one using converted wave (PS) reflectivity. The images presented were extracted from The Leading Edge v18(11), page 1278 (courtesy of The Society of Exploration Geophysicists, 1999). The PP reflectivity is disrupted throughout most of the section due to gas in shallow zones. The PS reflectivity images the shallow fault well and shows good event continuity. No labels for the axes were provided.

Over the years, the reflection method has continuously improved. It is interesting to note that two of the leaps forward in imaging were due to a brilliant solution of a rather simple problem and to an extension of that method to an additional dimension. These are the common mid-point stacking method (Mayne, 1962) and the 3D reflection method (Walton, 1972), respectively.

Imaging quality progressed in the early days so rapidly that reflection studies of sedimentary basins provided enough insight of their geology and structure, even to the extent that a field of expertise known as "seismic stratigraphy" emerged by the early 1960's (Boggs, 1987).

1.2.1 State of the Art Reflection Seismology

The past two decades have seen an even greater progress in the seismic reflection imaging of rock structures at depth. During this time the seismic reflection method has evolved from a procedure capable of imaging only simple, sedimentary basin strata to one capable of resolving highly complex structures that have experienced considerable deformation (see figure 1.1). This enormous increase in resolving power is chiefly attributed to the

development of 3D survey methodology and prestack migration. Deep crustal structures may now be laterally resolved to much less than 100 m; quite comparable to the long obtained similar vertical resolution. Furthermore, S and converted waves, seldomly considered in the early studies, are now used to produce reflectivity images in addition to P waves (see figure 1.3).

Today, the reflection method comes closer than any other prospecting technique to providing a structural picture of subsurface, comparable to what could be obtained from a mass of boreholes in close proximity.

1.3 Seismic Reflection Imaging in Igneous and Metamorphic Terrains

Although the structure of crystalline (igneous and metamorphic) terrains is difficult to map compared to sedimentary domains, there is value in updating knowledge about these regions. Measured by nothing else but sheer volume, igneous and metamorphic rocks must be considered as integral elements of our environment. These rocks constitute all but a few percent of the Earth's crust (Stokes and Judson, 1968). The bulk of the mineral riches, excluding fossil fuels and fresh water, are found in them. Moreover, a large part of sedimentary material is derived from the igneous and metamorphic rocks.

Because: a) drilling is extremely expensive and its penetration restricted to the very top of the Earth's crust, b) geologic data provide surface information that can be extrapolated in depth only so far, and c) geophysical methods other than reflection seismology have limited resolution and/or depth of penetration, it is logical to consider seismic reflection imaging for the systematic exploration of the crystalline crust. However, crystalline igneous-metamorphic rocks are formations wherein the geometry of the structures is often much more complicated and at a much finer scale than in sedimentary basins. Thus, a lot of enthusiasm, courage, time, and even chance discovery has been needed to bring this technique to crystalline environments.

1.3.1 Common Observations in the Early Crustal Work

[1] In 1950 the Shell Oil Company crew working in an area covered by clinker beds in Big Horn County, Montana, near the Wyoming border was greatly troubled by unusually long low frequency surface waves that were completely masking the reflections from the target sediments. To study this phenomenon, the camera was set to record for over 10 seconds. During the interpretation of the recorded seismograms, Arne Junger (Junger, 1951) noticed for the first time coherent reflections apparently coming from depths where no sediments could possibly exist. This chance discovery cast a new light on the reflection technique, particularly on the possibility of using it to explore the crystalline basement of the Earth's crust. Several successful experiments followed (Widess and Taylor, 1959; Kanasewich and Cumming, 1965; Dix, 1965; Dohr and Fuchs, 1967; Clowes, Kanasewich and Cumming, 1968; Clowes and Kanasewich, 1970; Smithson, Shive and Brown, 1977) and gradually confirmed Junger's conclusions.

Researchers leading early surveys focused on demonstrating that the coherent events recorded at late times on the seismograms are indeed reflections from within the crystalline crust. The alternative explanations were multiple reflections from the overlaying sediments or reflected refractions. The likelihood of reflected refractions was eliminated using cross-spreads and simple examination of recordings was enough to reject the possibility of multiple energy.

The seismic character of the reflections was explored carefully, while some attention was also given to their geological origin. Reflections varied greatly in time and appearance from place to place and displayed spatial continuity in the range from a few hundred meters to a couple of kilometers. The origin of reflectivity was explained as being closely related to the base of the "granitic" layer (in Europe also known as Conrad discontinuity) and/or the base of the "basaltic" layer (better known as Mohorovičić discontinuity). What was interpreted as the Conrad and Moho "discontinuities" appeared on the sections as transition zones.

These were the core common elements of the early reflection experiments in igneous and metamorphic rocks. Although the surveys were related by sharing the same goal (to extend the application of reflection seismology to crystalline terrains) each of them contributed plenty of original information. What follows are some of the selected ex-

[1] With due respect to the significant work done in the field of reflection imaging of the crystalline terrains which has been published in languages other than English, this historical overview does not purport to be a globally comprehensive one.

amples. Geological reconnaissance investigations of the igneous and metamorphic rocks on or near the surface indicate they may be quite heterogeneous. This led Arne Junger (1951) to postulate that similar reflection generating rock patterns might be present at greater depths. Widess and Taylor (1959) were the first to correlate reflections from the Wichita mountains crystalline basement in Oklahoma with the density log. The possibility of multiple energy from the overlaying sediments was further discarded by Dix (1965) who carried out a survey in Mojave desert, California, where no reflections from the alluvial cover just 100 meters thick were observed. Researchers from West Germany were the first to systematically gather deep reflection data in cooperation with the oil and gas industry. Furthermore, they suggested the use of controlled sources for the crystalline crust investigations and noticed (what they interpreted as) subcrustal reflections at two way traveltime of up to 25 seconds (Dohr and Fuchs, 1967). In Canada, synthetic seismograms were used to prove that the crustal reflections were not multiples from the overlaying sedimentary strata (Clowes, Kanasewich and Cumming, 1968). Clowes and Kanasewich (1970) later added frequency and depth dependent attenuation to their modeling routine to study the reflections that they attributed to the Riel[2] and Moho discontinuities, and they found that models consisting of first-order (jump) discontinuities or intermittences, linear gradients in velocity over depth intervals less than one wavelength, or isolated step-like velocity increases were generally unacceptable. Only the layered transition zone models comprised of thin sills of alternating high and low velocity material satisfied most of the observational data. Smithson *et al.* (1977) examined data from the first reflection survey over an area of exposed crystalline rocks. The section they obtained resembled in many ways seismic profiles gathered in sedimentary basins.

The early work on extending the seismic reflection method to study the crystalline crust often represented an isolated effort of a single individual or a group of scientists. In spite of that, their efforts enriched the technique and led the way to the systematic, well planned and funded projects to probe the continents and their margins.

1.3.2 Regional Studies of the Continents and their Margins

In science, major advances in observation are commonly followed by major steps forward in understanding. Several decades ago it was recognized that in earth sciences the next

[2]Conrad discontinuity is the European term for the base of the "granitic" layer and any reference to it in North America implies petrological or structural correlation. Therefore, Clowes, Kanasewich and Cumming (1968) named the corresponding boundary in North America, Riel discontinuity.

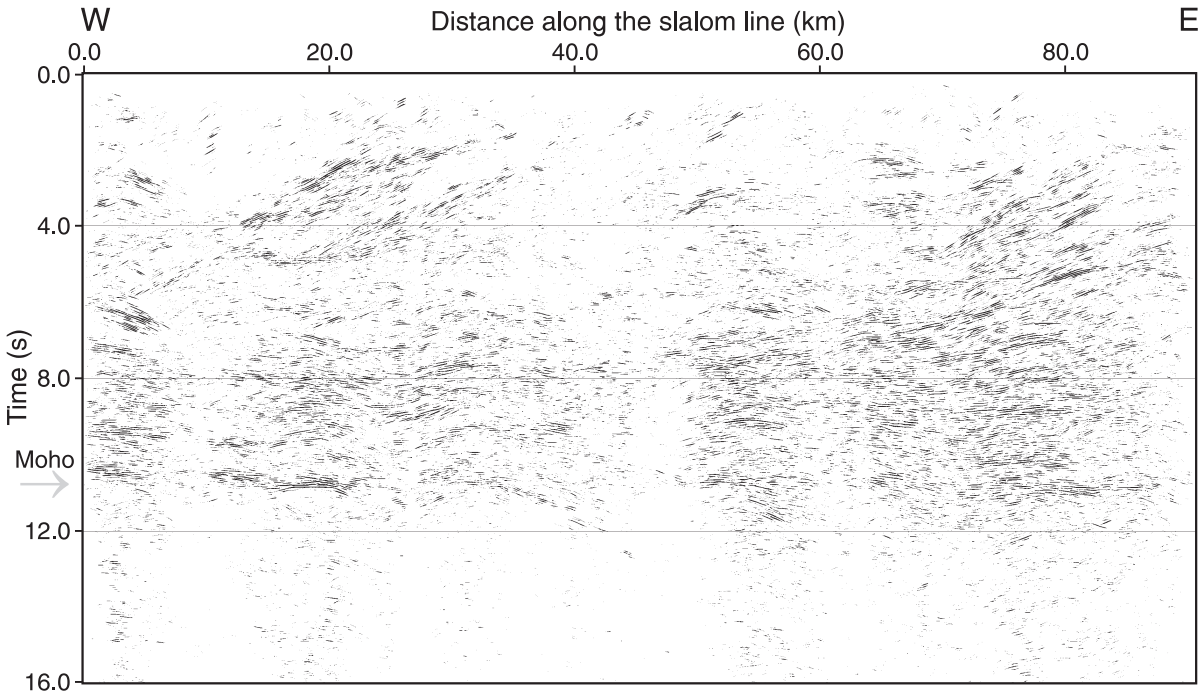

Figure 1.4: Unmigrated crustal profile SBC 10 from the Southern Cordillera transect (Courtesy of Lithoprobe Seismic Processing Facility). The section exhibits typical crustal features: a) Relatively little of the reflectivity is observed in the top few seconds of the data; b) Most of the reflectivity recorded originates within the middle and lower crust; c) Moho discontinuity is relatively well defined; d) Little or no reflectivity occurs within the upper upper-mantle. Profile SBC 10, likewise most of the seismic profiles done in crystalline terrains, is a P wave reflectivity image.

paramount source of new observational information could be high resolution seismic reflection profiling of the deep crust. As a result, COCORP (Consortium for Continental Reflection Profiling) was established in the United States of America in 1974 (Matthews and Smith, 1987). This was the first coordinated study of the Earth's crust and the upper upper-mantle for which deep seismic reflection profiling provided the core of the data. The success of the COCORP project resulted in the rapid spread of the technique, and indirectly, it initiated[3] many similar systematic multidisciplinary projects around the globe.

Canadian geoscientists became involved with integrated deep crustal studies in 1984 with the institution of the phase I of LITHOPROBE (Clowes (editor) 1984, 1989, 1993, and Garland, 1986). Presently, the LITHOPROBE project is in its fifth phase (Clowes (editor), 1997).

[3]An exhaustive list of the projects and their abbreviations can be found, for example, in the work of Matthews and Smith (1987).

The former Soviet Union and its successors have consistently carried out comprehensive studies of the continental crust since 1960's (Fuchs et al. (editors), 1990). However, the nucleus of the work carried out in the former Soviet Union was focused on very deep drilling and tens of thousands of kilometers of refraction profiles.

P wave seismic reflection imaging of the whole crust and mantle lithosphere has proved itself to be very successful (a typical crustal reflectivity profile is shown in figure 1.4). Multidisciplinary collaborative earth science projects have unveiled the present regional structure of the continents along tens of thousands of kilometers of deep seismic reflection profiles. As the data are gathered at an ever-increasing rate, and the computational power improves, it appears that the most difficult challenge in the future will be to put this information in a geologic perspective, local and global.

1.3.3 Detailed Seismic Reflection Studies for Mineral Exploration

The application range of reflection seismology has been pushed continuously. For example, 2D and 3D techniques are used for coal mining at the exploration stage (Urošević and Juhlin, 1997, Cocker et al., 1997), for high resolution near-surface geological and engineering studies (Steeples and Miller, 1990, Siahkoohi, 1997) and for hydro-thermal investigations, though to a significantly lesser extent. This leaves undoubtedly mineral[4] exploration, particularly in hard-rock environments as one of the last frontiers for application of the seismic reflection method.

There exist two simple reasons for extending reflection seismology to "hunt" for minerals. First, some of the valuable mineral deposits are found in mixed environments of interchanging crystalline and sedimentary rocks. These terrains exhibit some similarities to sedimentary basins where reflection imaging provides the highest quality information about the subsurface structure. Second, a large gap exists, specifically in hard-rock mediums, between the exploration depth attainable with conventional geophysical techniques and depth from which ore can be mined economically. Even with the modern large loop time-domain electromagnetic systems the depth of exploration is extended to only about 500 meters, or several times the size of the target (Milkereit et al., 1997). Magneto-telluric methods are being investigated but have not yet shown capability to resolve discrete sul-

[4]The term "mineral" is often taken to include naturally occurring materials like coal, oil and gas, coral, pearl, etc. Here and throughout this work the term is used in a stricter sense of "inorganic natural material".

phide bodies at depth. If modern mining methods are capable of economically extracting ore to depths of at least up to 2500 meters, then it is only natural to see a significant interest in developing a new tool to detect to these deposits.

Given the advances in seismic data acquisition, processing and interpretation, which have taken place especially in the last couple of decades, large mining companies seem to be focusing their exploration endeavors towards exploiting the seismic reflection technique as the most promising one to detect, and even more so to delineate massive ore bodies at depth (Salisbury et al., 1996). The first at least moderately successful tests with the 2D seismic reflection method began in Southern Africa in 1982 (Stevenson and Durrheim, 1997). The targets were gold (Witwatersrand Basin), platinum (Bushweld Complex) and base metal (Tsumeb, Kombat and Otjihase) mineralizations. One could have foreseen that a region as famous for its splendid mineral resources and rich mining history as Southern Africa is, would encourage bringing in new technology to mineral exploration. However, in addition to their tradition, they had a "helping hand" with regards to their geologic settings. Most of the deposits in Southern Africa occur within gently dipping interbedded igneous, metamorphic and sedimentary rocks or in pipe-like paleokarst features covered with younger sediments (Stevenson and Durrheim, 1997). The same region has also seen the first 3D seismic reflection mineral project in 1991 named Oryx (Eaton et al., 1997). Since then, Anglo American Corporation alone has done four 3D surveys (Pretorius et al., 1997).

Canada, another natural resource giant, followed shortly after with 2D and 3D seismic reflection experiments in the domain of mineral investigations (Adam et. al., 1997, 1998, Eaton et. al. 1997, Milkereit et. al. 1997, etc.). The imaging tasks in Canada are much more complex as most of the mineral wealth resides in greenstone belts characterized by steeply dipping structures and ore bodies of irregular shape. Nevertheless, surveys done in Canada added to the initial success achieved in Southern Africa.

The application of seismic reflection technology in petroleum and mineral exploration is parallel to a certain extent whether working in two or three dimensions. The 2D method is used predominantly at exploration stage to delineate basic subsurface structure and look for possible targets, while the 3D method is used mostly for mine planning.

Arguably the most successful seismic reflection survey for mineral exploration took place in 1994 in the Republic of South Africa at Vaal Reefs Number 10 Shaft Gold Mine. On the basis of the 3D data cube interpretation the mine design was completed for the entire life of the mine, and that is until the year 2010 (Pretorius et al., 1997). The total survey

coast of $1.07 million (USD) would fund in 1994 only one multiply deflected 3000 meters deep drill hole (somewhat over the average depth to this deposit). Case histories like this one indicate that reflection seismology is a useful and economically plausible tool in mineral exploration.

1.4 Origin of the Continental Crustal Reflections

Much can be inferred about the interfacial geometry between different materials at depth through reflectivity[5] imaging. The ultimate goal of geology, however, is to conduct a successful geologic interpretation, for which knowledge on what causes the reflectivity within the crust is necessary. To facilitate the latter discussion on the possible sources of imaged reflectivity two divisions of the continental crust are presented.

On the basis of geological and seismic reflection data, the continental crust may be loosely divided into (Rudnick and Fountain, 1995): an upper (0 to ~10-15 km), middle (~10-15 to ~20-25 km) and lower (>~20-25 km) crust. Under any sediment cover, the upper crust consists chiefly of deformed low to medium grade metamorphic supracrustal rocks ("greenstones") intruded by large volumes of granitoids rocks. The middle crust contains similar rocks but in the upper amphibolite facies, which are also found in surface outcrop or as xenoliths in intrusions. The lower crust is believed to consist of metamorphic rocks in the granulite facies, that are accessible either as occasional large tracts of surface outcrop (high grade terrains) or as fragments carried from great depths in volcanic conduits (xenoliths).

Considering the type of the information used to study the origin of reflectivity, the continental crust may be partitioned into the *visible crust* (0 to ~3-6 km) and *remote crust* (>~3-6 km). The visible and remote crust are investigated in two ways: in-situ by petrological and geochemical methods performed on surface rock specimens and core samples extracted from the boreholes; and remotely by means of geophysical techniques. However, the knowledge gathered about the remote crust is of much greater uncertainty

[5]Almost all of the surveys done in crystalline terrains are P wave reflectivity studies. P wave reflectivity occurs at boundaries between mediums exhibiting different acoustic impedances. Wherever a broad wavefront impinges orthogonally on a broad surface that marks the change in acoustic impedance (Z) the amount of energy reflected back will mostly depend on the reflection coefficient R. IF Z_1 is the acoustic impedance of the medium the incident and reflected waves propagate in and Z_2 is the acoustic impedance of the second medium forming the boundary with the first medium, $R = \frac{Z_2 - Z_1}{Z_2 + Z_1}$. Acoustic impedance itself is proportional to the product of density (ρ) and compressional wave velocity V_{P} of the medium examined. The reflection coefficient also depends on the angle of incidence.

as rock samples obtained on the surface or in the drill holes are only believed to be originating from the depths greater than ~3-6 km. Even if they truly do come from far below, they are found in very different conditions than those that exist at great depths. Furthermore, the resolving power of the remote techniques decays as a function of depth.

1.4.1 The Visible Crust

The simplest way of gaining a general view of among which superimposed rock groups reflectivity will occur, is to observe the Nafe-Drake curve (figure 1.5) and look for large impedance contrasts. Sediments take up the largest area enclosed by the curve and their acoustic properties are best known. These rocks show large variations in P wave velocity, the dominant cause of reflectivity in sedimentary basins. A huge impedance contrast between many sedimentary and crystalline rocks exists and practically every boundary between them is a strong reflector of elastic energy. For igneous and metamorphic rocks alone, as a rule of thumb, an impedance difference of about 2.5×10^5 g/cm^2s gives a reflection coefficient of 0.06, the minimum coefficient required for a clearly visible reflection in most basement settings after allowance has been made for noise (Salisbury et al., 1997). This means that lithological boundaries of overlaying felsic, mafic and ultramafic rocks, and even some boundaries within felsic and even more so within mafic and ultramafic rocks, could possibly be imaged. The process of metamorphism can significantly change acoustic properties of rocks. A good example is serpentinite, a rock formed by the metamorphism of ultrabasic rocks rich in olivine and pyroxene, that has a significantly lower acoustic impedance than its source rock.

Reflectivity is also strongly influenced by porosity, fluid type and fluid saturation of rocks. Although these factors have a much smaller impact in hard-rock environments because the porosity of these rocks is relatively low outside the weathering zone, their impact is big enough to make various shear zones acoustically visible.

The overall effect is that many of the important lithological and structural contacts in crystalline and mixed (sedimentary/crystalline) terrains, regardless of their origin, are strong enough reflectors to be successfully imaged by the reflection seismology.

The geologic processes causing juxtaposition of acoustically very different lithological units may be divided into five principal categories (modified from Green et al, 1990): (1) depositional layering; (2) intrusive layering; (3) tectonically imposed layering, including shear zones of various type; (4) metamorphic layering; and (5) hydrothermal phenomena.

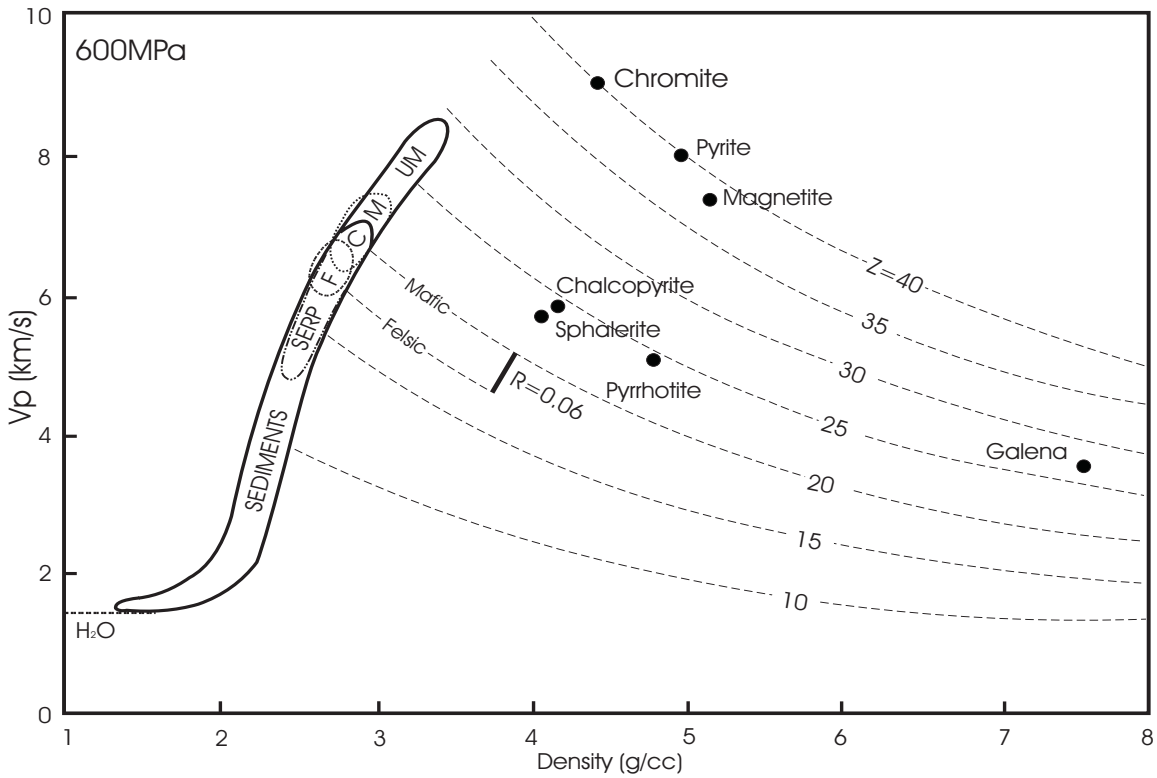

Figure 1.5: Compressional wave velocities (V_P) versus densities at an arbitrary confining pressure of 600 MPa, for selected base metal ore minerals superimposed on the Nafe-Drake curve for common rocks. Dashed lines represent lines of constant impedance (Z); bar shows minimum impedance contrast (about 2.5×10^5 g/cm^2s) required to give strong reflections (R=0.06). Abbreviations: F = felsic; M = mafic; C = carbonates; SERP = serpentinite; and UM = ultramafic. Figure adapted from Salisbury et al. (1996).

While each of the principal categories is fairly complex and may be further divided into sub-groups, only the hydrothermal processes will be discussed in greater detail, for they bear great importance to the genesis of many ore deposits.

Of the two main types of hydrothermal activity: (a) deposition and (b) alteration processes (e.g. serpentanisation, kaolinisation, etc.), deposition is generally regarded "responsible" for the origin of massive sulphide deposits, the main source of the base metal (e.g. Cu, Pb, Zn, etc.) ores. The ore may form VMS (volcanogenic massive sulphide) deposits near the mid-ocean ridges where strong and continuous volcanic activity occurs, it may fill the fissures within the rocks that surround an igneous intrusion, or it may completely replace the rocks that enclose the intrusion.

In any type of a well stratified media where mineral deposits take layered form, reflection seismology has a fair chance of imaging them, if not directly then indirectly, by imaging some other marker horizon that structurally follows the deposit. This type of "piggy-back

riding" is not feasible when VMS and other large non-conformable deposits are examined. These ore bodies can be imaged only if their impedance contrast with the host rock is large enough to cause reflections visible on the seismograms.

Laboratory measurements of density and longitudinal velocity of common ore minerals (some examples are given in the figure 1.5) show that these minerals occupy V_{P} field that is distinct from that of common rocks. The ore minerals differ from common rocks especially by exhibiting much higher densities, while V_{P} takes a wide range of values. Mostly because of their high densities, ore minerals have higher impedances than the common felsic to mafic host rocks. The impedance of the ore is governed by the simple mixing rules causing ores of even intermediate grades to have high acoustic impedances relative to the host rock (Salisbury et al., 1996). This suggests that the large ore bodies, in particular VMS deposits, should make strong reflectors.

Similar conclusions were drawn from in-situ measurements at various mining cites across Canada, including Sudbury, Timmins, Val d'Ore, Matagami, Bathurst and Myra Falls. Density and acoustic velocity logs show that massive sulphide bodies generally exhibit strong acoustic impedances with the surrounding rocks (Pflug et al., 1997). These logs also show that many rock interfaces in crystalline terrains appear to be strong acoustic boundaries and therefore may also produce strong reflectivity (figure 1.6).

In addition to predicting what could possibly be imaged in terms of ore deposits and general structure in the crystalline and mixed terrains via laboratory measurements and well logging, it is beneficial to also look at what has already been imaged by reflection seismology. Table 1.3 is a summary of selected seismic reflection surveys done. It explains briefly survey type, what was the target and what was imaged. Only surveys for mineral exploration were included because they are supported by a large wealth of borehole information.

The information presented in the table 1.3 indicates that there is a high correlation between what lithological contacts are predicted to yield strong reflections and which ones do. However, for any type of generalization much more data needs to be collected and examined.

1.4.2 The Remote Crust

The structural understanding of the remote continental crust has improved dramatically over the last decade as a result of detailed seismological studies, and studies of the

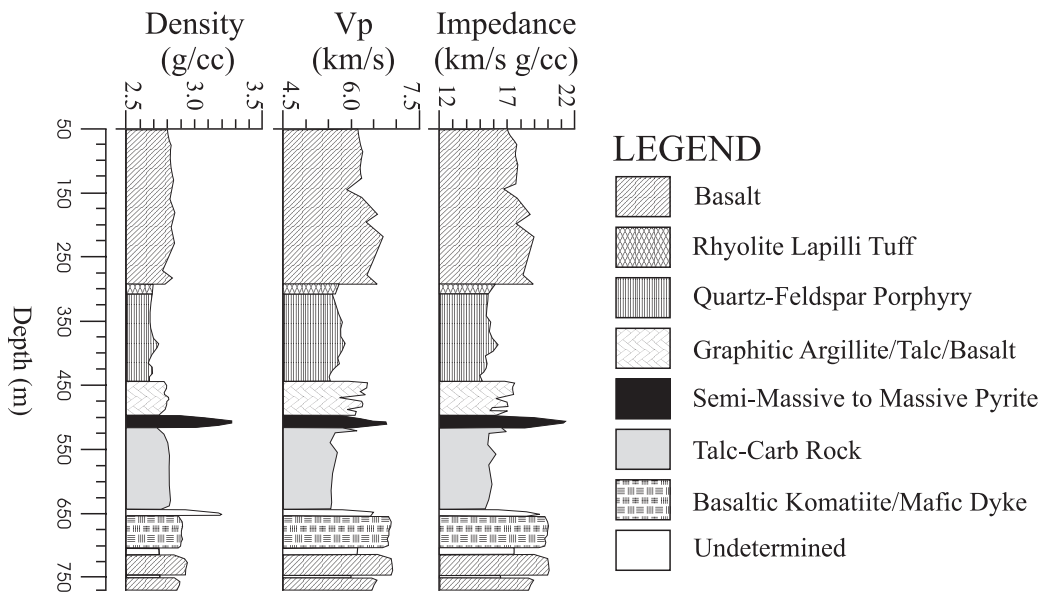

Figure 1.6: Density, P-wave velocity (V_P) and acoustic impedance logs from the Kidd Creek copper-zinc mine. Most of the acoustic impedance contrasts associated with changes in lithology indicate contacts that would cause seismic reflections and would be clearly visible in the reflection data. Figure adapted from Pflug et al. (1997).

Table 1.3: Summary of desired and imaged lithological contacts for a number of selected seismic reflection surveys done for mineral exploration.

Survey type and aim	*Region*	*Lithological target(s)*	*Contact(s) imaged partially or fully*	*Reference(s)*
2D exploration	Manitouwadge Greenstone Belt, Canada	VMS sulphides within the volcanic rocks	-Trondhjemite/volcanics, just above where most VMS deposits occur	Roberts et al., 1997.
2D exploration	Athabasca Basin Canada	Unconformity type high-grade uranium deposit	Red bed formations overlaying the gneissic basement	Hajnal et al., 1997.
2D and 3D exploration	Matagami Canada	-"Key tuffite" embedded between tholeiitic and basaltic formations, hosts VMS deposits -Two main ore bodies	-"Key tuffite" against tholeiitic and basaltic lavas -Massive sulphide ores against the host rock -Rhyolite/Gabro	Adam et al., 1997. Adam et al., 1998.
3D exploration	Sudbury Canada	-Massive sulphides against mafic norite -Norite against basic to ultrabasic rocks	-Norite against gabro, massive sulphides & basic to ultrabasic rocks	Milkereit et al., 1997.
3D mine planning	Witwatersrand Basin South Africa	Ventersdorp goldbearing sandstone "reef" conformably overlied by the Klipriviersberg lavas	-Unconformity between arenaceous rocks and Klipriviersberg lavas -Alternating lavas, shales and quartzites	Pretorius et al., 1997.

middle and lower crustal rocks worldwide. Among the most fundamental discoveries of the crustal reflection profiling is the pronounced reflectivity of the middle and lower crust that is often unmatched in the upper crust above or upper mantle below (Klemperer, 1987a). However, the causes of the deep crustal reflectivity are still hotly debated.

The difficulty in determining the composition of the deep crust can be best understood by examining the lower crust. The bulk of what is known about the lower crust has been obtained through both the investigation of granulites and from seismology. Granulites that occur in the surface tracts (granulite terrains, in which felsic rocks dominate) and those that are carried as small fragments to the Earth's surface in rapidly ascending magmas (xenoliths, which are dominated by mafic rocks) show large compositional differences. Furthermore, granulite terrains exhibit a very heterogeneous nature. As described by Rudnick and Fountain (1995), most pressure-temperature (P-T) paths for granulite terrains record adiabatic decompression. Yet a significant proportion (35%) record isobaric cooling. According to these authors, granulite terrains that experienced adiabatic decompression may not be truly representative of the lower crust and are dominated by felsic composition. The smaller portion of granulite terrains that experienced isobaric cooling may have resided for long periods of time in the lower crust, and have significantly larger component of mafic lithologies resulting in bimodal distribution of rock types. In composition they resemble much closer granulite xenoliths. But it is not well known even if the granulite xenoliths (predominantly mafic) are representative of the lower crust. They might simply be a deep-seated manifestation of the volcanism that transports them to the surface. Also, the felsic granulite xenoliths are possibly underrepresented in the overall granulite xenolith populations because of their dissolution in the host mafic magma.

The problems in determining rock type(s) from available seismic velocities make it even more difficult to determine the composition of the lower crust and resolve the ambiguity in the information gathered from granulite studies. The seismic reflection method has a high resolution in determining structure, but has almost no resolving power when it comes to P wave velocities. That is the case not only in the lower crust but also throughout most of the crystalline crust. The refraction method, on the other hand, may provide quite accurate seismic velocities, but suffers from very low resolution.

In spite of the many difficulties in determining the composition of the remote crust the data collected and analyzed in the past couple of decades has paved the way to a large number of models for the origin of reflectivity in it. Part of the reflectivity may

Table 1.4: Summary of the mean longitudinal velocity (V_P), density (ρ) and acoustic impedance (Z) for continental crustal rocks formed in the middle and lower crust. In small samples, all of the rock types listed exhibit considerable ranges around the mean values ($\sim\pm5\%$). Adapted from Rudnick and Fountain, (1995).

Amphibolite facies			
Rock type	ρ g/cm^3	(V_P) (km/s)	Z (Kgs/m^2)
Felsic gneisses	2.690	6.355	17.09×10^6
Pelitic gneisses	2.801	6.477	18.14×10^6
Mafic gneisses	3.028	7.018	21.25×10^6
Granulite facies			
Rock type	ρ g/cm^3	(V_P) (km/s)	Z (Kgs/m^2)
Felsic	2.706	6.529	17.67×10^6
Intermediate	2.859	6.727	19.23×10^6
Pelitic gneisses	3.007	7.091	21.32×10^6
Mafic: all rocks	3.038	7.226	21.95×10^6
Mafic: garnet-bearing	3.099	7.326	22.70×10^6
Mafic: garnet-free	3.003	7.169	21.52×10^6
Anorthosites: all rocks	2.798	7.108	19.88×10^6
Anorthosites: garnet-bearing	2.893	7.405	21.42×10^6
Anorthosites: garnet-free	2.743	6.944	19.05×10^6
Upper Mantle			
Rock type	ρ g/cm^3	(V_P) (km/s)	Z (Kgs/m^2)
Eclogites	3.432	8.095	27.78×10^6
Ultramafic rocks	3.290	8.199	26.97×10^6

be explained by the processes of the juxtaposition of different lithologies (for selected examples look in the table 1.4) which is similar to what was already stated for the visible crust:

(1) Primary depositional layering;
(2) Primary intrusive layering;
(3) Tectonically imposed layering, including various types of shear zones; and
(4) Metamorphic layering.

However, the middle and lower crust often exhibit higher reflectivity than the upper crust, while the seismic surveys over exposed granulite terrains reveal these rocks as seismically relatively transparent (Klemperer, 1987a). Essentially, this means that either the processing of seismic reflection data is selective in terms of better imaging of the deeper crust, or there are additional sources that contribute to the overall picture of higher reflectivity in the deep crust. The latest developments in research seem to favour both factors. Upper crust in crystalline terrains is most often characterized by a complex

pattern of smaller, steeply-dipping geologic bodies. The middle and lower crust exhibit more continuous horizontal to subhorizontal layering. The smaller, more shallow, and strongly dipping events are much harder to image and may have been lost during the processing, particularly of the early crustal data. The seismic reflection method is slowly becoming better adapted for imaging such events, and as a result there is an increase in the amount of "captured" reflection events originating from the shallow crust. At the same time it is believed that the high reflectivity of the deeper crust could be caused by the following (Klemperer, 1987a, 1987b, Rudnick and Fountain, 1995):

(5) Ductile strain banding;
(6) Free fluids; and
(7) Molten and partially molten bodies.

The mentioned phenomena that are possibly causing the higher reflectivity of the middle and lower crust are temperature and pressure dependent, and therefore might be of a transient nature.

In addition to the juxtaposed different lithology, and increased temperature and pressure, anisotropy and constructive interference may cause and/or enhance reflections. Seismic anisotropy and constructive interference seem to be particularly related to metamorphic layering, ductile strain banding and faulting.

1.5 Aim of the Research Project and the Structure of the Thesis

The study presented in this work was undertaken because the thesis author has a great interest in seismic reflection imaging and because reflectivity imaging in crystalline terrains is one of the geophysics investigation areas that, being relatively new, still provides exciting research opportunities and a lot of room for improvement.

Almost all of the seismic reflection data acquired in crystalline terrains has been collected by high fold 2D profiling on crooked lines. The aim of this work was to improve the imaging of such data, for this is equivalent to an overall improvement in seismic reflection imaging of crystalline terrains.

Generally, 2D crooked line data is processed as if it was acquired on a straight line profile. The single most important observation exploited in this thesis work is that the high fold 2D crooked line profiling is truly a 3D survey of a swath of terrain around the slalom

line and thus potentially carries 3D structural information about the events imaged. Most of the work done in this study was centered at designing processes to extract 3D geometry of the imaged events and use that information to improve signal focusing. The remainder of the research was set with a goal to design processes which will minimize the damaging effect of crooked line geometry and 3D structures on the resulting 2D image, when extracting 3D information is not practical.

A part of the research time was dedicated to designing a ray-Born modeling code and producing various modeled data sets which would allow for tests of the designed processes. About an equal amount of time as for modeling was allocated for tests on actual data sets collected in crystalline terrains.

In order to present the results achieved during this research project, as clearly as possible, the reminder of the thesis is organized as follows:

- A detailed statement of the research problem supported by simple model and real data examples is presented in Chapter 2;
- The suggested solutions for improved imaging are explained fully in Chapter 3;
- Chapter 4 describes extensive tests of the designed processes on seven synthetic data sets that include responses from a few diffraction points to many reflectors with various orientation relative to the survey line;
- In Chapter 5, the developed techniques are tested on real data. In addition, the complete processing stream is explained in detail;
- Reflectivity images obtained are presented and geologically interpreted within Chapter 6; and
- In Chapter 7 conclusions are given, followed by the suggestions for the related future research.

The ray-Born code used to produce modeled data is described in Appendix A (a short introduction is also given in Chapter 4). Whenever modeled data was used, a brief description of the main parameters characterizing it (acquisition geometry, reflectors' geometry, wavelet type, etc.) is given. Additional information about the models used is provided in Appendix B. The two actual data sets processed are Line 23 from the southern Abitibi subprovince and Sturgeon Lake Line from the central Wabigoon subprovince.

Their acquisition parameters are described in detail in Appendix C. The geographic locations of the seismic lines, as well as the geology of the area intersected by the slalom lines, are graphically presented in the posters appended at the back of the thesis.

Chapter 2

Focusing Problems

Unlike sedimentary basins where topography is gentle and vegetation is very low or cleared, crystalline terrains are often forested and their topography is rugged. The combined effect of the high-inaccessibility of crystalline terrains and the high-cost of seismic reflection investigations, in particular of the 3D method, leaves 2D crooked line profiling as the best compromise for reflectivity imaging of igneous and metamorphic rocks. Imaging on crooked lines has always been considered difficult, if not problematic, and to somewhat improve image quality data is usually acquired at a high density (high fold).

The standard practise has been to process high fold 2D crooked line data as if they were acquired on a straight line. But to ignore the 3D character of 2D crooked line profiles often results in poor quality of the obtained images. The effects of signal defocusing due to treating 2D crooked line data as if they were acquired on a straight line are examined in this chapter.

2.1 CMP Stack

Procedures required to process 2D straight line data are well known and their objectives were already briefly introduced in section 1.1.2. The first reflectivity image is usually formed by the common mid-point (CMP) stack and is called a stacked section or a synthetic zero offset seismic time section (SZOSTS).

CMP stacking is an integral part of the CMP method and has a very distinct place in the processing stream. It represents the main link between prestack and poststack data processing and is a process during which the prestack data volume is "collapsed" into a

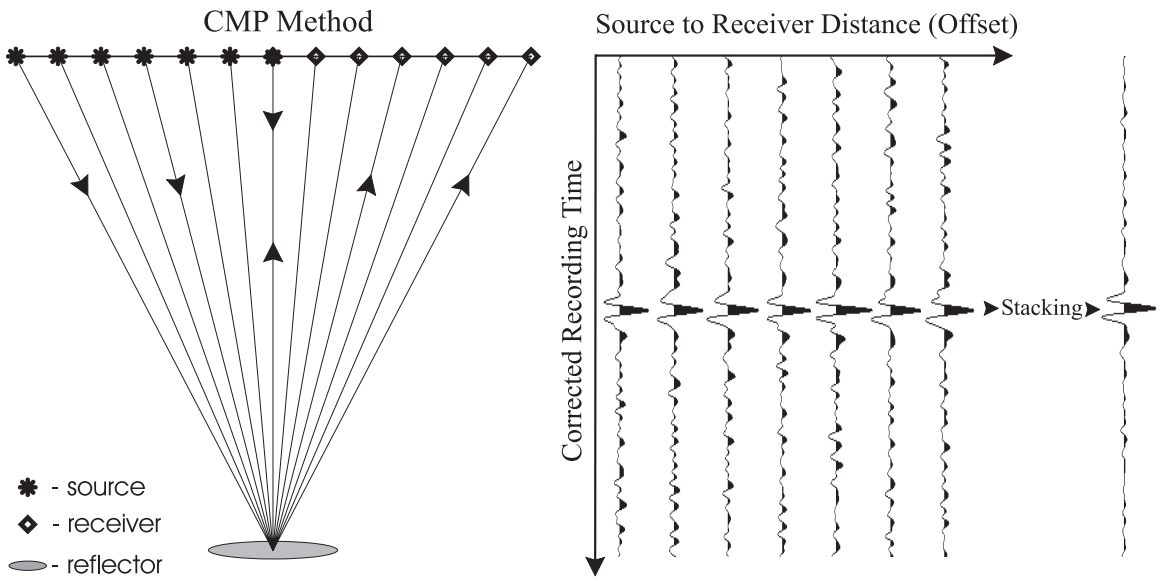

Figure 2.1: The left part of the figure depicts the way in which the CMP method acquires multiple signal from the same area of the reflector. After applying necessary time shifts, signal is aligned in time (the right part of the figure) and stacked (far right). Note the dramatic improvement in the S/N ratio of the stacked trace.

much smaller volume (stacked section).

The CMP method was invented in the 1950s. In 1962 (Mayne) the first publication explaining this method came out. The basic idea of the CMP method (figure 2.1) is to "illuminate" subsurface areas of interest from various energy sources, and record the response using many geophones. Sources and receivers are placed at the Earth's surface. Because sources and receivers are not coincident, signals received from the common subsurface area require time shifts before they can be combined. The CMP stack is used to combine the signals after they are aligned. In this procedure a set of NMO corrected data traces within each CMP gather is averaged along constant time.

Although stacking is a very simple procedure it has an immense impact on the imaging quality. When the signal is well aligned in time, stacking significantly increases signal to noise (S/N) ratio (see figure 2.1). For this reason, the CMP method became the standard procedure to acquire both 2D and 3D seismic reflection data.

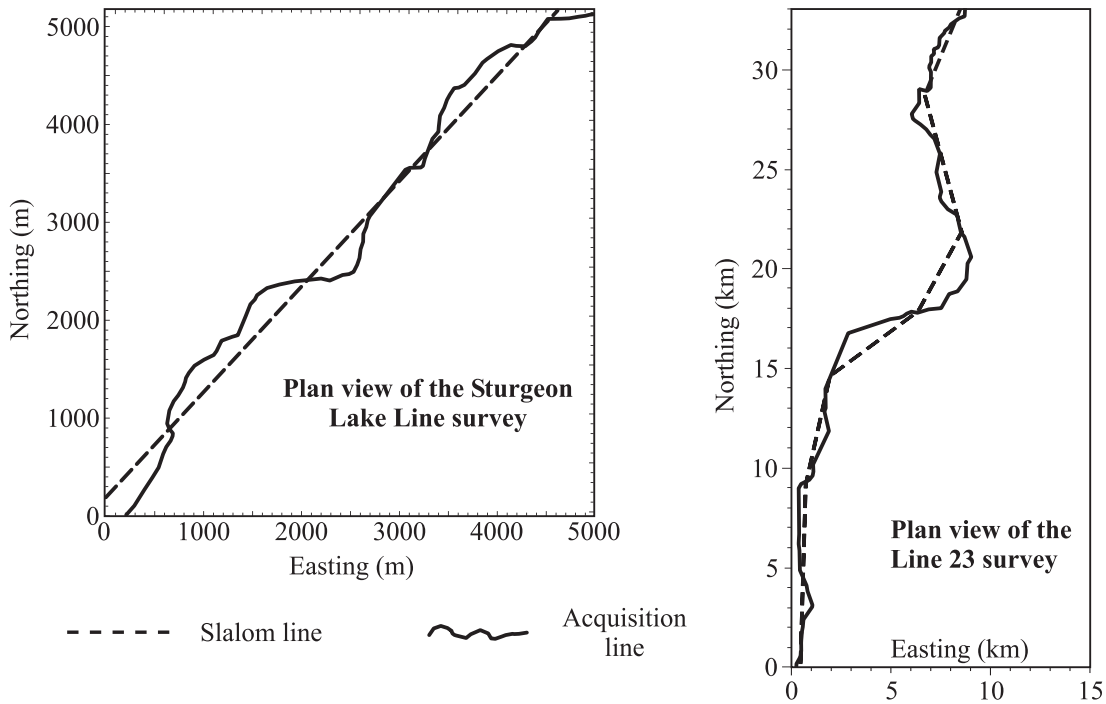

Figure 2.2: Plan view of the real data surveys examined in this study.

2.2 Stacking Data from Crystalline Terrains

Figure 2.2 shows a plan view of the two profiles examined in this study. High resolution Sturgeon Lake Line data was acquired for mining purposes in the central Wabigoon subprovince. Regional Line 23 data was collected for crustal scale studies in the southern Abitibi subprovince. Both surveys were carried out on fairly crooked roads. Data from the two surveys were prepared for stacking with great care by applying selected standard seismic processing techniques. The procedures used included: static time shifts for removal of the effects of overburden and uneven elevation, amplitude corrections for geometrical spreading, surface consistent deconvolution and surface consistent amplitude corrections for removing the effects of the source and receiver environment, bandpass filtering and slant stack filtering to enhance reflected P waves over other signals, CMP binning[1], dynamic time shifts (normal moveout and dip moveout removal) to compensate for non-coincident sources and receivers, as well as several other processes.

[1]Seismic data is organized into CMP gathers or CMP bin gathers depending on the acquisition geometry of the survey. When a seismic profile is straight all mid-points fall on the survey line. Because mid-points overlap on the survey line, common mid-points exists and are used to form groups of traces called CMP gathers. When a seismic profile is crooked mid-points cover an area around the survey line. This area is divided into many smaller parts called bins, and data traces whose mid-points fall in the same bins form CMP bin gathers.

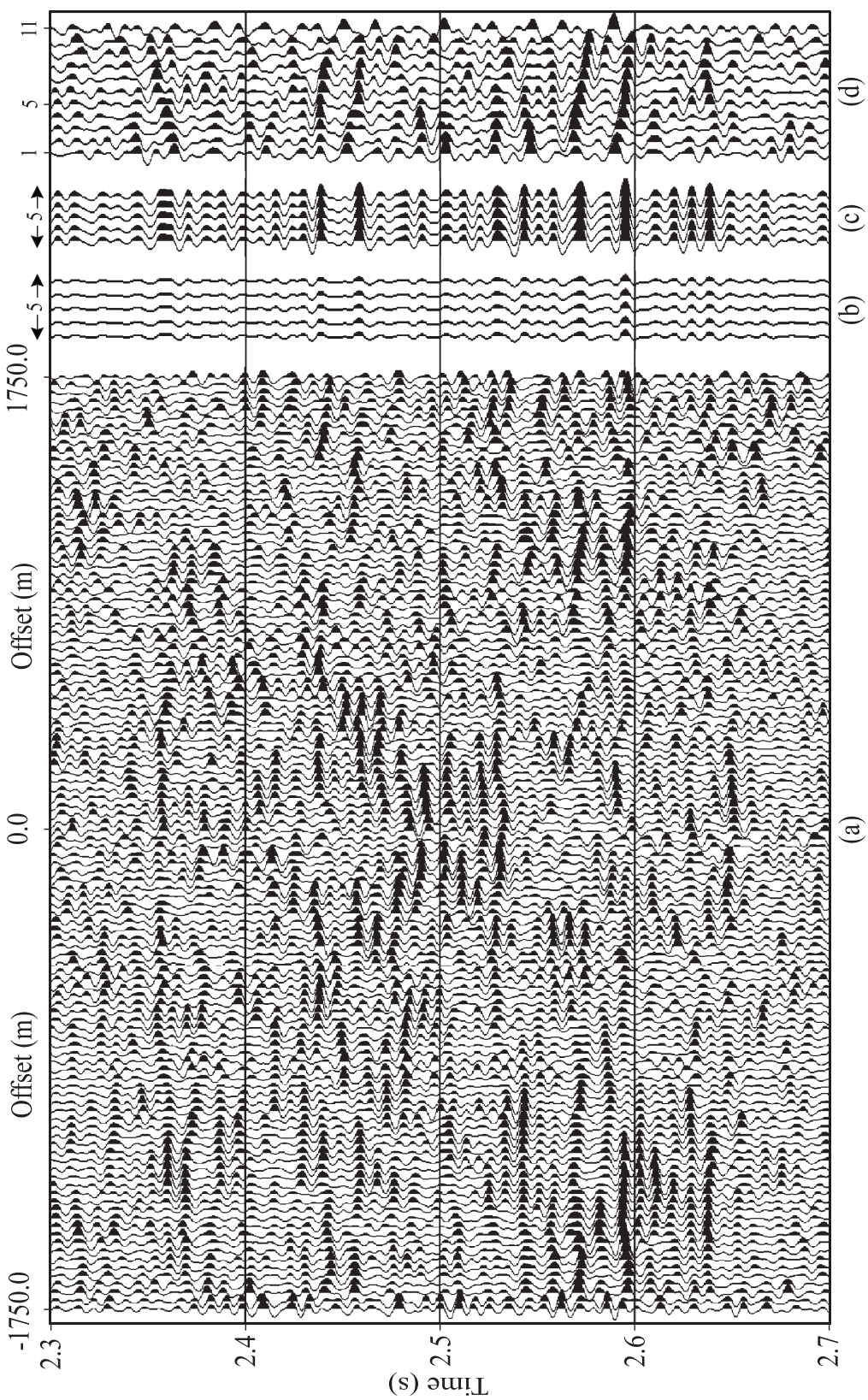

The figure is comprised of four parts. Part (a) is a section of the CMP BIN gather 4555 of Sturgeon Lake Line. Note the abundance of reflected energy that mostly is not well aligned in time. When stacked, this data yields a trace shown repeated five times in part (b). The reflection amplitudes of the stacked trace are much lower indicating large loss of energy during stacking. The wavelet shape for many events changes and the events on the stacked trace are often placed at the average position of a few reflectors. Some of the reflected events don't even pass the "stacking filter". The same stacked trace repeated five times but amplitude gained is presented in part (c). Part (d) depicts a small section of the Sturgeon Lake Line profile that includes the presented stacked trace (trace 5) and several neighboring traces. Note that only a few events are continuous over the presented section length of about 200 meters.

Figure 2.3: Signal loss when stacking seismic reflection data from crystalline terrains.

A part of a typical Sturgeon Lake Line CMP bin gather "ready" for stacking is shown in figure 2.3.a. Reflected energy in the gather is abundant as seen by the good trace to trace correlation, but despite all the effort it is not aligned well in time and does not span the full offset range even for a single event. The stacked trace of this poorly aligned data is given in figure 2.3.b repeated five times. The reflection amplitudes in the stacked trace are much lower than in the input traces, indicating major signal loss. The mostly much broader peaks of the events in the stacked trace point out that the loss is particularly large at the high end of the signal's frequency spectrum. To bring the stacked trace (2.3.b) to an approximately same energy level as that of the input traces (2.3.a), the stacked trace amplitudes must be increased significantly (2.3.c). More effects of stacking become evident after boosting the amplitudes. For example: a) some of the events did not even pass the stacking filter, b) others that did, often had their wavelet shape changed; and c) occasionally, an output event on the stacked trace is a result of combining signals from different input events. Figure 2.3.d shows a small section of the Sturgeon Lake profile that includes the stacked trace shown in figure 2.3.c. This figure reveals that although the signal is not well aligned within the CMP bin gathers, its distribution must be quite consistent (only gently vary) across neighboring CMP bins as some of the events exhibit continuity over all stacked traces shown (200 m). Because the stack filter is stable, the stacked sections (after boosting the amplitudes) often exhibit many events and therefore leave a false impression that imaging has worked well.

The poor signal alignment and signal loss during stacking is not a distinctive feature of the Sturgeon Lake Line. Results very similar to the ones shown in figure 2.2 are also obtained for Line 23 data. In fact, a well time-aligned reflector with a continuity over the full offset range is seldomly observed in CMP bin gathers of crystalline seismic reflection data.

Large signal loss is regularly observed when stacking data from a crystalline geological terrain. The CMP method does not perform as designed and shown in figure 2.1. But the signal loss is only a consequence of stacking. The real cause of signal loss stems from the poor data alignment which depends on several prestack processes.

2.3 Prestack Data Processing

Prestack data processing, prestack data volume, and its compression through the process of stacking into a stacked section (seismic profile), can be well visualized using stacking

charts. An example of a stacking chart is given in figure 2.4.a. Though this plan view doesn't really show the true geometry of the acquisition, it gives an idea of how the data surveying is carried out. Data collected into a prestack data volume can be organized into various types of gathers, which include: common shot, common mid-point, common receiver and common offset gathers. Most of prestack data processing is gather oriented, with the majority of procedures done on common shot and common mid-point gathers. Figure 2.4.b shows the same stacking chart from figure 2.4.a but in a perspective. Seismic traces are given for one of the CMP gathers, and signals pertaining to the reflection event are well aligned in time. The stacked trace for this event would look similar to the stacked trace in figure 2.1 (far right).

Although a prestack processing sequence may include many steps there are only several fundamental goals to achieve:

- Remove bad data;
- Enhance reflections;
- Minimize noise;
- Align signal for stack.

Output quality of several of the prestack procedures (e.g., band filtering, some amplitude corrections, deconvolution, etc.) does not, or only partially depends on the geometry of the survey, spatial orientation and distribution of the subsurface structures, and the performance of previously applied processes. Other prestack procedures, particularly ones used to estimate time shifts necessary to align data before stack, are highly dependent on the same factors.

Figure 2.3 shows that most of the goals of prestack data processing are achieved for the examined data. Amplitudes are well balanced and reflections are crisp. The only major problem still present in data is the poor time alignment of the reflected signal.

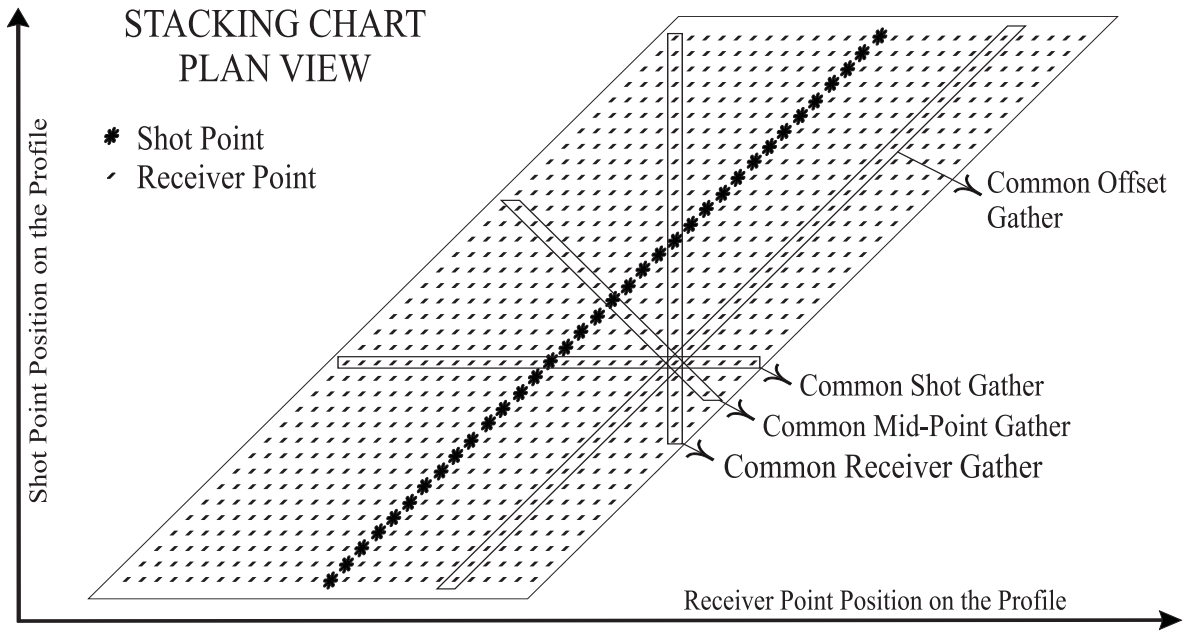

(a)

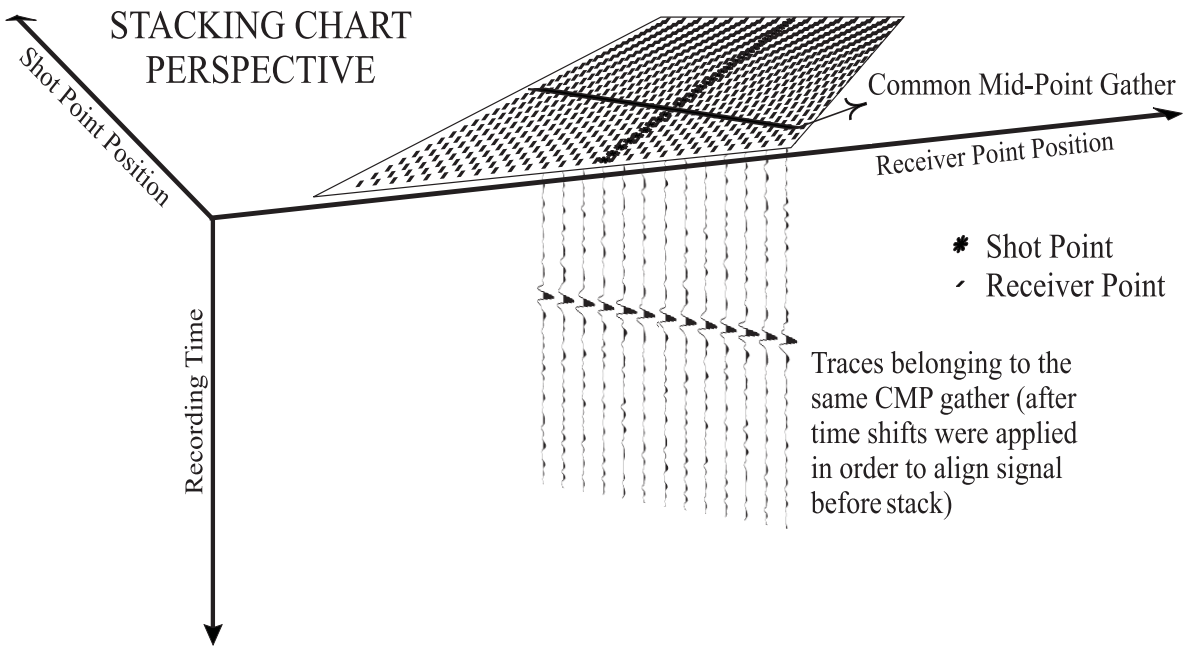

(b)

Figure 2.4: (a) Plan view of a stacking chart. (b) Perspective view of the same stacking chart.

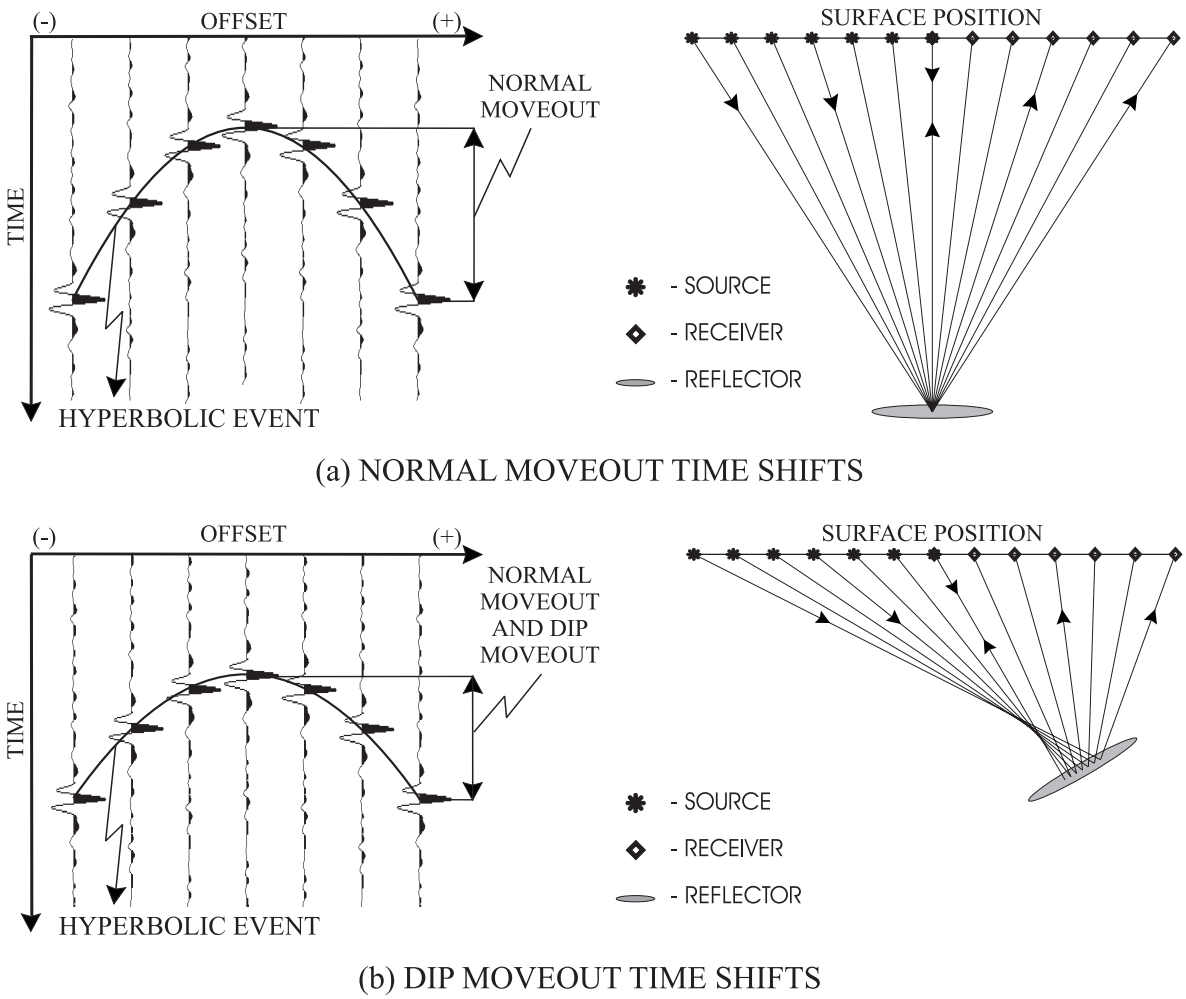

Figure 2.5: Normal moveout (NMO) and dip moveout (DMO) (parts(a) and (b) of the figure respectively) are a consequence of the non-zero offset data acquisition.

2.4 Standard Procedures for Signal Time Alignment

To align for stacking data acquired by straight line surveying, usually three types of time shifts[2,3] must be determined and removed. First in the processing stream are the static time shifts, second are the normal moveout (NMO) time shifts, and third are the dip moveout (DMO) time shifts.

[2]Various procedures used to determine and remove static, normal moveout (NMO), and dip moveout (DMO) time shifts are discussed in Chapter 5 which focuses on seismic reflection data processing.

[3]In seismic literature, to remove the static, NMO and DMO time shifts is often referred to as "to apply static, NMO and DMO corrections". Although this terminology is used in this thesis because it is convenient and conventional, it is also misleading because these time shifts are related to the planned geometry of the survey and do not arise from any kind of error.

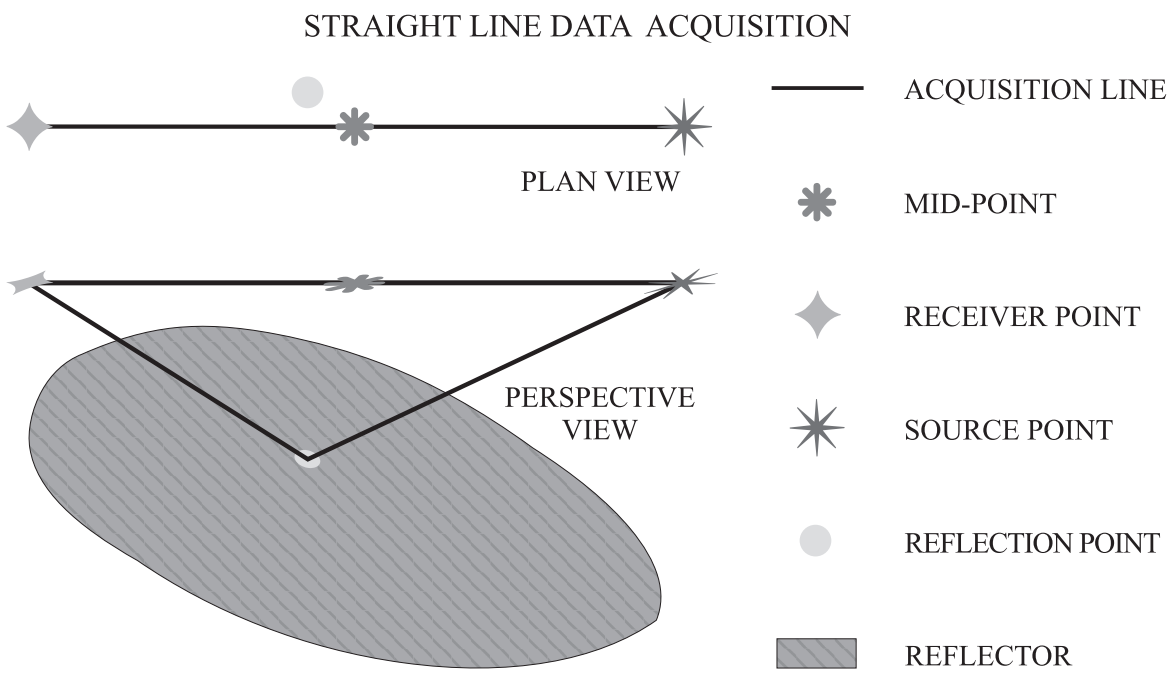

Figure 2.6: When an imaged reflector has a dip component towards the straight line survey, the sampled part of the reflector is not lying below the line of the profile.

Static corrections involve constant time shifts of whole seismic traces (hence the name static), and are designed to remove the influence of the topography and the low-velocity layer, frequently called the weathering zone. The effect of the topography and the weathering zone on the traveltime of the reflected signal is often so strong (10s to 100s of ms) and variable, that if neglected many events are completely lost in the final sections.

Data surveying using the CMP method is carried out in such a way that the majority of the recordings (and in many cases all of them) are gathered with the seismic energy sources being some distance away from the receivers (right half of the figure 2.5.a). This distance is called offset (x). The further apart the source and receiver are, the longer the traveltime t to the event is (left half of the figure 2.5.a):

$$t^2 = t_0^2 + \mathrm{p_x^2 x^2}, \tag{2.1}$$

where $\mathrm{p_x}$ is slowness ($1/V_{\mathrm{RMS}}$) in the direction of the survey line, V_{RMS} is the root mean square velocity to the reflector and (t_0) is the zero offset time. To position the events at the zero offset time, which is necessary for stacking, NMO corrections ($t - t_0$) must be applied. These corrections are often referred to as dynamic, because they are different not only for each seismic trace, but change for each time sample.

When the reflectors are dipping, the reflection signals recorded still form NMO hyperbolas

(left half of the figure 2.5.b), but they are slightly less "bent" than they would be if the reflectors were horizontal (figure 2.5.a). The curvature of the NMO hyperbola becomes weaker because the "reflection point" moves in the up dip direction as the offset gets larger (right half of the figure 2.5.b). The traveltime (t) is calculated again using equation 2.1 but with a different slowness p_x (see Appendix E) which can be adequately approximated as:

$$p_x^2 = \frac{1}{V_{\mathrm{RMS}}^2} - \frac{\sin^2\theta_x}{V_{\mathrm{RMS}}^2}, \tag{2.2}$$

where θ_x is the dip component of the reflector along the survey line. To remove the additional effect produced by the unknown in-line dip of the reflectors, dip moveout (DMO) corrections (more correctly dip moveout partial migration) must be applied to the data. These corrections are also dynamic, and involve more than a simpler trace-to-trace mapping of data. The dip moveout time shift is particularly strong for the shallow events that appear at early times in the seismic records.

For most sedimentary basin data sets, static, NMO, and DMO corrections are capable of achieving a good time alignment of reflected signals before the stack. This is largely due to straight line profiling and the relatively high continuity and smoothness of the reflectors, a major property of sedimentary basins. Then the subsequent stacking usually results in high quality sections.

Although imaging in sediments is good, obtained profiles seldomly represent vertical cross sections of reflectivity below the acquisition lines. Figure 2.6 shows that a reflector that has a dip component perpendicular to the profile direction will not be sampled directly below the line of survey. But because all mid-points fall on the acquisition line, a straight line of reflectivity is sampled along the reflector. On the image, this line exhibits an apparent in-line dip of the reflector. Therefore, the obtained reflectivity images still have a clear meaning, but an additional processing step - migration - is required to fully recover the true geometry.

In sedimentary basins in which the dip and strike of the strata is unknown but only 2D surveying can be employed, the true dip of the events is resolved by using multiple profiles that are usually perpendicular to each other.

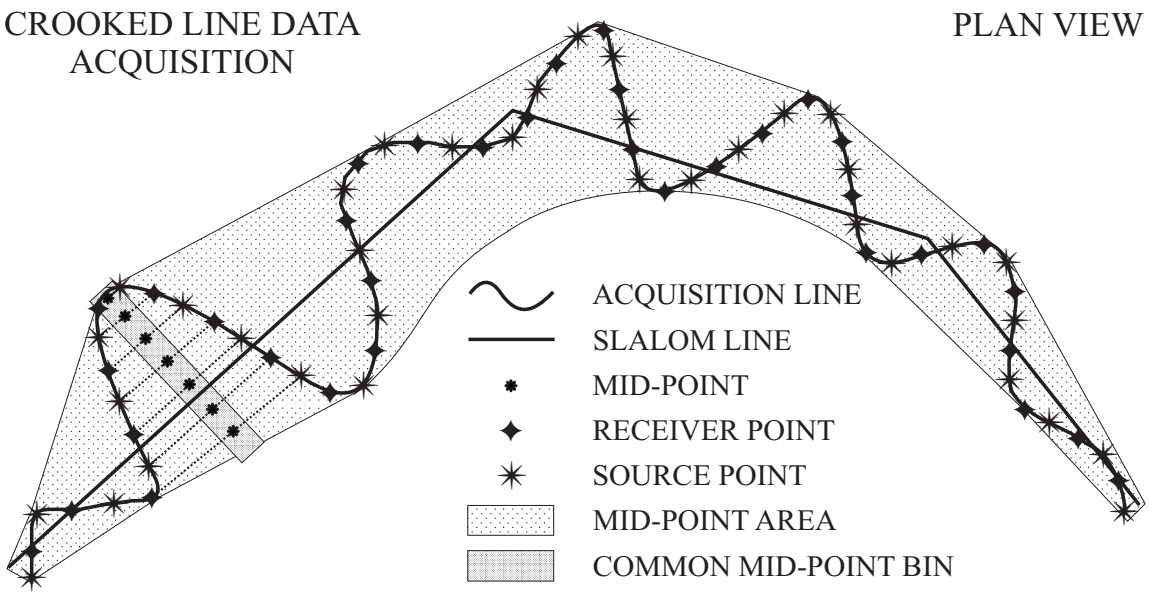

Figure 2.7: Crystalline terrains are rugged and seismic reflection data collection must be carried out almost exclusively on the local roads. Since the roads thread through the country side, the seismic acquisition lines are crooked. Crooked line geometry adds significant uncertainty to the gathered data and complicates the data processing. Here presented is a plan view of the typical 2D crooked line data acquisition.

2.5 Reasons Standard Procedures Fail to Align Seismic Data from Crystalline Terrains

Accuracy of the time shifts used to align reflected signal before stack is lower in the crystalline terrains than in the sedimentary basins due to:

1. Acquisition geometry; and
2. Reflector geometry.

1. 2D seismic profiling on crooked lines (figure 2.7) results in mid-point scattering. Mid-points cover an area many kilometers long, and generally a few hundred to a few thousand meters wide. The mid-point scattering translates into subsurface sampling of a much larger area for the crooked line surveys than for the straight line surveys. As a result, the same amount of data for both survey types describes the subsurface area of a significantly different size, leading directly into the higher uncertainty of the data collected on crooked lines. The slalom line is drawn approximately through the middle of the mid-point distribution and has a similar length to the area covered with mid-points. It represents the intersection between the future section and the surface of the studied

area. When the crooked lines are long, the slalom line may be composed of a number of straight line segments of varying size and azimuth. The mid-point area is divided into bins and the CMP gathers in the straight line acquisition become CMP bin gathers in the crooked line acquisition. The standard procedure is to process crooked line data as if all of the mid-points were found on the slalom line.

Effects on statics. When the acquisition line is crooked the waves refracted at the base of the weathering zone travel through the whole subsurface approximately outlined by the mid-point area. Unfortunately, there isn't enough information to form a 3D model of the low velocity layer and use it to determine the static time shifts. Because treating the refractions as if they traveled only beneath the acquisition line is a gross simplification of reality, the static time shifts so determined are less accurate for stations on crooked lines than for stations on straight lines.

Effects on NMO removal. To successfully remove NMO time shifts, an accurate root mean square (RMS) velocity model is necessary. For the data gathered on crooked lines that means a 3D RMS velocity model. However, it is even difficult to extract an accurate 2D RMS velocity model from crooked line data, as large changes in velocities seem to have little effect on the quality of signal alignment.

Effects on DMO removal. The accuracy of applied DMO corrections is not highly dependent on the RMS velocity models but is, for example, sensitive to the source-receiver azimuth variation (see Appendix E) and to the presence of zero data traces in "constant" offset gathers upon which DMO operates, which are both common in crooked line crystalline surveys. Zero data traces found in constant offset gathers occur because of the uneven shot distribution.

Cross dip moveout (CDMO). Crooked line data acquisition is really a 3D survey of a swath of terrain around the slalom line. Instead of mapping a line of reflectivity from a single reflector during straight line surveying, a whole band of reflectivity is recorded about the same reflector when employing crooked line profiling. In the figure 2.7 a CMP bin, and some of the mid-points belonging to it are shown. If any of the subsurface reflectors have a dip component in the direction perpendicular the slalom line, then the signal arrival times from that event will have a cross dip moveout (see Appendix E for details), in addition to the time shifts found in the seismic data gathered on straight lines. The total traveltime (source-reflector-receiver) can now be expressed as:

$$t^2 = (t_0 + \mathrm{p_y y})^2 + \mathrm{p_x^2 x^2}, \tag{2.3}$$

where most of the notation is the same as in 2.1 and 2.2, y is the cross-line offset[4] and p_y is the slowness in the direction perpendicular to the slalom line.

$$p_y = \frac{-2\sin\theta_y\cos\theta_x}{V_{RMS}(1-\sin^2\theta_x\sin^2\theta_y)^{\frac{1}{2}}}, \tag{2.4}$$

where θ_y is the dip component of the reflector perpendicular to the slalom line. In order to make the bands of reflectivity meaningful and interpretable on a 2D section cross dip moveout (CDMO) must be removed. However, CDMO is mostly neglected or inadequately treated when imaging in on crooked lines.

NMO, DMO and CDMO are interdependent making it more difficult to determine them. In addition, the CDMO makes it impossible to successfully apply any type of existing residual statics methods and thus prevents improvements to the static solution.

2. In crystalline terrains reflective imaging is further complicated by the reflectors' geometry which is highly complex, to the point that reflections might more accurately be called scattering. The complicated shapes and layering of reflecting interfaces can produce erratically high amplitude reflections where the amplitude of reflected (scattered) events is strongly dependent on the scattering angle. As a result, observed reflections may exhibit an excellent phase coherence over a limited aperture (offset) range, but the coherence reduces over wider offset ranges and events may drastically shift in phase. In other words, even if some of the reflectors are continuous, their reflectivity might not be. Since the stacking (RMS) velocity is obtained by analyzing reflector time shifts, erratic reflectivity can greatly reduce the accuracy with which it can be estimated.

The distribution and orientation of reflectors in the imaged space often results in significant overlapping of the reflective responses on the sections. The overlapping causes further difficulties to time shift analyses as well as to the whole imaging process.

2.6 Can the 3D Character of 2D Crooked Line Data be Neglected?

A better understanding of the effects of 2D crooked line surveying and 3D reflectors' geometry may be gained by examining modeled data. Figure 2.8 shows in a perspective the Sturgeon Lake Line survey geometry and a 30^0 dipping layer. The plan view of

[4]The cross-line or transverse offsets are a consequence of the crooked line acquisition and represent the shortest distance from the mid-points to the slalom line.

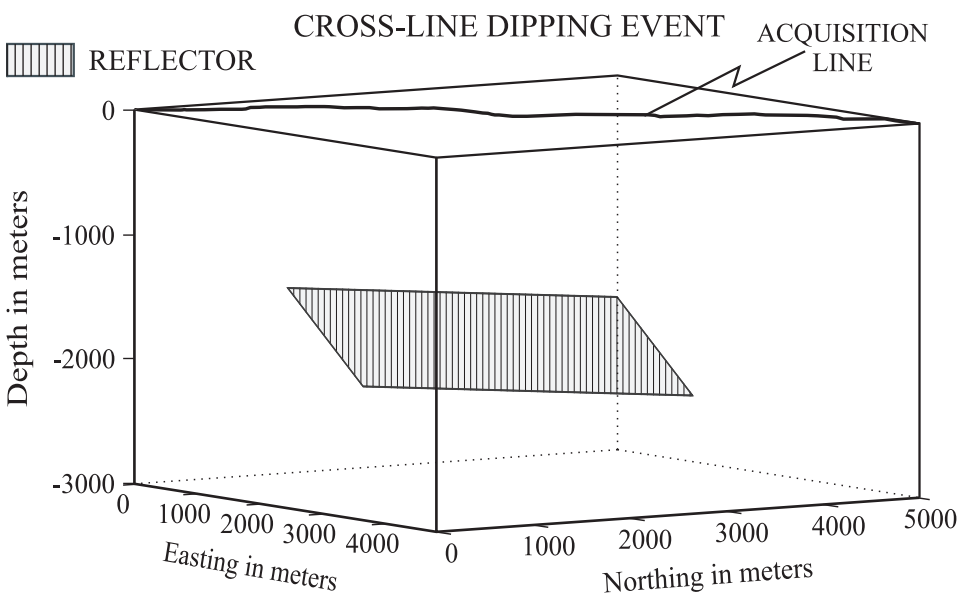

Figure 2.8: A perspective view of the Sturgeon Lake Line survey and the 30^0 mainly cross dipping reflective event.

the Sturgeon Lake Line is given in figure 2.2. The dip of a model reflective event is predominantly towards the survey line (it is mainly cross dipping). Models of a horizontal and a 30^0 in-line dipping event were also studied but are not shown in this figure. Events in all three models have the same size and are positioned to return the reflected energy back towards the acquisition line. Their top parts are at the depth of 1500 meters and they are embedded in a medium with a constant velocity of 6000 m/s. By using: a) a ray-Born modeling code (see Chapter 4 and Appendix A), b) the three physical models described, and c) the Sturgeon Lake Line survey geometry with the reduced number of shot points to one third, three synthetic data sets were produced. Signal sources were represented by the Butterworth minimum phase wavelet with the frequency limits of 20-300 Hz. Random noise was added to the output.

Although an actual survey geometry was applied for modeling, the synthetic seismic reflection response of the modeled reflectors lacks the complexity observed in real crystalline data. This is because the simple flat sheet models used to simulate the reflectors are much simpler than the structural reality found in igneous and metamorphic terrains. The reflection events are perfectly flat and the only feature similar to the layering in crystalline terrains was their small continuity. The weathering zone is not included in the models so static shifts are not required, the P wave velocity is constant and known, and the noise is only of the random type. However, in spite of their simplicity, the models serve their purpose well and help us understand the main difficulties encountered when

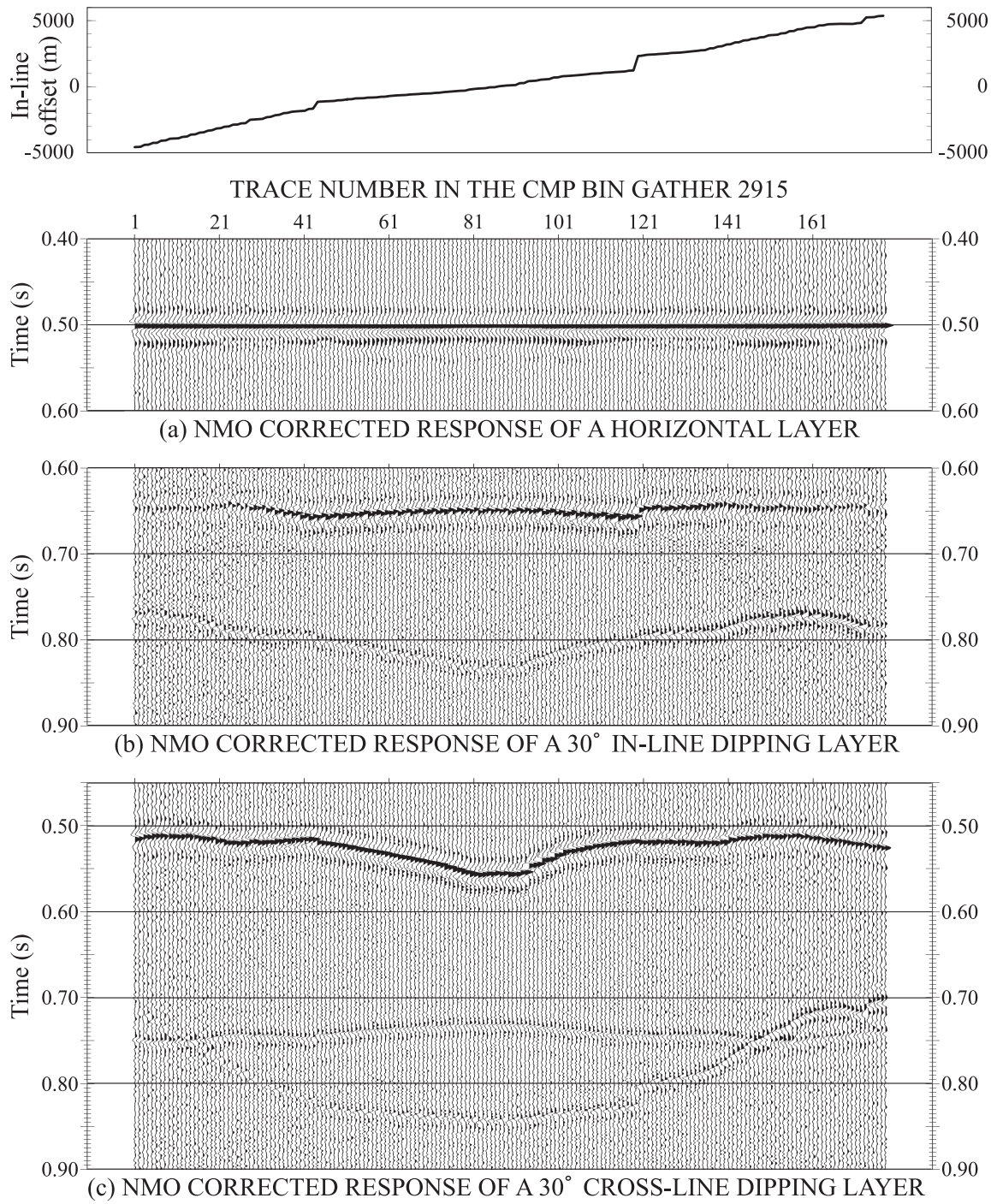

Figure 2.9: The figure features the CMP bin gather 2915 located at the middle of the acquisition line. The reflective responses of a horizontal event (part (a)), a 30^0 mostly in-line dipping event (part (b)), and a 30^0 mostly cross-line dipping event (part (c)) are shown. The very top of the figure depicts the offsets of the traces in the gather. Note how the signal for the dipping layers is not well aligned in time and will cause signal loss if stacking is applied over the full offset range. For more information about the characteristics of the modeled data please refer to the main body of text.

imaging on crooked lines in hard-rock environments.

Figure 2.9 depicts the CMP bin gather 2915 (the middle of the survey line) after the NMO time shifts were removed using the optimum stacking velocity for each of the events. The very top of the figure show the offset of the traces in the gather. Irregular shot distribution causes some jumps in the offsets. The horizontal event (part (a)) has signals that are well aligned and will stack well for all of the offsets. 30^0 mostly in-line and mostly cross-line dipping events (parts (b) and (c)), on the other hand, are not well aligned and will stack poorly over the full offset range.

There was no need to remove the DMO and NMO time shifts separately because single in-line dipping events can always be aligned well by removing both time shifts simultaneously using a higher velocity ($V_{RMS}/cos\theta$, where V_{RMS} is the root mean square velocity and θ is the dip angle) than the true RMS velocity to the event. Therefore, the residual time shifts in part (b) of figure 2.9 are attributed to unaccounted cross dip moveout (CDMO) and the effect of the source-receiver azimuth variation.

When the cross dip component of the true dip becomes large (part (c) of figure 2.9) the CDMO becomes many times larger than the dominant period of the signal. The signal focusing observed is extremely poor.

To better understand what happens to signal during stacking, a cumulative stack of the CMP bin 2915 for all three modeled events is given in the figure 2.10. The offset range for the cumulative stack (top of the figure 2.10) was increased by 200 meters at each step, starting from the largest negative offset. The stacked traces are normalized by the trace count, so that the amplitude of the coherent signal should (if perfectly aligned in time) remain constant and that of the incoherent noise should fall in proportion to the square root of the count. For the horizontal event (2.10.a) this holds true, but what figure 2.10 indicates for both dipping events is that all amplitudes fall with the increasing fold. Moreover, minor wavelet changes and signal shifts in time on the trace-to-trace basis accumulate slowly to an intolerable degree over the full offset range.

Data traces in the CMP bin gather 2915 show strong correlation between in-line offset and cross-line offset. This is a general characteristic of all crooked line data. Over small in-line offset ranges, cross-line offset and source-receiver azimuth vary smoothly and little. Thus, stacking data over small offset ranges (for data shown in figure 2.9 <200-300 m) without DMO and CDMO removed is not damaging to signal.

In conclusion, figures 2.9 and 2.10 illustrate that even when many of the effects of the

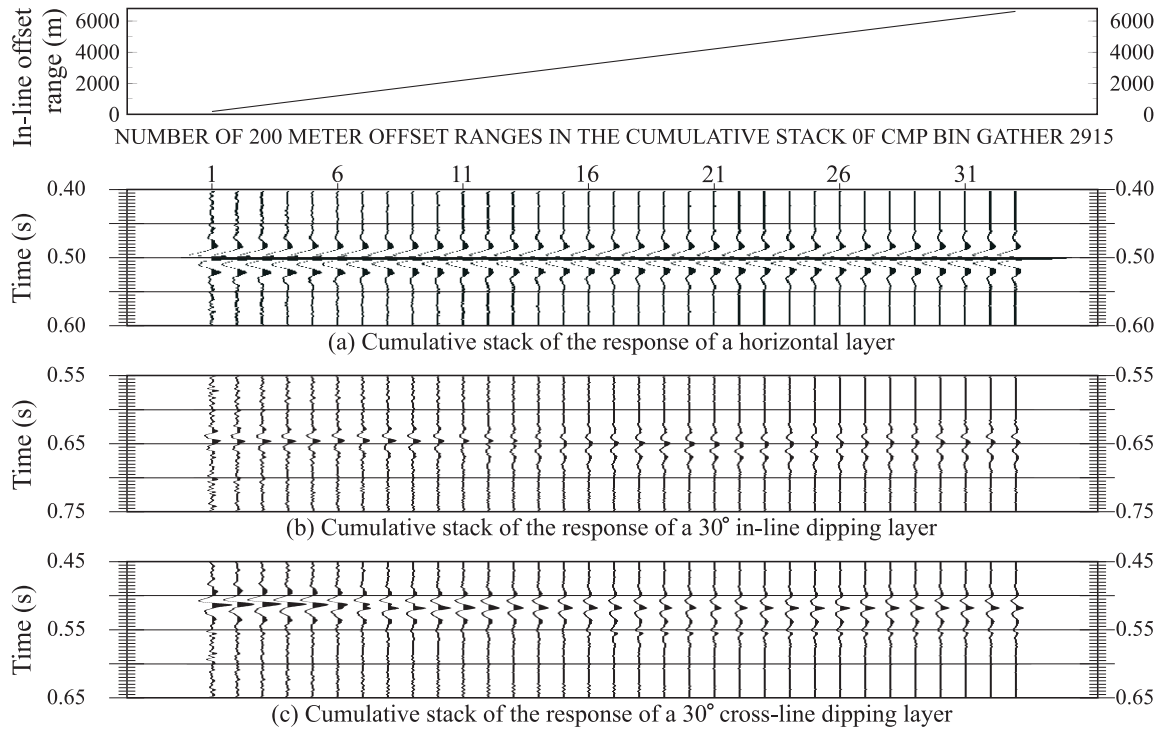

Figure 2.10: Cumulative stacks of the CMP bin gather 2915 for the horizontal (part (a)), in-line dipping (part (b)), and cross-line dipping (part (c)) modeled layers are presented. The offset window size for cumulative stack, top part of the figure, was increased by 200 meters at each step.

complex reflectors' geometry are not taken into account, the data acquired on crooked lines over the events exhibiting even a very small component of cross dip can not be aligned well in time if only the standard time shifts are applied. Stacking over the full offset range would results in signal loss. However, stacking over carefully chosen small offset ranges can be usefully exploited because it reduces the data volume and can improve signal-to-noise ratio.

2.7 Possible Directions for Improved Imaging

The previous sections in Chapter 2 show that for a truly successful imaging the 3D geometry of 2D crooked line data must be accounted for. This thesis research work has mostly been centered on exploring and designing procedures to usefully exploit the inherent 3D information of 2D crooked line data to reveal the true geometry of reflectors.

One of the possible directions to take to improve the imaging on crooked lines is indirectly suggested by the analysis in the previous sections. It consists of determining cross dip

time shifts in addition to the static, NMO and DMO time shifts, and then collapsing the recorded bands of reflectivity into single lines. By this method, the extracted 3D information would be used to better focus the data before the stack. The subsequent stack would result in an improved section. Therefore, whatever 3D information is obtained by the cross dip analysis would have to be expressed on a 2D section.

Another approach is to prestack migrate the data into a 3D volume. This method would bypass the DMO and cross dip moveout analysis but still needs estimation of a velocity model. Furthermore, it might solve the problem of the overlapping reflective response of various events that can occur on 2D sections. The idea is that the 3D information about the 3D geometry of the imaged structures can best be preserved and expressed if the imaging procedures are carried out in 3D data space.

But the crooked line data has a very limited amount of 3D information about the structures surrounding the survey line. It would be unwise to assume that the 3D information will be extracted in every single case study. Methods that are more tolerant to poor signal focusing than the standard stack is should also be developed to optimize the imaging when the procedures designed to extract the 3D information fail.

Even 2D crooked line seismic reflection profiles are moderately large computational data sets and regardless of the processing direction(s) taken, to obtain the final image(s) requires vast CPU power. The simplest measure of profile size is the total number of data words in the set: $N_d = n_t\, n_s\, n_r$, where n_t is the number of time samples per trace, n_s is the number of source points, and n_r is the number of active receivers per shot. The numbers for the Sturgeon Lake Line and Line 23 are: $\sim 263 \times 10^6$ and $\sim 435 \times 10^6$, respectively. The data needed for a 2D cross section of the earth are: $N_c = n_{\mathrm{T}}\, n_b\, L$, where n_{T} is the number of time samples in the output trace (same or smaller than n_t), n_b is the number if bins per unit length of slalom line, and L is the length of survey profile on slalom line. The average fold of the survey is $(n_s\, n_r)/(n_b\, L)$, and the data redundancy is $\frac{N_d}{N_c}$.

Most seismic procedures up to the CMP stack are operations on each data point taking up $k\, N_d$ computer CPU cycles for execution, where k is a constant for a particular process, and is generally less than 10^2 to 10^3. This is no problem. However, difficulties do arise with some processes where k becomes large, of order $(n_t\, n_r)$ or more as is the case with migrations and some multidimensional filters. It is therefore highly desirable to remove some of the data set redundancy before any of the multidimensional processes are applied. More than just computational convenience is at stake. Most of the multidimensional

processes (like DMO partial migration) are damaged by any irregularities in data density, and this can be removed or improved in an initial stage of data compaction.

2.8 Summary

Most of the seismic reflection surveying in crystalline terrains has been done on crooked lines. The standard procedure is to treat 2D crooked line data as if it was acquired on a straight line profile. By doing so the 3D character of the crooked line data is neglected. As a consequence, signal in CMP bin gathers is poorly focused and stacking the data results in significant signal loss. For a truly successful imaging the 3D character of 2D crooked line data must be accounted for. If such a process breaks down due to a limited amount and/or quality of the available 3D information, methods of combining trace signals other than the standard stack that are more tolerant to poor signal alignment may result in improved imaging.

Chapter 3

Solutions to Focusing Problems

Three directions have been explored in this study with the objective to improve imaging of 2D crooked line seismic reflection data from crystalline terrains. The directions taken required design of new data processing and modeling procedures and writing of many new codes. Grouped by the common research direction these procedures are:

1. The optimum cross dip stack (which includes multiple cross dip stack, identification of optimum cross dip, and synthesis of optimum cross dip stack) and the 3D poststack migration of the optimum cross dip stack;
2. The 3D prestack migration of swath 3D data;
3. The amplitude stack and the migration of the amplitude stack.

The first two groups of procedures have a common goal: to extract the 3D information from 2D crooked line data. But they differ in their approach. The third group is used to improve imaging when little or no 3D information can be extracted from the data.

The purpose of Chapter 3 is to conceptually introduce the various procedures I have designed and show where and how they fit within the whole data processing stream. More technical information (thought to be non-essential for this chapter and to elaborate the discussion) is provided at a later, more appropriate point in the thesis (Chapter 5). Because all of the procedures developed and stated above depend on a preliminary process designed and called "optimum offset range for partial stack", this procedure is explained first.

3.1 Processing Flow and the Procedures Designed

A better understanding of where the designed procedures fit in the data processing and why they have the potential to improve seismic reflection imaging in crystalline terrains may be gained by examining the data processing stream that now incorporates them. The processing stream[1] presented in tables 3.1 (prestack procedures) and 3.2 (poststack procedures[2]) was carefully selected by studying several 2D crooked line data sets from crystalline terrains.

Most of the processes stated in table 3.1 that precede the optimum limited offset range analysis, are routinely applied in seismic data processing. Geometry must be inserted in the trace headers as many of the processes applied later require that information. Field errors are fixed and bad data discarded through editing and muting. What remains is considered useful data, and various attempts are made to enhance it. For example, amplitudes of the data signals are balanced to ameliorate later processes such as noise removal and stacking. Deconvolution is used to improve the temporal resolution. To reduce the random noise a bandpass filter is applied, and to remove most of the coherent noise a slant stack filter is used. Filters such as a slant stack disturb the frequency content of the data, and the RHO filter rebalances it. The importance of the time shifts (static and NMO) was already discussed earlier in Chapter 2. Data is sorted into CMP bin gathers and transverse offsets are calculated and written into the headers. To calculate transverse offsets is not a standard procedure, but is a necessary one as they are needed for the cross dip analysis.

Optimum limited offset range analysis, the topic of the next subsection, is applied to find the maximum offset range at which data still stacks well phase coherently (standard stacking works well). Once this offset range is found, the prestack data volume is partially stacked within the maximum offset limits determined. In this manner, with minimal signal loss incurred, the prestack data volume is significantly reduced and is much easier to handle.

At this point the processing stream is divided in two. One way of imaging the data is to remove the DMO time shifts by applying a partial migration process on the optimum limited offset range stacks, and another is to position the reflective events in a 3D space

[1] An in depth chart of the processing stream together with a description of the procedures applied to the real data in this work is given in Chapter 5.

[2] Although not a poststack procedure 3D prestack migration is also included in table 3.2 to help visualize the three research directions taken in this study.

Table 3.1:

SIMPLIFIED SEISMIC REFLECTION DATA PROCESSING STREAM PRESTACK PROCEDURES (PART I)	
• GEOMETRY/EDITING/MUTING ➤ Entry of crooked line geometry survey ➤ Correction of field errors ➤ Bad data removal	
• PRELIMINARY DATA ENHANCEMENT ➤ Amplitude correction for geometrical spreading attenuation ➤ Surface consistent amplitude correction ➤ Surface consistent deconvolution ➤ Time varying trapezoid bandpass filter	
• WEATHERING LAYER ZONE TIME ANOMALIES REMOVAL ➤ First arrival picking ➤ Refraction static and elevation corrections	
• ATTENUATION OF UNWANTED SIGNAL (AIR WAVE, FIRST S-WAVE ARRIVALS SURFACE WAVES AND VIBRATORS' NOISE) ➤ Slant stack and RHO filters	
• CMP BIN SORT	
• TRANSVERSE (CROSS) OFFSETS CALCULATION	
• VELOCITY ANALYSIS AND NORMAL MOVE-OUT REMOVAL	
• OPTIMUM LIMITED OFFSET RANGE ANALYSIS; OFFSET RANGE BINNING	
• PRESTACK DATA VOLUME REDUCTION BY PARTIAL STACK ➤ Automatic gain control (AGC) ➤ Weighted semblance stack or root N stack in limited offset apertures ➤ Amplitude optimization ➤ Bandpass filter	
PROCESSING STREAM BREAKS IN TWO	
• DMO REMOVAL ON CONSTANT OFFSET SECTIONS	• 3D PRESTACK DEPTH MIGRATION (STANDARD AND AMPLITUDE)

Table 3.2:

<table>
<tr><th colspan="3">SIMPLIFIED SEISMIC REFLECTION DATA PROCESSING STREAM
POSTSTACK PROCEDURES (PART II)</th></tr>
<tr><th colspan="3">PROCESSING STREAM BREAKS IN THREE</th></tr>
<tr><td>• CROSS DIP ANALYSIS
➤ Maximum of likeliness map
➤ Slowness map</td><td>• AMPLITUDE STACK
➤ Stack absolute amplitutes raised to a power of 1 to 2</td><td rowspan="3">• 3D PRESTACK DEPTH MIGRATION (STANDARD AND AMPLITUDE)</td></tr>
<tr><td>• OPTIMUM CROSS DIP STACK</td><td rowspan="2">• MIGRATION OF THE AMPLITUDE STACK</td></tr>
<tr><td>• 3D MIGRATION OF THE OPTIMUM CROSS DIP STACK</td></tr>
<tr><td colspan="3">• INTERPRETATION SECTIONS</td></tr>
</table>

by a single step called 3D prestack migration. DMO ‘free” data can be further treated as phase coherent or only amplitude coherent, breaking the processing stream into three. An assumption of phase coherence among the DMO corrected data leads into the cross dip analysis and the optimum cross dip stack. When DMO corrected data is considered amplitude coherent only, it is amplitude stacked. Both cross dip stack and amplitude stack can be migrated if the geometry of the imaged structures warrants it.

Various events in the data exhibit different degrees of phase coherence and it is often very difficult to determine how well are the partially stacked data time aligned in the CMP bin gathers. In other words, it is hard to estimate the amount of 3D information that the data carries. Because the main objective is to image the 3D geometry of the surveyed structures and because the cross dip analysis is computationally much faster than the 3D prestack migration, it is applied first.

3.2 Optimum Limited Offset Range for Partial Stack

Several seismic procedures (particularly 3D prestack migration and DMO) require large CPU power to process every trace of a high fold 2D crooked line data volume. Also, the summations that are part of these processes are usually designed for regularly spaced data. In order to reduce and regularize the data volume a partial stack is applied. But

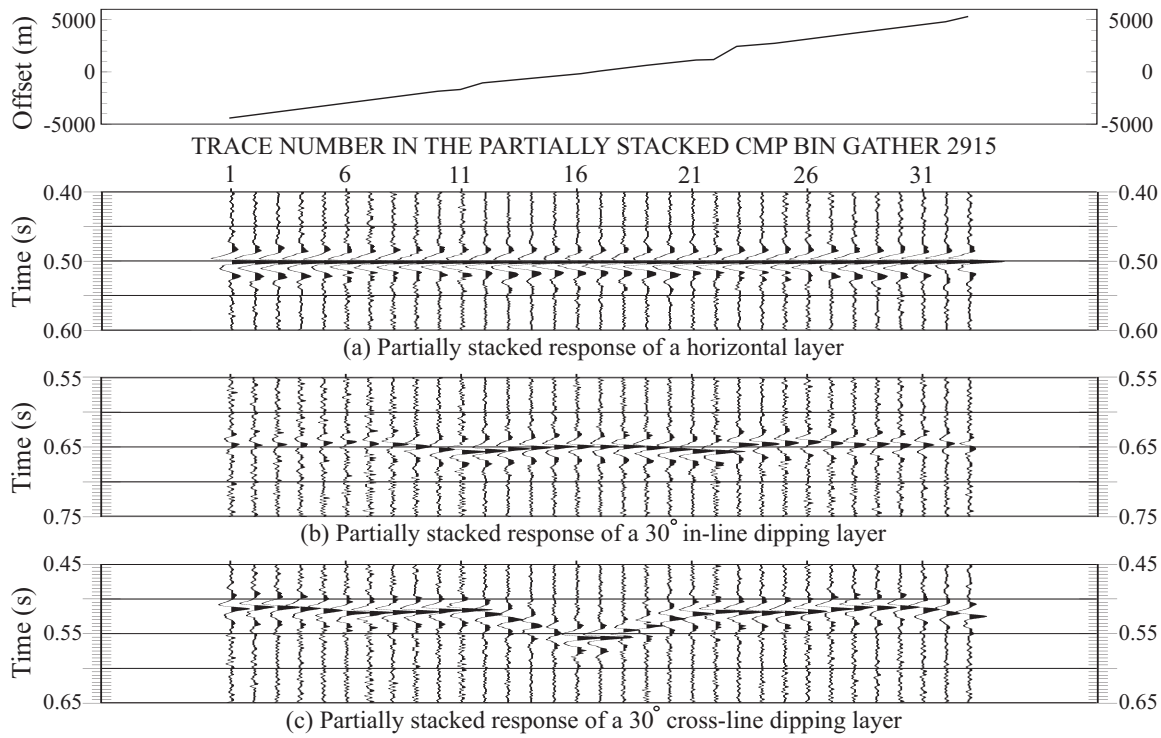

Figure 3.1: Partial stacks in 200 m bins of CMP 2915 for the horizontal (part (a)), in-line dipping (part (b)), and cross-line dipping (part (c)) modeled layers are presented. No zero traces are present in the partial stacks, as offset ranges without seismic traces were skipped. Top part of the figure shows the average trace offset of all traces found in the offset windows for the partial stack.

first one must determine the size of the offset windows or bins that will give an optimum result. This is not a trivial matter, because use of too wide windows will suffer from all the same problems as the standard CMP stack and too narrow ones will not reduce and regularize the data set sufficiently. We can use the NMO corrected model data of figure 2.9 to illustrate that partial stacking over the smaller offset ranges does not cause signal loss. Figure 3.1 shows data from figure 2.9 that has been partially stacked using an offset window 200 meters wide. Naturally, for the horizontal reflector there is no signal loss and all partially stacked traces show improved S/N ratio (figure 3.1.a). For the mostly in-line dipping event (figure 3.1.b) time error is sufficiently slowly varying with offset that there is little shift over a small window like 200 m. However, the same is not true for the mostly cross-line dipping event (figure 3.1.c). A few traces do exhibit signal loss near the middle of the gather where the time shifts associated with cross dip are most rapidly changing with offset. Obviously, the maximum range of offset for partial stack that causes little signal loss varies from one reflection event to another and with survey geometry. However, reflectors and their geometry are not identifiable at this stage of data

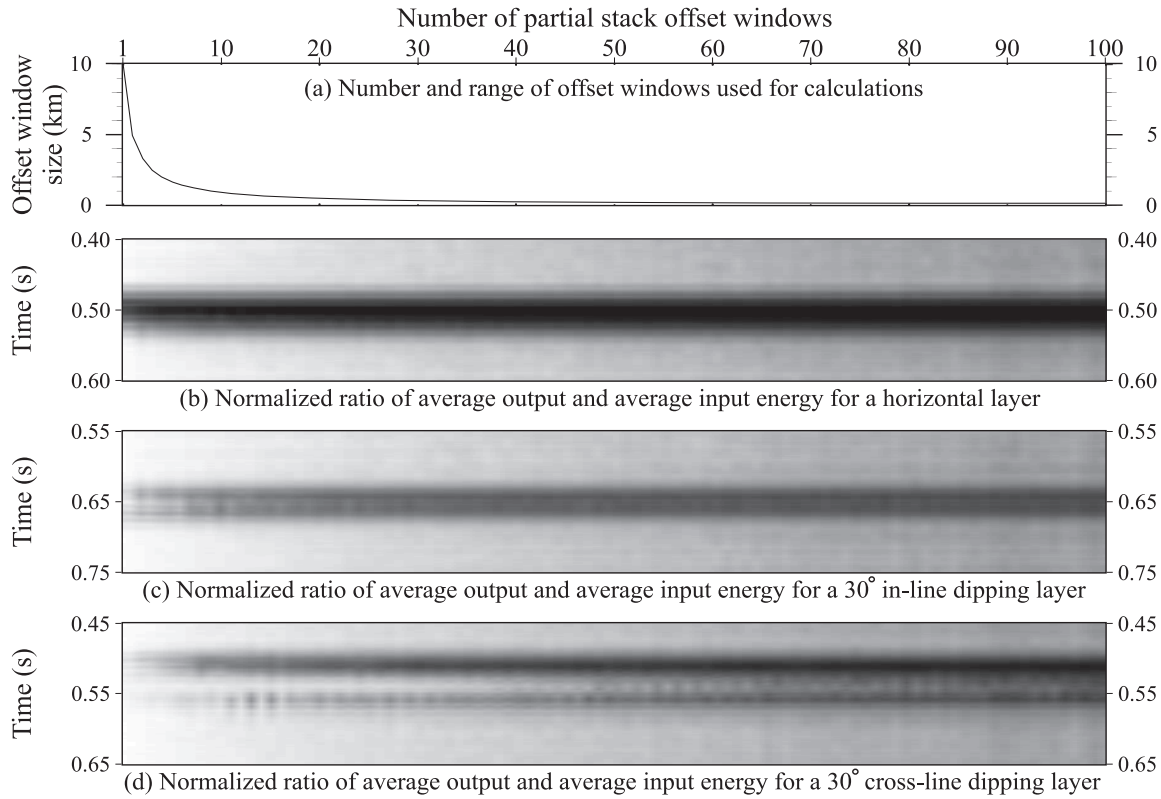

Figure 3.2: For the three modeled events a form of semblance was calculated using the synthetic data in CMP bin gather 2915. The semblance, plotted in gray scale, is given as a function of time and number of offset windows. For the in-line and cross-line dipping event, signal semblance is low until more than about 20 windows are used (offset range <500 m). Small scale plots shown in this figure are used to identify the approximate location of the highest ratio of signal semblance to random noise semblance.

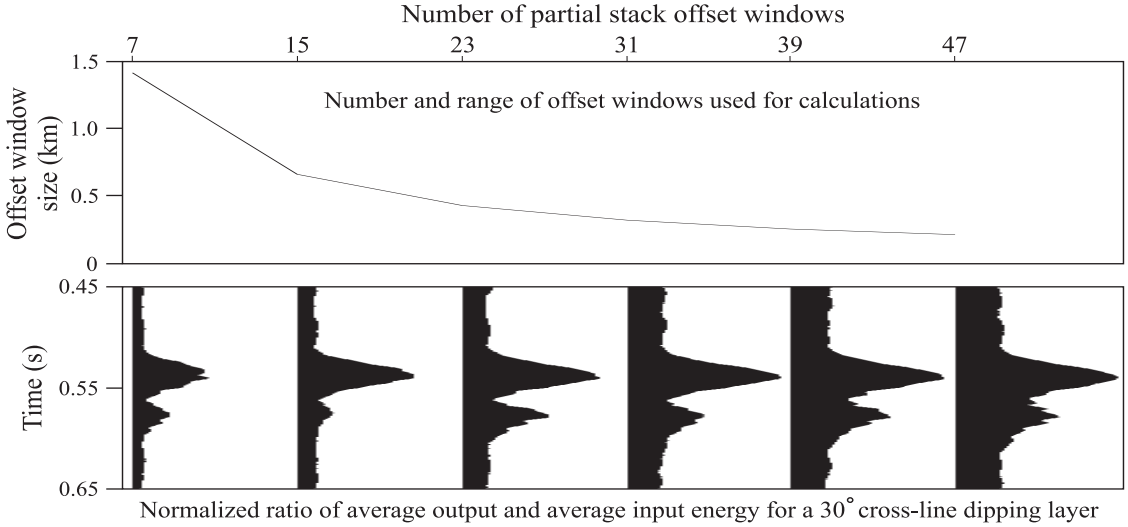

Figure 3.3: To find the optimum partial stack offset range for the cross-line dipping reflector, selected results from figure 3.2.(d) are enlarged and plotted in the variable area technique. The optimum offset window for partial stack is where the highest ratio of signal semblance to random noise semblance is observed (~350 m for this study).

processing; so the pragmatic solution is to apply statistical measures to the data itself to find an optimum set of offset windows for partial stack. This is the offset range at which partial stack preserves most of the coherent signal present in the records, somewhat reduces the random noise, and makes the prestack data set significantly smaller.

Figures 3.2 and 3.3 show the results obtained on the synthetic data of figure 2.9 by applying the procedure I designed to determine the optimum offset range at which to partially stack data (see figure captions for discussion). Full details of this procedure are given in Chapter 5 (5.3.4) where I show how it is done on real data. At this stage, it is only necessary to know that one can reduce the observed CMP gathers from their original form with a highly variable number of traces, quite variably distributed in offset, to a much smaller and more regular form (say 30-50 uniformly spaced offsets) without much loss of signal due to in-line and cross-line dip effects.

3.3 Cross Dip Study

Without much explicit consideration of the cross dip moveout (CDMO) a crooked line observational data set can be time corrected for surface effects, adjusted spectrally, filtered to enhance reflected P waves and partially stacked to compress it into a form where CMP bin gathers have traces with regularly spaced offsets. But any further progress towards obtaining a structural image from the data requires that CDMO be dealt with directly. The difficulty in this is that reflector cross dip is an unknown to be determined from the data, not an a priori known parameter; and the survey data set may or may not provide enough information to determine it satisfactorily. In this respect, the cross dip problem differs from the in-line problem where continuous coverage along the survey profile makes it possible to design in-line migration or partial migration algorithms that appropriately relocate the reflection events in the data volume into the 2D structural image or SZOST section, respectively.

That a cross dip "problem" exists with crooked line surveying is not new. Larner et. al. (1979) dealt with it many years ago but only for the simple case where all the imaged formations have one or two cross dips. Wang and West (1991b) took the problem a stage further, by treating the cross dip as an unknown but uniform over substantial parts of the SZOST section. My objective was to make cross dip a free parameter that can vary locally.

Figure 3.4 shows a part of figure 2.7 but in a perspective, together with a reflector dipping

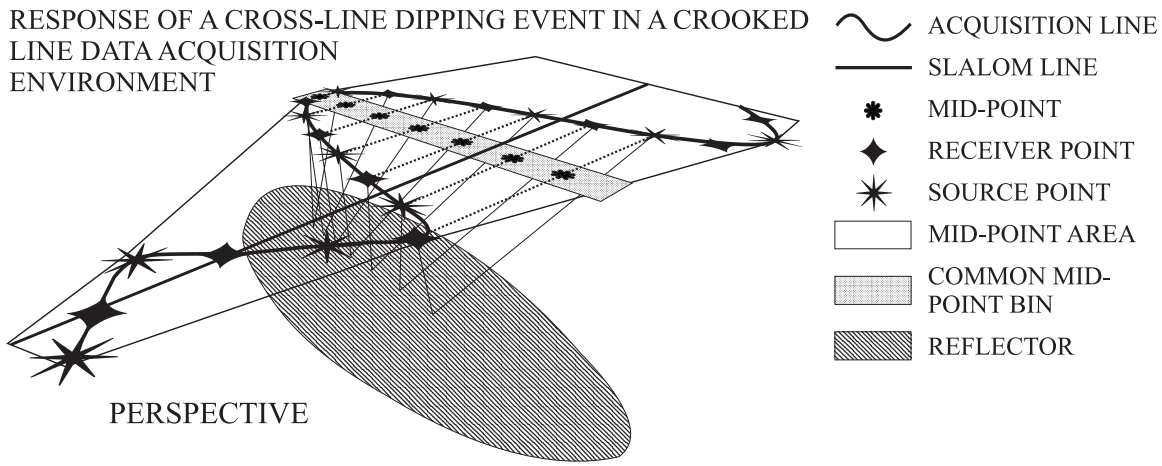

Figure 3.4: Perspective view of the crooked line seismic reflection data acquisition. Only a part of the figure 2.7 is shown in a perspective so that the picture does not become too saturated with events and unclear. A feature dipping mostly in the cross-line direction is added to the figure to explain the effect of the cross dip on the data acquired on crooked lines.

mostly in the cross-line direction. A basic grasp of the relationship between the source-receiver offset, cross-line offset, and the change in reflector traveltime that I here call cross dip moveout (CDMO) can be acquired by examining it. Within any single CMP bin gather and for any single reflector, both cross-line offset and CDMO vary slowly and systematically as a function of the source-receiver offset. For a given event, only traces with a substantially different source-receiver offset exhibit significant differences in CDMO. This is why it is possible in the first place to find an optimum limited offset range for partial stacking of the data. In a constant offset section the change in the CDMO along the slalom line (from CMP bin to CMP bin) is even milder. Thus we can expect dip moveout (DMO) to be essentially corrected by standard processing even if CDMO is present in the data. This can be verified in another way. For crooked line geometry, the algebraic expression for traveltime of the signal reflected from a dipping flat sheet in a host medium of uniform velocity is a function of many parameters (see the traveltime equations in section 2.5 and Appendix E). However, as long as the azimuths of the source-receiver offset do not vary greatly, various components of the traveltime can be well estimated independently. Therefore, NMO, DMO, and CDMO can be removed separately (see the processing flow in table 3.1).

The NMO and DMO are dealt with first in a standard fashion. After the velocity analysis, the data is NMO corrected, partially stacked and gathered into "constant" offset sections, and a standard DMO partial migration is applied. The traces in the DMO-"free" constant offset gathers are sorted back to CMP bin gathers and arranged by the increasing cross

offset.

The next process applied is the procedure designed in this study for removing CDMO, called a "locally optimum cross dip correction"[3]. It starts by creating a list of 20-100 cross slowness values P_y[4] that encompass the cross dip range of interest. Because reflector cross dip is generally unknown, the full range of cross slownesses (which must lie within $\pm$ the RMS velocity of the medium; typically $\sim \pm 0.17\ ms/m$) is selected for the cross dip study. For each cross slowness, the traces in the CMP bin gathers are time shifted according to their cross offset and stacked. In addition, the same shifted traces are used to calculate a slightly modified form of semblance (a signal likelihood measure). This creates two data volumes; the CMP stacked traces and their semblances, both sets having trace for each CMP bin on the slalom line and for each cross slowness. The semblance traces are then searched for local maximum values in time and cross slowness to form a 2D cross slowness map. This map is further optimized in time/space by filters that remove spurious values and smooth the data. Unreliable determinations of optimum cross slowness values are discarded. Where the cross slowness is determined reliably the appropriate parts of the associated CMP stacked traces are selected for the final section. The remaining parts of the data are assumed to have zero cross slowness. The final product obtained is an optimum cross dip stack, a 2D section that represents a more accurate image of the studied subsurface than the corresponding standard stack does. In addition, a cross dip map is formed in which the dip direction and intensity are best expressed using a color palette. This color cross dip map does not feature the true dips of the reflectors because data is examined for cross dip before migration. In spite of that, the optimum cross dip stack superimposed on the cross dip color map is a very useful interpretational tool. It provides 3D structural information about the imaged events in an easy to interpret, compact form (2D sections).

Together, an optimum local cross dip stack, the corresponding cross slowness map, and the size of the cross offset spread in each CMP bin provide enough information to position the imaged events in 3D space (Nedimović and West, 2000). I have designed a migration process for this purpose which required only a simple modification to a standard Kirchhoff poststack migrator (see section 5.5 for details).

[3]The technical details of the designed cross dip study are provided in section 5.4.

[4]Terms cross slowness and cross dip are both used for the discussion purposes to express the dip of the events towards a slalom line. The use of both terms is valid when: the source-receiver azimuth does not vary greatly, in-line dip component is relatively small, and RMS velocities are known, because equation 2.4 reduces to: $P_y \approx 2 \sin\theta_y / V_{RMS}$, where θ_y is cross dip component of the true reflector dip and V_{RMS} is the root-mean-square velocity.

3.4 3D Prestack Migration

One hopes that the local optimum cross dip stack (see section 3.3) will result in a much better section than the standard stack. But one must also recognize that this process has fundamental limitations, for instance, where the reflective responses of the imaged events overlap in the section, only the stronger will remain in the optimum cross dip stack; also an azimuth approximation was made. The only procedure that has a potential to preserve all of the recorded reflective events and position them correctly in space, is 3D prestack migration.

The possibility of obtaining a structural image from 2D crooked line seismic data by applying 3D migration methods is not a new idea. It has been discussed briefly by a variety of authors (e.g., Geiger, 1995, Geiger et al., 1995, and Bancroft et al. 1998). However, it usually is discussed more as a possibility than a practical solution to the imaging problem. This is not surprising because there are good arguments both pro and con this approach.

On the positive side, Kirchhoff prestack depth migration is a process that operates on input trace data in a trace sequential fashion and there are no fundamental limitations about the recording geometry of the traces. Thus, the irregular geometry of a 2D crooked line data set poses no direct technical problems at all for the migration algorithm.

On the negative side, there are many reservations in principle as to whether a useful result can be achieved in this manner. Although it is difficult to estimate in advance just how serious the problems may be in any specific case, one can see where they arise. They are fundamental to the whole concept of imaging complicated structures in space from reflection seismic data recordings that provide mainly time information (= distance or range information, once average propagation velocities are known).

Migration is often thought of as a process that can transform the traces in a SZOST section or volume, or the data in the original set of observed source-receiver traces, into a 2D or 3D image of reflectivity in space. In the simplest case, where survey is complete and the reflectivity contrast occurs on a large surface, there will be a one-for-one relationship between data points in the SZOST volume and in the image volume, so migration can then be considered as a mapping transformation from data space to image space. However, even in a constant velocity medium, simple mapping occurs only when the data set is complete (there are no absent or missing traces and data is uniformly sampled in time), signal to noise ratio high, and reflections arise from flat surfaces. If

any of these requirements are not met, migration may be a much more complicated and possibly a very incomplete or error prone process. This is easily illustrated by noting that migration is a linear operation in respect of input seismic trace amplitudes, and its operation can be understood by observing what it does with data that consists of only one non-zero value at a sample point in the observational time and position in space. Basically, the migration outputs a data volume that is non-zero at any space location that could possibly have generated data at the time and location of the input data point. Thus, reflection signal amplitude at one point in data space becomes reflectivity amplitude on a surface (3D) or line (2D) in image space (surface or line of possible reflectivity). Then, when data from nearby points in data space that arise from the same reflecting surface are migrated, they produce outputs on surfaces or lines of possible reflectivity that are slightly of different shape and/or position and only partially overlap with the surface from the first point. When all the data are included, interference will cancel out the reflectivity amplitude on most of the surfaces of possible reflectivity, but will enhance it where the reflections actually occurred. In this way, migration uses the spatial distribution of observation points to determine the true location of reflectors. Available data must be distributed through a sufficiently large space aperture to localize the actual reflection points. And if the survey does not provide sufficient aperture the migrator will smear reflectivity data values corresponding to the reflection point over an extended surface that indicates where the reflection point might have occurred.

An extreme example of aperture effects arises with 2D straight line profile surveys. Such data can be 2D migrated to a sectional plane (usually the vertical plane containing the survey line) under the assumption that the structures strike perpendicularly to that plane because the survey has a large aperture in the profile direction. If the 2D data set is complete and the survey profile sufficiently long, the 2D migration will be complete; and if the strike assumption is valid, the resulting section will describe the earth structure correctly.

However, this survey data has zero aperture in cross profile direction, and if it were fed to a 3D migrator, the result would be a 3D reflectivity volume that is the same as the 2D migrated section on the section plane but (except for a systematic amplitude factor) would be cylindrically symmetric about the survey line. This would express the fact that a 2D straight line survey cannot provide any information about cross dip of the reflectors. Also, unless the reflectors all have the same cross dip, the reflection points do not lie on one section plane.

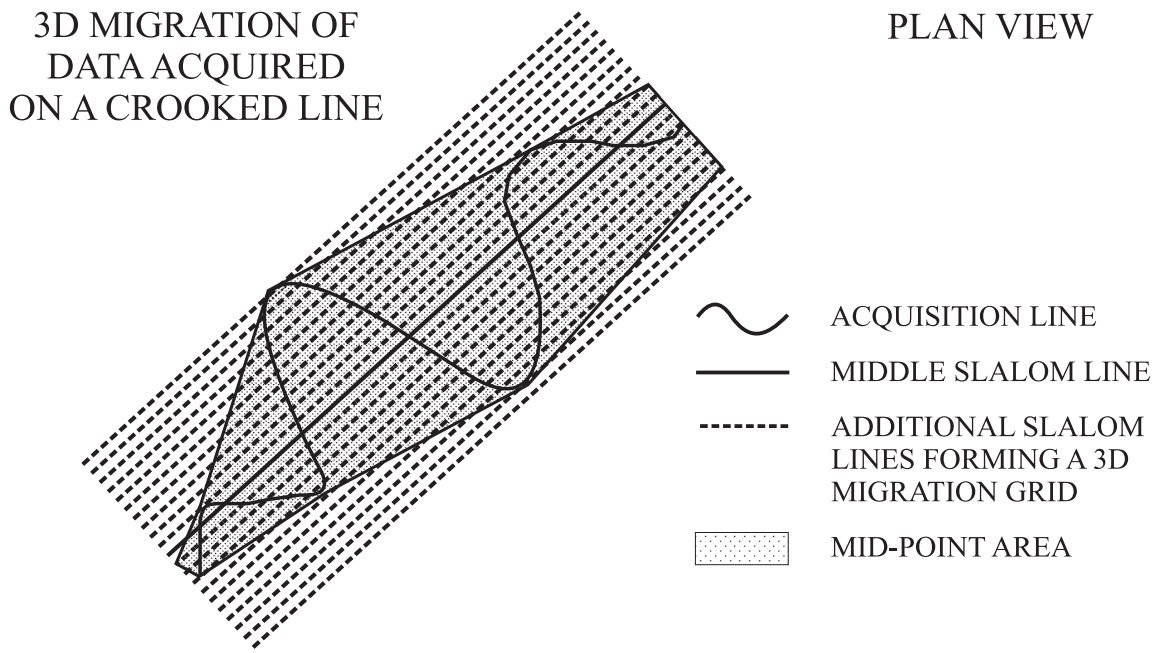

Figure 3.5: Data acquired by crooked profiling doesn't have to be migrated to the vertical plane of a chosen 2D line, called the slalom line. Instead, it can be migrated to a 3D data volume. The migrated data "cube" is later examined to learn more about the 3D structure of the imaged reflective events.

In applying a 3D migrator to 2D crooked line data, we are hoping that the survey geometry provides enough cross-line aperture that reflection points will be reasonably well localized in the cross-line direction. However, it must be recognized that this localization may be much less than is realizable in the profile direction, and it may vary considerably along the profile.

Perhaps even more serious consequence of the very small cross-line extent of the survey is that the appreciable reflection amplitude may not be observed from all reflectors beneath the survey line. Basically, only those parts of reflectivity interfaces that face towards the survey profile will be clearly imaged. Put another way, a crooked line survey may be able to determine the cross dip and the lateral position of any reflector that gives an appreciable reflection signal, but it will only receive appreciable reflection signal from those parts of reflecting surfaces that face towards the survey line. The 3D reflectivity image will therefore be, at best, a subset of what might be imaged in the 3D swath beneath the survey profile by a true 3D survey, and this limitation must be considered in any interpretation.

In order to migrate crooked line data to a 3D data volume I have designed a specialized procedure (see section 5.4 for more details). This procedure differs from the standard

Kirchhoff 3D prestack migrator only in terms of the input and output data geometries. As shown in figure 3.5 a 3D surface grid for migration is formed by placing additional 2D migration lines parallel the slalom line. The size and density of this grid is chosen to satisfy the investigation purpose and to avoid aliasing. When survey profiles are long, the slalom line may have a number of straight line segments. For each of these segments, a separate 3D migration output grid is formed and migration performed. The input data are three dimensional volumes (time, CMP bin, offset). The output data volumes should extend as far as the migration aperture can "reach".

The 3D data volumes obtained through the prestack migration can be analyzed in a similar way to any other seismic reflectivity data volume, except that limitations of the process must be taken into account.

The main disadvantage of 3D prestack migration is the enormous CPU power it requires. Furthermore, interpretation of a 3D data volume in which events are smeared over larger areas is a challenging and a very involved task. Interpretation becomes particularly lengthy if there are many volumes to examine for each seismic profile. But the fact that the 3D prestack migration has a potential to preserve and position all of the reflectivity/scattering to its true subsurface positions and reveal the true 3D geometry of the imaged structures is enough of an advantage over the cross dip study to warrant its application where necessary.

3.5 Amplitude Imaging

Despite all the effort, the methods discussed so far may not succeed in focusing the reflection signals of a crooked line survey into a satisfactory image. This may happen, for instance, because RMS velocity is too hard to estimate well, or even more so because the reflectors have such complicated structure that they act more like random scatterers than specular mirrors (Nedimović and West, 1998 and 1999). If this is the case, the only feasible solution then is to try to find a method of combining data traces that has a greater time (phase) tolerance than simple averaging (stacking). Such method would preferably enhance signals that approximately obey the travel time equations (2.3 and Appendix E).

In most other circumstances where waves are used to probe structures remotely (i.e.,

optical imaging, sonar, radar, etc.)[5], the dominant wavelength in the probe wavefield is very short in comparison to the distance the wavefield must travel and size of the objects to be probed. Thus, phase coherent specular reflection is not the key reflection process. In these methodologies, it is the scalar amplitude of the reflected signal (or similar quantity like envelope amplitude or energy) that is most commonly used as the measure of signal strength. For comparing signals observed at different locations that may be due to the same reflecting or scattering object, phase coherence is not expected. It is therefore worthwhile to study how we might implement something similar in seismic signal processing.

It is straight forward to convert seismic trace recordings $s(t)$ (which usually are directly relatable to instantaneous ground motion) to scalar amplitude $|s(t)|$, energy $s^2(t)$, or envelope amplitude $(s^2(t)+\{H[s(t)]\}^2)^{1/2}$, where H denotes the Hilbert transform. These time series are all positive, and "reflection signals" are then identifiable only as local increases or changes in the amplitude relative to some comparatively steady background level that can be considered noise. The tests done in this thesis research show that a simple way to extract these local changes from the steady noise background is to apply a low cut (usually 0 Hz) or bandpass frequency filter to the amplitude data.

In my investigation of time (or phase) tolerant stacking methods I have employed a simple measure of signal amplitude where the amplitude trace $a(t)$ is related to the usual seismic trace by:

$$a(t) = |s(t)|^P, \text{ where } 1 \leq P \leq 2. \tag{3.1}$$

With this measure, a constant amplitude sine wave $s(t)$ converts to a constant level and some higher frequency (even) harmonics. Random uncorrelated noise in the interval (-1,+1) converts to a noise in (0,+1). i.e., has a mean value of 0.5 and half the standard deviation of the original. Therefore, there may be some value in using the envelope amplitude $(s^2(t) + \{H[s(t)]\}^2)^{1/2}$ instead as the high frequency components would be reduced. However, experiments have shown no benefits commensurate with the additional computation cost, and even some unnecessary loss of resolution.

Producing amplitude stacks is a fairly simple procedure. Processing continues in a standard fashion to the point where the partially stacked and NMO and DMO corrected trace data would ordinarily be stacked into traces of the SZOST section. At this point, the traces in the CMP bin gathers are converted to absolute amplitudes and raised to

[5]For more details see for example Kock (1973), and Shearman and Clarke (1988)).

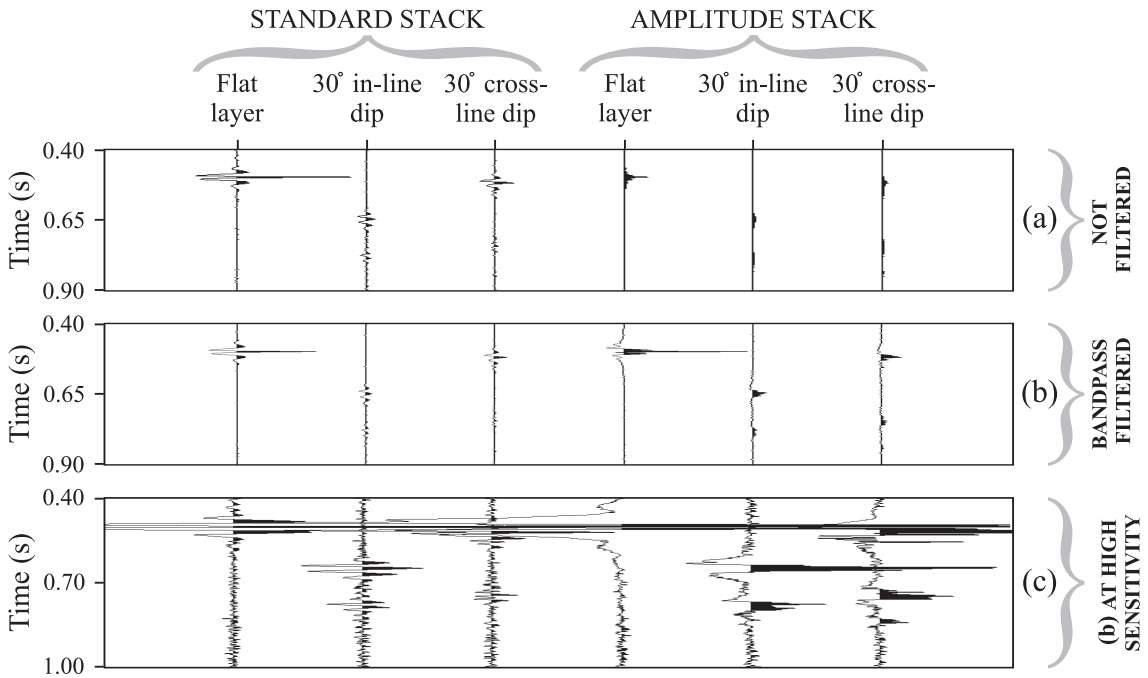

Figure 3.6: Standard stacks (traces 1 to 3) and amplitude stacks (traces 4 to 6) of partially stacked data from figure 3.1. Within each part of the figure (a, b, and c) stacked traces were balanced so that the random noise exhibits the same energy level. This can be visualized at late times in part (c), which is identical to part (b) except for the boosted amplitude levels. (b) is bandpass filtered (a). Standard stacks in (b) were bandpass filtered at 20-50-300-400 Hz, while amplitude stack were bandpass filtered at 0-20-300-400 Hz.

a selected power between one and two. They are then stacked in the usual way and a bandpass filter is applied to at least remove the slowly varying noise background from the all positive stacked trace. To optimize the amplitude stack, the filter may be applied before and/or after stacking.

Figures 3.6 and 3.7 illustrate test results obtained by standard and amplitude stacking of synthetic data shown in figure 3.1, which is comprised of partially stacked responses of a horizontal, a 30^0 mostly in-line, and a 30^0 mostly cross-line dipping event. Signal from both dipping events in the partially stacked traces of figure 3.1 shows severe time alignment problems mostly due to the unaccounted CDMO and to a smaller extent due to the varying source-receiver azimuth. For the 30^0 mostly cross-line and the 30^0 mostly in-line dipping event, the arrival time of the partially stacked signal differs up to 50 and 20 ms respectively; whereas the signal wavelet is a 20-300 Hz Butterworth minimum phase wavelet[6] with $\sim$5 ms half cycle width. Thus, in the left hand side of the figures 3.6 and 3.7 where the standard CMP stacked traces are presented, the dipping reflectors

[6]The Butterworth minimum phase wavelet in all figures looks more like a zero phase wavelet because synthetic data was bandpass filtered.

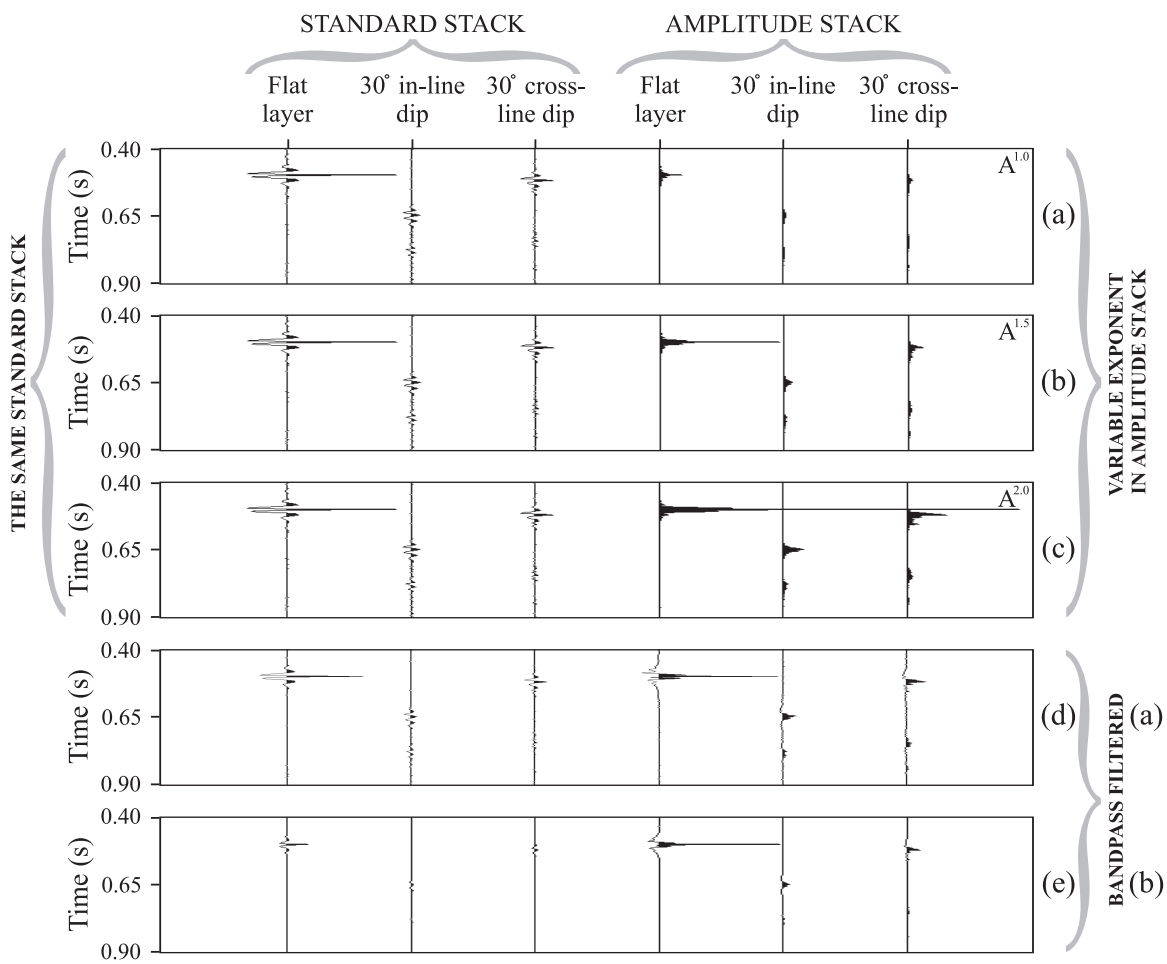

Figure 3.7: Standard stacks (traces 1 to 3) and amplitude stacks (traces 4 to 6) of partially stacked data from figure 3.1. The standard stacks for the first three parts are the same. The amplitude stack changes, as the absolute amplitudes are raised to the power of 1 for part (a), 1.5 for part (b), and 2 for part (c). Parts (d) and (e) of the figure are exactly the same as parts (a) and (b) respectively, except that parts (d) and (e) are band filtered. Standard stacks in (d) and (e) were bandpass filtered at 20-50-300-400 Hz, while the corresponding amplitude stacks were bandpass filtered at 0-20-300-400 Hz.

show as very weak and diffuse events compared to the horizontal one.

To show how the amplitude stacks compare with standard (phase) stacks, we first need to consider how noise is handled. The modeled data traces all contain random noise of the same amount in the entire time interval (0 to 2 s) and no reflection/diffraction signals occur beyond 0.9 s. The noise level in this part of the stacked traces therefore will not depend on reflector dip. It will only depend on stacking and post filtering.

Since most seismic data processing has much difficulty preserving true amplitudes, it is the relative amplitudes of signals and noise that are important. To see this, the trace amplitudes in each panel of figures 3.6 and 3.7 have been scaled to have the same noise

levels (observe the amplitudes at late times in figure 3.6.(c)). This does not alter the relative amplitudes within any of the trace groups but shows how amplitude stacking (with and without a post filter) affects signal-to-noise (S/N) ratio.

Figure 3.6 shows the results when a power of one is used in the amplitude computation. In (a), where no low cut is applied, the noise after amplitude stack is relatively larger than in the standard stack. Thus, although both the standard and amplitude stacks yield signals for the three events that are of similar relative magnitude, there is a reduction in S/N ratio with the amplitude method. However, the result is opposite after the bandpass filter (0-20-300-400 Hz), with the amplitude stack about twice better. (Note that the flat layer standard stack in (a) and the flat layer amplitude stack (b) have been assigned ~unit plot amplitude).

The effect of changing the exponent in amplitude stacking is illustrated in figure 3.7. First, raising the exponent raises considerably the S/N ratio of the amplitude stacks, both with and without filtering. However, it also increases the contrast between the three events because it heavily favours large amplitudes. Thus, an exponent value as large as two may be undesirable.

A notion commonly held among practicing reflection seismologists is that the larger the bandwidth of the seismic signal, the better will be the resolution of the subsurface imaged. Figure 3.1 indicates that this holds true only if all of the data are well aligned (phase coherent). If the signal cannot be well aligned, there is nothing to gain by broadening the frequency spectrum of the wavelet. Actually, as the processing proceeds, the sharpness of the events on the image might decay (high frequency components attenuate).

The theory of migration has been developed based on the assumption of phase coherence in the signals. If the signals are converted to amplitudes at any processing stage before migration, one of the main concerns must be whether the obtained amplitude SZOST section can be migrated. Various tests of this have been carried out during this study. All have shown that amplitude sections can be successfully migrated, i.e., migrated amplitude stacks of comparable quality to migrated standard stacks can be obtained (see also section 5.5).

As an example, poststack phase shift depth migration was applied to four point diffractors in a uniform medium. Synthetic data for the test was produced by using a straight line geometry and a regular surface sampling (no shot or receiver skips). A Klauder wavelet (10 to 150 Hz) was applied in generating data, and the P-wave velocity of the medium

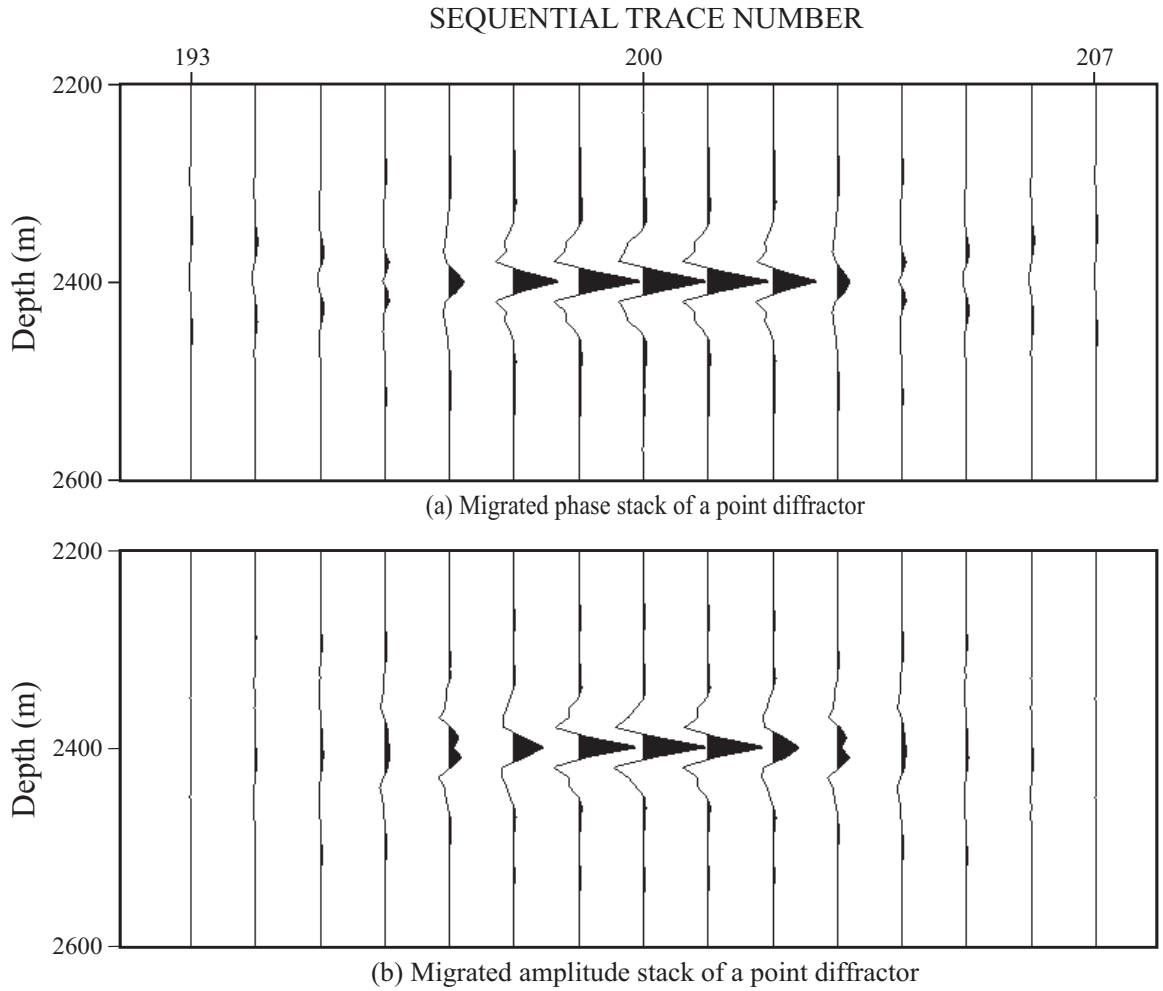

Figure 3.8: The figure shows a migrated standard stack (part(a)), and a migrated amplitude stack (part(b)), of a small diffractor. The diffractor was positioned at the depth of 2400 meters directly below the middle of the seismic profile with a straight line geometry.

was 6000 m/s. Four diffractors were positioned directly below the middle of the line at the depth of 300, 600, 1200 and 2400 meters. The data was free of any time anomalies. Both standard and amplitude CMP stacks of the data were formed and then migrated. Before the amplitude stack, absolute amplitudes were raised to a power of 1.5.

Figure 3.8 depicts both migrations of the diffractor at 2400 meters depth at a large scale. It is clear that both results exhibit approximately the same focusing. However, to achieve the good focusing in the migrated amplitude stack, bandpass filters must be applied after the CMP stack and after the migration. The first filter (0-20-120-150 Hz) is applied on the amplitude stack to remove the DC shift containing a large amount of random noise. The low cut of the filter is always positioned at 0 Hz. The amplitude stack is frequency filtered again after migration, but this time the filter used is usually the same as the one

used for the migrated standard stack (5-15-40-50 $cycle/km$ in the case presented in the figure 3.8).

In conclusion, amplitude stacking seems to be an effective imaging technique that may perform better than standard processing when the signal can not be well aligned for stack. The obtained amplitude sections can be migrated. If the velocities are poorly determined, and/or large residual static problem exists, and/or the reflective surfaces have a very complex shape, better imaging may be also achieved by 3D prestack migrating amplitude instead of phase data. However, the amplitude method is essentially a measure of last resort.

3.6 Summary

Two procedures have been designed to try to extract 3D structural information from 2D crooked line data acquired in crystalline terrains. The first one is an attempt to identify the cross slowness associated with each reflected event and correct the prestack event arrival times on this basis. The result is a locally optimized 2D SZOST section that also features the extracted cross dip information as a color background. The second procedure is a 3D prestack migration in which a 3D image data volume is obtained. The optimum cross dip method is very much faster computationally, and should provide an improved 2D image that is compact, easy to interpret, and fortified with the obtained 3D information. However, some of the 3D information is lost during the cross dip stack where the reflective responses of the events overlap in the section. The 3D migration requires a lot of CPU power and its output can be difficult to interpret, but at least theoretically it preserves and positions accurately in space all of the recorded reflectivity.

The third procedure called the amplitude stack was also designed to optimize the imaging when the signal phase coherence is lost. Amplitude stacks show great potential, can be migrated using standard techniques, and are extremely fast to produce.

The subsequent chapters of this thesis provide more details of the proposed methods, and test them on modeled and real data extensively. The modeled cases have very simple reflector shape, but the geometry of the data acquisition is that of the actual example crooked line surveys.

Chapter 4

Examples on Modeled Data

Chapter 4 is designed to test the ideas and imaging techniques discussed in Chapter 3. The directions taken to improve imaging in crystalline terrains were tested on various subsurface models by producing the corresponding synthetic seismic reflection data, processing it, and examining the results.

To compute the synthetic data sets examined in this chapter, a ray-Born modeling algorithm and seven numerical models were designed by this author, and were used together with the crooked line geometries of the real data sets processed in Chapter 5[1].

4.1 Ray-Born Modeling

The examination of synthetic seismic data provides a tremendous insight on how to process real data. In geologic environments such as crystalline terrains, where diffractors dominate over the reflectors, the ray-Born method is capable of providing particularly useful synthetic (modeled) data sets because, for example, exact amplitudes, multiple reflections, and converted wave types are not required.

Ray-Born modeling combines the ideas embedded in both asymptotic ray theory and Born scattering approximation. In the Born approximation, the scattered wave field is assumed to be weak in comparison to the primary field. Furthermore, if the condition is satisfied that the volume of the scattering inclusion is small relative to the wavelengths, the scattering is called Rayleigh scattering and is expressed by very simple

[1]The two crooked line profiles studied in this thesis are the high resolution Sturgeon Lake Line acquired for mining purposes and the regional Line 23 collected for crustal studies.

equations. The response of larger scatterers can be calculated by integrating the point scattering kernel expression, as long as the weak scattering approximation still holds. Reflectors in the models used in this study were represented by many Rayleigh point scatterers and their response to the impinging primary wavefield was computed by numerical integration. In the ray-Born method, the travel times of "rays" having paths source→point-scatterer→receiver is calculated by the asymptotic ray method. Asymptotic ray theory is also used to calculate amplitude decay due to spherical divergence along the ray paths. Since all my modeling used a uniform velocity background medium, the asymptotic expressions are exact.

Brief mathematical descriptions of the asymptotic ray theory, the Born approximation, and the Rayleigh scattering are given in Appendix A. The ray-Born algorithm developed to model data in this thesis is also found in Appendix A.

Modeling methods capable of producing more complete and more accurate synthetic data than the one used do exist. However, they require much more computer time. Gigabytes of synthetic data produced during this work took months of CPU time on the fastest workstation computer available to me, and any additional computation was not possible if the project was to be completed. It is important to note that real acquisition geometries and reflectors of realistic size were used during modeling. Shot records were formed by summing the response of hundreds of thousands of point scatterers for each trace. I believe that the synthetic data formed and examined during the course of this study was the best possible compromise at the time.

4.2 Characteristics of the Modeled Data

During modeling, only the P wave response of point scatterers due to the P waves propagating directly from the source was calculated. Therefore, the main difference between the real and synthetic data in this thesis is the absence of any type of systematic noise (vibrator noise, surface waves, air waves, refracted P and S waves, etc.), converted waves (e.g., PS), and multiple energy, in the synthetic data. When modeling, the P wave velocity of the medium was assumed constant at 6 km/s. The introduction of a vertically varying velocity (one of the options in the modeling code) was not necessary as the crystalline mediums can be viewed as relatively homogeneous at large scales. Mild vertical variations in the velocity do not introduce significant local changes to the reflection arrival times and therefore, do not cause much misalignment of the data signal. The

wavelet does not change as a function of time in the synthetic data because no anelastic attenuation was incorporated in the modeling code used. The complexity of the real seismic reflectors is not matched in the numerical models, where, although the reflectors were freely oriented in space and of variable size and attitude, they are still flat surfaces. In some cases, to simulate the response caused by the reflectors' complexity found in real environments, small surface consistent[2] static shifts were added to the traces. Random white noise was added to all of the synthetic data formed.

The synthetic data sets obtained for this thesis study represent a gross simplification to the geologic reality in the crystalline terrains. However, they do contain enough of the problematic features of real data to test the proposed imaging techniques. A technique that cannot handle the model data is unlikely to be helpful on real data.

The relative simplicity of the synthetic data allows the tests to employ a much shorter processing sequence than is needed for real data, as many of the procedures shown in table 3.1 can be skipped. To reach the point where the processing stream breaks into two: only entry of crooked line geometry, amplitude correction for geometrical spreading, bandpass filter, CMP bin sort, transverse offsets calculations, velocity analysis and NMO removal, optimum limited offset range analysis, and partial stack, need be applied . The procedures[3] that come after the processing breaks into two are identical to those used on real data.

Detailed description of all models presented in Chapter 4, including the modeling parameters, is given in the Appendix B. A purpose summary for each of the synthetic data sets follows:

- Model A data were used to carry out basic tests of 3D prestack migration (standard and amplitude) on point diffractors;
- Model B data were used to study time anomalies in CMP bin gathers due to crooked line surveying when no cross dip problem is present, as well as to test 3D prestack migration;
- Model C data were used to study cross dip moveout and the effectiveness of the optimum cross dip stack;

[2]An attribute or parameter of a set of seismic traces is said to be "surface consistent" when it is a function only of source and/or receiver position, and does not change each time that position is used to generate a trace. Traveltime anomalies due to overburden thickness or site elevation are good examples.

[3]Seismic data processing procedures are explained in Chapter 5.

- Model D data were used to test the effectiveness of the optimum cross dip stack, 3D prestack migration, and amplitude stack when both DMO and CDMO are very large;
- Model E data were used to test the same techniques tested on Model D data, but on a different (regional) survey scale. In addition, the effects of slalom line azimuth variation and the Fresnel zone radius were also studied;
- Model F and G data were used to test all of the designed procedures when the imaging is further complicated by the overlapping reflector responses.

4.3 Point Diffractors

The first tests of the standard and amplitude 3D prestack migration are very simple. These tests were carried out on data produced using only four point diffractors of Model A (figure 4.1) and the Sturgeon Lake Line survey geometry[4]. Two of the diffracting points are approximately under the survey line and two are offset $\sim$1500 m to one side. More information about Model A is given in the caption of figure 4.1 and Appendix B.

Special effort was taken during processing of Model A data to preserve the diffraction signature in the partial stacks. For the CMP bins lying at the ends of the slalom line, this meant using NMO correction velocities higher than the medium velocity. The offset range analysis indicated that the optimum partial stack is obtained with an offset window 300 meters wide.

Both the offset window partially stacked standard (phase) data and an amplitude conversion of it were 3D prestack migrated. As this was just a preliminary test, only several planes of migrated data volume were computed. To see if the result is robust to large time errors a second pair of tests was conducted wherein twice the static anomalies estimated for the Sturgeon Lake Line real data were added to the synthetic data before the partial stack. Both sets of standard and amplitude migrated depth traces were bandpass filtered (2-6-24-36 $cycle/m$ and 0-4-24-36 $cycle/m$ respectively).

Figure 4.2 shows the three migrated vertical slices extracted from the standard 3D data volume. The slices are 1500 meters apart. One pair of the diffraction points approximately lies in the vertical slice (a), while the other pair lies almost below the slalom

[4]Survey geometries of the Sturgeon Lake Line and Line 23 are both not only fairly crooked, but also exhibit uneven shot point distribution (see figure 5.1)

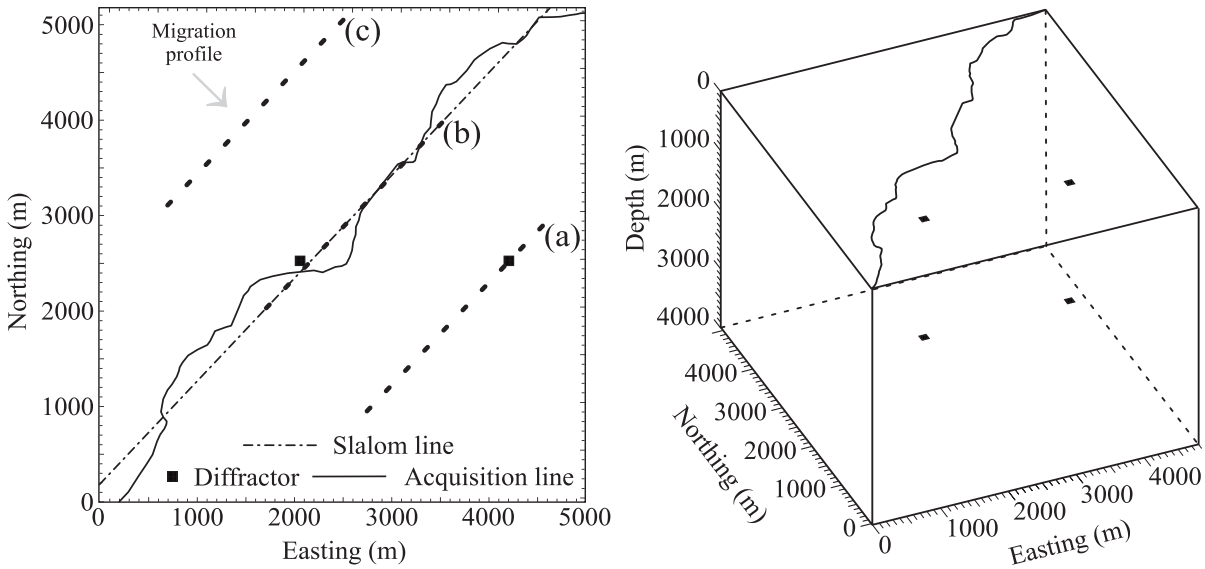

Figure 4.1: Plan and perspective view of Model A. Two of the diffractors lie close to the slalom line, at depths of 1000 and 3000 meters. The other two diffractors are at a distance of ∼1500 meters perpendicular to the slalom line. Their depths are also 1000 and 3000 meters. Dashed lines (a), (b) and (c) on the plan view show the surface extent of the vertical slices of migrated data presented in figure 4.2.

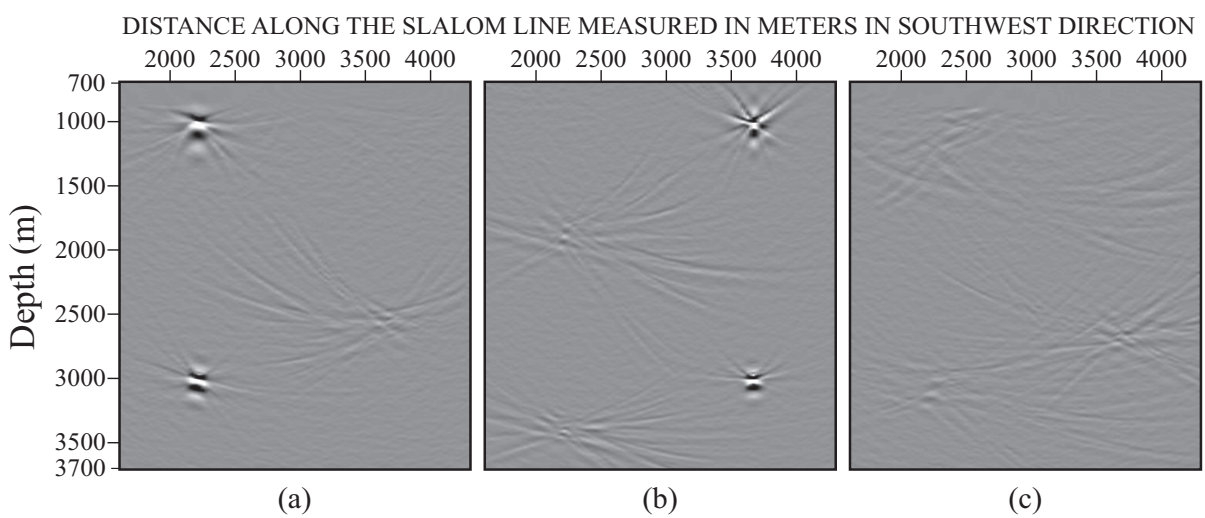

Figure 4.2: Three parallel vertical slices (a), (b) and (c) (the dashed lines in figure 4.1) from the standard 3D prestack depth migrated volume of Model A. (a) shows a part of the profile 1500 meters southeast of the slalom line. (b) is a part of the profile that corresponds geographically to the actual slalom line. (c) is a part of the profile 1500 meters northwest from the slalom line.

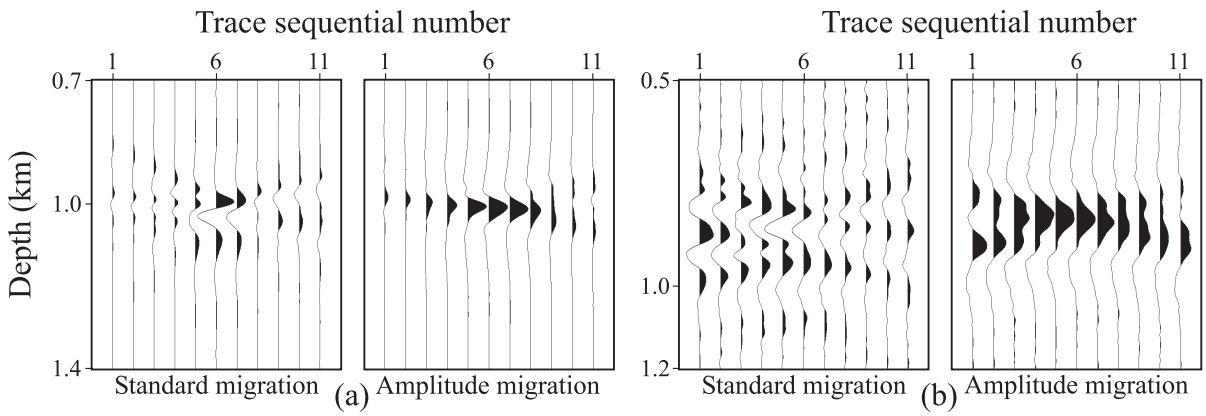

Figure 4.3: Signal focusing by 3D prestack depth migration. A small window around the upper diffractor in figure 4.2.a is shown. Part (a) of the figure represents data that is free from static anomalies. Data in part (b) have static shifts.

line and in the vertical slice (b). The third slice (c) is not positioned close to any of the diffraction points to see if serious artifacts develop far from the diffraction points. The obtained vertical slices 4.2.(b) and 4.2.(c) show results that are in line with what the migration theory predicts. Diffractors in 4.2.(b) are focused well at their true subsurface positions. 4.2.(c) shows no appreciable events. The focusing of the diffracted energy in 4.2.(a) at its true points of radiation is surprisingly good considering the irregularity of the survey geometry and the small ($\sim$350 m) average swath width of the survey.

In figure 4.3 the results are zoomed so that the diffraction point close to the slalom line and at the depth of 1000 meters is clearly visible. The migration of (figure 4.3.a) appears to focus standard and amplitude data equally well when they are free of any static anomalies. For the data with static shifts (figure 4.3.b) the amplitude migration focuses better. The strongest signal for phase data (part (b)) does not even appear in trace 6 at the true diffractor position. Note that the data with static shifts no longer focuses at the depth of 1000 meters. Static shifts have moved the signal to earlier times which appropriately translates into smaller depths.

Model A data and the tests performed on it are elementary. However, the results obtained are far reaching. They show that the 3D prestack migration can image well the energy diffracted by point scatterers located anywhere in the area that encloses the survey, despite the limitations of the data recorded on crooked lines. The results obtained also show that the artifacts created by the incomplete and irregular data set are not exceedingly strong. For data exhibiting large unaccounted static time shifts, migrating amplitude instead standard data may improve focusing.

4.4 In-line Dipping Reflectors

Model B and the acquisition geometry of the Sturgeon Lake Line (see figure 4.4 and Appendix B), were used to produce a seismic reflection data set. This data set is useful for testing crooked line focusing problems associated purely with the in-line dip.

Careful inspection of the CMP bin gathers of Model B data reveals a variation in the reflection time arrivals from the single events, even after applying static, NMO, and DMO time corrections. This unwanted time variation that causes signal misalignment is a result of the crooked survey geometry. The misaligned signal shown in figure 4.5.(e) corresponds to the 75^0 in-line dipping reflector. The weak event $\sim$50 ms later is a diffraction from the plate edge. Several factors that may cause the traveltime differences are plotted in the top four boxes of the figure 4.5 (see the figure caption for explanations). The effects of the in-line and cross-line offset, the in-line and cross-line reflector's dip, and the source-receiver azimuth are well understood (see Appendix E). But for the case presented, reflector's cross dip is zero (cross-line offset has no effect on the traveltime). The effect of the in-line dip and in-line offset are accounted for by removing the NMO and DMO. Furthermore, the source-receiver azimuth variation is so small that it can hardly produce significant differences in the traveltime.

Trace to trace change in the signal's arrival time illustrated in figure 4.5.(e) appears to mostly follow the change in the in-line component of the distance from the mid-points to the center of the CMP bin. The change in the signal traveltime due to this distance is a function of its magnitude and the dip of the reflector. Therefore, the width of the CMP bins, being a "tunable" parameter, must be given an adequate attention during data processing. The maximum CMP bin width at which no significant loss of information occurs when the data is stacked must be determined and used to group the data traces. Lateral resolution and aliasing during poststack migration (Yilmaz, 1987) put additional constraint on the maximum CMP bin width. But there are limits to reducing the width of the CMP bins as well. Having more data traces in a CMP bin gather (equals larger CMP bin width) is advantageous for imaging, because the obtained result is less ambiguous. The most useful CMP bin width is the one that allows the gather to include as many of the data traces that can be fruitfully explored as possible.

The optimal CMP bin width for Sturgeon Lake Line geometry is 20 meters. Even the standard stack is robust enough to incur only a small information loss at high frequencies due the slight misalignment of signal at this CMP bin width. The final stacks obtained

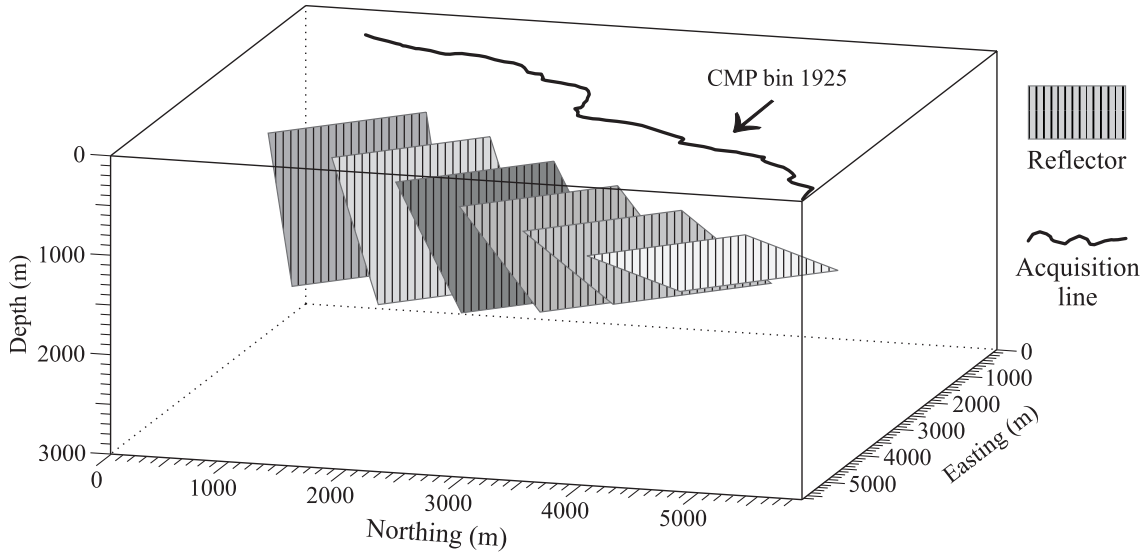

Figure 4.4: Model B features six events dipping in the general direction of the seismic acquisition line at 0, 15, 30, 45, 60 and 75 degrees. All of the reflective patches are squares with 1500 meter sides. The acquisition geometry is that of the Sturgeon Lake Line.

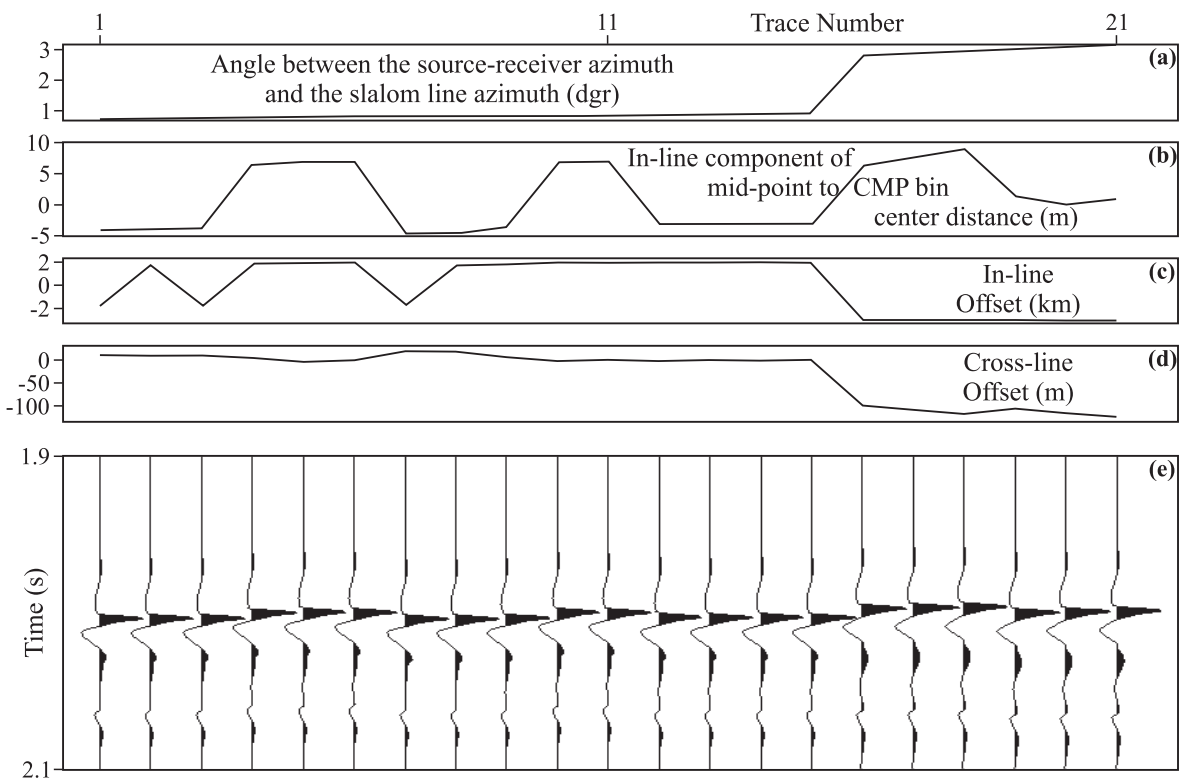

Figure 4.5: A small part of the CMP bin gather 1925 of Model B data is presented in part (e). In addition, several chosen headers indicating: (a) the angle between the azimuth of the source-receiver direction and the azimuth of the slalom line; (b) horizontal distance from the actual mid-points to the center of the CMP bin in the direction of the slalom line; (c) trace in-line offset; and (d) trace cross-line offset, are shown.

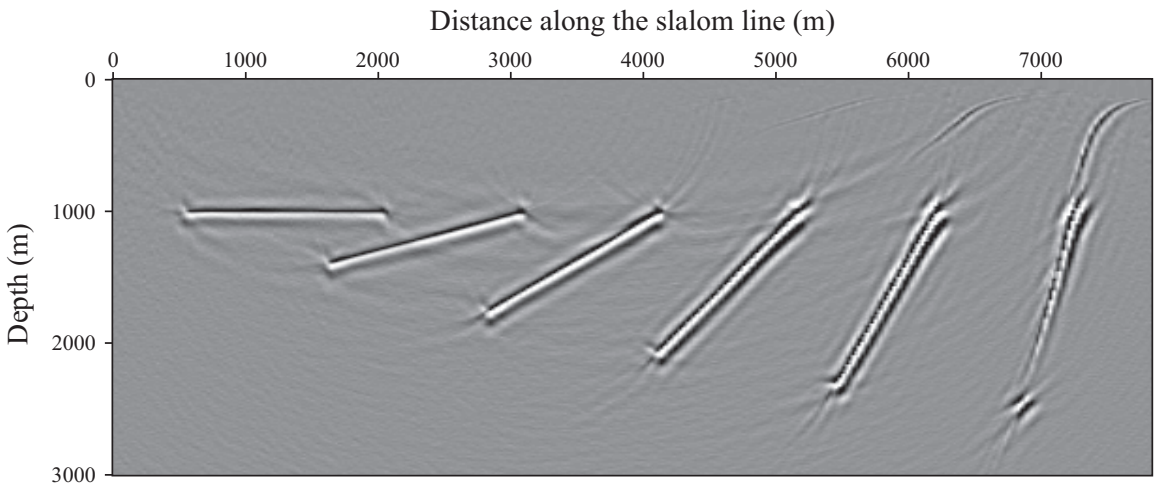

Figure 4.6: A vertical section along the slalom line extracted from the 3D prestack depth migrated data volume of Model B. Distance along the imaged profile increases in the southwest direction.

(but not shown) undisputably confirm this.

The optimum limited offset range analysis on CMP bin gathers indicated that good partial stacks are formed with offset windows as large as 500 meters. In spite of the shortness of the Sturgeon Lake Line (∼7 km), standard 3D prestack depth migration (figure 4.6) accurately captures most of the in-line dipping events below the slalom line. A somewhat longer survey would be necessary to completely image the two steepest events. A large stretching (∼750%) was allowed during the 3D prestack depth migration, and this was essential in obtaining a good image of the steeply dipping reflectors.

4.5 Cross-line Dipping Reflectors

Cross-line dipping reflectors of Model C and the geometry of the Sturgeon Lake Line (figure 4.7 and Appendix B), were used to form a synthetic data set. Model C data was specifically designed to investigate the cross dip moveout (CDMO) time "anomaly" and test the procedures designed to remove it.

The first observation, which is very important, was that regardless of the type of standard velocity analysis employed (velocity spectrum method, constant velocity stack, and velocity panels method (Sheriff, R. E. and Geldart, L. P., 1983)), no truly meaningful result could be obtained. Since only the CDMO and NMO were present in the data, velocity analysis must have been hindered by a large and complex cross dip moveout.

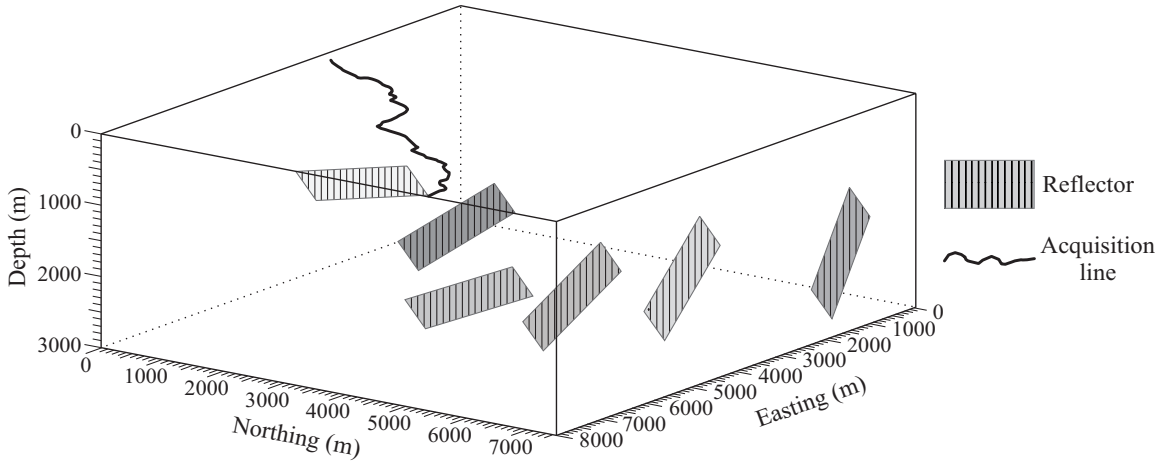

Figure 4.7: Model C is comprised of six reflective layers that dip towards the acquisition/slalom line (∼SE). The events are squares with 1500 meter sides and true dips of 0, 15, 30, 45, 60 and 70 degrees. The acquisition geometry is that of the Sturgeon Lake Line. The top parts of all events are positioned at the depth of 1500 meters.

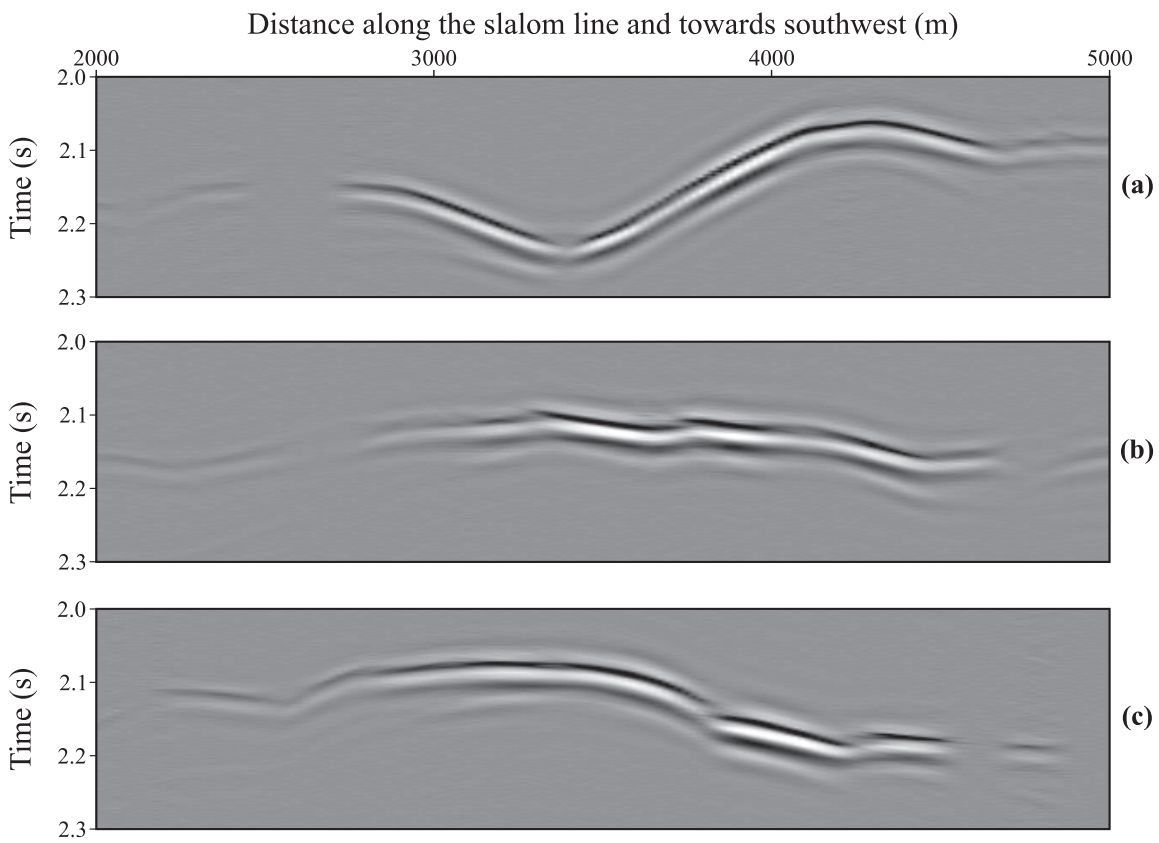

Figure 4.8: Blow ups of "constant offset" sections formed by partial stacking the 70^0 dipping event of Model C. Positive and negative offset ranges are combined, stacked and coherency filtered. From top to bottom the offset ranges of the partial stacks included are: 0-250, 2000-2250, and 4000-4250 meters. As expected, the time shifts due to variable cross offset are also extremely variable with in-line offset. Nevertheless, they do not cause much difficulty for partial stacking over 250 m windows.

But for Model C data the true medium velocity is known, and to continue with data processing only a rough stacking velocity model was required.

The optimum limited offset range analysis resulted in a maximum offset window for a partial stack of 250 meters. The data was partially stacked in two ways; by keeping positive and negative offset windows separate, and by combining them. Due to the irregular shot distribution, partial stacks using the same offset range but different offset sign, are not identical. However, the obtained results show that these partial stacks differ only slightly and can be combined.

Figure 4.8 depicts one NMO corrected and coherency filtered partial stacks (0-250, 2000-2250, and 4000-4250 meters) of the 70^0 dipping reflector. A striking feature of the partial stacks is that the arrival time of the reflections rapidly changes as a function of the offset range and CMP bin position. If a straight line survey had been used during modeling, the reflection response acquired from the same cross dipping reflector would have a constant traveltime on all partial stacks after the NMO corrections. The further step of combining the partial stacks into a final image would be simple. But in figure 4.8 the variation in the arrival time reaches 150 ms (the maximum for the Model C data is 200 ms). This traveltime variation is almost solely due to the cross dip moveout, and is very large considering that the average size of the cross spread is only $\sim$350 m. The CDMO is directly related to the shape and orientation of the acquisition and slalom lines and strongly depends on the dip and orientation of the reflectors (see section 2.5 and Appendix E for details).

Figure 4.9 illustrates the importance of the CDMO analysis and the CDMO removal. Parts a1, b1, and c1, are segments of the Model C stacked section featuring 0^0, 45^0, and 70^0 dipping reflectors. While the response of the horizontal reflector is easy to recognize, both of the dipping events on the stacked section appear as numerous, short in-line dipping beds. Changing the stacking velocities cannot focus the cross dipping events on the stacked section, unlike the in-line dipping reflectors. The reflective pattern shown only changes its shape and the velocity analysis fails to produce an accurate velocity model. In order to focus the cross dipping events on a stacked section, in addition to knowing the velocity of the medium, it is also necessary to determine and remove the cross dip moveout. This is done by employing the procedures explained in sections 3.3 and 5.4.

Parts a2, b2, and c2 of the figure 4.9 show the 0^0, 45^0, and 70^0 dipping events after the local optimum cross dip stack. The reflected energy is focused for the cross dipping

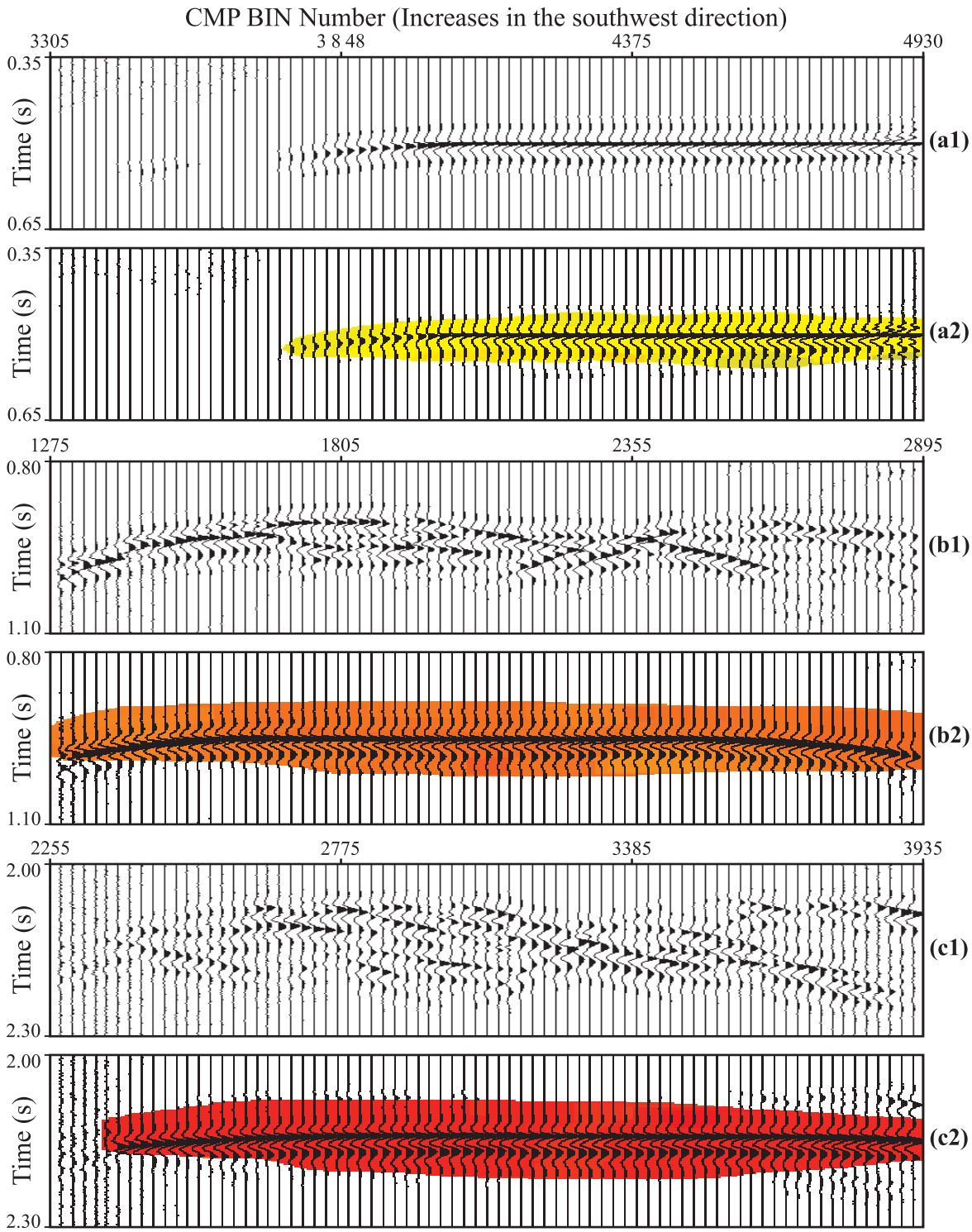

Figure 4.9: Parts a1, b1, and c1 are stacks of 0^0, 45^0, and 70^0 dipping reflective layers of Model C. The corresponding optimum cross dip stacks are shown in parts a2, b2 and c2. Parts with the optimum cross dip stacks (a2, b2, and c2) show in color areas, in which reliable values of the cross dip angle were determined. The determined dips depicted by color approximately match the dips of the reflectors given in the Model C. Data within these areas was stacked at an angle that corresponds to the given color (see the color palette in figure 4.12).

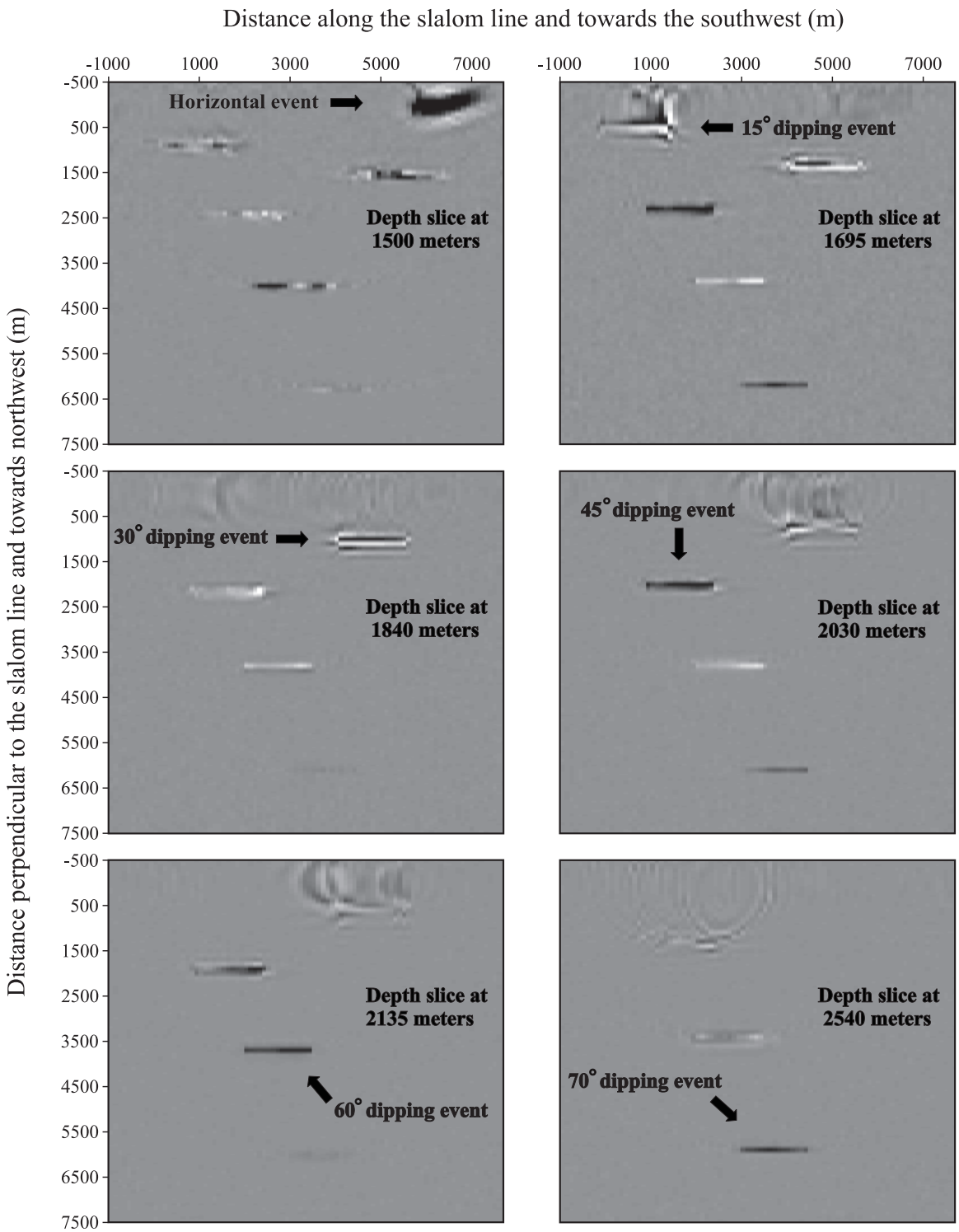

Figure 4.10: Six selected depth slices (at 1500, 1695, 1840, 2030, 2135, and 2540 m) of the 3D prestack depth migrated volume of Model C data. The depth slices are plotted in the variable density grey scale technique. Large positive and negative amplitudes are black and white respectively. All of the depth slices cut through more than one event. However, to avoid oversaturating the depth slices, only the event for which that particular slice represents the best image is indicated.

events and S/N ratio is dramatically improved. The cross dip events exhibit the same expression as horizontal events do on the 2D images; they become interpretable on the 2D seismic profiles. In addition, the cross dip of the reflectors (0^0 - yellow, 45^0 - orange, and 70^0 - red) is acquired and superimposed on the stacked image as colored background to aid interpretation.

The cross dip moveout for most of the events in Model C is so large that the amplitude stack cannot do much to improve the situation. Although better than the standard stack, the results are not satisfactory and are not shown.

The Model C data (after partial stack) was prestack depth migrated to a 3D data volume (8.8x8.0x3.0 km) using standard and amplitude traces. Migration of absolute amplitudes raised to a power of 1.5 resulted in the best focusing of the migrated images. The obtained data volume has a coarse surface sampling rate (100x100 m), but is densely sampled in depth (5 m). Six selected depth slices are presented in figure 4.10. A large area of the reflectors with mild (15^0) or no (0^0) cross dip is imaged in the top two depth slices of figure 4.10. Areas of comparable size are imaged for the events with mild to strong cross-line dips, but because they dip, their cross section in a depth slice becomes small. Remarkably, the 3D prestack migration was able to position the reflectors accurately in space, although artifacts outside the reflectors are not negligible..

Tests of the cross dip study and 3D prestack migration on Model C data have both resulted in highly successful images, which illustrate that it should be possible to image simple cross dipping structures using data acquired on crooked profiles.

4.6 Reflectors with Both In-line and Cross-line Dip Components

Model D (figure 4.11 and Appendix B) was designed as a severe test of the various imaging processes. It uses the geometry of the Sturgeon Lake Line (figure 4.11 and Appendix B) and comprises four layers dipping south at 15^0, 30^0, 45^0, and 60^0, whereas the processing (slalom) line used for all modeled data A through D is straight and directed southwest (figure 4.1) at an azimuth of $\sim 222.90^0$ (SW). Apparent in-line and cross-line dip for each of the events are approximately equal. For the four reflectors with the true dips of 15^0, 30^0, 45^0, and 60^0, the apparent dips take values of $\sim 7.5^0$, $\sim 15.0^0$, $\sim 22.5^0$, and $\sim 30.0^0$, respectively.

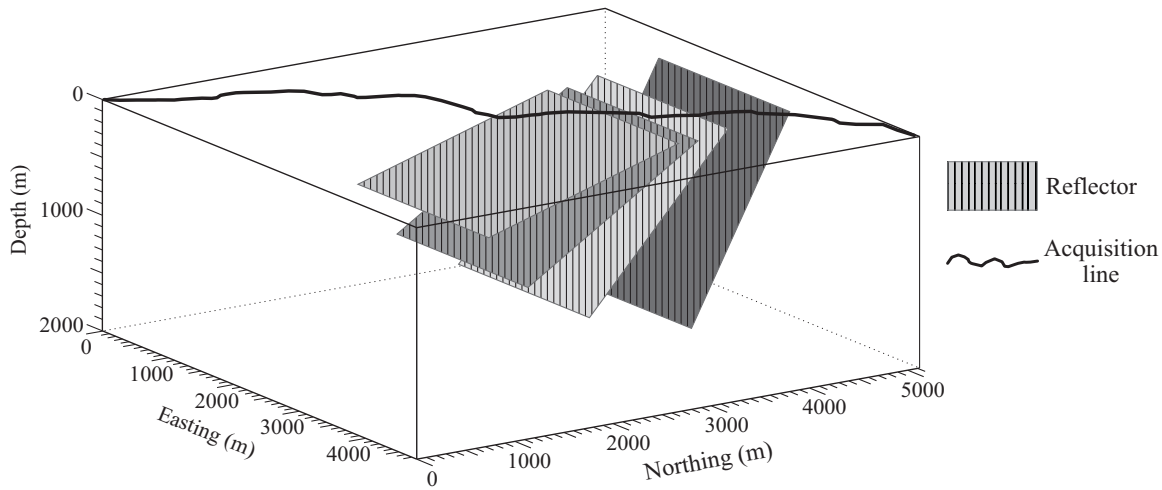

Figure 4.11: Model D is made of four layers that dip south at 15, 30, 45, and 60 degrees. The reflectors are squares and have sides 2000 meters long. The acquisition geometry is that of the Sturgeon Lake Line.

While the cross dip moveout (CDMO) does not depend on the reflector's depth, the amount of dip moveout (DMO) is strongly correlated with it. Because in Model D all reflectors are very shallow and exhibit in-line and cross-line dip, both DMO and CDMO time anomalies are large. The imaging is further complicated by placing the reflectors close to each other to cause interference among the reflected responses of neighboring events.

The offset window for partial stack, obtained through the optimum limited offset range analysis on Model D data, is found to be 225 meters. Data was partially stacked using this range, and positive and negative ranges were combined. The DMO correction was applied to the coherency filtered partial stacks, followed by amplitude stack, standard stack, cross dip analysis and cross dip stack. Figure 4.12 shows, from top to bottom, amplitude stack, standard stack, and local optimum cross dip stack of Model D data.

None of the stacks are migrated, causing reflectors to appear much wider then they truly are. Signal is better focused in the amplitude stack than in the standard stack. The local optimum cross dip stack images the reflectors best, though the cross dip indicated by color has not been determined uniformly. Cross dip is determined more accurately at the deeper parts of all four reflectors because the reflected signal from the neighboring reflectors interferes less as the events get more separated at greater depths. Moreover, the DMO, which is not completely removed from partial stack events that exhibit a wavy character due to the CDMO, is better dealt with at a greater depth where its magnitude is smaller. Still, the average color of the events accurately depicts the apparent cross dip

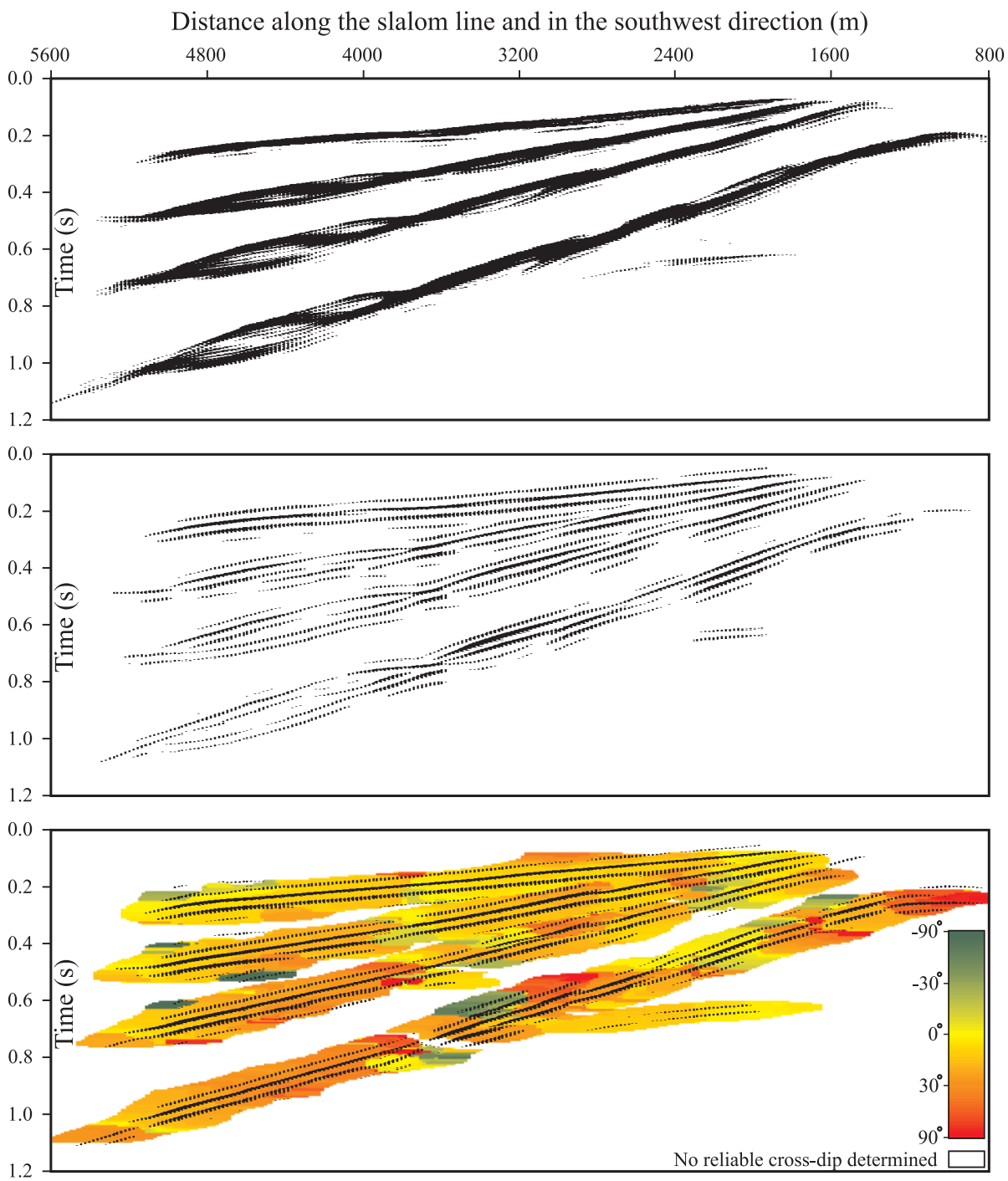

Figure 4.12: Presented are, from top to bottom, amplitude stack, standard stack, and local optimum cross dip stack, of Model D data. Stacks are plotted in the variable area technique, with positive peaks filled. The local optimum cross dip stack (bottom part of the figure) has a color background indicating the apparent cross dip associated with the events. On the left side of the local optimum cross dip stack a color pallet that translates the color into a cross dip value in degrees is given. The shades of green represent the apparent northwest cross dip, while the shades of red represent the apparent southeast cross dip of reflectors. Note that the white color indicates no reliable cross dip determined.

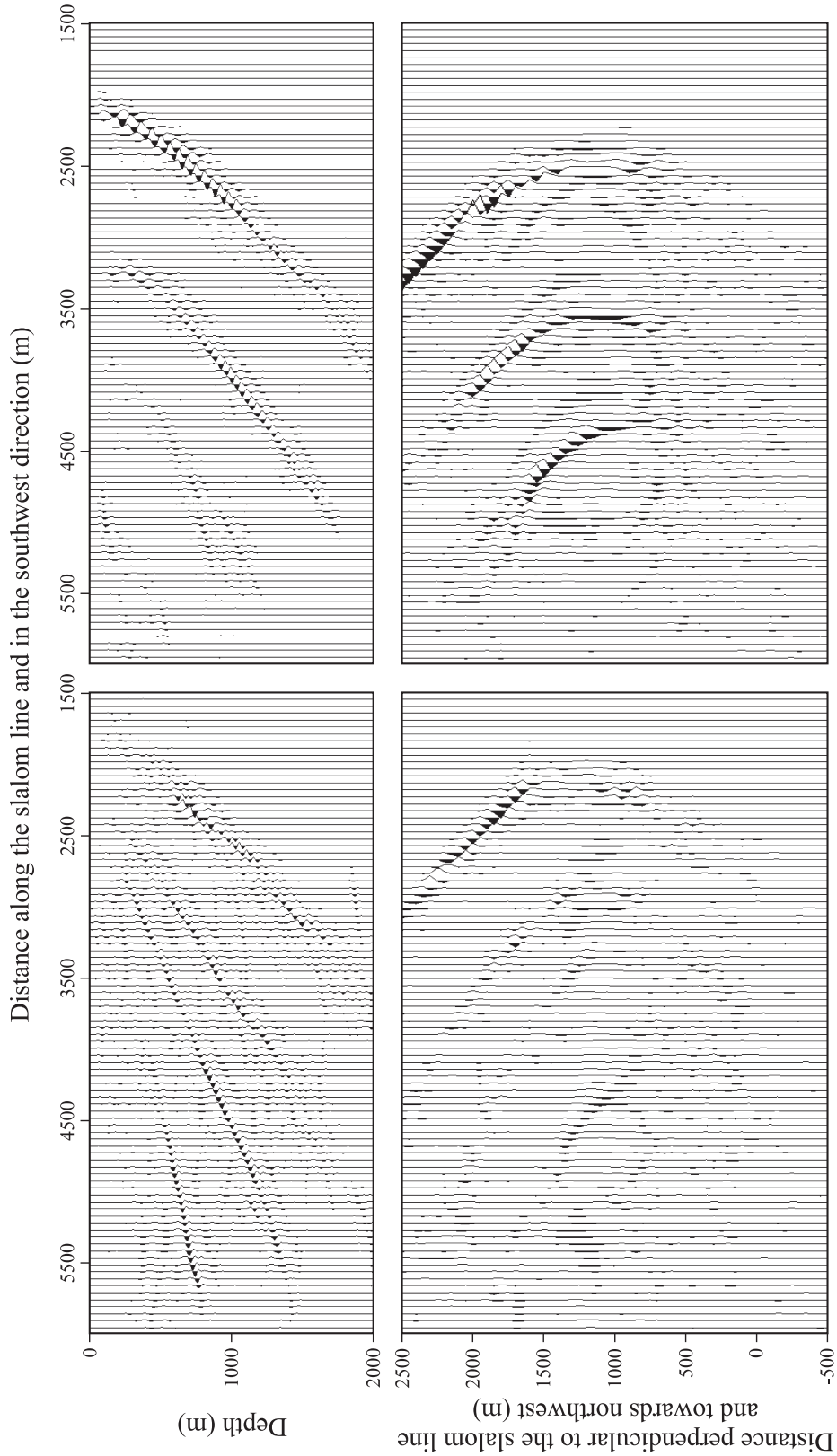

Top two parts of the figure are depth profiles. The profiles are parallel to the slalom line and at a cross-offset of 1250 (left) and 1850 (right) meters to the northwest. Due to the coarse sampling rate in the direction of the slalom line, and perpendicular to it, the figures are not smooth. The left profile better illustrates the focusing of the upper two, mildly dipping layers. The profile on the right depicts two more steeply dipping layers. Below the depth profiles, two depth slices of the 3D migrated volume are presented. The first one (left) is at the depth of 530 meters and shows the 60 degree dipping layer. On the right, depth slice taken at 950 meters shows the 45, 30, and 15 degree dipping layers imaged well.

Figure 4.13: Profiles and slices through 3D prestack depth migrated volume of Model D data.

of the events. Although the events are not migrated, their in-line dips on the section are similar to the true apparent dips. This is mostly due to the relatively small projected in-line dip of the reflectors (max $\sim 30^0$).

Model D data was prestack depth migrated to a 3D (6.8x3.0x2.0 km) data volume. Best focusing was achieved when absolute amplitudes raised to a power of 1.5 were migrated. The migrated data volume has a coarse surface sampling rate (50x50 m), but is well sampled at intervals at 5 meters in depth. Two profiles parallel to the slalom line, and two depth slices, all extracted from the migrated data volume, are presented in figure 4.13 (see the figure caption for more details).

Figures 4.12 and 4.13 illustrate that the cross dip study and the 3D prestack migration are capable of imaging arbitrary oriented simple shallow 3D structures whose reflection responses partially overlap in the 2D crooked line data. Amplitude stack has produced better images than the standard stack when the cross dip moveout was neglected.

4.7 The Effects of Survey Scale, Slalom Line Azimuth Variation, and the Fresnel Zone Radius

To test the applicability of the designed imaging procedures on regional, crustal scale seismic reflection surveys, three more models (E, F and G)[5] were formed. The E, F and G synthetic data sets were computed by employing the survey geometry of Line 23 (figure 4.14). The Sturgeon Lake data set differs from the Line 23 data set in two essential ways. The processing (slalom) line is straight with only one segment, and the spread length (maximum in-line offset) is large compared with the depth of exploration, whereas Line 23 has a very crooked multiple segment processing line but a relatively shorter spread (compared to reflector depth).

Model E is comprised of 15 reflectors in 3 easily separable groups of 5. The most northerly group has all 5 reflectors predominantly dipping in the cross-line direction at 45^0 true dip. The two southernmost groups of five reflectors are positioned to direct their reflective response towards the middle segment of the acquisition line where they will partially overlap in the time section. This is also where the acquisition line is most crooked. Both

[5]The complete information about modeling parameters for all synthetic data sets (A through G) is provided in Appendix B.

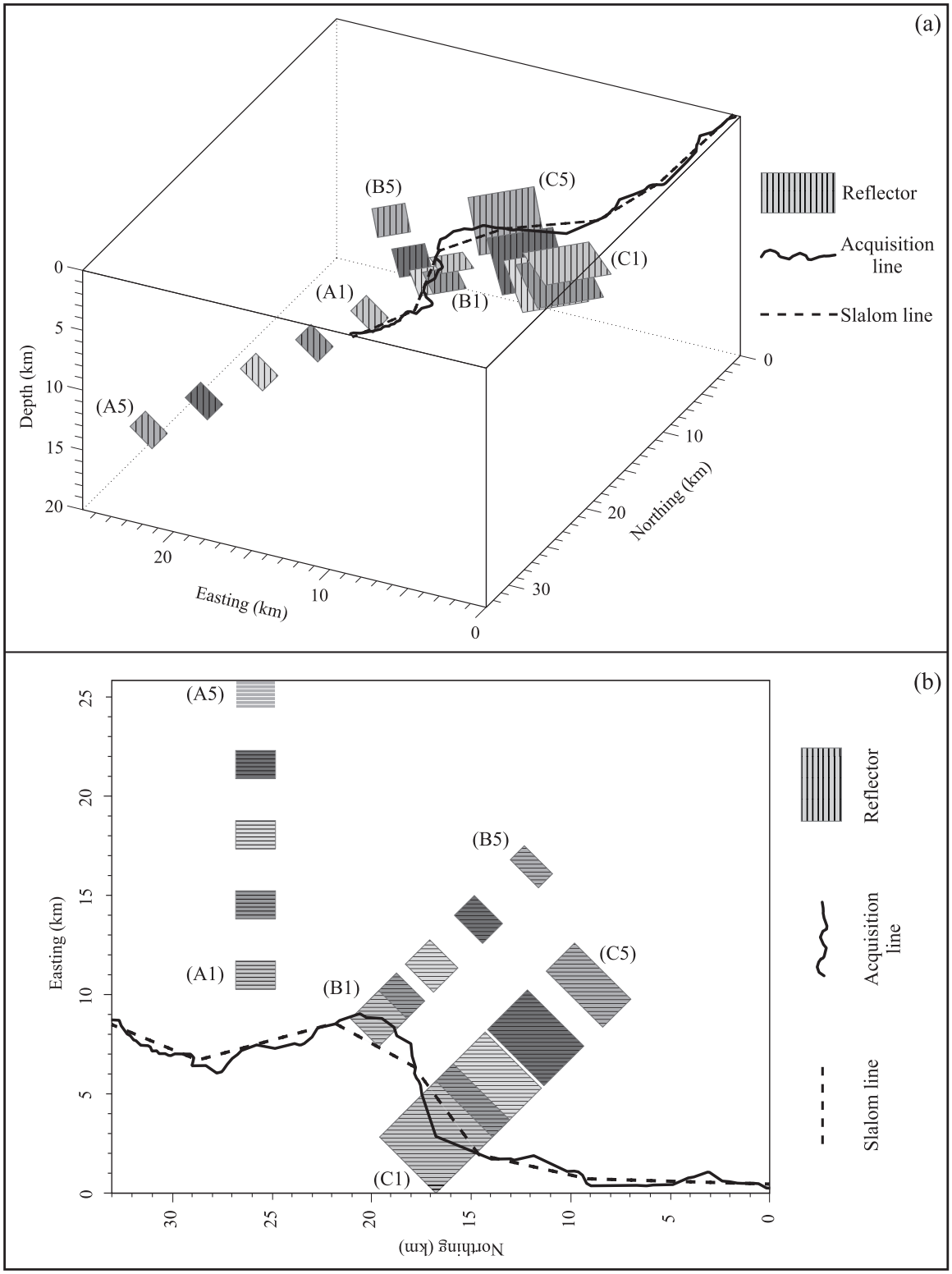

Figure 4.14: Model E is composed of 3 groups of 5 reflectors, and the geometry of the Abitibi-Grenville transect Line 23. Parts (a) and (b) of the figure are a perspective and a plan view of the model respectively. All of the reflective events are squares. The smaller reflectors have sides that are 2000 meters long while the larger reflectors have sides of 4000 meters.

southernmost groups contain reflectors dipping at 0^0, 15^0, 30^0, 45^0, and 60^0. All (except the horizontal one) exhibit both in-line and cross-line components of dip.

Examination of the Model E data yielded an optimum limited offset range for partial stack of 400 meters. This window is approximately twice the size of the offset windows found by analyzing model C and D Sturgeon Lake data, and simply reflects the larger scale of the regional survey on the relatively lower and narrower frequency band of the wavelet used[6]. The data were partially stacked, DMO corrected, and coherency filtered. The processes applied subsequently were amplitude stack, standard stack, cross dip analysis, and optimum cross dip stack. AGC shadow, visible on all sections (figures 4.15 and 4.16), is due to the automatic gain control which was applied to data before stack.

Figure 4.15 shows the standard stack (part (b)) and the amplitude stack (part (c)). Azimuth of the slalom line is presented in part (a). The general direction of the slalom line is south. The two deepest and furthermost cross dipping events (relative to the slalom line) are not shown. Predominantly cross dipping reflectors (three events on the left of the figure 4.15) exhibit a very similar signature, thus confirming that the cross dip moveout (CDMO) is not a function of depth. A mildly lower S/N ratio of the more distant cross dipping events is not only a result of spherical wave propagation, but is also due to the effect of the Fresnel Zone radius size, which is for these reflectors larger than the radius of a circle that can be inscribed in them.

The third group of the events (furthest to southwest) has a stronger signal on the standard stack than the other two groups (figure 4.15.(b)). Reflectors that comprise this group have an area that is four times the size of other reflectors in Model E. However, the main reason for their better signal focusing isn't their size but rather a smaller amount of wobbling of the acquisition line in the region where these reflector direct the energy back to the acquisition/slalom line. Local wobbling of the acquisition line is particularly destructive for signal focusing. Thus, reflector group C produces much clearer events than groups A and B, because, although the acquisition line diverges greatly from the processing line, it is relatively straight. However, the better signal focusing of the C reflectors should not be mistaken for a more accurate imaging, as figure 4.16 later shows. The standard stack (figure 4.15.(b)) illustrates once again that the larger the cross dip component of the reflector is, the stronger the signal defocusing is. Imaging becomes poorer where the slalom line changes its azimuth. Events corresponding to A and B

[6]Klauder zero phase wavelet (10 to 56 Hz) was used to simulate the source during modeling of data for regional studies. Butterworth minimum phase wavelet (20 to 300 Hz) was used to simulate the source when computing the data for high resolution studies. See Appendix B for more details.

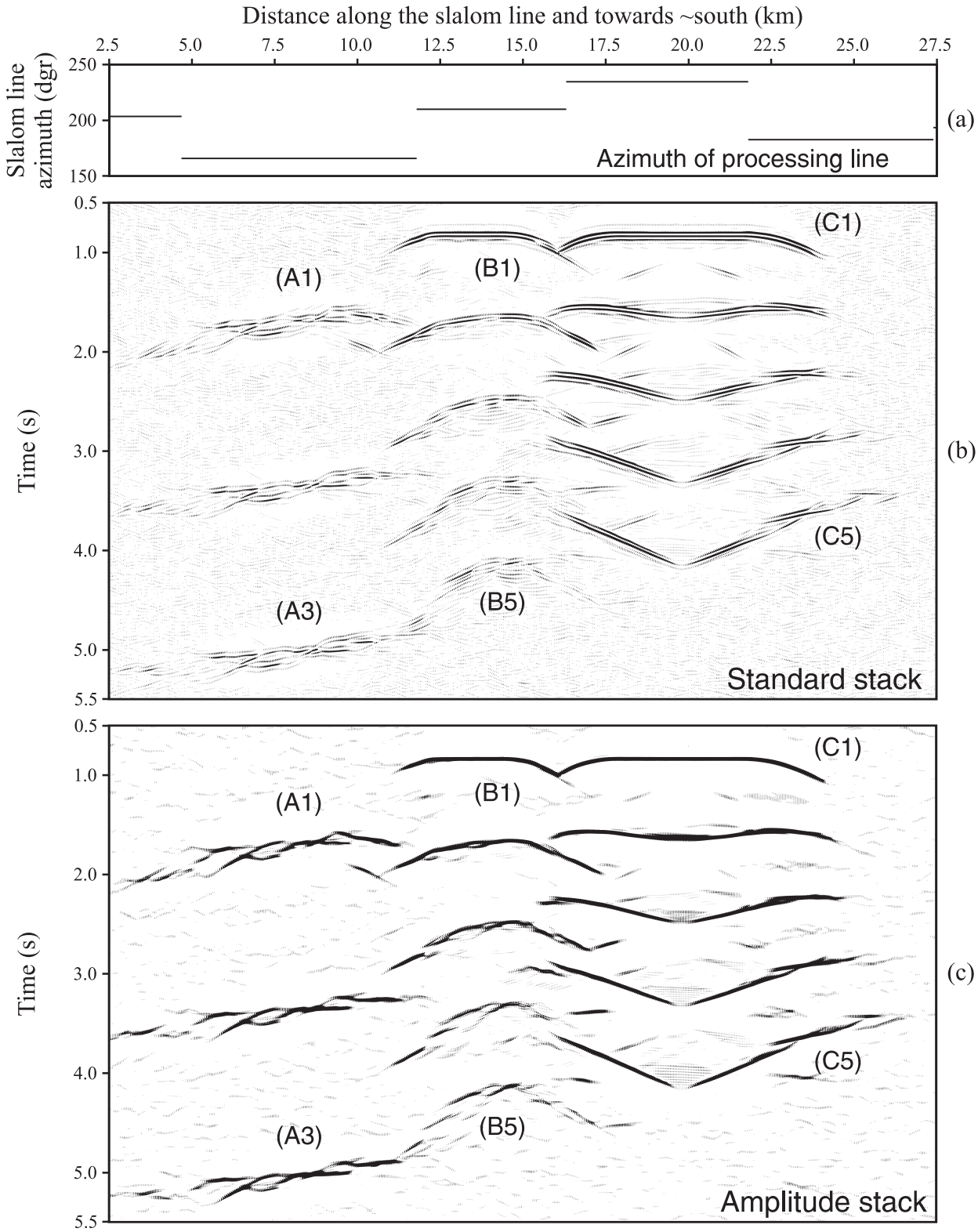

Figure 4.15: CMP bin stacks of Model E data with DMO but no CDMO corrections. The amplitude stack shows significantly higher S/N ratio. Most of the breaks in imaged reflectors occur where the slalom line changes its azimuth. However, strong disruptions also occur where the slalom line is straight but the acquisition line abruptly changes its direction (20 km south).

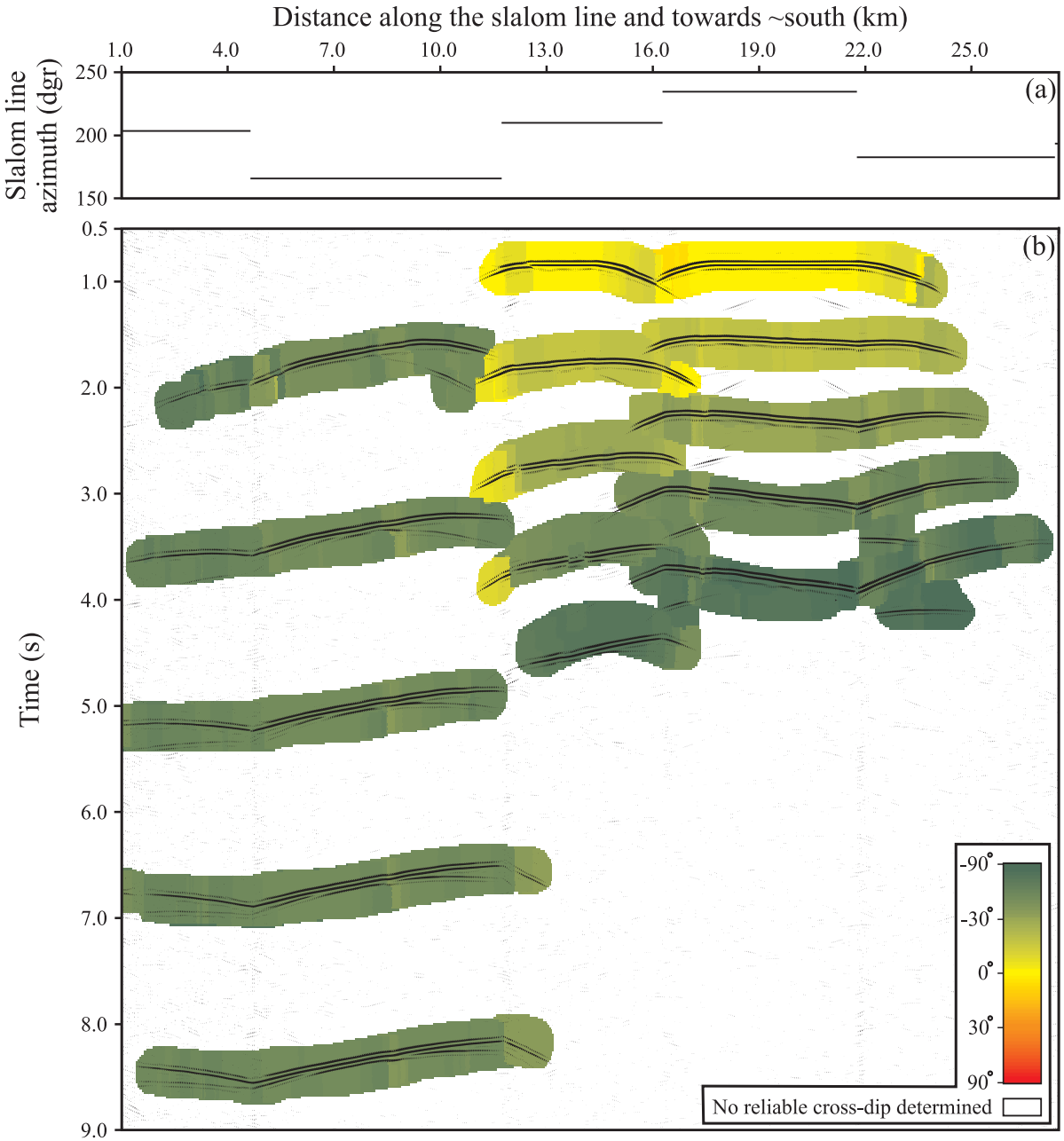

Figure 4.16: Slalom line azimuth (a) and optimum cross dip stack of Model E data. Cross dip color map is given in the lower right corner of part (b). All fifteen reflectors are included in the image presented. Where no reliable cross dip was determined data was stacked at a zero cross dip (white areas). Cross dip analysis provides important information for accurate interpretation. Cross dip correction significantly improves: continuity of reflectors, signal focusing (which translates into a much better S/N ratio), and accuracy of imaging. Note that the changes in in-line dip occur exactly where slalom line azimuth changes, as they should.

groups of reflectors spread in space greatly apart from each other as their distance from the acquisition/slalom line increases (figure 4.14). In spite of that, the only difference noticeable in the standard and amplitude stacks is that the reflection responses from the further events arrive at a later time. This underlies the need to plot the slalom line azimuths on top of the sections, for interpretation purposes. In addition, figure 4.15.(b) shows that the main breaks in the image of the flat beds exhibiting a cross dip component do not always appear where the slalom line changes its azimuth. For the standard stack of Model E data (figure 4.15.(b)), the most significant break occurs in the largest group of the reflectors where the slalom line is straight but the acquisition line, also otherwise straight, experiences an abrupt change in direction.

The amplitude section (figure 4.15.(c)), though exhibiting the same problems as standard section, shows a higher signal focusing and a better S/N ratio. Nevertheless, when the events exhibit a cross dip component, neither standard nor amplitude stack is an accurate and informative enough image to allow migration to place these events in their true subsurface positions.

Figure 4.16 shows the local optimum cross dip stack (b) and the slalom line azimuth (a) of Model E data. Compare the local optimum cross dip stack (figure 4.16) with the corresponding standard and amplitude stacks (figure 4.15). Cross dip analysis and cross dip stack dramatically improve the imaging (for more information please read figure 4.16 caption). The reflectors are continuous along the straight slalom line segments. The only breaks, as expected, occur where the slalom line changes direction. Signal focusing and S/N ratio is far better than for the standard and amplitude stacks.

The obtained local optimum cross dip section can be poststack 3D migrated using the procedure explained in section 5.5. But this is not necessary. The true dip and orientation of a reflector can be obtained wherever the reflectors' apparent in-line and apparent cross-line dips (see Appendix F) can be estimated in the cross dip section.

Model E data (after partial stacking into offset windows) were prestack depth migrated to a 3D data volume (25.0x30.0x20.0 km). Due to insufficient computer resources, amplitude migration was not tested. Although the migrated data grid had only a very coarse sampling rate in all directions (100x100x100 m), it took 12 full days for one migration run on the fastest available computer, a SUN ultra sparc 10 workstation. One east-west profile with the northing of 25.3 km is extracted from the the 3D data volume and presented in figure 4.17. The easting and the northing of the profile correspond to the easting and northing as given in figure 4.14. The cross dipping reflectors are imaged

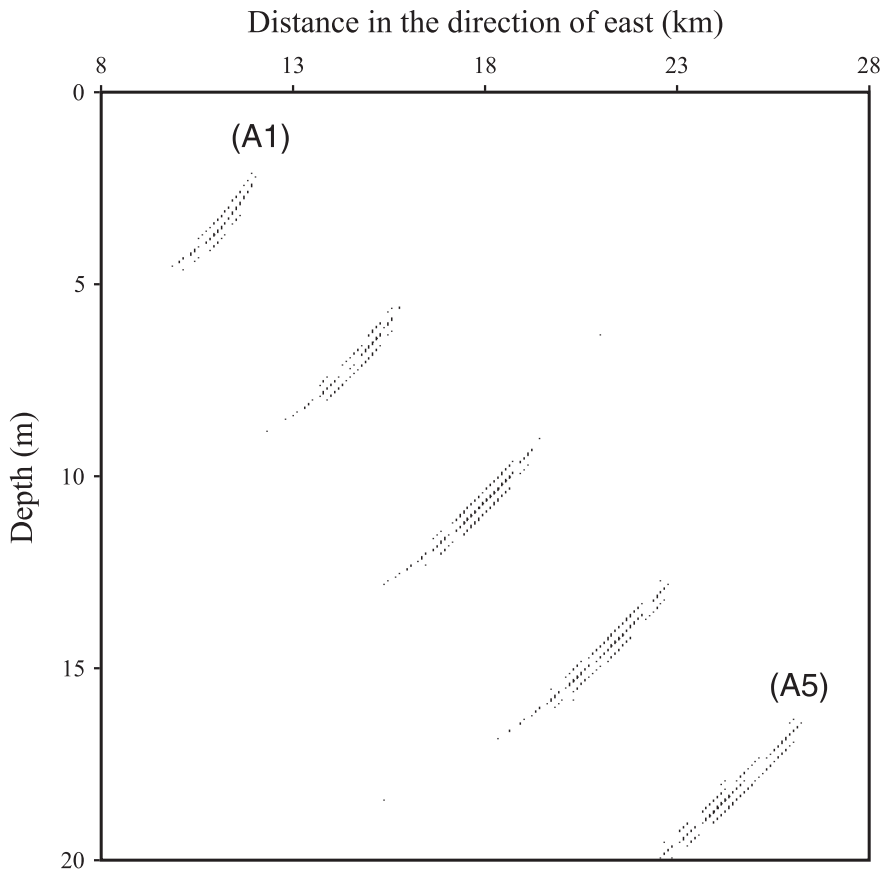

Figure 4.17: East-west vertical section in the 3D prestack depth migrated volume of Model E data. The northing of the profile is 25.3 km. Note that the section shown in is approximately perpendicular to the optimum choice of a profile for the 2D migration.

fairly well, even at a large distance from the acquisition and slalom lines, although their upper and lower edges are diffuse.

The study carried out on Model E data shows that:

- The wavelet frequency content affects the width of the optimum limited offset range for partial stack;
- The redundancy of the 2D crooked line data (large CMP bin fold) is essential for successful imaging of relatively small events found at large distances from the survey line;
- The change in slalom line direction strongly affects the obtained image. Therefore, it is critical for interpretation to plot the azimuth of a slalom line above the corresponding local optimum cross dip stack.

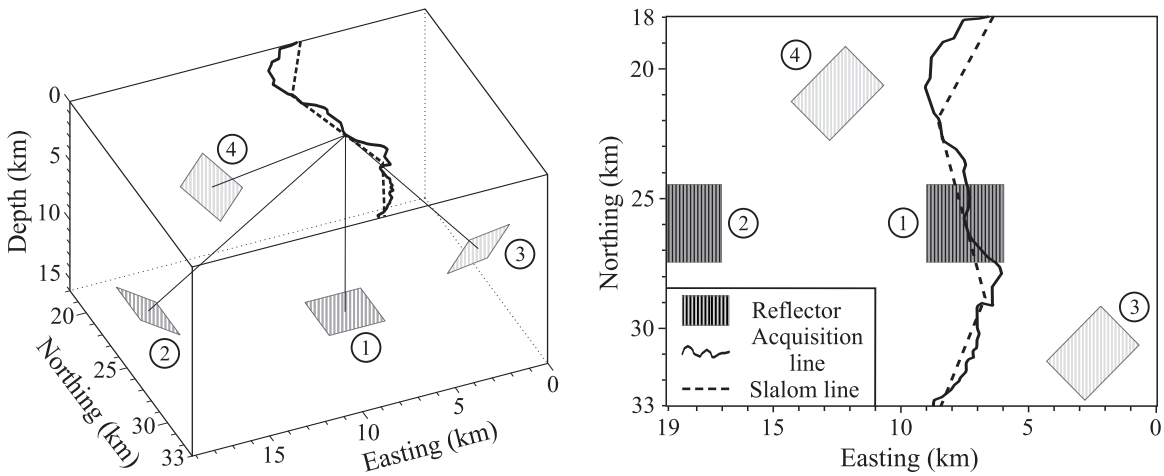

Figure 4.18: Models F and G are both comprised of two pairs of reflectors whose responses overlap at the indicated parts of the acquisition/slalom lines. Survey geometry of the northern third of the Abitibi-Grenville transect Line 23 was used to compute Model F and Model G data. The left and right part of the figure are a perspective view and a plan view of the models respectively. All of the reflectors are squares with sides 3000 meters long.

Most importantly, examination of Model E data reinforces the conclusion that imaging of 2D crooked line data must include either cross dip moveout removal before stack or 3D prestack migration, or both.

4.8 Reflectors with Overlapping Response

Data recorded during 2D crooked line seismic reflection surveying in crystalline terrains represents the reflective response of all the reflectors in the general vicinity of the acquisition line that happen to face the acquisition profile . Consequently, such data is rich in reflective responses that overlap in time and trace location even though the reflectors may be far apart. Models F and G (figure 4.18 and Appendix B) were formed to test the capability of the optimum cross dip stack and 3D prestack migration to separate the overlapping signals and position the reflectors correctly in space. Since the 3D prestack migration is a linear process in signal amplitude, there should be no problems from overlap as long as the velocity estimation is reasonably successful. The optimum cross dip stack may be affected, however.

Both models are geometrically identical and consist of two pairs of reflecting plates specially designed so that their reflective responses overlap on the chosen slalom line. They differ in the reflection coefficients assigned to the plates. Reflectors 3 and 4, that rep-

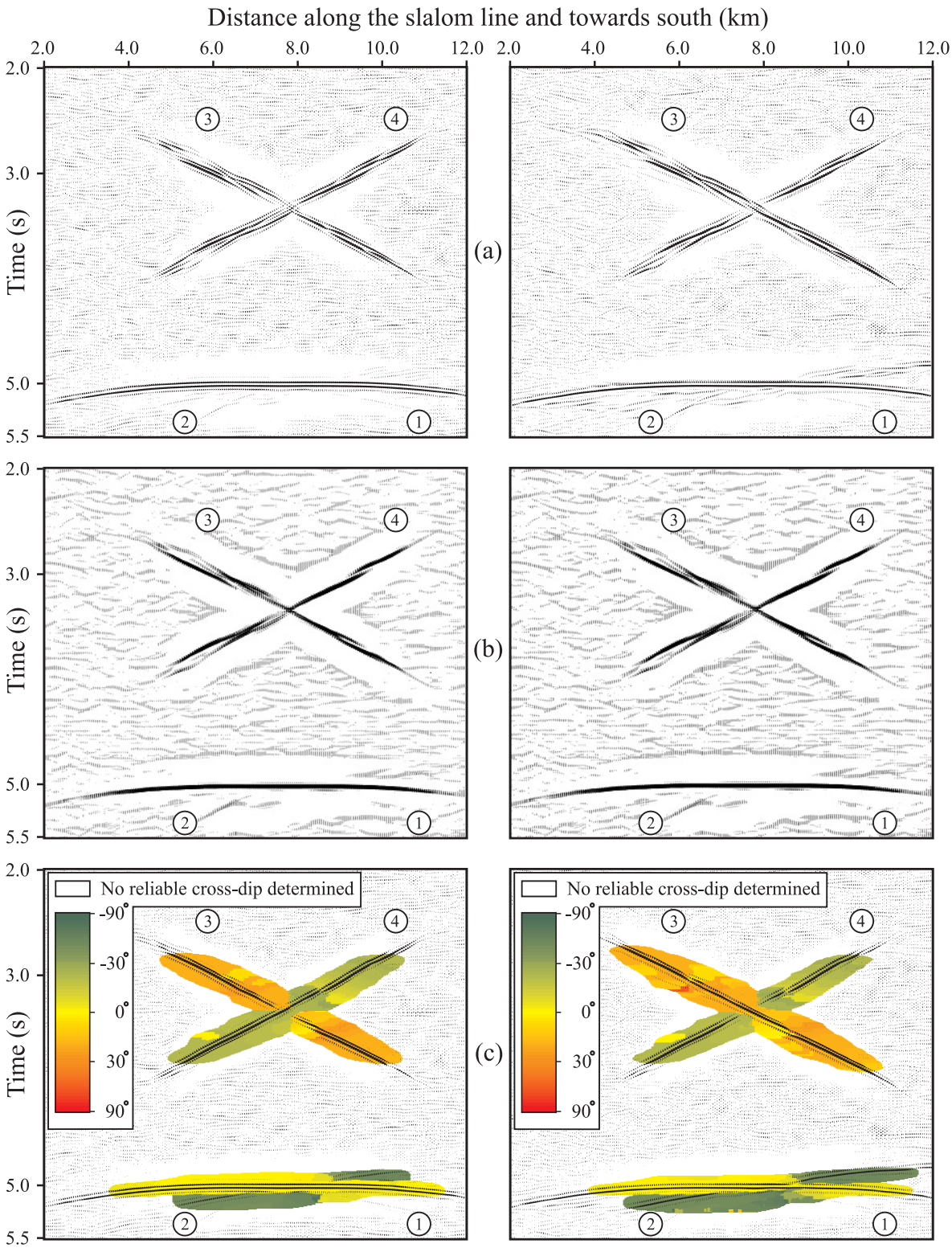

Figure 4.19: Results of Model F and Model G data examination. Standard stack (a), amplitude stack (b), and local optimum cross dip stack (c) images are shown. The left part of the figure corresponds to Model F results while on the right are the Model G results. Cross dips are indicated in color.

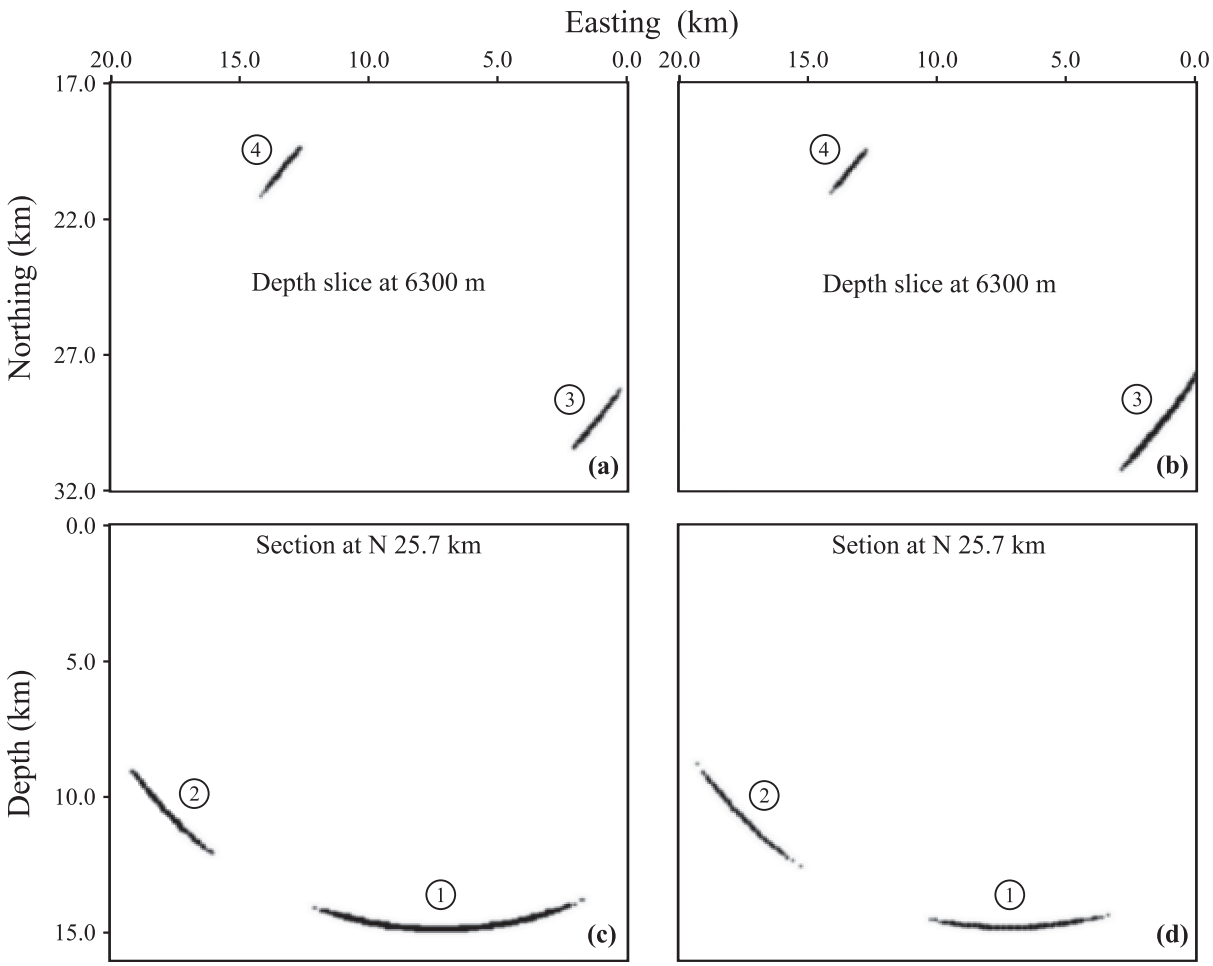

Figure 4.20: Depth slices and profiles through the 3D prestack migrated amplitude data of Model F (left side of the figure) and Model G (right side of the figure). The top part of the figure are depth slices while the bottom part of the figure are depth profiles.

resent the pair closer to the acquisition line, dip at 45^0 and exhibit similar in-line and cross-line dip components. The pair further away from the acquisition line is composed of reflectors 1 and 2 that dip at 0^0 and 45^0 respectively. Reflector 2 is mostly cross dipping. All reflectors have identical reflection coefficients in Model F. In Model G, reflection coefficients of reflectors 2 and 4 are doubled.

Data traces were synthesized for Model F and Model G and were processed to SZOST sections in the exact same way as those from Model E (see section 4.7). The results obtained are shown for Model F on the left side of figure 4.19, and for Model G on the right side. AGC was applied to all stacks to boost the background noise. Still, signal focusing and S/N ratio for the amplitude and optimum cross dip stacks are better than for the standard stack. In agreement with the results obtained on previous models,

the highest imaging accuracy and the most subsurface information is obtained with the optimum cross dip stack.

A summary of the most important conclusions inferred by interpreting figure 4.19 images follows:

- The information about cross dips of the events whose reflective responses overlap can be extracted from the data, unless the events have very similar in-line dip and strongly overlap;
- Where two events overlap, the stronger event will tend to obliterate the weaker. Event amplitude depends on several geometrical factors in addition to the reflectivity of the reflector;
- The current imaging methodology (including the procedures designed by this thesis author) is unable to completely remove various time "anomalies" embedded in the data acquired on crooked lines, and therefore acts like a mild filter that disfavors strongly dipping events, specially ones with a large cross dip component. This is clearly seen by poor imaging of reflector 2 where its response overlaps the horizontal reflector (1). However, this is also due to vertical "geophones".

Because of the computer limitations, only amplitude 3D prestack depth migration was applied to Model F and Model G data volumes. The sampling rate in the output volume (25.0x20.0x16.0 km) was very coarse for all three dimensions (100x100x100 m). Figure 4.20 depicts the results of these migration. The events are fairly well imaged on both, depth slices and depth profiles. The better focusing of the horizontal event and the change in the reflection coefficients are evident. However, many artifacts are present in the migrated data volume and they would be easily visible if the plot amplitudes were brought up.

A procedure designed to 3D poststack migrate a local optimum cross dip stack (see section 5.5 for more details) was tested on Model G data. Figure 4.21 compares the result from it with the result from the prestack amplitude migration. Although depth profiles 4.21.(a) and 4.21.(b) do not have the same northing, they both cut across reflectors 1 and 2. Because reflectors 1 and 2 overlap in the cross dip stack, they exhibit breaks, or are imaged only partially in the 3D poststack migrated volume. The 3D prestack migration images the reflectors much better than the 3D poststack migration. But the 3D poststack

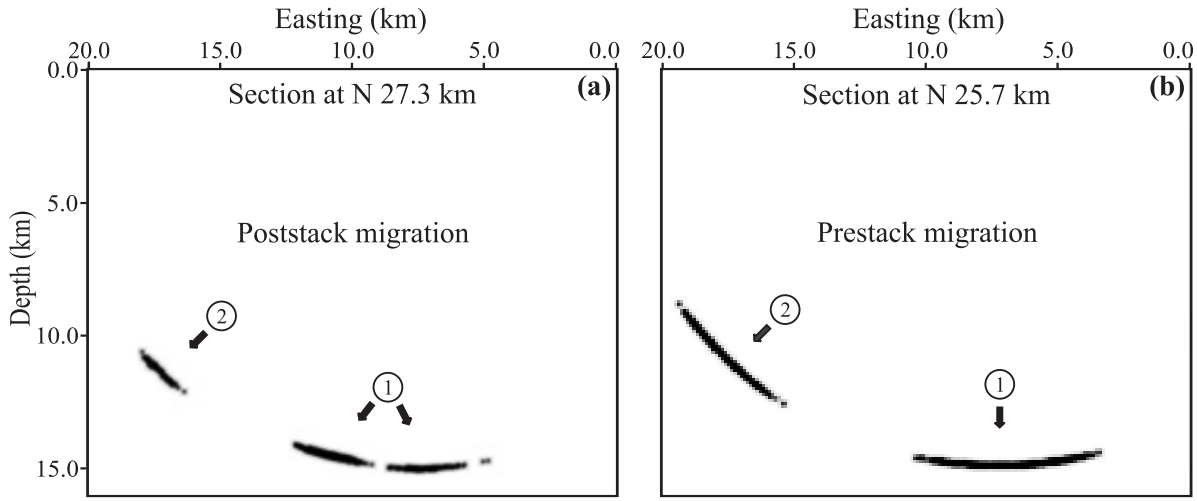

Figure 4.21: Migrated sections for Model G; (a) poststack and (b) prestack. The poststack migration has some difficulty where events overlap and cross dip is poorly determined.

migration is computationally much faster, provides very useful images, and may be used when there aren't enough resources and time to perform a 3D prestack migration.

4.9 Summary

Seven synthetic seismic reflection data sets were computed using:

- A ray-Born modeling technique;
- Crooked line acquisition geometries of high resolution Sturgeon Lake Line or regional Abitibi-Grenville Line 23;
- Models that range from several point diffractors to 15 plate-like reflectors.

Selected data sets were processed to SZOSTS using standard and amplitude stacking with DMO correction but no CDMO correction, and with the locally optimized cross dip correction method, and to 3D images using Kirchhoff 3D prestack migration.

The examination of the synthetic seismic data has clearly shown that:

- In forming SZOST section the cross dip moveout is often the largest time "anomaly" in the 2D crooked line seismic reflection data sets, more important for instance than the DMO anomaly. It is therefore absolutely essential to try to determine and

remove the cross dip moveout from the data, and/or apply a 3D prestack migration to the crooked line profiles;

- If the local cross dip moveout is successfully determined and then removed, the events are much better focused and are projected correctly on the plane of a chosen 2D slalom line. The S/N ratio also is significantly improved, and the apparent cross dip information obtained indicates where the events truly lie in a 3D space;

- Although the 2D crooked line data offset aperture in the cross-line direction is very small, 3D prestack depth migration yields surprisingly useful results.

- When cross dip analysis fails or is not applied, imaging in a SZOST section tends to be poor. Images of best quality are obtained by applying the measure of last resort: amplitude stack.

Chapter 5

Examples on Real Data

The ideas and imaging techniques presented in Chapter 3 and tested on synthetic data in Chapter 4 were subsequently applied to real data. The focus of Chapter 5 are the procedures used and the results so obtained.

Both chosen profiles[1] are fairly crooked and exhibit general characteristics of the type/scale of 2D crooked line surveys they represent (regional or high resolution). One of the chosen seismic profiles is the Abitibi-Grenville transect Line 23, a regional profile collected for crustal studies as part of the Lithoprobe project. Line 23 was acquired in the Abitibi greenstone belt and is 41.4 km long, listening time was 18 s, receiver spacing 50 m, and spread length 12 km. The energy source used was a group of 4 vibrators operated several times to cover an interval of 100 m. The source signal had a frequency range from 10 to 56 Hz. The second profile is the high resolution Sturgeon Lake Line, acquired for mining purposes in the Wabigoon greenstone belt. The Sturgeon Lake Line is 7.84 km long, all 393 receivers spaced at 20 m were recording for 3 s each of the shots separated by 40 m. Small explosive charges (0.5 kg) were used as sources of energy. The recorded signal has a wide bandwidth ranging from several Hz to a few hundred Hz.

A large variety of computational processes were applied while examining the real data in this study. Chapter 5 aims mainly at explaining novel procedures and innovative ways of applying the standard ones. To keep the thesis write-up within reasonable limits, commercial software applications used are only explained briefly. References point the interested reader to the literature that encompasses details. Simple tools that I developed because they were not available in the commercial software packages (e.g. surgical mute,

[1]Detailed acquisition parameters for both profiles are given in Appendix C. Plan views of the surveys drawn over the geologic maps are shown in Posters 1 and 2 appended at the back of the thesis.

various amplitude scaling techniques, etc.) are also only briefly explained.

Insight software version 5.1.1 of the Landmark Graphics Corporation was the core commercial software package used to examine Sturgeon Lake Line and Line 23 data. GLI3D package version 2.04 of Hampson-Russell Software Services Ltd was applied to determine static corrections. Numerous additional software routines were programmed by myself and incorporated as modules into the Insight 5.1.1 software package.

5.1 Processing Flow

Table 5.1 illustrates the processing flow applied to Sturgeon Lake Line and Line 23 data. Although the two seismic data sets examined were collected for different purposes, with different acquisition parameters, basically the same processing stream was applied to both lines but with different parameter setup. Such a course was possible because of the similarity in the two geologic environments (igneous and metamorphic rocks) and geometry (crooked lines). To keep the illustration of the processing flow (table 5.1) terse and clear, iteration indications, and selected smaller processes (e.g., resampling) that are not applied to both data sets, are not included in table 5.1. Processes shown in table 5.1, as well as the intentionally omitted ones, are all explained in the text.

5.2 Preliminary Data Processing

Crooked line geometry

Plan view plots of Sturgeon Lake Line and Line 23 surveys are given in figures 2.2, 4.1 and 4.14. Stacking charts for the Sturgeon Lake Line and Line 23 are shown in figure 5.1. For both surveys the receiver spacing was regular at 20 m and 50 m respectively, but the shot positioning was quite irregular due to rugged terrain. The surface acquisition diagrams of figure 5.1 clearly show that uniform spatial sampling for both lines exists only in the shot domain. Therefore, processes applicable in multiple space domains (for example, slant stack filtering), that operate on more than one trace at any time, are preferably done in the shot domain.

Table 5.1:

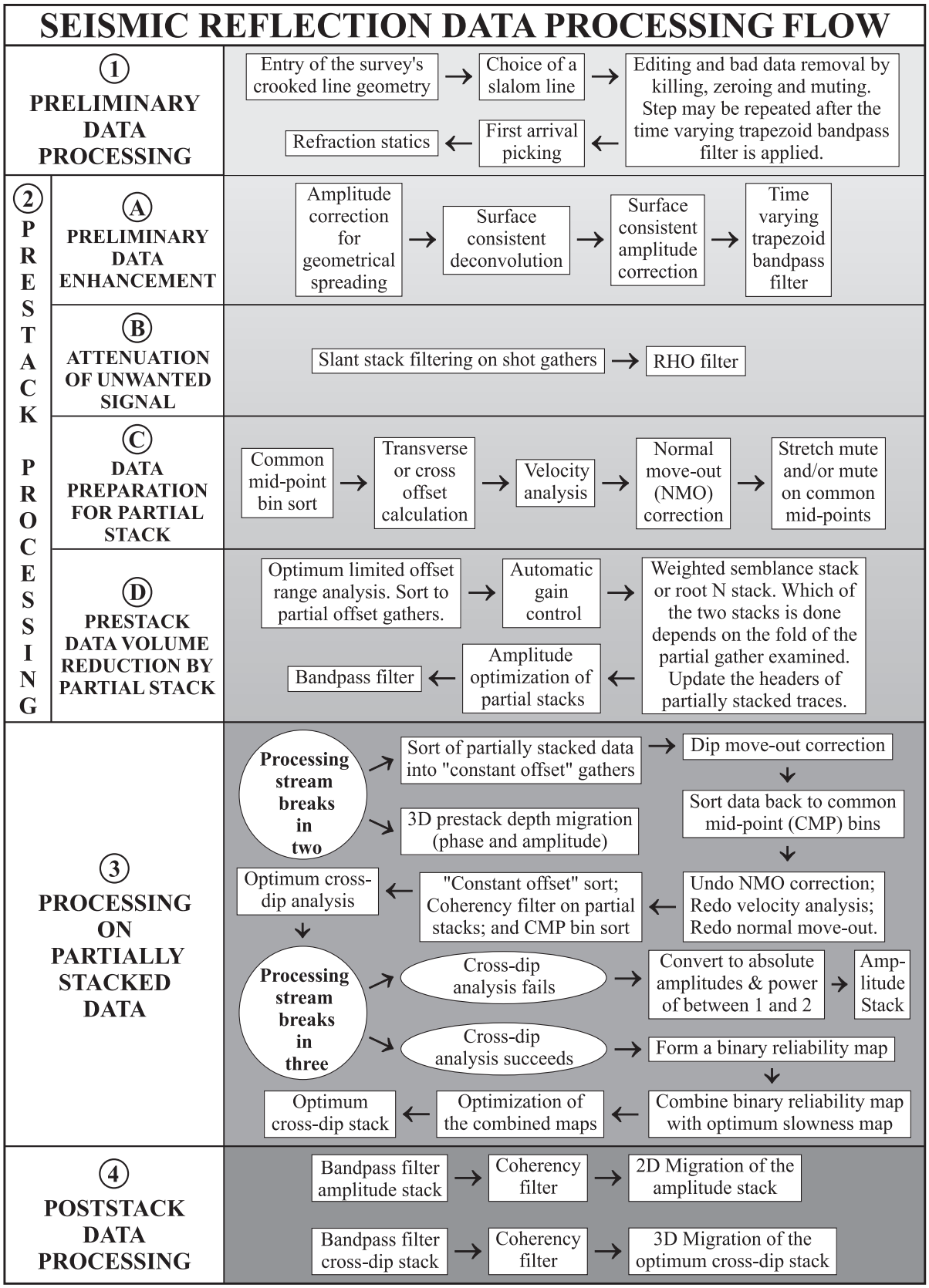
SEISMIC REFLECTION DATA PROCESSING FLOW
1 PRELIMINARY DATA PROCESSING
Entry of the survey's crooked line geometry
Choice of a slalom line
Editing and bad data removal by killing, zeroing and muting. Step may be repeated after the time varying trapezoid bandpass filter is applied.
First arrival picking
Refraction statics
2 PRESTACK PROCESSING
A PRELIMINARY DATA ENHANCEMENT
Amplitude correction for geometrical spreading
Surface consistent deconvolution
Surface consistent amplitude correction
Time varying trapezoid bandpass filter
B ATTENUATION OF UNWANTED SIGNAL
Slant stack filtering on shot gathers
RHO filter
C DATA PREPARATION FOR PARTIAL STACK
Common mid-point bin sort
Transverse or cross offset calculation
Velocity analysis
Normal move-out (NMO) correction
Stretch mute and/or mute on common mid-points
D PRESTACK DATA VOLUME REDUCTION BY PARTIAL STACK
Optimum limited offset range analysis. Sort to partial offset gathers.
Automatic gain control
Weighted semblance stack or root N stack. Which of the two stacks is done depends on the fold of the partial gather examined. Update the headers of partially stacked traces.
Amplitude optimization of partial stacks
Bandpass filter
3 PROCESSING ON PARTIALLY STACKED DATA
Processing stream breaks in two
Sort of partially stacked data into "constant offset" gathers
Dip move-out correction
Sort data back to common mid-point (CMP) bins
3D prestack depth migration (phase and amplitude)
Undo NMO correction; Redo velocity analysis; Redo normal move-out.
"Constant offset" sort; Coherency filter on partial stacks; and CMP bin sort
Optimum cross-dip analysis
Processing stream breaks in three
Cross-dip analysis fails
Convert to absolute amplitudes & power of between 1 and 2
Amp-litude Stack
Cross-dip analysis succeeds
Form a binary reliability map
Combine binary reliability map with optimum slowness map
Optimization of the combined maps
Optimum cross-dip stack
4 POSTSTACK DATA PROCESSING
Bandpass filter amplitude stack
Coherency filter
2D Migration of the amplitude stack
Bandpass filter cross-dip stack
Coherency filter
3D Migration of the optimum cross-dip stack

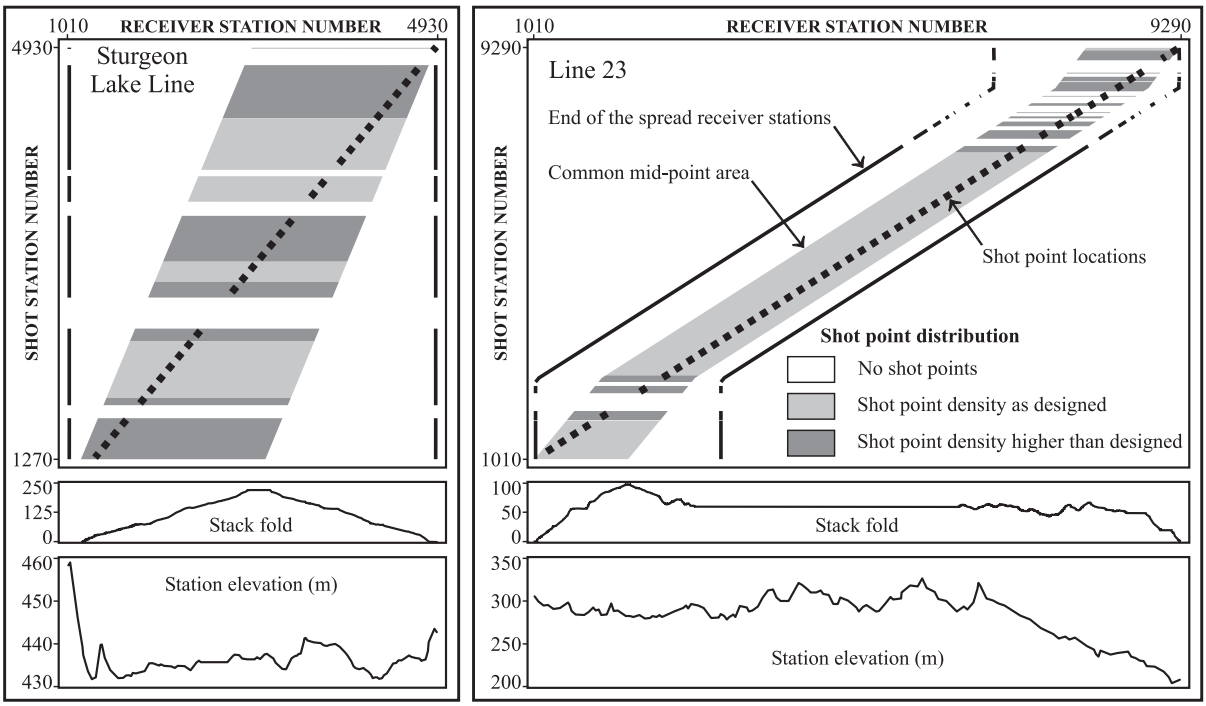

Figure 5.1: From top to bottom, the figure shows a surface acquisition diagram, stack fold, and station elevation graph, for both Sturgeon Lake Line (left side) and Line 23 (right side).

Choice of a slalom line

Reference or processing profile for construction of the SZOST section can be either a smooth, at most gently curved line through the mid-point distribution, or it may be one or a series of straight segments. Results presented in Chapter 4 show that a smooth processing line, or too many straight line segments in a slalom line would reduce the stack quality and make interpretation practically impossible. However, too few straight segments force the line to drift too far from the center of the mid-point distribution, making the cross dip moveout large and reducing the reliability of the local optimum cross dip stack. Choosing a slalom line is obviously a matter of compromise. I chose to use straight line segments in both cases (see figures 2.2, 4.1 and 4.14). Once the shape of a slalom line is decided, bins (rectangles) of desired size are formed and centered along the slalom line. The bin height is usually as large as necessary in order to include all scattered mid-points. For the constraints on the bin width please see section 4.4. The bin widths for the Sturgeon Lake Line and Line 23 were chosen to be 20 m and 50 m, while the bin heights were 600 m and 3000 m respectively.

Resampling and bandpass filtering

The spectral range of Line 23 trace data is close to the frequency range (12 - 56 Hz) of the vibrator sweep sent to the ground by the vibrating trucks during the data acquisition. The sampling rate during the acquisition was 4 ms, allowing for subsequent resampling to 8 ms where necessary to speed up the processing. Data resampling to 8 ms brought the Nyquist frequency down to 62.5 Hz, which is still above the highest frequency of the signal but close enough to cause problems for some algorithms. Resampling was followed by a bandpass filter (10-15–46-56 Hz).

Sturgeon Lake Line data were collected with the sample rate of 1 ms (Nyquist frequency is at 500 Hz) and no resampling was applied. The Sturgeon Lake Line raw shot records contain an unusual amount of high frequency signal for records of 3 s time length. The signal drops below the background noise levels only at frequencies above $\sim$400 Hz. Prestack frequency limits used to bandpass filter data were set at 10-30–300-400 Hz.

Editing and bad data removal

In spite of the best efforts of present day acquisition technology, noisy and bad traces are commonly found in raw shot gathers. Such traces must be first identified and then removed from the data. Abnormal traces may be located manually or by using an automatic procedure. There are various approaches to automatic editing. For instance, Mayrand and Milkereit (1988) discard bad traces in two ways: based on the strength (actually weakness) of the first arrivals, and based on the noise-power estimates.

The data used for this thesis work were manually edited because of the flexibility this allows. When the whole traces were bad, zeroing was preferred to killing, as long as there were no more than a few bad adjacent traces. If only parts of the traces were too noisy, surgical muting was applied. A program was written to simultaneously apply surgical mute and zeroing to the whole data set. The procedure was repeated just before the slant stack filtering, which has a capability to restore the signal in the zeroed and muted traces. Polarity errors were found only among Line 23 traces and were corrected.

First arrival picking

Picking first arrivals on shot gather is a necessary step when the solution to the static problem is sought via refraction methods. Similar to editing, first arrival picking can be

done interactively, or by using an automated algorithm. Automated procedures usually include (Coppens, 1985): reduction of uncorrelated noise (e.g., coherency filtering on constant offset gathers), search for a sudden increase in energy on each trace (several criteria exist), and repicking of mispicks (e.g., error prediction filter on picked time curves). If time permits, interactive first arrival picking done in synchrony with trace editing is the best choice, as it yields superior static solution to the one obtained using first arrival picks from an automated procedure.

Regardless of the method chosen (interactive or automated), the greater consistency in determining the first arrivals is achieved by picking the apex of the first peak or trough. The constant time shift introduced by picking the first positive (or in some cases negative peak), instead of the onset of the first arrival, will have only a minor affect on the thickness of the first layer. If desired, the introduced delay can be estimated and removed.

First arrival picks used in this thesis work were obtained interactively. The apex of the first peak was chosen as the first arrival for Sturgeon Lake Line data. For Line 23 data, the apex of the first trough was selected for picking.

Static corrections

There are three major approaches to statics computation: *field statics, refraction statics, and residual statics.* Separate field measurement (shot hole shooting method, separate refraction profiles, etc.) was not carried out for the profiles examined in this thesis, leaving refraction statics methods as the only alternative.

Refraction statics techniques may generally be classified into the following headings:

- Slope/intercept methods (e.g., see Dobrin and Savit, 1988);
- Delay time methods (e.g., see Hawkins, 1961);
- Reciprocal methods (e.g., see Barry, 1967);
- General linear inverse (GLI) methods (e.g., see Hampson and Russell, 1984);
- Time-term (TT) methods (e.g., see Farrell and Euwema, 1984).

GLI and TT methods incorporate contemporary approaches to refraction statics determination. Farrell and Euwema's (1984) TT algorithm and Hampson and Russell's (1984)

GLI algorithm, the leading techniques among their peers, were both applied to data in this thesis. Both TT and GLI methods use some form of the early refraction methods (slope/intercept, delay time, and reciprocal) to shape the initial model of the near surface studied. Once the initial model of the near surface is formed, TT methods use a least square traveltime decomposition to compute delay times and layer velocities. The problem is non-linear because delay times also depend on velocities, and the final solution is iteratively found. GLI methods are also founded on an iterative least square inversion. The key difference between the two methods is the way in which the iterations are guided by updating the input model. Particularly deserving of mention is Hampson and Russell's (1984) GLI method which applies ray-tracing in order to calculate first breaks on all traces of the iteratively updated model. The model changes are done to minimize the difference between the computed and observed first arrivals, during which close monitoring for geological and physical constraints is conducted.

The static corrections obtained for the Sturgeon Lake Line and Line 23 data were appraised by looking at:

- The surface consistency of statics themselves;
- The continuity of events in various prestack domains;
- The structural and stratigraphical validity of stacked data;
- The surface diagrams of the first breaks.

Several simple programs were written to aid this process. The analysis indicated with a high level of certainty that a two layer model solution of the Hampson and Russell's GLI algorithm yields the best statics for both seismic lines processed. The results (figure 4.2) are stable, acceptable geologically, and were applied to the data.

Generally, neither field nor refraction statics can fully compensate for the effect of the near surface (Yilmaz, 1987). The remedy for the "left-over" statics are residual static corrections. All the residual static methods rely on Ronen and Claerbout's (1985) stack power optimization or some similar measure to estimate the effectiveness of the obtained statics solution. According to their common characteristics, residual statics techniques can be loosely clustered into: *correlation methods, linear inversion methods* (e.g., see Taner et al., 1974, and Wiggins et al., 1976) and *non-linear inversion methods* (e.g. see Rothman, 1985 and 1986, and Dahl-Jensen, 1989). Today, correlation statics are only

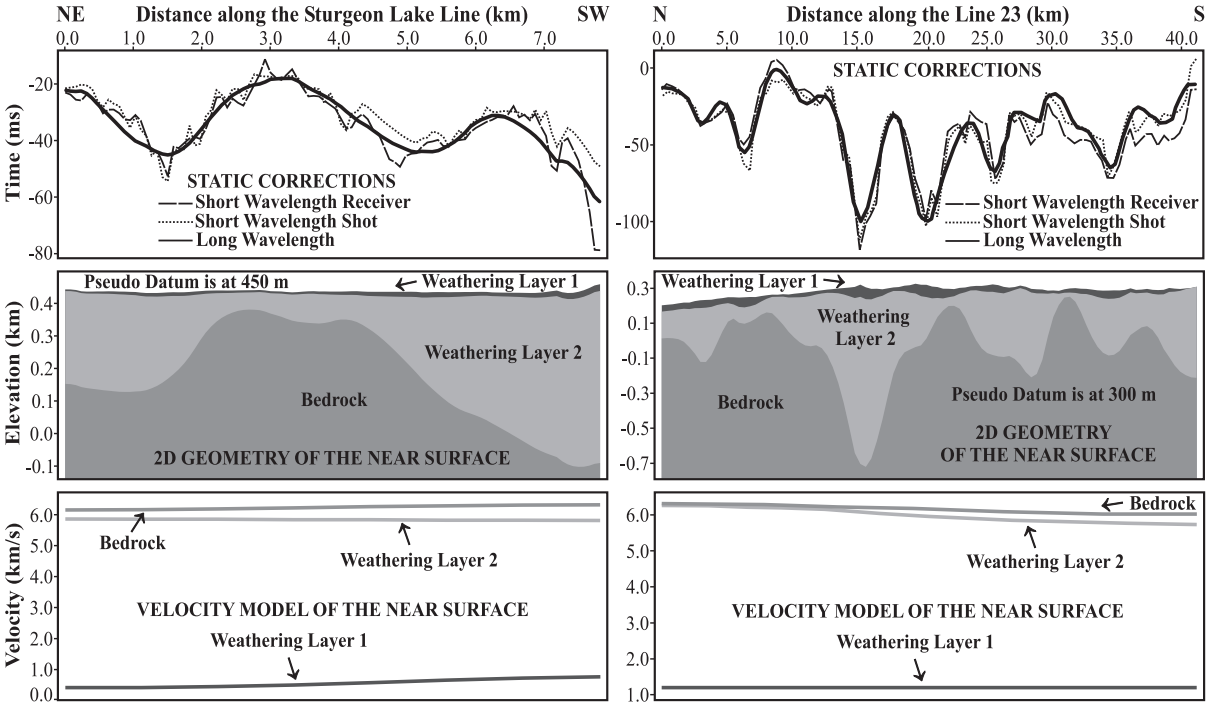

Figure 5.2: The refraction statics results for Sturgeon Lake Line (left side) and Line 23 data are shown at the top. Elevation corrections are already included in the results. The geometry of the corresponding physical models (middle) and their primary velocity distributions (bottom) are also included in the figure. Note the stability of the velocity models.

used at an initial stage of the two latter groups of methods. Linear inversion methods of residual statics have many parallels with the corresponding refraction statics methods.

Crooked line surveying does not provide sufficient information to form a 3D geologic model of the near surface. Assuming a 2D geometry of the weathered zone may result in a somewhat less accurate estimate of statics than with data acquired on straight lines. Furthermore, these estimates cannot be improved at a later processing stage because the cross dip moveout (CDMO) dwarfs the residual statics that become indistinguishable. This is why, when processing crooked line seismic data from crystalline terrains, a great effort for a high quality solution to refraction statics is not only justified, but necessary.

5.3 Prestack Data Processing

5.3.1 Preliminary data enhancement

Several preliminary enhancements were applied to the data and had notable beneficial effects. Correction for geometrical spreading removed the largest amplitude differences

in the data. Surface consistent deconvolution considerably compensated for the non-spikeness of the shot wavelet as well as other near surface influences on the wavelet, and balanced the amplitude spectra well. Surface consistent amplitude correction was a remarkable remedy for the near surface amplitude deviations. Static corrections aligned events well, which can be noticed even after the deconvolution has compressed the wavelet appreciably. Much of the low frequency noise was cut off by a time varying trapezoid bandpass filter. Figure 5.3 illustrates the results obtained using Sturgeon Lake Line data. Similar results were obtained for Line 23.

5.3.2 Attenuation of random noise and unwanted signal

Coherent noise is quite prominent in the examined data in this thesis and clearly visible in figures 5.3.(a) and 5.3.(b). For the Sturgeon Lake Line it consists of: first P-wave arrivals, first S-wave arrivals, surface waves, and source related low frequency noise that is partially due to a slow propagating air wave (see figure 5.3.(a)). Line 23 exhibits the same types of coherent noise, except that there is additional source-generated noise related to the use of vibrators. In many shot gathers it completely dominates the near offset traces (see figure 5.4.(a)).

Three 2D techniques were tested to choose an optimum filter to remove coherent noise on shot gathers: F-K (frequency-wavenumber) filtering (e.g. see Chapter 17, Kanasewich, 1981), F-X prediction and dip rejection filtering (Wang and West, 1991), and local slant stack filtering (e.g. see Chapter 5, Claerbout, 1985, and Chapman, 1981). The best results were obtained with the local slant stack (see figure 5.4), a method for a local wave field decomposition into its plane wave constituents. The local slant stack's ability to work well on small data windows, to produce the least artifacts and (in theory) not to require regular sampling in space domain, are its main advantages.

A normal moveout correction was applied before the local slant stack, which was designed to remove the dipping events using an operator of 11 traces for the Sturgeon Lake Line and 9 traces for the Line 23. The slownesses used to reconstruct the data had limits of $\pm 1.6\ ms/trace$ for Sturgeon Lake Line and $\pm 4.0\ ms/trace$ for Line 23.

The results achieved on suppressing the coherent noise by using the local slant stack filtering are remarkable (see figure 5.4). Unfortunately, the results obtained are somewhat less than optimal because the available software was not of a general purpose (it required the slowness to be specified per trace, not per offset) so no gain was materialized on local

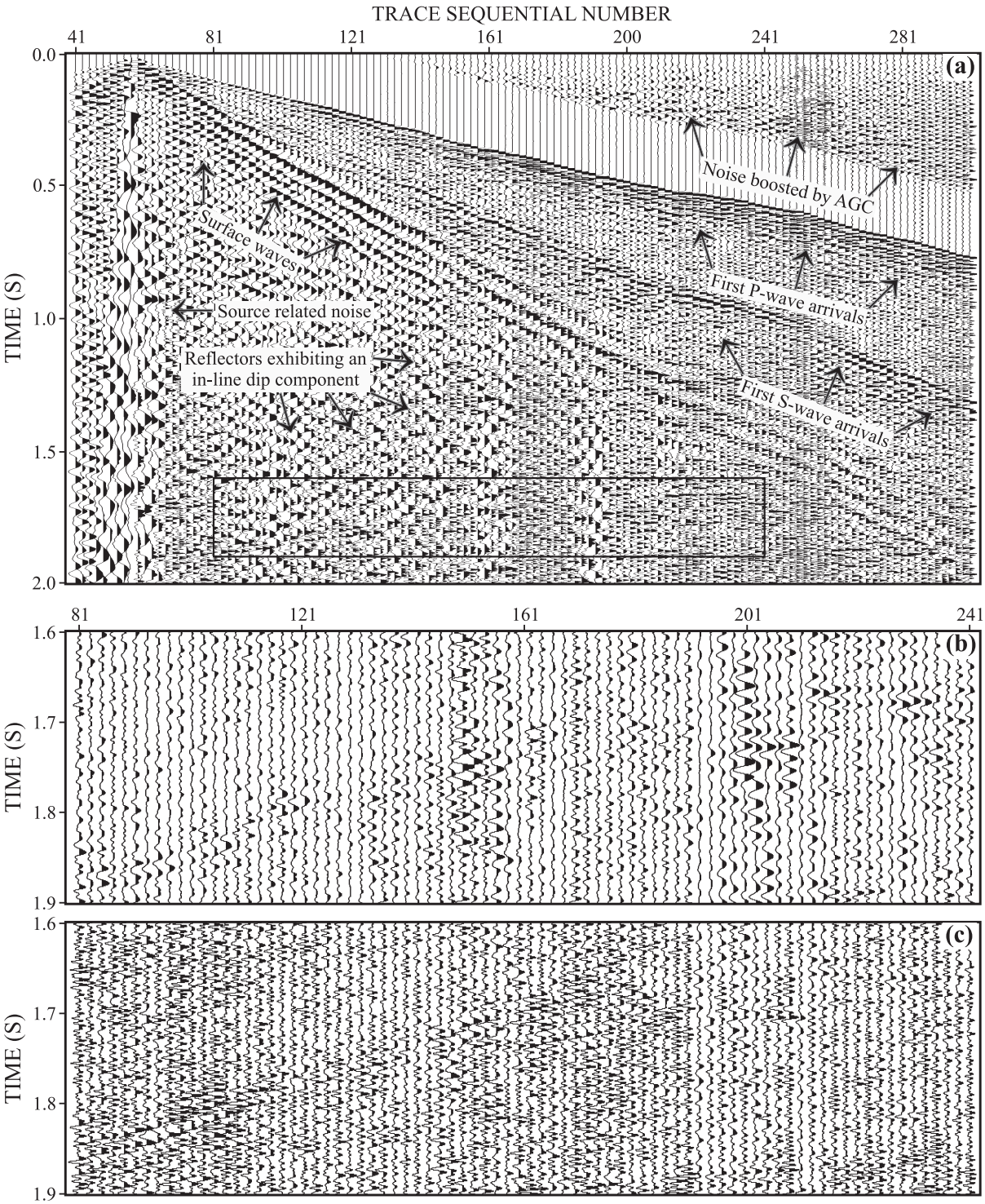

Figure 5.3: Part (a) of the figure is a typical shot gather of the Sturgeon Lake Line after application of automatic gain control (AGC). Signal and various types of noise strongly intersperse. The marked rectangle in part (a), depicting a group of in-line dipping events, is enlarged and shown in parts (b) and (c). Part (b) has only a correction for spherical divergence, while part (c), in addition to the correction for the divergence, has surface consistent deconvolution, surface consistent amplitude correction and refraction statics applied. No AGC was applied to parts (b) and (c). Every second trace is plotted.

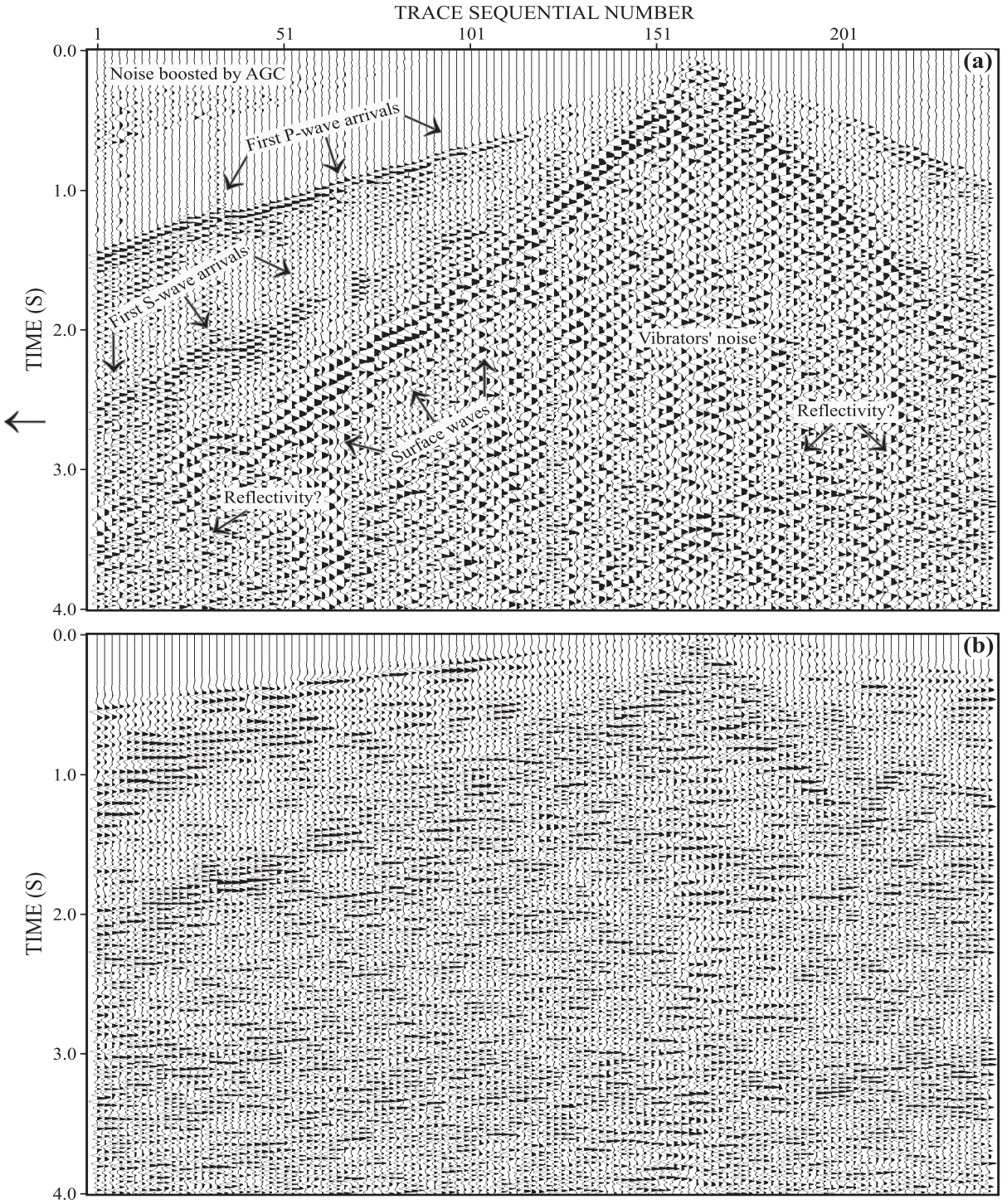

Figure 5.4: A part of a very noisy shot gather 189 of Line 23 was selected (a) to demonstrate the merits of preliminary data enhancement and noise attenuation techniques employed (b), in particular the local slant stack. Only hints of reflections are visible on (a). Note the dramatic improvement in the data on (b). The reflectivity becomes quite apparent. For display purposes AGC was applied to both gathers, and every second trace was plotted. Data in (b) is NMO corrected and muted up to the first arrivals.

slant stack's flexibility regarding the space sampling. Notice that due to the inability of the program to apply offset dependent local slant stack, the largest unattenuated coherent noise appears around trace number 30 (figure 5.4), where the crookedness of the acquisition line strongly affects the source-receiver offsets. The bends on the acquisition line can easily be observed by following the first breaks.

To compensate for the radon transform's (slant stack's) theoretical w^{-1} spectral attenuation, spectral adjustments were made using a "rho" filter (Claerbout, 1985) which multiplies the selected part of the amplitude spectra by the corresponding frequency taken to an arbitrary power. For both data sets the power used was 0.8. The full range of the signal's spectrum was balanced.

5.3.3 Data preparation for partial stack

CMP bin sort and transverse offsets

All further processing steps require that data be sorted into common mid-point (CMP) bins (see sections 2.3 and 2.5). After sorting, the CMP gathers of both data sets show a high and mostly uniform fold. This indicates a good choice of slalom lines and CMP bin size.

Cross offset between the mid-point and the slalom line is not needed in standard processing but is essential in the processing I have developed. This and the source-receiver azimuths were stored in the trace headers.

Velocity analysis and NMO correction

Both CMP stacking and migration require estimates of root-mean-square (rms) velocity in the earth. A wide range of velocity analysis techniques have been developed in the past. All are usually applied in the CMP domain and are basically similar. At most, three somewhat distinct approaches may be singled out: constant velocity stacks, velocity spectrum methods, and velocity panels methods.

Regardless of the method employed, seismic events in both data sets exhibit a tenacious insensitivity to changing stacking velocities. Velocity spectrums show strong dispersion of the events and change dramatically with location of the CMP point. Peaks in semblance for one CMP gather are sometimes scattered in such a way that their distribution almost

resembles a random one. Focusing does not improve substantially even when only limited offset ranges are used to compute velocity spectrums.

Both DMO and CDMO cause serious problems for velocity analysis since it assumes a standard NMO time versus offset relationship. Wang and West (1993) devised a method of velocity analysis that allows for dip moveout, and suggested applying it locally at places in the data where cross offsets are small. Unfortunately, even when this method is successful, there are only a few places along the line where the velocities can be estimated in this manner. At best, RMS velocities are estimated for a few to several events within the 3D space enclosed by the seismic line. But all is not bad: refraction surveys and acoustic velocity logs show that the general velocity variation in crystalline terrains is relatively small, and the inaccuracies in the determined velocities will not have a large degrading effect on the imaging process.

Muting

Three types of mute were applied in processing the data: a first arrival mute, an NMO stretch mute and a CMP surgical mute. While the first arrival mute could be considered as a cosmetical procedure, NMO stretch mute and/or CMP bin mute are critical for the data quality at early times. The NMO mute is usually applied as a part of an NMO correction to eradicate the overly stretched data. Because the NMO stretch mute is an automatic procedure, it lacks flexibility and may leave some of the unwanted signal, or it may remove some of the desired one. The CMP mute is designed by examining the NMO corrected CMP gathers and "marking out" large offset, early time parts of the record that are unlikely to stack properly. In this thesis, only a mild NMO stretch mute was applied to remove the most visible artifacts of the NMO correction. The CMP surgical mute was then used to assure that no inappropriate events remain in data before stack.

5.3.4 Prestack data volume reduction by partial stack

Optimum limited offset range analysis and sort to partial offset gathers

The reasons to determine an optimum offset range for partial stack were explained in detail in section 3.2. Tests carried out on synthetic and real data using several techniques have shown that when efficiency and quality are both of concern, statistical analysis of data using semblance yields the best offset range for partial stack in an optimal way.

Semblance is a measure of coherence that can take values from zero for random noise, to one for an identical signal on all traces. Neidell and Taner (1971) defined the semblance between (multi-trace) time signals as a normalized output/input energy ratio:

$$S_k = \frac{\sum_{j=k-(N/2)}^{k+(N/2)} \left[\sum_{i=1}^{M} f_{i,j} \right]^2}{M \sum_{j=k-(N/2)}^{k+(N/2)} \sum_{i=1}^{M} f_{i,j}^2}, \tag{5.1}$$

where S_k is the computed semblance value at k^{th} time sample, $f_{i,j}$ is the amplitude of jth sample in i^{th} trace, and M is the number of traces in the gather. The averages include from each trace $N+1$ samples symmetrically disposed about sample k.

In partial stacks we are dealing with sets of similar multi trace records and we need a collective semblance $\bar{S}_k$ for the whole set. Thus, in order to determine the optimum offset windows for partial stack, NMO corrected CMP bin gathers are first searched along constant time trajectories for $\bar{S}_k$, which is a normalized ratio of average output and average input energy for a given offset window size.

$$\bar{S}_k = \frac{\sum_{l=1}^{L} \frac{\left[\sum_{j=k-(N/2)}^{k+(N/2)} \left[\sum_{i=1}^{M_l} f_{i,j,l} \right]^2 \right]}{M_l}}{\sum_{l=1}^{L} \sum_{j=k-(N/2)}^{k+(N/2)} \sum_{i=1}^{M_l} f_{i,j,l}^2}. \tag{5.2}$$

l is the index of the partial gathers within a full CMP gather. L is the number of offset windows in the examined gather (for the pre-specified offset window size). M_l is the number of traces found in offset window l. To form a map of $\bar{S}_k$, the procedure is repeated for a large number of different offset windows.

The optimum size of offset window for partial stack, for both modeled and real data, were obtained by analyzing the maps of $\bar{S}_k$ values and averaging the results gained over at least several CMP bin gathers. Figure 5.5 illustrates the $\bar{S}_k$ maps obtained for one CMP bin gather from both lines. The $\bar{S}_k$ defined in this thesis work and given by equation 5.2 is a good measure when the signal has more energy than noise. If it was the other way around, and the signal was weaker than the noise, the average of the semblance for all the offset windows would likely be a better choice.

The results obtained by applying the optimum limited offset range analysis for a partial stack on the two seismic lines examined in this work point to a $\sim 200-250$ m window

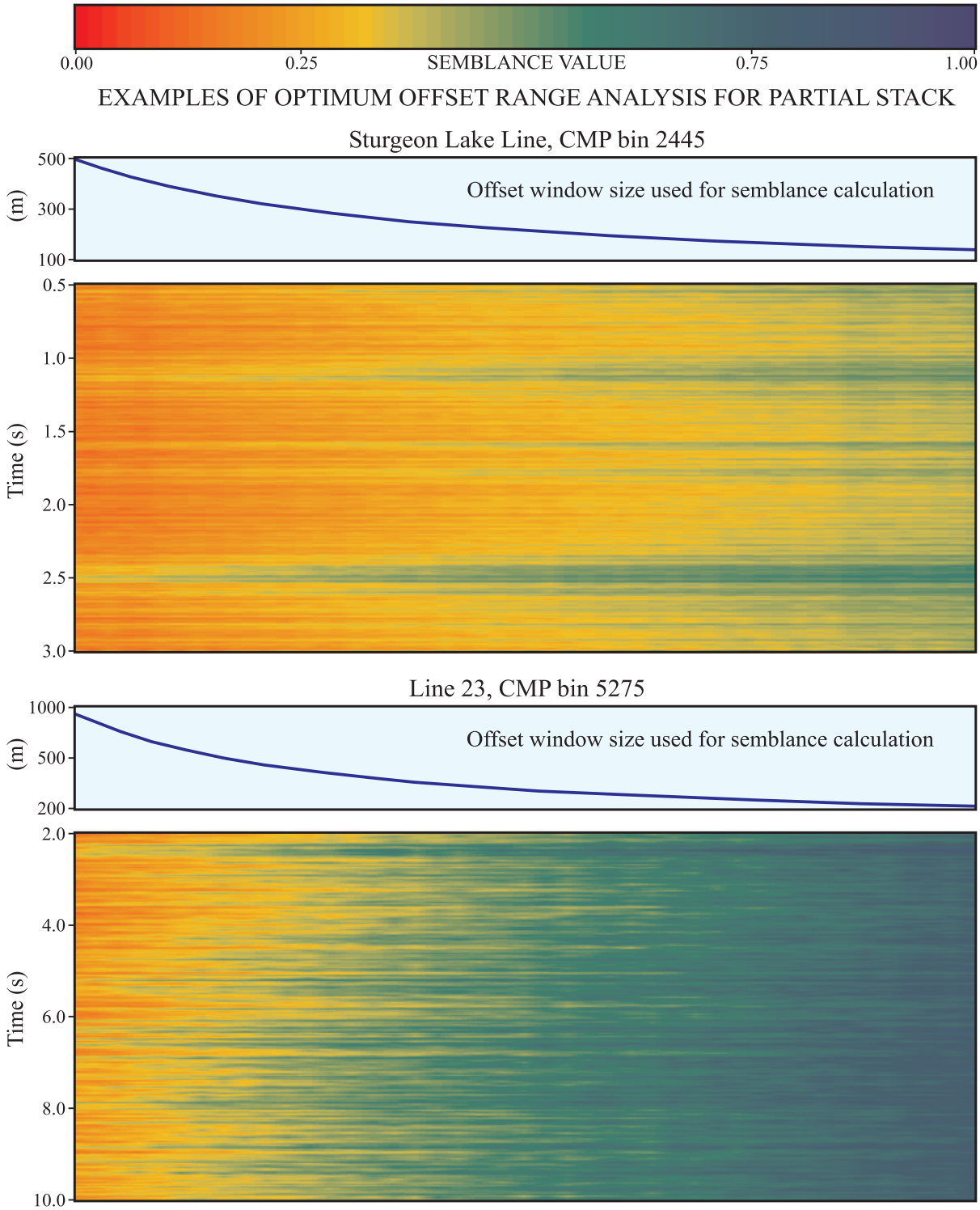

Figure 5.5: The very top of the figure is the $\bar{S}_k$ color pallet. Below are the $\bar{S}_k$ maps for Sturgeon Lake Line CMP bin 2445 and Line 23 CMP bin 5275. Even these single CMP bin maps already indicate an optimum offset window size for a partial stack of $\sim$200$-$250 m for the Sturgeon Lake Line data, and $\sim$500 m for the Line 23 data.

for the Sturgeon Lake Line data, and a ~500 m window for the Line 23 data. All of the data was subsequently sorted into partial offset gathers.

Automatic gain control

Amplitude corrections for spherical divergence, the near surface effects, and the source and receiver inconsistencies were applied and were very helpful, yet the P wave reflection signals after the local slant stack and other filters were not well balanced from trace to trace in CMP gathers. This likely arose from the fact that the amplitude balancing employed had to be done before filtering.

To bring trace amplitudes to a similar level for all offsets and all times data amplitudes were balanced using an automatic gain control (AGC) algorithm. Time windows for AGC of 0.4 s and 1.0 s were used for the Sturgeon Lake Line and Line 23, respectively.

Some researchers that prefer to continue with the true amplitude processing (for example, Mayrand and Milkereit, 1988), argue in favor of discarding the traces with "abnormal" amplitudes. This leads to a large, double-digit percentage reduction of data. For the data studied in this thesis, better results were obtained by giving up on true amplitude processing and keeping all of the traces.

A weighted semblance stack and a root N stack

The logic behind the partial stack of data was explained in the section 3.2 and selection of the offset windows for partial stack has been described in the earlier part of this chapter. The intent of the partial stack is to reduce the large number of traces ($\sim$ 200) in a CMP gather to ~20 to 50 traces with more regularly spaced offsets. A practical problem that arises in doing this is that the number of traces in the limited offset partial gathers varies enormously from none to many tens. Because of the relatively low S/N ratio in the individual traces, it is to be expected that the output from partial stack of a large gather will be of much lower amplitude than the input traces, but of higher S/N ratio than for instance, a one trace gather for which the stacked trace is the same as the input trace. To avoid substantial loss of information in the final stacking I have employed two methods: a weighted semblance stack and a root N stack. Both are forms of weighted averaging. Because of the differences among various data sets, the weights are determined individually for each data set studied.

The weighted semblance stack (S_{WS}) is calculated in the following manner:

$$S_{\mathrm{WS}} = S_s \left[S_k \left(\frac{N}{T} \right)^{\left(\frac{1-S_k}{Q} \right)} \right]^P , \tag{5.3}$$

where S_s is the standard stack, S_k is the semblance as described by equation 5.1, N is the fold of the partial offset gather, T is the threshold fold, and Q and P are arbitrary parameters. T, Q and P are determined by looking at the theoretical curves and examining the partial stacks. Semblance is always calculated for a time window, while the standard stack is computed for only one sample at a time.

The Root N stack (S_{RN}) follows a simple relationship,

$$S_{\mathrm{RN}} = S_s N^{(1-a)}, \tag{5.4}$$

where a is the fold power (N^a) and the rest of the notation is the same as in the equation 5.3.

Rudimentary tests done on the examined synthetic and real data have shown that the stack quality peaks when a fold dependent dual weighting is applied. In this processing, the weighted semblance stack was used when the partial offset gathers exhibited a fold larger than a chosen threshold and the root N stack[2] was applied to the rest of the data. The need for a dual nature of the weights stems from the efficiency of the weighted semblance stack, which overly filters the data when the fold is low.

Identical weighted semblance stack and root N stack parameters were used for both data sets processed. T was 4, Q was 0.8, P was 0.5, and a was 0.45. Zero traces were formed for CMP bin positions and partial offset ranges that did not have any input traces for partial stack. Prestack data sets were compressed by partial stack to $\sim\frac{1}{5}$ of their original size.

Because the output traces of the limited offset range partial stack are treated as recordings at a single point in all following processes, new geometry parameters had to be created for those traces. Headers of the stacked traces were updated by averaging, while the headers of the zero traces were computed by interpolating.

[2]It is important to distinguish between the root N stack used in this study, and the "N^{th}-root stack" (e.g., see McFadden et al, 1986) that is commonly encountered in literature. The fundamental difference between the two lies in the way the root operator is applied. For the root N stack, the root operates on the fold, while the data remains unchanged. The exact opposite is found in the Nth-root stack where the root operates on data, and the fold stays the same.

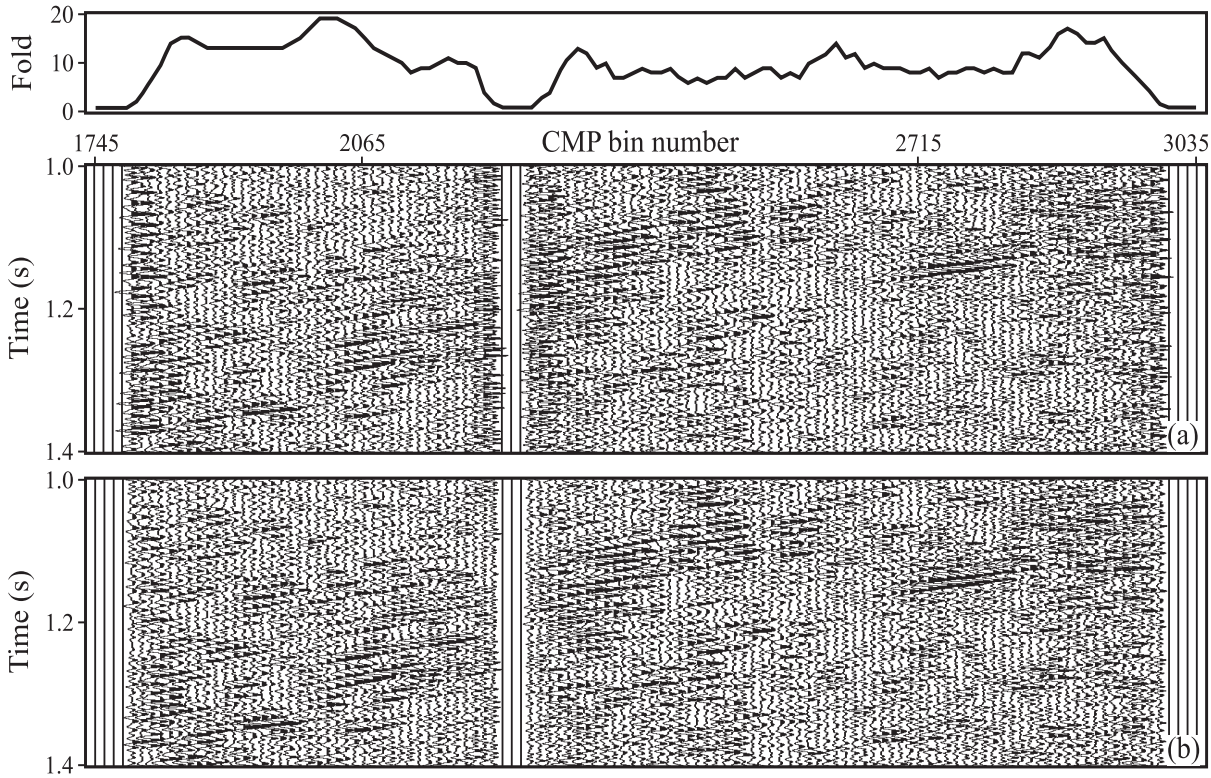

Figure 5.6: A segment of the $1875 - 2125$ m partial stack of the Sturgeon Lake Line before (a) and after (b) amplitude balancing. The top of the figure is the fold of the partial offset gathers before stack. Zero traces, represented by vertical lines, are traces for which there was no input to stack.

Amplitude optimization of partial stacks

Even with the above-described methods of balancing the partial stacks it was found that stacked traces from the semblance and root method showed different energy levels. The differences are easily recognizable in figure 5.6.a. The root N stacked traces exhibit a higher energy level than the weighted semblance stacked traces. However, their S/N ratio is significantly lower. Clearly, the weighted semblance stack is a much stronger filter than the root N stack. Because it is reasonable to believe that the signal that has "survived " partial stacking is more likely to be the signal of interest when it is derived from many traces, the weighted semblance stacked traces were balanced to exhibit a larger amplitude level than the root N stack traces. This was done by applying a simple empirical formula,

$$S_{\mathrm{ABWS}} = S_{\mathrm{WS}} \left[\frac{\overline{|S_{\mathrm{RN}}|}}{\overline{|S_{\mathrm{WS}}|}} \right]^{b}, \tag{5.5}$$

to each sample of all weighted semblance stack traces. S_{ABWS} is the amplitude balanced weighted semblance stack, S_{WS} is the weighted semblance stack before amplitude bal-

ancing, $\overline{|S_{\mathrm{RN}}|}$ is the average absolute amplitude of the root N stack traces, $\overline{|S_{\mathrm{WS}}|}$ is the average absolute amplitude of the weighted semblance stack traces, and b is an empirically determined power. The amplitude balancing process is done for each partial offset stack section separately. Figure 5.6.b illustrates the effectiveness of the equation 5.5. Near the ends of the line and near the gaps, where the amount of data falls, the trace amplitude falls also. The power b applied to both data sets was set at 1.15.

Stacking seemed to alter the frequency spectrum of the data somewhat, thus the amplitude balanced partial stacks were afterwards bandpass filtered. A new low cut frequency for the Sturgeon Lake Line was set at 10 Hz, and a new low pass at 30 Hz.

5.4 Processing on Partially Stacked Data

There are two possible courses of action after the partial stack (see table 5.1). One is to 3D prestack migrate the partially stacked data; the other is to apply DMO and CDMO time corrections that lead towards a 2D stacked section, and then apply poststack migration.

5.4.1 3D prestack depth migration

Migration is the key to repositioning seismic reflection events to their true subsurface locations. It dates back since at least the 1940s (Schneider, 1978), when migration was done by drawing. In 1954, Hagedoorn provided a firm theoretical base for the migration of time sections, which was put to numerical use immediately after the first commercial computers became available in the 1960s. Such migration techniques were based on a diffraction summation. The 1970s witnessed an explosive growth of seismic migration methods, many of which are frequently discussed to a great extent in seismic literature (e.g., Berkhout, 1980, Claerbout, 1985, Yilmaz, 1987).

The reasons for applying a 3D prestack migration of 2D crooked line data are detailed in section 3.4 (see also, Nedimović and West, 2000). 3D prestack migration tests on synthetic 2D crooked line data (Chapter 4, and Nedimović and West, 2000) prove that the technique is useful and has a great potential for further application on real data. Kirchhoff migration (e.g., see Claerbout, 1985, Yilmaz, 1987) code used to 3D prestack migrate 2D crooked line data was written by this thesis author. What is unconventional about the code designed and the migration applied in this study, is an uncommon relationship between the input (2D crooked line data) and the output (a 3D volume of choice).

The code was written for a medium with slowly and vertically varying velocity, which is certainly adequate when dealing with data from crystalline terrains that are often migrated using a single velocity. The migration results are output in depth. When significant lateral variations in velocity exist, depth migration that utilizes some sort of ray-tracing is necessary (e.g., Hubral, 1977).

A standard stacking procedure, or simple data averaging along the offset axis, was used to compute partial stacks for the prestack migration. The offset range utilized in the partial stack of the Sturgeon Lake Line was 200 m, which is at the lower end of the range obtained by the optimum limited offset range analysis (see section 5.3.4). Line 23 data was not prestack migrated mostly because of the lack of sufficient CPU power.

It is easy to recognize the reasons for applying different partial stacks before: a) DMO and CDMO removal (see section 5.3.4), and b) 3D prestack migration. Because prestack migration is ideally applied on data that are not partially stacked, choosing the smallest possible offset range for the partial stack is the best compromise when a full prestack migration can not be applied due to a limited CPU power available. Contrary to prestack migration, when the next processing step is a DMO removal, it is attractive to reduce the zero trace padding, and thus the amount of DMO artifacts, by making the offset range for the partial stack as large as possible. Because the smaller offset window for partial stack results in a lower trace fold of the partial offset gathers, the standard stack was an appropriate tool to partially stack data for the 3D migration. Also, 3D prestack migration is not so sensitive to amplitude variation.

In order to scale the migration run time for the Sturgeon Lake Line to something realizable, the size of the desired output volume was set at to 9720(length) x 6012(width) x 6000(depth) m. In addition, a low sampling rate was set in all three directions (18 m), and to prevent time domain aliasing, data was bandpass filtered at 10-20–80-100 Hz. Even this coarsely sampled 3D prestack depth migration took three weeks of full CPU power on the fastest available computer, a 330 MHz SUN ultrasparc station 10.

5.4.2 Locally Optimum Cross Dip Corrected CMP Stack

Dip move-out correction

Dix (1955) and Levin (1971) have shown for a constant velocity medium that a "reflection" due to a dipping reflector has an NMO velocity (V_{NMO}) related to the true

subsurface velocity (V) by a cosine of the reflector's dip (θ): $V_{\text{NMO}} = V/\cos\theta$. The change in an NMO velocity for a dipping event, relative to the horizontal one, is caused by the sampling of different reflection points along the reflector's dip line, in the up dip direction and away from the zero offset reflection (see figure 2.5.b). Contrary to the dipping events, and heedless of the source-receiver distance, all common mid-points sample a common reflection point in the case of a horizontal reflector. The easiest way to deal with the problems introduced by the in-line dip of the reflectors is just to remove the NMO using the best stacking velocities. Unfortunately, this is not satisfactory if conflicting dips exist because the conventional NMO correction permits only one choice of V_{NMO} for a particular CMP and travel time. Where conflicting dips are common, a DMO correction must be applied.

The classic method is that of Hale (1984), and it is a sort of migration applied to constant offset time sections of each offset distance. Newer, more computationally effective methods are now available.

A fast log-stretch dip moveout correction based on the "exact log DMO" algorithm (Liner, 1990, and Liner and Bleistein, 1988) was applied to "common" offset gathers of both data sets examined. Tests on synthetic impulse response data in this thesis confirmed that the exact log DMO has the desired elliptical geometry of the Hale's (1984) DMO, meaning that the DMO correction performs well even at far offsets and large dips. Although some arbitrary amount of data at very early times is irretrievably lost, the great advantage of the log-stretch DMO is its speed. Log-stretch DMO is many times faster than Hale's DMO.

After DMO removal, the data were sorted back to the CMP bin domain and the NMO correction was undone. This was followed by a new velocity analysis and the new NMO corrections. The newly estimated velocities for both profiles were much smoother and more consistent along the profile than the previously estimated stacking velocities. The DMO correction certainly has removed much of the effect of dipping events on stacking velocities.

Coherency filtering

Reflectors in crystalline terrains lack the continuity and smoothness of reflectors in sedimentary basins, and they often overlap and interfere locally with one another. To improve their continuity and facilitate interpretation, coherency filters are frequently applied. In

this work, the use of coherency filters was extended beyond the final sections, with partial offset stacks being coherency filtered also. Model data shows that the use of coherency filters on partial offset stacks is not only justified, but a necessary step for a successful cross dip analysis that follows. Moreover, if the designed coherency filters are kept weak, they can be applied before and after the DMO correction for even better final results.

A local slant stack was used for all of the coherency filtering done in this thesis work. It is the same method as was applied earlier to locally decompose the wave field and attenuate coherent noise (see section 5.3.2). However, the local slant stack parameters needed to coherency filter data differ from the parameters (see section 5.3.2) utilized to attenuate noise. The number of traces in the filter is usually larger, and a mild semblance weighting of the decomposed wave field is often exercised as an option. Most importantly, the range of dips passed must include all existing real dips[3].

Cross dip analysis

Much has already been said about the cross dip analysis and cross dip corrections (see sections 2.5, 2.6 and 3.3). More specifically, the very reasons for an existence of a cross dip moveout, the necessity to try to remove it, and the general approach to take when doing so, have been detailed. In this section, the methodology and software developed[4], the parameters that yield the best results, and the quality of the obtained results are discussed.

The cross dip corrected stack is implemented by the equation:

$$S_{\text{CD}}(x,\tau,p_y) = \frac{1}{N(x,\tau,p_y)}\sum_{i=1}^{N} D_i(x, t = \tau + p_y y_i), \tag{5.6}$$

where S_{CD} is a set of cross slowness stacks and is a function of CMP bin position (x), zero offset time (τ) and cross slowness p_y, N is the number of live traces in the CMP gather, D_i are the limited window, partially stacked trace data, and y_i is a cross offset of ith trace. y_i is available in the header of trace D_i. An equispaced set of p_y is chosen that covers an appropriate range not exceeding $\pm(2/V_{rms})$.

[3]After taking into account scaling factors, dips above $\sim 45^0$ on stacked seismic sections can not originate from true reflectors.

[4] The module written for the cross dip analysis incorporates various approaches, though similar, to extracting the cross dip information. The combination of parameters given defines the approach taken. While all of the approaches to extracting the cross dip information were tested in great detail, it is impossible within the scope of this thesis to treat them all. As done for the other techniques developed and software written, only the approach that led to the best results is explained.

The set of constant cross slowness stacks is then analyzed in a similar way as constant velocity stacks are used in velocity analysis. Measures of coherency are calculated for each x, t point or patch in the section and searched for maxima as a function of p_y. Then a final cross dip section is formed by applying the optimum p_y value in the stack.

In this thesis work, I have strived for a quantitatively determined estimate of the optimum local cross dip slowness, which means that it is to be determined for each data point of an output section independently using a numerical technique. The numerical procedure found to yield the best cross dip information follows[4]:- Equation 5.6 is essentially a kind of $\tau - p$ transformed CMP stack wherein partially stacked, NMO and DMO corrected and coherency filtered CMP bin gathers are transformed to $S_{\text{CD}}(x, \tau, p_y)$. Then to decide what value of p_y gives the best S_{CD} a running absolute amplitude average of the normalized slant stacks (S_{ACD}) is retained:

$$S_{\text{ACD}}(x, \tau, p_y) = \frac{1}{L+1} \sum_{l=-L/2}^{L/2} |S_{\text{CD}}(x, \tau + l\Delta\tau, p_y)|, \tag{5.7}$$

where $L + 1$ is the size of a running average window and $\Delta\tau$ is the time sample interval. Coherency of the signal along the slant lines is measured next by computing a running average of a normalized weighted slowness semblance (S_{WP}),

$$S_{\text{WP}}(x, \tau, p_y) = \frac{1}{L+1} \sum_{l=-L/2}^{L/2} \left[\frac{\left[\sum_{i=1}^{N} D_i(x, t = \tau + l\Delta\tau + p_y y_i) \right]^2}{N(x, \tau, p) D_i^2(x, t = \tau + l\Delta\tau + p_y y_i)} \right]^a, \tag{5.8}$$

where a is a power weight of the slowness semblance and the rest of notation is the same as in equations 5.6 and 5.7. The slowness semblance weighted absolute amplitude slant stacks are obtained as,

$$S_{\text{SWCD}}(x, \tau, p_y) = S_{\text{ACD}}(x, \tau, p_y) S_{\text{WP}}(x, \tau, p_y). \tag{5.9}$$

A search across P_y at every x and τ data point for a maximum value of S_{SWCD} is carried out first using a small sliding time window. For ${}_{\text{MAX}}S_{\text{SWCD}}$ found in the search window, the corresponding cross slowness value is extracted and assigned to the middle time sample of the search window. A new data array called the cross slowness map is obtained and before it is output into a file, a 1D median filter is applied to it. The window of the median filter is usually somewhat larger than the ${}_{\text{MAX}}S_{\text{SWCD}}$ search window.

Two data files, ${}_{\text{MAX}}S_{\text{SWCD}}$ and a reliability map based on it, are output in addition to the cross slowness map. These two maps can later be used to determine which parts of the cross slowness maps are to be considered as reliable.

The two profiles examined were processed using cross slowness bounds ($\pm 0.\dot{3}\ ms/m$) set so that assuming media velocities $\geq$6000 m/s, all possible cross dips ($\pm 90^0$) were tested. The cross slowness bounds are set in accord with the RMS velocities determined after the DMO correction. The applied running average windows corresponded to the dominant signal periods of the data, 14 ms for the Sturgeon Lake Line, and 35 ms for the Line 23. The sliding windows used for determining the ${}_{\text{MAX}}S_{\text{SWCD}}$ value and the 1D median filter, were set at 5 ms and 9 ms for the Sturgeon Lake Line, and 16 ms and 32 ms for the Line 23.

For many of the events in the Sturgeon Lake Line data, the dominant cross dip was successfully determined. Yet, only a portion of major events in the Line 23 carried sufficient extractable cross dip information. Furthermore, the quality of the extractable cross dip information was higher for the Sturgeon Like Line than for the Line 23, which is later reflected in the optimum cross dip stacks obtained. The cross dip analysis results obtained on real data in this thesis are generally of an inferior quality in comparison to the results obtained for modeled data. Such outcome was anticipated, and is due to a much greater complexity of the real data.

Cross slowness maps

The cross dip analysis developed in this thesis automatically produces an x, τ map of "optimum" cross slowness value. When a region of a seismic section lacks events, the corresponding part of a cross slowness map shows a random pattern, and stacking at this "optimum" cross slowness degrades the image quality. For an optimum cross dip stack to succeed, it is necessary to distinguish between reliably and unreliably determined cross slownesses, on the cross slowness map. This is done by producing a binary reliability map, which is a section composed of samples that only take two values. Where the reliability is zero, it is best to use a default value of p_y (usually zero) in the stack. In the maps of optimum p_y no color is assigned where the reliability is insufficient.

There are a variety of ways to form a binary reliability map. The amplitude stack proved to be the most rewarding option.

A software module was written to produce the binary reliability maps. The module initially calculates an RMS amplitude of the input data set, and then converts all of the input data samples smaller than a chosen threshold value to zero, and all the other samples to one. A threshold value is expressed as a percentage of the computed RMS

amplitude of the whole data set. Then a 2D median filter[5] is applied to eliminate scattered small points of variation. A good choice for the size of a 2D median filter lies in the range from ∼5 to ∼9 traces, and a few to ∼9 samples, but is best determined for each data set separately.

A second module combines the binary reliability map with the cross slowness map. The output file has the same values as the original cross slowness map wherever the binary reliability map indicates a reliable measurement. Where the binary reliability map indicated an unreliably determined cross slowness, an arbitrarily assigned background value that falls outside of the range of possible cross slownesses is assigned to the output sample. Before outputting this new cross slowness map, a 2D mode filter is applied. This replaces the local value in the map with the most common value in a patch around the filtered point. Experience shows that 2D mode filters that have the size that lies in a range from several to ∼21 traces/samples, yield best results for the cross slowness maps processed. However, not all modal values are retained. If the population of an obtained mode is less than some arbitrarily assigned percentage of the total population examined, the background value is assigned to the middle sample. Tests on modeled and real data show that this threshold percentage can be anywhere between ∼5% and ∼30%. A small extension of the reliably determined cross slownesses over the background area after the 2D mode filtering is found to improve imaging in this study.

Optimum cross dip stack

A separate program was written to perform the local optimum cross dip stack. The program reads cross slowness values from a cross slowness map and stacks the corresponding input data accordingly. For the regions of a section where no cross slowness values were reliably determined, data is stacked at a zero cross slowness.

The local optimum cross dip stacks obtained for the two lines processed were bandpass and coherency filtered, before being presented in Posters 1 and 2, and discussed in Chapter 6. In addition, the final cross dip maps are shown as a background to the local optimum cross dip stacks and are used to aid interpretation. Figure 5.7 is an excerpt

[5]The software written during the course of this study was never fully optimized. A good example are the median filters that turned out to be a computational burden, particularly when the median filter windows were large. Significant reduction in the median filter run time can potentially be achieved by using fast algorithms such as the one suggested by Huang et al., 1979. If the software produced in this thesis is to be ever commercialized, it would have to be tested for efficiency, and a number of modules would have to be rewritten.

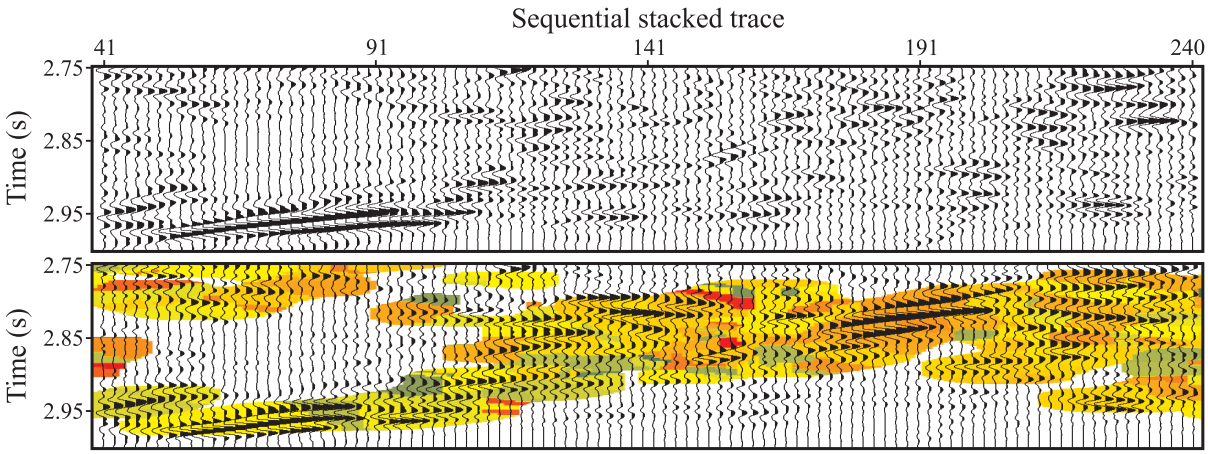

Figure 5.7: A part of an optimum cross dip stack and a standard stack of the Sturgeon Lake Line. The cross dip color map is identical to the one used for all synthetic data in Chapter 4. Most of the improvement in the optimum cross dip stack relative to the standard one is gained where larger areas of similar cross dips are reliably determined. Look at the orange area around the trace 190. Clearly, the standard stack alone would mislead an interpretation.

from the local optimum cross dip stack of the Sturgeon Lake Line. The extracted cross dip is only the dominant one. Where the dominant cross dip "quickly" changes along the profile, a local optimum cross dip stack can appear to be less visually pleasing than the corresponding ordinary stack. However, local optimum cross dip stacks always bear more structural information and lead to a better interpretation.

Amplitude stacking

Because the optimum cross dip analysis was only partially successful on Line 23 data, this data was also amplitude stacked. Several amplitude sections were obtained by raising data amplitudes to a different power before the stack. The overall best section was obtained using the exponent of 1.5. However, using an exponent of 2 and not balancing the amplitudes nor filtering the data after the stack improves imaging of the Moho discontinuity (see results in Poster 1).

Sturgeon Lake Line data were also amplitude stacked but only to test the post stack amplitude migration.

5.5 Poststack Data Processing

3D migration of optimum cross dip stacks

All of the resources for migrating 2D crooked line data into a 3D volume are not exhausted by the 3D prestack migration (see section 5.4.1). A more economical method is to poststack migrate an optimum cross dip stack. Modification to a standard Kirchhoff poststack migrator is necessary, but simple. The optimum cross dip stacked data, the corresponding cross slownesses map, and the cross offset spread size are all used to form a 3D poststack migrated data volume. Before applying the 3D poststack migration, optimum cross dip stacks are bandpass and coherency filtered. The geometry for one

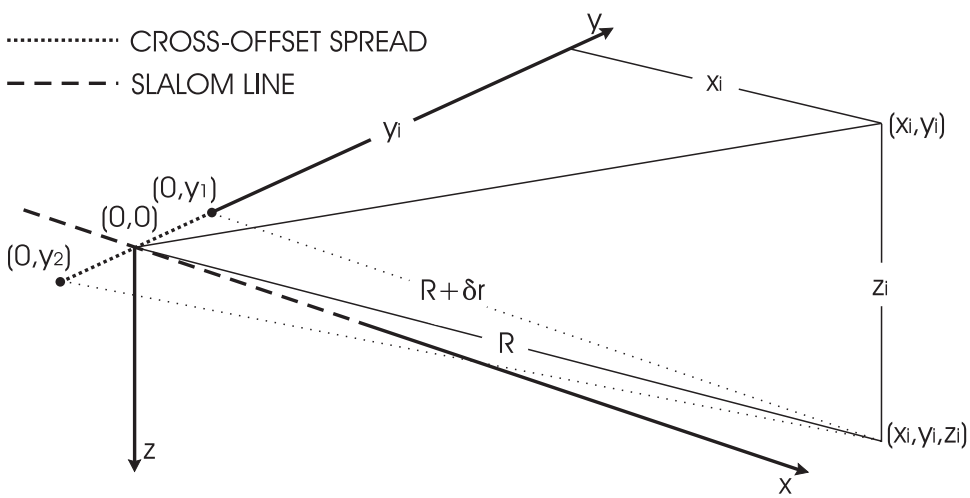

Figure 5.8: The geometry for the 3D poststack migrator. The stacked trace on the slalom line is at the origin of space coordinates $(0,0)$. The image point (x_i, y_i, z_i) is at the distance R from point $(0,0)$. Points $Y_1(0, y_1)$ and $Y_2(0, y_2)$ mark the lateral extent of the cross offset spread in the CMP bin.

image point in a 3D space, and one trace of the optimum cross dip stacked data is shown if figure 5.8. The datum to be migrated from the data trace at $(0,0)$ to the image point at (x_i, y_i, z_i) is found at time $t = 2R/v_{\text{RMS}}$, where v_{RMS} is the root mean square velocity. For other imaginary traces lying on the cross-line $Y_1(0, y_1)$–$Y_2(0, y_2)$, data to migrate to the image point would be found at the time t shifted by a δt. The δt time shift is a function of the cross offset y_c and the cross slowness p_t, extracted at time t from the same trace $(0,0)$ of the corresponding cross slowness map. The change of R to $R + \delta R$ can be approximated for each pair, data trace – image point, using a binomial series:

$$R + \delta R \;=\; \left(x_i^2 + (y_i - y_c)^2 + z_i^2)\right)^{\frac{1}{2}}$$

$$
\begin{aligned}
&= R\left(1 - \frac{2y_i y_c}{R^2} + \frac{y_c^2}{R^2}\right)^{\frac{1}{2}} \qquad (5.10)\\
&\simeq R\left(1 - \frac{2y_i y_c}{R^2} + \frac{y_c^2}{2R^2}\right).
\end{aligned}
$$

Thus, the total time shift equals:

$$\delta t = 2p_t y_c - \frac{2y_i y_c}{v_{\text{RMS}} R} + \frac{y_c^2}{v_{\text{RMS}} R}. \qquad (5.11)$$

By substituting y_1 and y_2 instead of y_c, extreme time shifts are found. Data in the time window $(t + \delta t)_{max}$ to $(t + \delta t)_{min}$ is averaged and added to the image point (x_i, y_i, z_i). The averaging simply acts as a focusing filter for migration. The process is repeated for each output image point and all of the data samples of every single input optimum cross dip stack trace.

Results obtained on synthetic data and shown in section 4.8 and Nedimović and West (2000) illustrate that a 3D poststack migration of a local optimum cross dip stack proposed in this thesis is a very effective method of migrating the events to their true subsurface positions. However, the 3D poststack migration of local optimum cross dip stacks can only position correctly in space the dominant events. When the data is dominated by cross dipping events that overlap on the section, as was the case with the real data in this thesis, a better option is to 3D prestack migrate the data.

2D migration of amplitude stacks

2D amplitude stacks can be migrated in the same fashion as standard phase data, except that any low frequency limit in the migration algorithms need to be set several times lower than normal (Nedimović and West 1999). It is also necessary to to remove the average value (zero frequency component of the amplitude trace static shift) while retaining all of the low frequencies that correspond to the envelope variation of the original seismic trace data. For example, low cut and low pass for the Sturgeon Lake Line were set at 0 and 20 Hz, respectively. Amplitudes before migration are normalized by the AGC. When the amplitude differences of the signal remain large even after the AGC, raising all amplitudes to some arbitrary power that is less than one, tends to improve the migrated amplitude stack.

Although there was no need to migrate amplitude stacks in this study, a part of the experimental work done is presented in Figure 5.9 to illustrate that the technique is

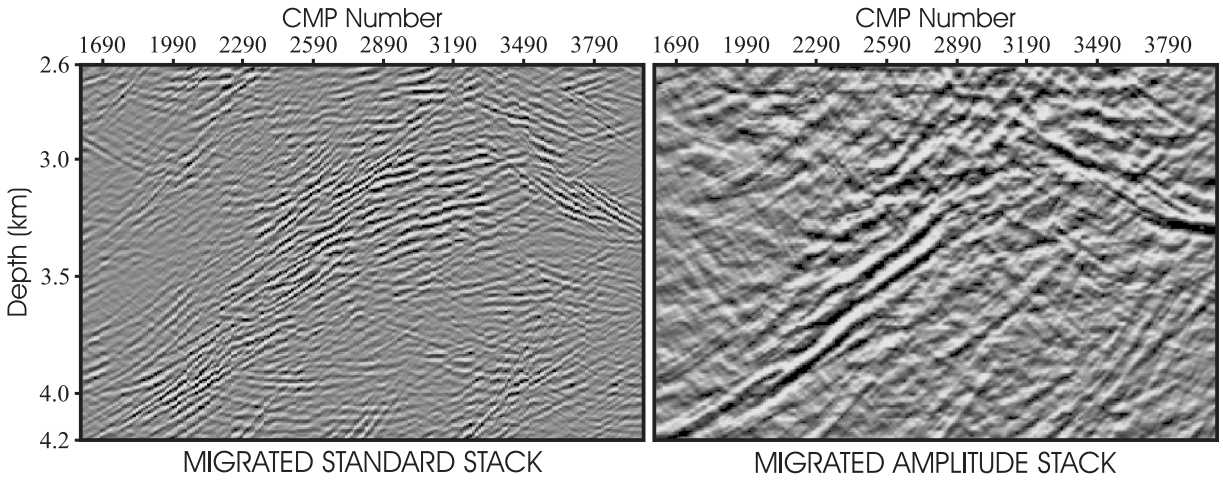

Figure 5.9: Middle sections of the Sturgeon Lake Line poststack migrated standard and amplitude stacks. The migrated amplitude stack gives a better rendition of the relative strength of the reflectors, has better event continuity and reveals a few events that are suppressed in the migrated standard stack. Although resolution is nominally far superior in the phase data, the multicyclic nature of most events makes the real resolution comparable or worse than on the amplitude section.

applicable to real data and useful. The Figure shows a part of the migrated amplitude and standard stacks of the Sturgeon Lake Line.

Chapter 6

Interpretation

6.1 Introduction

The purpose of Chapter 6 is to present the seismic images obtained using the processing techniques designed and to explain how they relate to the geology of the investigated areas. Considering the steep dips of the contacts crossed and the inability of the seismic reflective imaging to extract near vertical events from surface survey data such as examined in this study, much correlation between the obtained images and the intersected geology is not expected. This is especially true for the data of crustal Line 23, which is of lesser quality than the Sturgeon Lake data. Nevertheless, the regional and detailed general geology in the vicinity of the two seismic profiles examined is first introduced. Knowledge of the mapped geology in the areas studied is not only necessary for a simple correlation with the shallow imaged features, but can also provide important clues about the structure imaged at a greater depth.

The seismic lines examined in this thesis are located in the Superior Province of the Canadian Shield. The exact position of both lines can be visualized on the detailed geologic maps provided (see poster 1 section Ba and poster 2 section A)[1]. The maps feature parts of the Abitibi and Sturgeon Lake greenstone belts transected by the seismic profiles.

Because of the nature of a 2D crooked line acquisition, only ribbons of reflectivity across acoustically different geological contacts that face the profile are recorded. Even if the

[1]From hereupon figures in the posters will be referred to by the poster and section name together. For example, poster 1 section Ba will be called poster $1Ba$. However, please note that there are only two posters, poster 1 and poster 2, appended at the back of the thesis.

3D position of these reflectivity bands was accurately known, such partial and scattered information about the 3D structure would make complete geological interpretation difficult to say the least. In an ideal case of 2D imaging, each of the reflectivity ribbons will correspond to a single event in the optimum cross dip stack. If the events overlap on the optimum cross dip stack, only the stronger ones usually remain on the section. 3D prestack migration attempts to preserve all the ribbons of reflectivity and position them accurately in space. However, the limitations of the 2D crooked line data limit the focusing ability of the 3D prestack migration and reflectivity bands often appear larger than they are. Amplitude stacks have been produced as the best compromise when the 3D information can not be extracted.

Although techniques developed during the course of this study provide more informative images than the standard techniques do, they only represent a relative improvement in imaging. The limitations of the techniques and data used to produce images presented in this chapter are well understood and taken into account during the interpretation.

6.2 General characteristics of the Archean Greenstone Belts

[2]Although prior to 25 years ago it was debated if greenstones represent an Archean phenomenon (Windley, 1981), it became clear during the last decade that greenstones have formed throughout geologic time (Condie, 1994b, and references therein). Still, the formation of greenstones was not linear in time. Many of the greenstone belts have formed during the prominent peaks in greenstone eruption and/or tectonic collision events that occur at 2700, 1900, 1300, and 1100 Ma (Condie, 1994b). Today it seems to be equally clear that greenstone belts can form in different geologic settings (Condie, 1994b). Modern, plate tectonics related analogies proposed for the setting of the Archean greenstone belts include aborted intra-cratonic rifts, continental margins and various oceanic settings (Green et al. 1990b). The models on the development of greenstone belts, most consistent with geological relationships and geochemical data on the one hand, and a priori expectations of plate tectonics behavior on the other, are those of a closed continental marginal basin (Windley, 1981).

[2]Appendix D provides a brief introduction on the history of plate tectonics and the structure of the Archean crust. The most recent subdivision of the Superior Province into major tectonic units is also included.

Archean greenstone belts lie in granite-greenstone terrains, represent 10-20% of their volume, and are linear to irregular shaped synformal supracrustal successions (Condie, 1981). Most belts range from 10 to 50 km in width and 100 to 300 km in length. They contain exposed stratigraphic thicknesses reaching 10 to 20 km, but these may not be true stratigraphic thicknesses, as geophysical studies do not find commensurate deep roots to the folds. Geochronologically well controlled greenstone belts, such as those in the Superior Province, show an age span of as much as 300 Ma, although individual building blocks, lithotectonic assemblages, usually span less than 20 Ma (Thurston, 1994).

Regardless of when, where, and how the greenstone belts were formed, they typically contain mafic volcanic rocks and feature low to medium grade metamorphic assemblages, yet otherwise display a great diversity in lithology, stratigraphy, age, basement cover relations and structural deformation (Goodwin, 1981). The fold axes and major faults generally parallel the synformal axis (Condie, 1981). Surrounding granitic domains are comprised of gneissic complexes, intrusive bodies, batholiths, and late discordant plutons. Greenstone successions are chiefly composed of pillowed, mafic volcanic rocks, but occasionally calc-alkaline volcanic rocks increase in abundance with the increase in stratigraphic height, and ultramafic and komatiitic lavas may appear abundant in the lower successions. Sediments are usually minor constituents of the greenstone belts, but are nonetheless very important ones, in particular of the upper stratigraphic levels. They are dominantly graywacke-argillite, chert, and clastic sediments. The basement upon which the greenstones were erupted could be made of large intrusive plutons or older gneissic complexes, but this remains an area of speculation. Vertical tectonic forces appear to have dominated during the deformation of the preserved greenstone belts.

6.3 The Abitibi Greenstone Belt, with an Emphasis on the South-Central Part

The east-west trending Abitibi greenstone belt, located in the western Abitibi Subprovince, is the largest greenstone belt in the world (Jackson and Fyon, 1991). It reaches 700 km in length and 200 km in width (Dimroth et al., 1982), and is unique in the Canadian Shield for its high ratio of supracrustal to intrusive rocks (Jackson and Fyon, 1991). The Abitibi greenstone belt is economically important as it contains a diverse spectrum of richly mineralized deposits.

Figure 6.1 illustrates a simplified form of the Abitibi greenstone belt's main constituents,

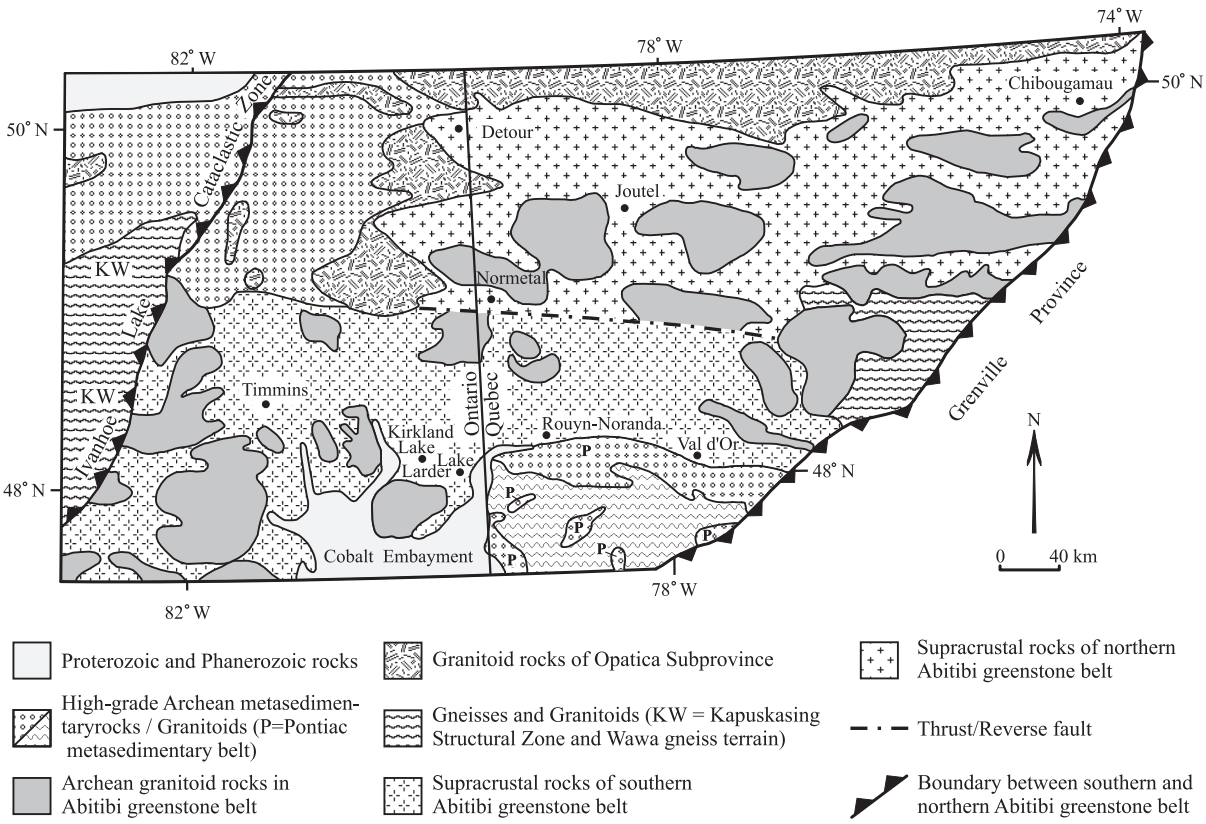

Figure 6.1: Simplified map of the Abitibi greenstone belt (after Jackson and Fyon, 1991).

and most of the bounding domains (see also figure 6.2). To the south are the Ramsey-Algoma granitoid complex, the Cobalt Embayment and the Pontiac Subprovince; to the north is the Archean Opatica Subprovince; to the west is the Ivanhoe Lake cataclastic zone marking the eastern boundary of the Kapuskasing Structural Zone; and to the south-east is the Proterozoic Grenville Province.

Dimroth et al. (1982 and 1983b) divided the Abitibi greenstone belt into northern internal zone and southern external zone, essentially, northern and southern belts. Line 23 crosses the southern belt.

Most supracrustal assemblages and synvolcanic intrusions found in the southern Abitibi greenstone belt formed between ~2750 and ~2700 Ma (Corfu et al., 1989). Widespread felsic magmatism that followed (~2700 to ~2680 Ma) initially involved emplacement of foliated tonalite-granodiorite batholiths, but in later stages changed and more massive granite, feldspar ± quartz porphyry, and syenite bodies were formed (Corfu et al., 1989). During and subsequent to this magmatism, fluvial-alluvial clastic metasedimentary rocks and alkalic metavolcanic rocks of the Timiskaming group formed and are now spatially

associated with the Destor-Porcupine and Cadillac-Larder fault zones (Jackson et al., 1990, and references therein).

The metavolcanic rocks that predate the magmatism form well defined komatiitic, tholeiitic and calcalkalic rock suites (e.g., Dimroth et al., 1982). Repetitive occurrence of similar suites in the "stratigraphic column" has been attributed to cyclic volcanism (Jackson et al., 1990, and references therein). Geochronological data indicate that some similar suites were erupted at different times (Corfu et al., 1989). Furthermore, the same data also indicate repetition due to thrusting and/or lateral juxtaposition. Bedding and tectonic fabric of the southern belt generally dips between 90^0 and 45^0 (Jackson and Fyon, 1991). Shallow dips are present mostly in the center of the Blake River group, southwest of Timmins. There are north- and south-verging thrust faults that both predate and post-date deposition of the Timiskaming group (Jackson, et al., 1990, and references therein). The regional synthesis indicates that structures were strongly affected by the protracted north-south compression active during their formation (Dimroth et al. 1983a). A metamorphic grade within the supracrustal rocks is generally subgreenschist to greenschist facies, with amphibolite facies in the vicinity of the intrusions.

Steeply dipping, east-striking, regional shear zones that are associated with large gold deposits transect the Abitibi Subprovince and partially mark the boundary between the subprovince and the Pontiac Metasedimentary Belt (e.g., Dimroth et al., 1983a). These regional shear zones have been variously interpreted as synvolcanic normal faults that were reactivated during regional deformation, as strike-slip faults associated with tectonic accretion, and as regional thrust faults (Jackson et al., 1990, and references therein).

Generally east-west trending and upright folds, steeply dipping foliations and steeply plunging stretching lineations, also characterize the southern Abitibi greenstone belt.

6.4 Geology of the Area Intersected by the Line 23

Poster 1*Ba* is a detailed map of the area surrounding lines 23 and 24 based on the MERQ-OGS map (1984). The corresponding stratigraphic legend and symbols are shown in the same poster. Both lines were acquired in the the central Larder Lake area of the Kirkland Lake region (for more information about the lines please see Appendix C).

Several workers have suggested that the Abitibi greenstone belt consists of two major volcanic cycles, named cycle II and cycle III, whereas cycles I and IV occur only locally

(MERQ - OGS, 1984, and references therein). All of the geological units shown in poster $1Ba$ are classified by the discrete volcanic cycle they belong to (if this can be established) and are presented in the stratigraphic legend. Lithology of the geologic units, as well as some of the existing ages (as the main source of age data, Corfu, et al., 1989, was used) are given in the stratigraphic legend also.

According to the geologic map of the poster $1Ba$, Line 23 crosses eight distinct geologic units, some of them up to several times. In addition, it cuts across a few faults and shear zones, and passes close to a few more geologic units. Although many metavolcanic and metasedimentary rock assemblages are intersected, the dips of their contacts measured at the surface are generally so steep that it is unlikely that they will be imaged. The same is true for the layering within each assemblage. A higher possibility exists to image the rock units with milder dips that are found in the vicinity of the Line 23. For example, Line 23 passes close to the Nipissing diabase, which is actually composed of gabbroic rocks that intrude the Huronian Supergroup in the form of dykes, sills and undulating sheets up to several hundred meters thick (Bennett, 1991). Such sills and undulating sheets could well be imaged if they focus the reflected energy back towards the profile. Another example is the contact between the Proterozoic Huronian Supergroup and the Archean Abitibi belt (poster $1Ba$), which might have a shallow dip.

The LCSZ and other similar shear zones penetrate deeply into the crust, because their lateral extent is hundreds of kilometers. Although very steep, these shear zones might be imaged indirectly if they are wide enough to change the reflectivity patterns. This type of imaging is highly unlikely for the faults which appear to have a relatively minor vertical and lateral separation, and are relatively narrow.

The following explanation[3] of the relationships between the intersected geology, is a summary of the work published by Jensen (1978), Jackson and Fyon (1991), and Jackson et al. (1995), and includes somewhat differing interpretations and more recent geochronological data than that of MERQ-OGS (1984) and shown in poster $1Ba$:

- The Kinojévis South assemblage ($\sim$2701 Ma) is unconformably overlain by the younger ($\sim$2685 to $\sim$2675 Ma) Timiskaming assemblage;
- The Timiskaming assemblage is moderately to steeply south-dipping and south-facing assemblage that is cut by numerous faults. It has a very complex and not

[3]The word assemblage used in this explanation has the same meaning as the word group in the poster $1Ba$. It appears that the use of the word assemblage has become more appropriate in the past decade.

well defined relationship with the turbiditic metasedimentary rocks south of the Larder-Cadillac Lake shear zone, called the Hearst assemblage;

- The Larder-Cadillac Lake shear zone (LCSZ) appears to be a steeply to moderately south dipping fault;
- The Hearst assemblage (in the poster $1Ba$ called the Porcupine Group) is dominantly metasedimentary. It structurally and unconformably overlies the $\sim$2705 Ma old metavolcanic rocks of the Larder Lake assemblage;
- The Larder Lake assemblage, according to studies more recent than that shown on the MERQ-OGS map (1984), is bounded on the south by the McElroy assemblage. The part of the boundary crossed by the Line 23 is most probably marked by the Lincoln-Nipissing shear zone (LNSZ).
- The McElroy assemblage (in the poster $1Ba$ called the Ultramafic sills) is a northwest trending homoclinal succession of massive to pillowed mafic flows that dips moderately to steeply towards north. The nature of its southern contact with the Skead assemblage is not known.
- The Skead assemblage ($\sim$2701 Ma old) has steeply dipping, north-facing lithology, and is bounded on the southwest by the Catharine assemblage. The boundary is interpreted as a sheared primary contact.
- The Catharine formation of the Catharine-Pacaud assemblage is overlain by the younger Skead assemblage. The units of the Catharine-Pacaud assemblage all consistently face away from the Round Lake batholith.
- The Huronian Supergroup sediments of Proterozoic age are intersected by the very southern tip of the Line 23. These formations typically have very low dips, which contrasts all of the above described steeply and moderately dipping contacts. The most abundant and widespread igneous rocks intruding the Huronian Supergroup are the gabbroic rocks of the "Nipissing Diabase".

Several granitoid bodies crop out near the Line 23. Their acoustic properties differ from that of the metavolcanic and metasedimentary rocks. If their contacts with the greenstones are favorably oriented towards the profile, some parts of them may be imaged also.

6.5 Structure Imaged by the Line 23

The results obtained in this study are certainly not the first images of the Line 23 data. These data have been examined and interpreted, and the results published, by at least one research group prior to this thesis work (see for example Jackson et al., 1995). Moreover, images of most of the Lithoprobe reflection profiles, including Line 23, are publicly available and can be downlaoded over the internet from the Lithoprobe Seismic Processing Facility (LSPF). Line 23 and the surrounding reflection profiles (16, 16a, 17, 18, 21 and 24) obtained from the LSPF are shown in poster $1A$. A map illustrating the geographic position of the profiles is centrally located within the poster. Based on the presented profiles, general characteristics of the featured region can be summarized as follows:

- The crust is reflective while the upper upper-mantle is not, which makes the Moho discontinuity traceable at many places along the profiles;
- Reflectors are relatively short, with a maximum uninterrupted length reaching a few kilometers. Highly reflective zones that stretch much longer (dozens of kilometers) can be distinguished but they are composed of many reflectors of smaller extent;
- The least reflective part of the data is the top few seconds. This region is almost devoid of reflectivity on all sections;
- The pronounced vertical banding present in all sections is almost certainly not a crustal signature, but rather a result of the data processing style employed.

Images of the Line 23 data obtained in this study are presented in posters $1Bb$, $1Bc$, $1Bd$ and $1Be$. The images represent, in order of their appearance, a standard stack superimposed on a cross dip color map ($1Bb$), an amplitude stack ($1Bc$), a profile showing the top $\sim$3 s of the 2D prestack migrated data ($1Bd$), and a part of an amplitude stack that was formed with the goal of delineating the Moho discontinuity ($1Be$). For the interpretation purposes, surface geology intersected by the slalom line is given on the top of the posters $1Bb$, $1Bc$ and $1Bd$, and above it, azimuth of the slalom line.

General crustal structure and trends are best observed by viewing the amplitude stack (poster $1Bc$) sideways and from a distance greater than usual. Interestingly, making the image many times smaller than that shown on poster $1Bc$ helps the interpretation, but the image must be examined at a closer distance. This is in stark contrast with the way

standard stacks are examined (generally, the larger the plot the better). Because relatively little cross dip information was extracted, instead of the cross dip stack, standard stack of the Line 23 was superimposed on the cross dip color map (poster $1Bb$). This image is particularly useful for examining details. The image of the 2D prestack migrated data (poster $1Bd$) shows little reflectivity and therefore elucidates the point brought up by the cross dip studies, which is that some of the main events imaged do not lie below the Line 23. Poster $1Be$ shows that the Moho discontinuity can be well delineated along a large segment of the profile, but more importantly confirms the notion often stressed in this thesis, that no image satisfies all purposes. Thorough and accurate interpretation requires many approaches to data processing.

Three seismically distinct regions, two transition zones, and two shear zones within the crust and below the Line 23 can be discerned and described[4] (see poster $1Bf$). Although distinct, these crustal regions and zones are seismically anything but homogeneous.

Region I. No direct correlation between the surface geology and the shallowest imaged events, $\sim$500 m deep, can be made. Although reflectivity dips in various directions, subhorizontal events dominate (posters $1Bb$ and $1Bc$), which is not consistent with the generally strongly dipping features of the surface geology. This can be attributed to a biased imaging process that "favored" horizontal and subhorizontal events. Alternatively, the dip of the structures might rapidly change to become generally subhorizontal even at shallow depths. These subhorizontal events appear to outline a basin-like structure that shallows towards the Proterozoic Huronian sediments (poster $1Bb$). The form of this structure satisfies the definition of a greenstone belt, an irregularly shaped synformal supracrustal succession. Most of the reflective events are short, reaching a maximum length of approximately several hundred meters. Cross dip analysis had a limited success with the cross dip determined only for a small portion of the events (poster $1Bb$).

Shear zones. Shearing may effect the reflectivity of the crust in at least two ways: a) It may cause a crust "seen" as weakly-reflective because of its steep contacts, to appear more reflective/diffractive, if the rock mixing due to shearing forms new layering with a dip closer to the horizontal; and b) It may also disrupt and reduce the reflectivity in an otherwise reflective crust featuring horizontal and subhorizontal events by breaking them into many smaller reflectors/diffractors whose responses interfere. If the mentioned effects of shearing truly represent a crustal reality beneath the Line 23, then the steeply

[4]In the following discussion, the poster name/number points to the seismic image that (best) illustrates the currently described part of the interpretation profile presented in poster $1Bf$.

dipping Larder-Cadillac and Lincoln-Nipissing shear zones appear to be imaged (posters $1Bb$ and $1Bc$). Over their full extent in depth, both shear zones exhibit a similar dip to the one determined at the surface. LCSZ can be traced to depths of up to $\sim$15 km, while LNSZ is traced "only" up to a depth of about 6 km .

Transition zone I. The largest concentrated amount of reflectivity is found in transition zone I. Regardless of the fact that some of this reflectivity certainly does not originate directly below the Line 23 (e.g. most of the reflectivity at $\sim$2 s near the north end of the line comes from a side - poster $1Bb$), it is reasonable to believe that this transition zone might approximately outline the sheared contact between the greenstones and the basement structure in the Line 23 area (poster $1Bc$). The 2D prestack migration (poster $1Bd$) that tends to best focus the reflectivity coming from straight below the profile, shows that only a part of the reflectivity registered in the transition zone I originates below the slalom line. Furthermore, it also shows that the events of the transition zone I below the slalom line are mainly dipping towards north (poster $1Bd$). This is also in agreement with what the cross dip analysis indicates.

Region II. This part of the crust is mostly void of reflections (posters $1Bc$ and $1Bb$) and might represent the basement upon which the greenstones were erupted or plutons that invade their base. In any case, it appears to be made of more homogeneous materials than the region I, and likely consists of large intrusive plutons or an older gneissic complex.

Region III. Extensive and mildly north dipping reflectivity characterizes this part of the crust (poster $1Bc$ and $1Bb$). The origin of this reflectivity is unknown (see Chapter 1 for the possible sources of deep crustal reflectivity) and cannot be determined from the images obtained. However, because of the closeness of the Proterozoic Nipissing diabase, it can be speculated that the lower crust may be intruded by numerous sills and undulating sheets. Though these gabbroic intrusions are rarely recognized on the surface north of the present limits of the Huronian Supergroup exposures, it seems plausible that their extent is larger at greater depths. Perpendicular to the Line 23 lies Line 24. The two lines "touch" along the southern third of the Line 23. At their junction point and within the region III, observed reflectivities (posters $1A$, $1Bc$ and $1Bb$) match in arrival time, type and abundance on both profiles. The varying cross dip extracted from the Line 23 data also agrees with the wide spectrum of in-line dips found in the Line 24 profile.

Transition zone II. This is a zone in which reflectivity starts to weaken (at $\sim$10 s - poster $1Bc$ and $1Bb$), and completely diminishes below what is here interpreted as the

Moho discontinuity (poster $1Be$). The dip of the events is same as in the region III, which is mild and towards north.

Moho discontinuity The special amplitude processing (see Chapter 4 for details) was done in order to image the Moho discontinuity better. Poster $1Be$ is a result of such processing and shows a part of the amplitude profile in which the Moho discontinuity is most pronounced. The Moho Discontinuity dips at $\sim 10^0 - 15^0$ towards north, meaning that the crust thickens as the line gets deeper into the Archean "territory". Assuming the average velocity of the crust of 7.0 km/s, the average Moho depth below the Line 23 is $\sim$44 km.

6.6 The Sturgeon Lake Greenstone Belt

The Sturgeon Lake greenstone belt is situated in the central region of the granite-greenstone Wabigoon Subprovince (see figure 6.2). The 900 km long east-trending Wabigoon Subprovince, alike the Abitibi Subprovince, is one of the most extensively mapped regions in Ontario. The geological mapping is strongly supported by widespread geochronological data and various geophysical investigations. The following information about the central Wabigoon Subprovince, and in particular about the Sturgeon Lake greenstone belt, is a brief outline of the Wabigoon Subprovince (Blackburn et al., 1991) and Sturgeon Lake area (Trowell, 1983) synopses. Both studies, Blackburn et al. (1991) and Trowell (1983), bind together the work of many generations of researchers.

The Wabigoon Subprovince is bordered to the south by the metasedimentary Quetico Subprovince, to the north-west by the metaplutonic Winnipeg River Subprovince, and to the north-east by the metasedimentary to migmatitic English River Subprovince. The Proterozoic Trans-Hudson Orogen limits the extent of the Wabigoon Subprovince towards east and west. The subprovince is also cut by the Proterozoic diabase Nipigon Embayment.

The greenstone belts of the central Wabigoon region, including the Sturgeon Lake greenstone belt, are small. They lie engulfed in a see of granitoid and gneissic rocks. The gneissic domical bodies are one of the oldest in the Wabigoon Subprovince. Some are dated older than $\sim$3075 Ma. Granitoid rocks are of trimodal nature: a) in some parts of the central Wabigoon region they form a basement complex underlying $\sim$3000 Ma old greenstones; b) some granitoid are petrogenetically and geochronologically linked with volcanism; and c) some are post tectonic, and appear both marginal and internal to

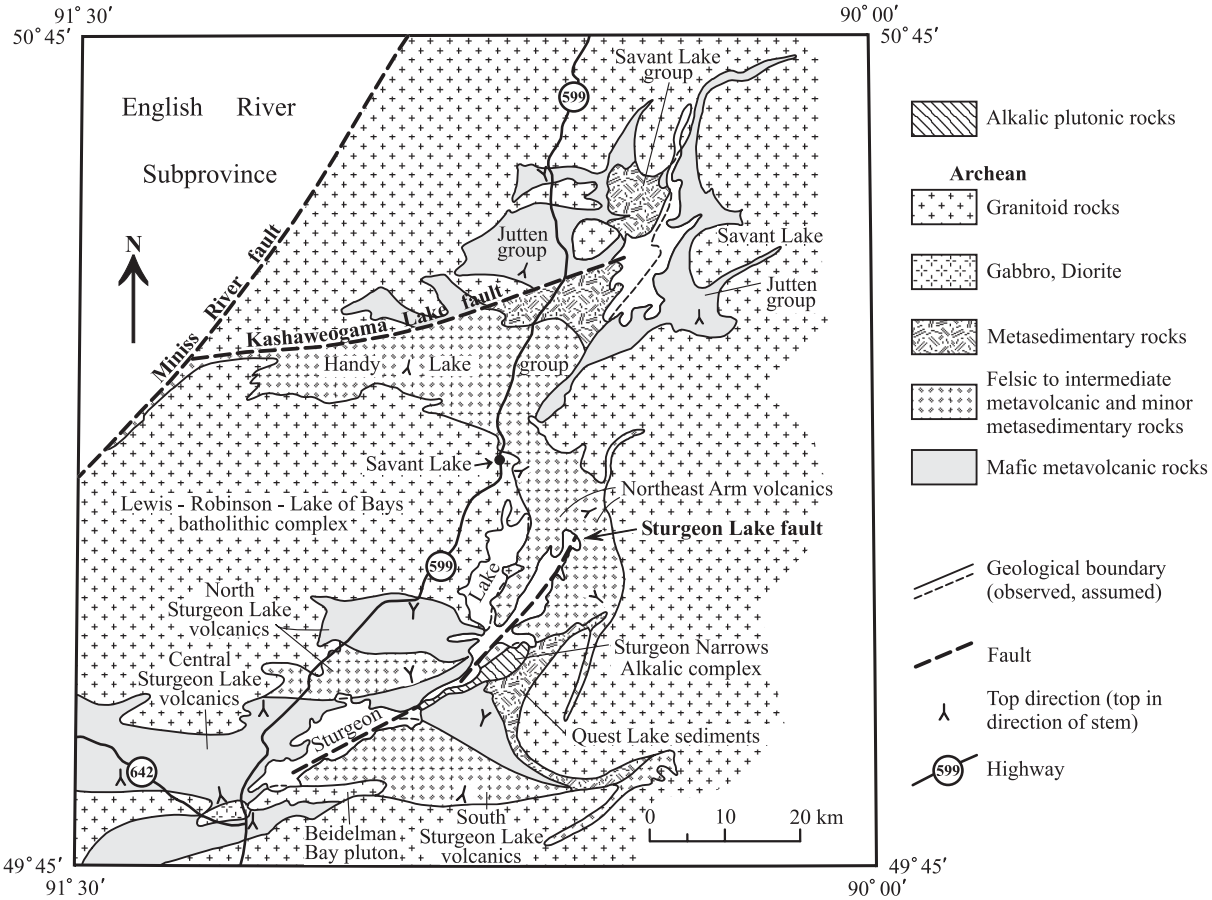

Figure 6.2: Geologic map of the Sturgeon Lake and Savant Lake greenstone belts (after Blackburn et al., 1991).

supracrustal belts. The greenstones themselves are almost uniformly of low metamorphic grade.

The Sturgeon Lake area covers ~2700 km^2. This area is located 76 km east of Sioux Lookout and constitutes the south-central region of figure 6.2. The area is composed chiefly of the Sturgeon Lake greenstone belt, and to a lesser extent of batholithic granitic complexes. These intrusive complexes are predominantly composed of trondhjemite and granodiorite, and limit the extent of the greenstones.

On the basis of lithology and geographic distribution, the greenstone stratigraphic succession has been subdivided into four assemblages. These assemblages are composed of several volcanic cycles. Each cycle exhibits similar composition. Lower units are mafic metavolcanics and upper unit are intermediate to felsic metavolcanics. A hiatus in volcanism, a change in chemistry, or a period of sedimentation, demarcate cycle and assemblage boundaries. Two major periods of clastic sedimentation can be distinguished.

Lower mafic volcanics are dominantly intruded by subvolcanic gabbroic and ultramafic rocks, but the same intrusive material is also extensively found in the felsic to intermediate fragmentals and clastic metasediments.

The metavolcanics, metasediments, mafic and ultramafic intrusions, and felsic epizonal intrusions are all metamorphosed. The metamorphic grade ranges from greenschist to lower amphibolite.

6.7 Geology of the Area Intersected by the Sturgeon Lake Line

The exact location of the Sturgeon Lake Line, illustrated on a detailed geologic map given in poster $2A$, coincides with the central part of the South Sturgeon Lake assemblage.

Four volcanic cycles compose the South Sturgeon Lake assemblage, and all of them are fully or partially intersected by the Sturgeon Lake Line. From the south-western to the north-eastern tip of the slalom line they are: (1) the Darkwater Lake Cycle; (2) the Claw Lake Cycle; (3) the Lyon Lake Cycle; and (4) the South Shore Cycle. Neither these volcanic cycles, nor their individual constituents called formations, are outlined on the geologic map shown in poster $2A$. The reason for not including them is that such a level of detail would obscure the general picture. Furthermore, it is highly unlikely that the boundaries between these formations and cycles could be correlated with the reflective events on the seismic images. This is because even the individual formations themselves are heterogeneous. Moreover, though the individual formations are locally continuous and can be traced from several to tens of kilometers, their boundaries are transitional, difficult to define, and subject to change. However, the very nature of the heterogeneous and highly layered South Sturgeon Lake assemblage indicates that the general structural trends could be highly reflective and therefore visible on the seismic images. Surprisingly, no dip information was available for the units. Still, one could guess that they have a generally steep dip at the surface, which is a common observation for metavolcanics in most of the greenstone belts.

The Sturgeon Lake Line (poster $2A$) crosses three distinct geologic units that are dominated by several rock types. Along the slalom line and in the northwest direction, the following rocks are encountered:

- Mafic to intermediate metavolcanics (1)[5]: massive flows, some pillowed flows, and variable to fragmental pyroclastics;
- Felsic to intermediate metavolcanics (2): lapilli-tuff and lapillistone tuff;
- Mafic to intermediate metavolcanics (1): massive flows, and some pillowed flows;
- Felsic to intermediate metavolcanics(2): lapilli-tuff and lapillistone tuff;
- Mafic to intermediate metavolcanics (1): massive flows;
- Felsic to intermediate metavolcanics (2): lapilli-tuff and lapillistone tuff, occasional quartz, feldspar and quartz-feldspar porphyry intrusions. These rocks include a geophysically determined sulphide (pyrite-pyrrhotite) $\pm$ graphite ironstone (IF);
- Metasediments (3): wacke and a geophysically determined sulphide (pyrite-pyrrhotite) $\pm$graphitic ironstone;
- Mafic to intermediate metavolcanics (1): massive flows and porphyritic flows.

Not all geological units possibly sampled by the Sturgeon Lake data necessarily lie along the slalom line. Some units away from the line might underlie the South Sturgeon Lake assemblage. Of particular importance are units that lie south of the slalom line and are included in the surface area of the 3D prestack migrated seismic image. These units are:

- The Beidleman Bay Pluton (6): an epizonal granitoid sill primarily composed of trondhjemite, and minor granodiorite and quartz-diorite. Variously it is massive, foliated and sheared. The pluton is probably a subvolcanic intrusion comagmatic with the overlying metavolcanics, and may have played a major role in the generation of the massive sulphide deposits in the overlying units;
- The Bell Lake Alkalic Complex (8): an elliptical stock, younger than the Southern Granitic Complex which it intrudes;
- The Southern Granitic Complex (7,8): in the Bell Lake area is comprised of amphibolitic mafic metavolcanics that are extensively intruded by granodiorite-trondhjemite forming layered arrays of concordant sheets.

[5]These numbers identify the same geologic units as those given for the geologic map and stratigraphic legend of the poster 2*A*.

6.8 Structure Imaged by the Sturgeon Lake Line

Images obtained by examining the Sturgeon Lake Line data (posters $2B$, $2C$, $2D$ and $2E$) exhibit good 3D control and are more informative than those gained for the Line 23 (poster 1B). This is solely attributed to the higher quality of the Sturgeon Lake Line data.

Posters $2B$, $2C$, $2D$ and $2E$, reveal much about the structure beneath and in the vicinity of the Sturgeon Lake Line. Poster $2B$ includes a standard stack ($2Ba$), an optimum cross dip stack superimposed on a cross dip color map ($2Bb$), and a suite of constant cross dip panels ($1.5-2.0$ s) covering a range of cross dips from -30^0 to $+30^0$ with a step of 10^0 ($2Bc1$ to $2Bc7$). Schematic 2D interpretation that divides the upper crust below the Sturgeon Lake Line in three regions is illustrated in poster $2C$. A set of isosurface/slice images of the main events in the 3D prestack migrated data is shown in posters ($2Da$, $2Db$ and $2Dc$). The main events are also shown in posters $2Dd$ and $2De$ but using a combination of differently oriented slices. Poster $2Ea$ is a part of the vertical slice along the slalom line extracted from the 3D prestack migrated data volume. Two featured details are highlighted on this slice by using a different color-background. The deeper one represents an economically interesting zone while the shallower one is a zone that includes the contact between the greenstones and the Beidleman Bay Pluton. Posters $2Eb$ and $2Ec$ reveal the general structure of the economically interesting zone using both an isosurface/slice presentation ($2Eb$) and a combination of slices ($2Ec$). The contact between the Beidleman Bay Pluton and the mafic to intermediate metavolcanic rocks is particularly well imaged on an oblique vertical slice shown in poster $2Ed$. For the interpretation purposes, and wherever possible/useful the surface geology intersected by the slalom line is given at the top of sections/slices.

The most striking feature characterizing Sturgeon Lake Line data is its omnipresent reflectivity (posters $2Ba$ and $2Bb$). While this observed reflectivity is all pervasive, it differs in strength and character along the profile, and even more so with depth. The strongest events (posters $2D$, $2Ba$ and $2Bc$) are recorded at later times (1.5 to 3.0 s). The deepest of them are subhorizontal (posters $2Ba$ and $2Bb$) while the shallower ones dip towards north. The maximum possible depth sampled by the data is $\sim$9 km, meaning that only the upper crust is imaged.

Based on the reflectivity patterns observed (posters $2Ba$ and $2Bb$), the upper crust in the Sturgeon Lake area can be divided into three regions (poster $2C$). The boundaries

between these seismically distinct regions are nor sharp, nor always clearly defined. However, the schematic diagram presented in poster $2C$ appears to meaningfully outline the major regions of the upper crust in the area.

Region I. This region is the least reflective of the three (posters $2Ba$ and $2Bb$). Although many shallow events are visible, only the contact between the Beidleman Bay Pluton and the greenstones seems to be imaged well, and can be directly correlated with the geologic map shown in poster $2A$. A significant increase in reflectivity is observed in the lower part of the region I (posters $2Ba$ and $2Bb$). This is particularly true for the middle of the line, where the reflectivity becomes subhorizontal. That the horizontal and mildly dipping reflectors dominate the region I is probably due to the imaging process that is biased against the steeply dipping events and makes them less apparent on the seismic sections. The reflectivity in the lower part of the region I appears to outline a synformal structure, which agrees with the gross shape of the greenstone belts.

The structures observed on the reflective images of the Sturgeon Lake Line are in a general agreement with the results obtained by gravity modeling. Seismic imaging indicates that the depth of the greenstones in the Sturgeon Lake Line area reaches a maximum of $\sim$3 km (posters $2Ba$ and $2Bb$). Gravity modeling puts the depth of the Sturgeon Lake greenstone belt at $\sim$3 km. The general dip of the events here interpreted as greenstones, for which the cross dip was determined, is mild and towards north.

Region II. This part of the upper crust exhibits some of the strongest reflectivity observed (posters $2D$, $2Bb$, and $2Ba$). The imaged parts of the reflectors almost uniformly face towards $\sim$north (posters $2D$ and $2Bb$) and generally have steep dips. Despite the uniformity of the dip direction, the dip magnitude varies from one event to another which is easily observed on the constant cross dip panels (poster $2Bc$) formed for a part ($1.5-2.0$ s) of the region II. The approximate cross dip angle is marked on the poster for many of the important events. Cross dips determined for those events take a wide range of values (from $\sim 0^0$ to $\sim -25^0$). Because the in-line dip also varies and is often quite steep, it is probable that the true dip of the events imaged has an even larger variation than the one observed for the cross dips.

As a consequence of the general dip direction towards north, most parts of the reflectors imaged in the region II lie south-east of the slalom line. Poster $2D$ provides various views at the main events using isosurface and slice images. Images presented in poster $2D$ confirm the positioning and orientation of the main events first deduced from the much faster to produce optimum cross dip stack (poster $2Bb$).

Reflectors of the region II are probably associated with the intrusive rocks south of the greenstones (see previous section and poster $2A$). On the surface these intrusives exhibit many of the necessary prerequisites for abundant reflectivity.

Region III. Only a part of the region III appears to be imaged (posters $2Ba$ and $2Bb$). This region has the strongest reflective expression among the Sturgeon Lake Line data, but this is not so apparent due to amplitude equalization processes applied. The reflectivity is subhorizontal, with the events distributed beneath and to both sides of the slalom line (poster $2Bb$). The region III could, for example, represent a large batholith or a massive gneissic domain intruded by many sills.

Detail I. Posters $2Ba$, $2Bb$ and $2Ea$, all feature the economically interesting zone highlighted dull orange in poster $2Ea$. However, none of the these 2D images ($2Ba$, $2Bb$ and $2Ea$) provides enough information to delineate the structure accurately. Cross dip stack (poster 2Bb) indicates many overlapping events meaning that the structure probably has a complicated 3D shape.

The only images (posters $2Eb$ and $2Ec$) that at least partially resolve the structure in the economically interesting zone are obtained from a small cube of data that covers the zone of interest and is extracted from the full 3D prestack migrated data volume. It is very encouraging to see that it is possible, even on this small scale, to observe that the main isosurface bodies (posters $2Eb$) clearly depict a structure. A slice view of the same structure is given in poster $2Ec$. Most of the structure outlined dips roughly towards north, and may or may not contour the target mineralization, but certainly could represent a marker horizon to which the mineralization is possibly concordant.

Detail II. The reflectivity here interpreted as the contact between the Beidleman Bay Pluton and the adjacent mafic metavolcanics, is located in the zone highlighted pink in poster $2Ea$. This zone is also visible in posters $2Ba$ and $2Bb$. In spite of that, none of these relatively small scale 2D images clearly outline the contact. The image that best captures the contact between the Beidleman Bay Pluton and the greenstones is shown in poster $2Ed$. To achieve such good sharpness of the contact image it was necessary to orient a vertical slice more directly towards the contact ($\sim$ towards south).

6.9 Summary

Seismic reflection images of the Line 23 and the Sturgeon Lake Line, obtained using the techniques developed, described, and tested in this thesis, proved indispensable during interpretation. For example, these images were necessary to:

- Outline the possible basement of the greenstones on both profiles;
- Determine the general orientation and position of the main reflectors imaged in the Sturgeon Lake Line data;
- Determine the contact between the Beidleman Bay Pluton and the greenstones;
- To delineate a small scale structure within the Sturgeon Lake Line data that is possibly related to an economic target.

But the true highlight of this chapter is that:

- The examination the images presented in posters 1 and 2 has confirmed that the imaging methods developed in this thesis have a more general potential. They can possibly help determine, more accurately than before, the structure of the crystalline terrains.

Chapter 7

Conclusions

State of the Art in Reflection Seismology

The past two decades have been characterized by enormous progress in the seismic reflection imaging of rock structures at depth. During this time the seismic reflection method has evolved from a procedure capable of imaging only simple, sedimentary basin strata to one capable of imaging highly folded and faulted sedimentary piles and the detailed lateral heterogeneity of facies changes in coastal and fluvial sedimentation. This immense increase in lateral resolving power is chiefly attributed to the development of the 3D survey methodology and prestack migration. Structure at depths of several kilometers may now be laterally resolved to much less than 100 m; quite comparable to the long obtained similar vertical resolution. Furthermore, reflection seismology has also shown itself capable of imaging features within the crystalline igneous-metamorphic rocks: formations wherein the structures are often much more complicated and at a much finer scale than in sedimentary basins. Particularly successful and extensive has been seismic reflection imaging of the whole crust of the Earth. But the past decade has also witnessed the beginning, and then a dramatic increase in seismic exploration of the upper crystalline crust for mining purposes.

In principle, the more complex the geometry of the rock structure being explored, the greater the need for 3D surveying. This is because only a large survey aperture in both horizontal directions provides a migration process with sufficient information to unravel geometrically complex structures.

Seismic reflection Imaging in Crystalline Rocks

Traditionally, the objective of 2D seismic profiling has been to produce a single, high quality zero-offset section on which 2D migration can be applied. Then, if the surveyed structures are perfectly two dimensional with plunge axis horizontal and perpendicular to the survey profile, the interpreter will have an image that is a perfect cross-section of the structure. Even if the reflectors dip at various angles across the survey profile, but the surveying is done on a straight line, this image has a clear meaning. However, for cost and access reasons, most of seismic reflection data collected in crystalline terrains has been acquired by 2D profiling, typically carried out on fairly crooked roads. When the survey geometry is significantly crooked and the structures have appreciable cross dip, several vital 2D imaging processes may severely defocus. Particularly affected are the common mid-point (CMP) stack and profile migration because both procedures require combining data from a wide range of positions on the profile (over the stacking and migration apertures). Thus, satisfactory imaging of 2D crooked line survey data has traditionally been considered problematic.

The conceptual problems posed by imaging on crooked lines are known. Mainly, they originate from the cross-profile dip of the imaged structures and/or irregular position and density of mid-points (data). Lacking specialized processing software for such problems, the typical remedy has been to record a very high density of data (high fold), and hope that averaging (stacking) over the large number of data traces will overwhelm any imaging problems.

Research Focus

But 2D crooked line data need not be looked at as a problem. In fact, a high fold 2D crooked line profiling is really a 3D survey of a swath of terrain around the "slalom" line. Still, 2D crooked line profiling should not be compared with full 3D surveys because swath 3D data are limited in quantity, have an uneven distribution and a small range of source-receiver azimuths. Nonetheless, 3D swath data generally carries at least partial 3D information about the imaged structures, and it is indeed surprising that the opportunity to extract this information has not been thoroughly exploited before this thesis. Consequently, my research objective has been:

- To explore and develop processing methods which might usefully exploit the 3D character of the crooked line data to reveal the true geometry of reflectors;

- And, where that is not practical, to find alternative ways to minimize the deleterious effect of the crooked line geometry and 3D structures on the resulting 2D seismic image.

Research Projects and Procedures

I have carried out the work by developing several unique processing programs and subsequently testing them first on synthetic and then on real data. The main new processes and their objectives are:

1. The optimum local cross dip analysis and the optimum local cross dip stack;
2. The 3D prestack migration of 2D crooked line data;
3. The amplitude stack.

1. Due to the crooked line data acquisition, bands of reflectivity across the acoustic boundaries facing the profile are recorded instead of "simple lines", as it is the case in 2D straight line data surveying. In order to make these reflectivity bands meaningful and interpretable on a 2D seismic section, they must be collapsed into single events. This is exactly what the optimum local cross dip analysis and the optimum local cross dip stack are designed for.
2. To avoid problems caused by overlapping of reflection events on a 2D section, and preserve and position accurately in 3D space the reflectivity bands recorded, a process that 3D prestack migrates 2D crooked line data was also designed.
3. But the 3D structural information can not always be extracted from the crooked line data. When this is true, a high quality image of general subsurface features and trends can be obtained by amplitude stacking. To improve the signal to noise ratio before stacking, absolute amplitudes are raised to a power between one and two.

The synthetic data used for testing the developed processes was produced by a ray-Born modeling code, also designed by myself. Seven models that range from several point diffractors up to 15 reflectors were analyzed.

Two profiles, one collected for regional crustal studies and one high resolution acquired for mining purposes, were also used for testing the new techniques on real data. Both surveys were done in the Archean Superior Province.

Specific Conclusions from the Investigations

1. If the survey geometry is consistently crooked and results in a swath data distribution (cross offset) that is at the depth of interest a significant fraction of the Fresnel Zone radius wide, 3D prestack migration will sufficiently focus the events for interpretation. Data "fed" to the migration process has to be filtered (to remove non P wave signals) and amplitude balanced. When the data exhibits poor coherence, sharper images may be obtained by migrating absolute amplitudes raised to some power (between 1 to 2). To make the migration process computationally feasible, data volume has to be reduced manyfold by partial stack prior to migration. Even still, for its widespread use, 3D prestack migration is somewhat beyond the capability of a single CPU workstation processing (e.g., 2-3 weeks of CPU for a minimal migration).

2. Although it does not output a 3D data volume like 1., the optimum cross dip stack provides most of the same interpretative information in a shorter time interval, and should be routinely applied whenever warranted by the survey geometry. The image is formed by stacking the preconditioned partial stacks at a full range of cross dips followed by determination of optimum local cross dip of most events. In addition to improved stacking, cross dip information is obtained and is used for interpretation purposes as a color background to the cross dip stack. An important quality of this combined 2D image is the relative ease with which the concentrated information is analyzed. The main limitation is that cross dip will not be correctly determined when the reflection events of different cross dip intersect each other on a common time section. The stronger events obliterate the weaker ones, or when the events are of similar strength neither of them is well imaged in the region in which they overlap. The reflective events "captured" on an optimum cross dip stack can be properly positioned in space using a special 3D poststack migration also designed in this study. In addition to the local optimum cross dip stack, this procedure requires the corresponding slowness map and the local cross-profile spread size, and is much faster than 3D prestack migration.

3. 3D prestack migration and optimum cross dip CMP bin stacking depend on phase coherence of the reflected signals. Occasionally, serious survey geometry problems, various unaccounted time anomalies and strong noise signal, may severely reduce coherency of the reflected signal. When sufficient phase coherency is lacking, a more tolerant method of combining trace signals, such as amplitude stack is, may

be the best way to identify reflectors. I show that, contrary to common opinion, amplitude time-section can be poststack migrated.

General Conclusions

The most general conclusion from this study is that it is often possible to recover the 3D geometry of reflectors seen by a 2D crooked line survey. The biggest limitation of any 2D profile is that reflectors that do not face the survey line will not produce a sufficiently strong response to be imaged. 2D seismic sections obtained by standard CMP stacking of data collected in crystalline terrains often display numerous coherent reflection events, but these events are not coherent in the profile direction for as great a distance as might be expected from diffraction theory. This peculiar reflection characteristic is partially due to interference between the reflection wavelets from numerous fortuitous "glints" in the reflecting geology, and partially, as the modeling shows, to negligence of the 3D character of the data during processing. Since it is impossible for a 2D migration based on an approximate velocity model to undo all the imaging problems compounded into a standard stacked section, it is important to find and use other measures of reflection strength in interpreting Earth structure, such as those presented in this thesis.

7.1 Suggestions for Further Research

A selection of the research topics identified during this thesis study as potentially useful, but not undertaken, is briefly presented below:

- *A comparative study of modeled and real data in an area of strong geological control.* Such an area could be, for example, a large and extensively drilled mine site. Modeled data can be produced by using: a digital 3D model of the known subsurface, a ray-Born modeling algorithm, and the acquisition geometry of the already existing, or to be acquired, seismic reflection data;

- *An imaging study of the near-vertical shallow structures commonly observed in the Archean terrains.* Near-vertical reflections are often seen buried within the first arrival refraction "train". The information that the reflections carry is generally lost during data processing. In treating the reflection profiles as poorly designed VSP surveys lies an opportunity to possibly preserve and extract shallow near-vertical events, which could represent a missing link to the mapped surface geology;

- *Surface-consistent residual static estimation by local cross-dip stack-power maximization.* One of the major set-backs of the seismic reflection imaging in crystalline terrains is its inability to quantitatively check the quality of the refraction statics determined. In other words, residual static corrections can not be successfully applied to the 2D crooked line data acquired in crystalline terrains. It would probably be useful to test the suggested method using both linear and non-linear inversion techniques;

- *Amplitude stacking and migration in 3D and VSP studies of the crystalline crust.* Acquiring 3D seismic reflection data does not mean that all of the problems that exist in 2D crooked line data become completely non-existent. Occasionally, up to two thirds of the 3D data are rejected to improve the stack in crystalline terrains. Amplitude studies (stacking and migration) similar to the ones carried out in this thesis could represent a good remedy when the 3D data does not focus well before stack.

References

Adam, E., Arnold, G., Beaudry, C., Matthews, L., Milkereit, B., Perron, G. and Pineault, R., 1997. Seismic exploration for VMS deposits, Matagami, Québec. *Proceedings of Exploration 97: Fourth Decennial International Conference on Mineral Exploration,* 433–438.

Adam, E., Perron, G., Matthews, L. and Milkereit, B., 1998. 3–D seismic data processing for mineral exploration. *1998 SEG Expanded Abstracts.*

Aki, K. and Richards, P. G., 1980. Quantitative seismology. Volume I, Theory and methods. *W. H. Freeman and Company*, USA.

Bancroft, J. C., Geiger, H. D. and Margrave, G. F., 1998. The equivalent offset method of prestack time migration. *Geophysics,* **63(6)**, 2042–2053.

Barry, K. M., 1967. Delay time and its application to refraction profile interpretation. *Seismic Refraction Prospecting, Editor: Musgrave, A. W.* Tulsa, USA, 348–361.

Bennett G., Dressler, B. O. and Robertson, J. A, 1991. The Huronian Supergroup and associated intrusive rocks; in Geology of Ontario, *Ontario Geological Survey, Special Volume 4, Part I*, 549–592.

Berkhout, A. J., 1980. Seismic migration - Imaging of acoustic energy by wave field extrapolation. *Amsterdam/ New York, Elsevier Publishing Company,* Holland.

Blackburn, C. E., Johns, G.W., Ayer, J. and Davis, D. W., 1991. Wabigoon Subprovince; in Geology of Ontario, *Ontario Geological Survey, Special Volume 4, Part I*, 303–382.

Boggs, S. Jr., 1987. Principles of sedimentology and stratigraphy. *Merrill Publishing Company*, USA.

Card, K. D. and Ciesielski, A., 1986. Subdivisions of the Superior Province of the Canadian Shield. *Geoscience Canada*, **13:** 5–13.

Červený, V. and Ravindra, R., 1971. Theory of seismic head waves. *University of Toronto Press*, Canada.

Červený, V., 1972. Seismic rays and ray intensities in inhomogeneous anisotropic media. *Geophys. J. R. astr. Soc.*, **29**, 1–13.

Chapman, C. h., 1981. Generalized radon transforms and slant stacks. *Geophys. J. R. astr. Soc.,* **66,** 445–453.

Claerbout, J. F., 1985. Imaging the Earth's interior. *Blackwell Scientific Publications.*

Clowes, R. M., Kanasewich, E. R. and Cumming, G. L., 1968. Deep crustal seismic reflections at near-vertical incidence. *Geophysics,* **33(3),** 441–451.

Clowes, R. M. and Kanasewich, E. R., 1970. Seismic attenuation and the nature of reflecting horizons within the crust. *Journal of Geophysical Research,* **75(32),** 6693–6705.

Clowes, R. M. and Kanasewich, E. R., 1971. Digital filtering of deep crustal seismic reflections. *Canadian Journal of Earth Sciences,* **9,** 434–451.

Clowes, R. M., (editor) 1984. LITHOPROBE phase I proposal. LITHOPROBE - A coordinated national geoscience project. *The Geosci. Can.,* **11,** 122–126.

Clowes, R. M., (editor) 1989. LITHOPROBE phase III proposal - The evolution of a continent. *Published by the LITHOPROBE secretariat, The University of British Columbia, Vancouver, B.C.* 213 pages.

Clowes, R. M., (editor) 1993. LITHOPROBE phase IV proposal - Studies of the evolution of a continent. *Published by the LITHOPROBE secretariat, The University of British Columbia Vancouver, B.C.,* 290 pages.

Clowes, R. M., (editor) 1997. LITHOPROBE phase V proposal - Evolution of a continent revealed. *Published by the LITHOPROBE secretariat, The University of British Columbia, Vancouver, B.C.* 292 pages.

Cocker, J., Urošević, M. and Evans, B., 1997. A high resolution seismic survey to assist in mine planning. *Proceedings of Exploration 97: Fourth Decennial International Conference on Mineral Exploration,* 473–476.

Condie, K. C., 1981. Archean greenstone belts. Developments in Precambrian Geology 3. *Elsevier Scientific Publishing Company*, Amsterdam, The Netherlands, 434 pages.

Condie, K. C., 1994a. Introduction; in Archean crustal evolution (edited by: Condie, K. C.). Developments in Precambrian Geology 11. *Elsevier Science B. V.*, Amsterdam, The Netherlands, 1–10.

Condie, K. C., 1994b. Greenstones through time; in Archean crustal evolution (edited by: Condie, K. C.). Developments in Precambrian Geology 11. *Elsevier Science B. V.*, Amsterdam, The Netherlans, 85–120.

Corfu, F., Krough, T. E., Kwok, Y. Y. and Jensen, L. S., 1989. U-Pb zircon geochronology in the southwestern Abitibi greenstone belt, Superior Province. *Can. J. Earth Sci.*, **26:** 1747–1763.

Curtis, J. W., 1975. A multi-trace synthetic seismogram generator. *Bulletin of the Australian Society of Exploration Geophysicists*, **6(4)**, 91–99.

Dahl-Jensen, T., 1989. Static corrections on crystalline rocks. *Geophysical Prospecting,* **37,** 467–478.

Dimroth, E., Imreh, L., Rocheleau, M. and Goulet, N., 1982. Evolution of the south-central part of the Archean Abitibi belt, Quebec. Part I: Stratigraphy and paleogeographic model. *Can. J. Earth Sci.*, **19:** 1729–1758.

Dimroth, E., Imreh, L., Goulet, N. and Rocheleau, M., 1983a. Evolution of the south-central part of the Archean Abitibi belt, Quebec. Part II: Tectonic evolution and geomechanical model. *Can. J. Earth Sci.*, **20:** 1355–1373.

Dimroth, E., Imreh, L., Goulet, N. and Rocheleau, M., 1983b. Evolution of the south-central part of the Archean Abitibi belt, Quebec. Part III: Plutonic and metamorphic evolution and geotectonic model. *Can. J. Earth Sci.*, **20:** 1374–1388.

Dix, C. H., 1955. Seismic velocities from surface measurements. *Geophysics,* **20(1),** 68–86.

Dix, C. H., 1965. Reflection seismic crustal studies. *Geophysics,* **30(6),** 1068–1084.

Dobrin, M. B. and Savit, C. H., 1988. Introduction to geophysical prospecting. *McGraw–Hill, Inc.*

Dohr, G. and Fuchs, K., 1967. Statistical evaluation of deep crustal reflections in Germany. *Geophysics,* **33(6),** 951–967.

Eaton, D. W., Milkereit, B. and Adam, E., 1997. 3D seismic exploration. *Proceedings of Exploration 97: Fourth Decennial International Conference on Mineral Exploration,* 65–78.

Eaton, D. W., 1999. Weak elastic-wave scattering from massive sulphide ore bodies *Geophysics,* **64(1)**, 289–299.

Ewing M. W., Jardetzky, W. S. and Press, F., 1957. Elastic waves in layered media. In international series in the Earth sciences, *McGraw-Hill Book Company, Inc.,* USA.

Farrell, R. C. and Euwema, R. N., 1984. Refraction Statics. *Proceedings of the IEEE,* **72(10)**, 1316–1329.

Faria, E. L. and Stoffa, P. L., 1994. Traveltime computation in transversly isotropic media. *Geophysics,* **59(2)**, 272–281.

Fuchs, K., Kozlovsky, Ye. A., Kristov, A. I. and Zoback, M. D. (editors), 1990. Super–deep continental drilling and deep geophysical sounding. Kozlovsky, Ye. A. - The USSR integrated program of continental crust investigations and studies of the Earth's deep structure under the "GLOBUS" project. *Sprenger - Verlag Berlin Heidelberg,* 90–103.

Garland, G. D., (editor), 1986. LITHOPROBE phase II proposal - The third dimension. A coordinated national geoscience project. *Published by the LITHOPROBE secretariat, The University of British Columbia, Vancouver, B.C.,* 140 pages.

Geiger, H. D., 1995. Prestack migration of crustal data using common scatter point (CSP) migration technique. *LSPF Newsletter,* **8(1),** 79–81.

Geiger, H. D., Bancroft, J. C. and Foltinek, D., 1995. Prestack migration of crustal data using common scatterpoint (CSP) migration technique. *Canadian Society of Exploration Geophysicists National Convention, Expanded Abstracts* 49–50.

Goodwin, A. M., 1981. Achean plates and greenstone belts; in Precambrian Plate Tectonics (edited by: Kröner, A.). Developments in Precambrian Geology 4. *Elsevier Scientific Publishing Company,* Amsterdam, The Netherlans, 105–135.

Green, A., Milkereit, B., Percival, A., Davidson, A., Parrish, R., Cook, F., Geis, W., Cannon, W., Hutchinson, D., West, G. F. and Clowes R. M., 1990. Origin of deep crustal reflections: seismic profiling across high–grade metamor-

phic terrains in Canada. *Tectonics, Elsevier Science Publishers B.V., Amsterdam,* **173:** 627–638.

Green, A., Milkereit, B., Mayrand, L. J., Ludden, J. N., Hubert, C., Jackson, S. L., Sutcliffe, R. H., West, G. F., Verpaelst, P. and Simard, A., 1990b. Deep structure of an Archean greenstone terrane. *Nature*, **344:** 327–330.

Guest, W. S and Kendall, J-M., 1993. Modeling seismic waveforms in anisotropic inhomogeneous media using ray and Maslov asymptotic theory: applications to exploration seismology. *Canadian Journal of Exploration Geophysics,* **29(1),** 78–92.

Hajnal, Z., Annesley, I. R., White, D., Matthews, R. B., Sopuck, V., Koch, R., Leppin, M. and Ahuja, S., 1997. Sedimentary-hosted mineral deposits: a high-resolution seismic survey in the Athabasca Basin. *Proceedings of Exploration 97: Fourth Decennial International Conference on Mineral Exploration,* 421–432.

Hagedoorn, J. G., 1954. A process of seismic reflection interpretation. *Geophysical Prospecting,* **2**, 85–127.

Hale, D., 1984. Dip-moveout by Fourier transform. *Geophysics,* **49(6)**, 741–757.

Hawkins, L. V., 1961. The reciprocal method of routine shallow seismic refraction investigations. *Geophysics,* **26(6)**, 806–819.

Huang, T. S., Yang, G. J. and Tang, G. Y., 1979. A fast two-dimensional median filtering algorithm. *IEEE Transactions on Acoustics, Speech, and Signal Processing,* **ASSP-27(1))**, 13–18.

Hubral, P., 1977. Time migration - some ray theoretical aspects. *Geophysical Prospecting,* **25**, 738–735.

Humblin, K. W., 1991. Introduction to physical geology. *Macmillan Publishing Company,* New York, USA.

Jackson, L. S., Sutcliffe, R. H., Ludden, J. N., Hubert, C., Green, A. G., Milkereit, B., Mayrand, L., West, G. F. and Verpaelst, P., 1990. Southern Abitibi greenstone belt: Archean crustal structure from seismic-reflection profiles. *Geology*, **18:** 1086–1090.

Jackson S. L. and Fyon, J. A, 1991. The western Abitibi Subprovince in Ontario; in Geology of Ontario, *Ontario Geological Survey, Special Volume 4, Part I*, 405–484.

Jackson S. L., Cruden, A. R., White, D. and Milkereit, B., 1995. A seismic-reflection-based regional cross section of the southern Abitibi greenstone belt, *Can. J. Earth Sci.*, **(32)**, 135–148.

Jeffreys, H. Sir, 1950. The Earth: it's origin, history, and physical constitution. *4th edition, Cambridge University Press,* U.K.

Jensen, L. S., 1978. No. 10 Regional stratigraphy and structure of the Timmins-Kirkland Lake area, District of Cochran and Timiskaming and the Kirkland Lake-Larder Lake area, District of Timiskaming; In Summary of field work. *Ontario Geological Survey, Miscellaneous Paper*, **82:** 67–82.

Julian, B. R. and Gubbins, D., 1977. Three-dimensional seismic ray tracing. *Journal of Geophysical Research,* **43,** 95–113.

Junger, A., 1951. Deep reflections in Big Horn Country, Montana. *Geophysics,* **16**, 499–505.

Kanasewich, E. R., 1981. Time sequence analysis in geophysics. *The University of Alberta Press, Third Edition*, Canada.

Kanasewich, E. R. and Cumming, G.L., 1965. Near-vertical-incidence seismic reflections from the Conrad "discontinuity". *Journal of Geophysical Research,* **70(14),** 3441–3446.

Kendall, J-M., 1991. Contributions to the theory and modeling of seismic waves in anisotropic inhomogeneous media with applications to subduction zones. *Ph.D. Thesis, Queen's University, Kingston, Canada.*

Kim, S., 1999. ENO-DNO-PS: a stable, second-order accuracy eikonal solver. *Expanded Abstracts of the* 69th *Annual Meeting of the Society of Exploration Geophysicists, Houston, Texas,* **v1**, 1747–1750.

Klemperer, S. L., 1987a. A relation between continental heat flow and the seismic reflectivity of the lower crust. *Journal of Geophysics,* **61,** 1–11.

Klemperer, S. L. and the BIRPS group 1987b. Reflectivity of the crystalline crust: hypotheses and tests. *Geophys. J. R. astr. Soc.,* **89,** 217–222.

Kock, W. E., 1973. Radar, Sonar and Holography. *Academic Press, Inc.*, USA.

Kröner, A., 1981. Introduction; in Precambrian Plate Tectonics (edited by: Kröner, A.). Developments in Precambrian Geology 4. *Elsevier Scientific Publishing Company*, Amsterdam, The Netherlans, VII–VIII.

Larner, K. L., Gibson, B., Chambers, R. and Wiggins, R. A., 1979. Simultaneous estimation of residual statics and crossdip time corrections. *Geophysics*, **44(7)**, 1175–1192.

Leclair, A. D., Percival, J. A., Green, A. G., Jianjun, W., West, G. F. and Wang, W., 1994. Seismic reflection profiles across the Kapuskasing uplift. *Can. J. Earth Sci.*, **31**, 1016–1026.

Levin, F. K., 1971. Apparent velocity from dipping interface reflections. *Geophysics*, **36(3)**, 510–516.

Liner, C. L. and Bleistein, N. 1988. Comparative anatomy of common offset dip moveout. *Expanded Abstracts of the* 58th *Annual Meeting of the Society of Exploration Geophysicists, Anaheim, California*, **v2**, 1101–1105.

Liner, C. L., 1990. General theory and comparative anatomy of dip moveout. *Geophysics*, **55(5)**, 595–607.

Matthews, D. and Smith, C., 1987. Preface: deep seismic reflection profiling of the continental lithosphere. *Geophys. J. R. astr. Soc.,* **89,** VII–XII.

Mayne, H. W., 1962. Common reflection point horizontal data stacking techniques. *Geophysics,* **27(6)**, 927–938.

Mayrand, L. J. and Milkereit, B., 1988. Automated editing and true-amplitude stacking of seismic data. *Can. J. Earth. Sci.,* **25,** 1811–1823.

McCamy, K., Meyer, R. P. and Smith, T. J., 1962. Generally applicable solutions of Zoeppritz' amplitude equations. *Bulletin of the Seismological Society of America,* **52(4)**, 923–955.

McFadden, P. L., Drummond, B. J. and Kravis, S., 1986. The Nth-root stack: Theory, applications, and examples. *Geophysics,* **51(10)**, 1879–1892.

MERQ - OGS, 1984. Lithostratigraphic map of the Abitibi Subprovince; Ontario Geological Survey/Ministére de l'Énergie et des Ressources, Québec; 1:500000; catalogued as "Map 2484" in Ontario and "DV 83 - 16" in Québec.

Miles, J. W., 1960. Scattering of elastic waves by small inhomogeneities. *Geophysics,* **25(3)**, 642–648.

Milkereit, B, Berrer, E. K., Watts, A. and Roberts, B., 1997. Development of 3D seismic exploration technology for Ni-Cu deposits, Sudbury Basin. *Proceedings of Exploration 97: Fourth Decennial International Conference on Mineral Exploration,* 439–448.

Nedimović, M. R., Wang. W. and West, G. F., 1998. Focusing problems in reflection imaging of the crust. *8th International Symposium on Deep Seismic Profiling of the Continents and their Margins, Barcelona, Spain, Abstract Volume,* 42.

Nedimović, M. R. and West, G. F., 1999. Processing seismic reflection data from high fold, crooked line surveys in crystalline geological terrain. *Expanded Abstracts of the* 69th *Annual Meeting of the Society of Exploration Geophysicists, Houston, Texas,* **v2**, 1437–1440.

Nedimović, M. R. and West, G. F., 2000. Migrating 2D crooked line seismic reflection data from crystalline geological terrain. *Expanded Abstracts of the* 70th *Annual Meeting of the Society of Exploration Geophysicists, Calgary, Alberta,* In press.

Neidell, S. N., and Taner, T. M., 1971. Semblance and other coherency measures for multichannel data. *Geophysics*, **36**, 482–497.

OGS Map 2442, 1980. Sioux Lookout-Armstrong; in Geological Compilation Series, Kenora and Thunderbay Districts, Ontario Geological Survey, Ministry of Natural Resources; Scale 1:253440.

Pflug, K. A., Mwenifumbo, C. J. and Killeen, P.G., 1997. Full waveform acoustic logging applications in mineral exploration and mining. *Proceedings of Exploration 97: Fourth Decennial International Conference on Mineral Exploration,* 477–480.

Pretorius, C. C., Trewick, W. F. and Irons, C., 1997. Application of 3D seismics to mine planning at Vaal Reefs Gold Mine, Number 10 Shaft, Republic of Southern Africa. *Proceedings of Exploration 97: Fourth Decennial International Conference on Mineral Exploration,* 399–408.

Russell, B. H., 1989. Static corrections - a tutorial. *CSEG Recorder,* **v14)**, 16–30.

Richter, C. F., 1958. Elementary seismology. In series of books on geology, *San Francisco, W. H. Freeman*, USA.

Ricker, N., 1944. Wavelet functions and their wavelets. *Geophysics,* **9**, 314–323.

Ricker, N., 1953. The form and laws of propagation of seismic wavelets. *Geophysics,* **18**, 10–40.

Roberts, B., Zaleski, E., Adam, E., Perron, G., Petrie, L., Darch, W., Salisbury, M. H., Eaton, D. and Milkereit, B., 1997. Seismic exploration of the Manitouwadge Greenstone Belt, Ontario. *Proceedings of Exploration 97: Fourth Decennial International Conference on Mineral Exploration,* 451–454.

Ronen, J. and Claerbout, J. F., 1985. Surface-consistent residual static estimation by stack-power maximization. *Geophysics,* **50(12)**, 2759–2767.

Rothman, D. H., 1985. Nonlinear inversion, statistical mechanics, and residual statics estimation. *Geophysics,* **50(12)**, 2784–2796.

Rothman, D. H., 1986. Automatic estimation of large residual static corrections. *Geophysics,* **51(2)**, 332–346.

Rudnick, R. L. and Fountain, D. M., 1995. Nature and composition of the continental crust: a lower crustal perspective. *Reviews of Geophysics.* **33(3),** 267–309.

Ryan, H., 1994. Richer, Ormsby, Klauder, Butterworth - a choice of wavelets. *CSEG Recorder,* **v(19)**, September issue, 8–9.

Salisbury, M. H., Milkereit, B. and Bleeker, W., 1996. Seismic imaging of massive sulfide deposits: part I. Rock properties. *Economic Geology and the Bulletin of the Society of Economic Geologists,* **91,** 821–828.

Salisbury, M. H., Milkereit, B., Ascough, G. L., Schmitt, D. and Matthews, L., 1997. Physical properties and seismic imaging of massive sulphides. *Proceedings of Exploration 97: Fourth Decennial International Conference on Mineral Exploration,* 383–390.

Schneider, W. A., 1978. Integral formulation for migration in two and three dimensions. *Geophysics,* **43(1)**, 49–76.

Schneider, W. A. Jr., Kurt, A., Balch, A. H. and Kruse, C., 1992. A dynamic programming approach to first arrival traveltime computation in media with arbitrary

distributed velocities. *Geophysics,* **57(1)**, 39–50.

Siahkoohi, H. R., 1997. 3D seismic imaging of complex structures in near-surface deposits. *Ph.D. thesis, University of Toronto, Toronto, Canada.*

Shearman E. D. R. and Clarke, J., (editors) 1988. Radar development to 1945. *IEEE Radar, Navigation and Avionics Series 2.* Peter Peregrinus Ltd., London, United Kingdom. 8–13.

Smithson, S. B., Shive, P. N. and Brown, S. K., 1977. Seismic reflections from Precambrian crust. *Earth and Planetary Science Letters,* **37,** 333–338.

Steeples, D. W. and Miller, R. D., 1990. Seismic reflection methods applied to engineering, environmental, and groundwater problems. In Geotechnical and Environmental Geophysics; Volume I: Review and Tutorial, Edited by Ward, S. H. Series: Investigations in Geophysics, Volume 5; Neitzel, E. B., Series Editor. 1–30.

Stevenson, F. and Durrheim, R. J., 1997. Reflection seismics for gold, platinum and base metal exploration and mining in Southern Africa. *Proceedings of Exploration 97: Fourth Decennial International Conference on Mineral Exploration,* 391–398.

Stokes, W. L. and Judson, S., 1968. Introduction to geology: physical and historical. *Prentice-Hall, Inc.,* New Jersey, USA.

Taner, M. T., and Koehler, F., 1969. Velocity spectra - digital computer derivation and applications of velocity functions. *Geophysics,* **34(6),** 859–881.

Taner, M. T., Koehler, F. and Alhilali, K. A., 1974. Estimation and correction of near-surface time anomalies. *Geophysics,* **39(4),** 441–463.

Taner, M. T., Koehler, F., 1981. Surface consistent corrections. *Geophysics,* **46(1),** 17–22.

Thurston, P. C, 1991. Archean geology of Ontario: introduction; in Geology of Ontario, *Ontario Geological Survey, Special Volume 4, Part I*, 73–80.

Thurston, P. C., 1994. Archean volcanic patterns; in Archean crustal evolution (edited by: Condie, K. C.). Developments in Precambrian Geology 11. *Elsevier Science B. V.*, Amsterdam, The Netherlans, 45–84.

Trowell, N. F., 1983. Geology of the Sturgeon Lake area, Districts of Thunder Bay and Kenora; *Ontario Geological Survey Report 221. Accompanied by Maps 2456, 2457,*

and 2458, scale 1:50000, 1 Chart, and 1 sheet of Microfiche, 97 pages.

Urošević, M. and Juhlin, C., 1997. Information from walk-away VSP and cross-hole data using various wave modes: Tower Colliery, South Sydney Basin. *Proceedings of Exploration 97: Fourth Decennial International Conference on Mineral Exploration,* 461–466.

Vidale, J., 1988. Finite-difference calculation of travel times. *Bulletin of the Seismological Society of America,* **78(6)**, 2062–2076.

Vidale, J., 1990. Finite-difference calculation of traveltimes in three dimensions. *Geophysics,* **55(5)**, 521–526.

Vidale, J. and Houston, H., 1990. Rapid calculation of amplitudes. *Geophysics,* **55(11)**, 1504–1507.

Walton, G. G., 1972. Three dimensional seismic method. *Geophysics,* **37(3)**, 417–430.

Wang, W. and West, G. F., 1993. Signal enhancement and dip correction of stacking velocity spectra. *Geophysics Labs internal report, Department of Physics, University of Toronto.*

Wang, W. and West, G. F., 1991. F-X filters with dip rejection. *Expanded Abstracts of the* 61th *Annual Meeting of the Society of Exploration Geophysicists, Houston, Texas,* **(v2)**, 1436–1438.

Wang, W. and West, G. F., 1991b. Stacking Processes of Crooked Lines Using the SUN/INSIGHT System. *LSPF Newsletter* **4:** 13–18.

Widess, M. B. and Taylor, G. L., 1959. Seismic reflections from layering within the Precambrian basement complex, Oklahoma. *Geophysics,* **24(3)**, 417–425.

Widess, M. B., 1973. How thin is a thin bed? *Geophysics,* **38(6)**, 1176–1180.

Wiggins, R. A., Larner, K. L. and Wisecup, R. D., 1972. Residual statics analysis as a general linear inverse problem. *Geophysics,* **41(5)**, 922–938.

Williams, H. R., Scott, G. M., Sutcliffe, R. H., Bennett, G., Easton, R. M. and Armstrong D. K., 1992. Tectonic evolution of Ontario: summary and synthesis; in Geology of Ontario, *Ontario Geological Survey, Special Volume 4, Part 2*, 1255 - 1324.

Windley, B. F, 1981. Precambrian rocks in the light of the plate tectonic concept; in Precambrian Plate Tectonics (edited by: Kröner, A.). Developments in Precambrian Geology 4. *Elsevier Scientific Publishing Company*, Amsterdam, The Netherlans, 1–20.

Wu, R-S. and Aki, K., 1985. Scattering characteristics of elastic waves by an elastic heterogeneity. *Geophysics,* **50(4)**, 582–595.

Wu, R-S., 1989. The perturbation method in elastic wave scattering *Pure and Applied Geophysics,* **131(4)**, 605–637.

Yilmaz, O., 1987. Seismic data processing. *Series: Investigations in Geophysics, Volume 2, Society of Exploration Geophysicists*, USA.

Appendix A

Ray-Born Method

Ray-Born method combines principles and ideas found in the asymptotic ray theory and the Born scattering approximation. Here, a brief introduction to both asymptotic ray theory and Born scattering approximation are presented. This is preceded by the wave equation in time and frequency domain, and followed by the ray-Born algorithm used to model data in this thesis.

For the purpose of seismic studies, body forces like gravity are very small in comparison to inner stresses so they may be neglected. Furthermore, all motion is a very small perturbation from equilibrium position. Accordingly, the general equation of motion may be reduced to the wave equation in inhomogeneous anisotropic and purely elastic media:

$$\frac{\partial}{\partial x_i}\left[c_{ijkl}(\mathbf{x})\frac{\partial u_k(\mathbf{x},t)}{\partial x_l}\right] = \rho(\mathbf{x})\frac{\partial^2 u_j(\mathbf{x},t)}{\partial t^2}, \tag{A.1}$$

where u is the particle displacement, c_{ijkl} is the elasticity tensor, ρ is density, $\mathbf{x}$ is the position vector and t is time.

Using the Fourier transform time domain differentiation theorem; $f'(t) \leftrightarrow iwF(w)$, provided that $f(t) \to 0$ as $t \to \pm\infty$, wave equation A.1 may be written in frequency (w) domain as:

$$\frac{\partial}{\partial x_i}\left[c_{ijkl}(\mathbf{x})\frac{\partial \hat{u}_k(\mathbf{x},w)}{\partial x_l}\right] - w^2\rho(\mathbf{x})\hat{u}_j(\mathbf{x},w) = 0. \tag{A.2}$$

A.1 Asymptotic Ray Theory

Asymptotic ray theory can perhaps be thought of as a collection of verifiable intuitive ideas and approximations (Aki and Richards, 1980). Body waves travel with a local propagation velocity along the "ray paths" determined by Snell's law. The amplitude of the body waves arriving as a "wavefront" is determined by geometrical spreading. In the asymptotic ray method, intuition enters strongly even at the initial stage, at which a solution to the wave equation is sought in the form of an asymptotic series:

$$\hat{u}_k(\mathbf{x}, w) = \sum_{n=0}^{\infty} \frac{U_k^{(n)}(\mathbf{x})}{(-iw)^n} e^{iw\tau(\mathbf{x})}, \tag{A.3}$$

where $\tau(\mathbf{x})$ is the phase function or the travel time, and $U_k^{(n)}$ are the amplitude coefficients of the ray series.

Because the solution to the wave equation A.3 is expressed as an asymptotic expansion in inverse powers of frequency, it yields best results for high frequencies. Unfortunately it is not possible to derive a precise formula relating the frequency and degree of accuracy of the results for a given number of terms in the ray series (Červený and Ravindra, 1971). By substituting only the first term of the series A.3 into equation A.2 and collecting terms in powers of w the following is obtained:

$$-w^2 \left[c_{ijkl} U_k^{(0)} p_i p_l - \rho U_j^{(0)}\right] + iw \left[c_{ijkl} \frac{\partial U_k^{(0)}}{\partial x_l} p_i + \frac{\partial}{\partial x_i}(c_{ijkl} U_k^{(0)} p_l)\right] + \left[\frac{\partial}{\partial x_i}(c_{ijkl} \frac{\partial U_k^{(0)}}{\partial x_l})\right] = 0, \tag{A.4}$$

where $p_i(\mathbf{x}) = \partial\tau(\mathbf{x})/\partial x_i$ is the slowness vector that is normal to the wavefront $\tau(x_i) = constant$, and U_k^0, ρ, and c_{ijkl} continue to be functions of the position $(\mathbf{x})$. Since A.4 must hold for any value of w, the coefficients of each power must vanish. Therefore,

$$(a_{ijkl} p_i p_l - \delta_{jk}) U_k^{(0)} = 0, \tag{A.5}$$

taking into account that $a_{ijkl} = c_{ijkl}/\rho$. Equation A.5 is the well known *eikonal equation* (Červený and Ravindra, 1971). A non-trivial solution for $U_k^{(0)}$ of equation A.5 requires that,

$$\det|a_{ijkl} p_i p_l - \delta_{jk}| = 0. \tag{A.6}$$

Using $p_i = n_i/v_n$, where v_n is the normal or phase velocity of the wavefront (velocity in the direction perpendicular to the wavefront), and multiplying A.6 through by v_n^2 gives,

$$\det|n_i n_l a_{ijkl} - v_n^2 \delta_{jk}| = 0. \tag{A.7}$$

This characteristic equation is cubic with respect to v_n^2, with three real roots corresponding to a quasi-compressional ($qP-$) wave and two quasi-shear ($qS-$) waves (Kendall, 1991). The prefix "quasi" simply refers to the polarizations of these wave types not being exactly parallel (P-waves) or orthogonal (S-waves) to the ray directions (Guest and Kendall, 1993). There exist three wave "sheets" that agree with a propagating P-wave, fast S-wave and slow S-wave. Most often the direction in which the energy is transmitted, that coincides with the direction the wavefront moves and also represents the ray direction, is not perpendicular to the wavefront. The group or total velocity of a surface-area element of the wavefront v_i, that defines the direction of the energy transport, satisfies:

$$v_i p_i = \frac{|v_i| \cos i}{v_n} = 1. \tag{A.8}$$

In ray-tracing, the direction of particle motion is also of interest.

In an inhomogeneous isotropic medium, the elasticity tensor c_{ijkl} has a special form, and A.6 may be expressed as:

$$\left(\nabla\tau \cdot \nabla\tau - \frac{\rho}{\lambda + 2\mu}\right)\left(\nabla\tau \cdot \nabla\tau - \frac{\rho}{\mu}\right) = 0. \tag{A.9}$$

That is, τ satisfies the *eikonal equation*

$$(\nabla\tau)^2 = \frac{1}{c^2}, \tag{A.10}$$

where c is either the local P-wave speed, $\alpha = \sqrt{(\lambda(\mathbf{x}) + 2\mu(\mathbf{x}))/\rho(\mathbf{x})}$, or the local S-wave speed, $\beta = \sqrt{\mu(\mathbf{x}))/\rho(\mathbf{x})}$.

Since $p_i = \partial\tau/\partial x_i$, both *eikonal equations* A.5 and A.10 may be regarded as nonlinear, first-order partial differential equations for the wavefront or phase function or *eikonal* $\tau(\mathbf{x})$. In the asymptotic ray method, the travel time $\tau(\mathbf{x})$ is usually found by first deriving a set of 6 ordinary differential equations called the *ray equations*, from the partial differential equations A.5 or A.10. The set of six ordinary differential equations may then be solved using various methods of numerical integration. The development of these *ray equations* and the methods of solving them can, for example, be found in Červený and Ravindra (1971), Červený (1972), Julian and Gubbins (1977), Aki and Richards (1980), Kendall (1991), and Guest and Kendall (1993).

The equations (A.4 through A.10) are derived for the simplest asymptotic technique called geometrical or zeroth-order ray theory (ZRT). While ZRT is valid for a laterally varying media, it breaks down for certain interesting signals such as caustics, grazing

rays and head waves. To describe the head waves, first-order terms of the solution to the wave equation must be considered also (Červený and Ravindra, 1971).

In this thesis, crooked line geometries of existing profiles, and reflectors having the size assumed to be frequently found in crystalline terrains, were combined to model data. Because modeling using the Born approximation is always computationally heavy, and the velocities in crystalline terrains are quite homogeneous at large scales, ZRT for the case of an isotropic homogeneous medium was used to compute travel time ($\tau(\mathbf{x})$) of the P-wave arrivals. The *eikonal equation* A.10 for an isotropic homogeneous medium reduces to:

$$\tau = \frac{r}{\alpha}, \tag{A.11}$$

where r is the distance the ray traveled from the source, via reflector, to the receiver. At no computational expense, a horizontally stratified medium can be approximated by substituting in A.11 P-wave speed of the medium, α, with α_{rms}, the vertical root mean square velocity (Taner and Koehler, 1969). Approximating travel times in a medium with horizontal or very mildly dipping reflectors using the RMS velocity is valid only as long as the source-receiver offsets are relatively small when compared to the depth of the reflectors of interest.

In the last decade, many alternative methods for solving the *eikonal equation* based on the finite-differences or Fermat's principle have been developed. The driving force behind the activity has been the need to build efficient depth migrators, without compromising accuracy. Some of the valuable work done on the fast *eikonal* solvers was published by Vidale (1988 and 1990), Schneider et. al. (1992), Faria and Stoffa (1994) and Kim (1999). Would there be a need to expand the application of the ray-Born method developed in this thesis to inhomogeneous and/or anisotropic media, a good choice would be to incorporate one of the efficient *eikonal* solvers found in the referenced work.

When modeling, ray intensities are as important as travel times. To determine the amplitude of the ray solution, $U_k^{(0)}$, the w term in equation A.4 must be considered. For the anisotropic inhomogeneous media the *transport equation* is obtained by setting the coefficient of w to zero,

$$a_{ijkl}\frac{\partial U_k^{(0)}}{\partial x_l}p_i + \frac{1}{\rho}\frac{\partial}{\partial x_i}(a_{ijkl}U_k^{(0)}p_l) = 0. \tag{A.12}$$

After much work, a system of twelve ordinary differential equations, called *geometrical spreading equations*, can be derived from the *transport equation* A.12 (Guest and Kendall,

1993). Though somewhat simpler, the derivation of the *geometrical spreading equations* for the isotropic inhomogeneous media is also very involving. To obtain the ray intensities, this system of ordinary differential equations is solved numerically. For information on how to derive and solve *geometrical spreading equations* please consider the afore mentioned references for *ray equations*.

Because only a homogeneous isotropic media were considered in this thesis, amplitudes of the rays were scaled by the distance the rays traveled, i.e., $U_k^{(0)} \propto 1/r$. Again, would there be a need to expand the application of the ray-Born method developed in this thesis to inhomogeneous and/or anisotropic media, a good choice would be to incorporate one of the efficient, but less accurate solvers of the *transport equation* (e.g. Vidale and Houston, 1990).

A.2 Born Approximation for Weak Scattering

Abundant literature on the application of Born approximation in seismology, for modeling elastic-wave phenomena, can readily be found (see, for example, Miles, 1960, Wu and Aki, 1985, Wu, 1989, Eaton, 1999, and references therein). Here, an abbreviated derivation of Born scattering that closely follows the one presented by Eaton (1999), is presented because of its compactness.

Wave equation A.2 in the frequency domain, can be expressed in a compressed form by using the tensor notation

$$\rho(\mathbf{x})w^2\hat{u}_j(\mathbf{x},w) + [c_{ijkl}(\mathbf{x})\hat{u}_{k,l}(\mathbf{x},w)]_{,i} = 0, \tag{A.13}$$

where single subscripts denote components of a vector, multiple subscripts components of a tensor, subscripts following a comma indicate differentiation with respect to the corresponding Cartesian coordinate, and repeated subscripts imply a summation according to the usual convention.

Let us focus on the case of an isotropic medium, that is either a homogeneous or a slowly varying continuum. We may refer to it as a reference medium. Such a medium is characterized by the density $\rho^0(\mathbf{x})$ and a considerable simplified elasticity tensor $c^0_{ijkl}(\mathbf{x})$,

$$c^0_{ijkl}(\mathbf{x}) = \lambda^0(\mathbf{x})\delta_{ij}\delta_{kl} + \mu^0(\mathbf{x})(\delta_{ik}\delta_{jl} + \delta_{il}\delta_{jk}), \tag{A.14}$$

where $\lambda^0(\mathbf{x})$ and $\mu^0(\mathbf{x})$ are two independent constants known as the Lamé coefficients, and δ_{mn} is the Kronecker delta. Assume that a reference or primary wave field is a known

solution to

$$\rho^0(\mathbf{x})w^2\hat{u}^0_j(\mathbf{x},w) + [c^0_{ijkl}(\mathbf{x})\hat{u}^0_{k,l}(\mathbf{x},w)]_{,i} = 0. \tag{A.15}$$

Furthermore, suppose an arbitrary heterogeneity with the parameters

$$\begin{aligned} \rho(\mathbf{x}) &= \rho^0(\mathbf{x}) + \delta\rho(\mathbf{x}), \\ \lambda(\mathbf{x}) &= \lambda^0(\mathbf{x}) + \delta\lambda(\mathbf{x}), \text{ and} \\ \mu(\mathbf{x}) &= \mu^0(\mathbf{x}) + \delta\mu(\mathbf{x}), \end{aligned} \tag{A.16}$$

is embedded in the reference medium, where $\delta\rho$, $\delta\lambda$ and $\delta\mu$ are the deviations (perturbations) of the inclusion relative to the reference medium. For the reasons of compactness, $c_{ijkl} = c^0_{ijkl} + \delta C_{ijkl}$ will be used in further derivations instead of the Lamé coefficients. The total displacement field $\hat{\mathbf{u}}$, may be expressed as a sum of the primary wave field $\hat{\mathbf{u}}^0$, i.e., the field when there is no perturbation in the reference medium, and the scattered field $\hat{\mathbf{U}}$:

$$\hat{\mathbf{u}}(\mathbf{x},w) = \hat{\mathbf{u}}^0(\mathbf{x},w) + \hat{\mathbf{U}}(\mathbf{x},w). \tag{A.17}$$

By substituting A.17 into A.13, taking into account that the elastic perturbations are generally considered to be small in comparison to the corresponding parameters of the reference medium, the original problem A.13 can be reformulated into

$$\rho^0(\mathbf{x})w^2\hat{U}_j(\mathbf{x},w) + [c^0_{ijkl}(\mathbf{x})\hat{U}_{k,l}(\mathbf{x},w)]_{,i} = Q_j(\mathbf{x}), \tag{A.18}$$

where

$$Q_j(\mathbf{x}) = [\delta c_{ijkl}(\mathbf{x})\hat{u}_{k,l}(\mathbf{x},w)]_{,i} + \delta\rho(\mathbf{x})w^2\delta\hat{u}_j(\mathbf{x},w) \tag{A.19}$$

is an expression that represents equivalent body forces that arise from the interactions of the total wave field with the perturbations.

By introducing Green's functions for the reference medium, invoking the representation theorem (see Aki and Richards, 1980), and performing integration by parts, the scattered field $\hat{\mathbf{U}}$ can be written in the form of a volume integral,

$$\hat{U}_m(\mathbf{r},w) = \int_{\mathrm{V}} [\delta\rho(\mathbf{x})w^2\hat{u}_i(\mathbf{x},w)G^0_{mi}(\mathbf{r}|\mathbf{x},w) + \delta c_{ijkl}(\mathbf{x})\hat{u}_{k,l}(\mathbf{x},w)G^0_{mj,i}(\mathbf{r}|\mathbf{x},w)]d\mathbf{x}. \tag{A.20}$$

In the equation A.20, $G^0_{pq}(\mathbf{r}|\mathbf{x},w)$ is the Green's function for the reference medium giving p^{th} component of the particle motion at $\mathbf{r}$ due to a point force in the qth direction at $\mathbf{x}$. Equation A.20 is nonlinear, because the integrand includes a contribution from $\mathbf{U}$; it is valid for weak scattering, when $\mathbf{U} \ll \mathbf{u}^0$.

When the scattered field $\mathbf{U}$ is weak in comparison to the primary field $\mathbf{u}^0$, the total field $\mathbf{u}$ in the equation A.20 can be approximated by the primary field $\mathbf{u}^0$. This is the (first) Born approximation. By applying the Born approximation to the equation A.20 an explicit formula for the scattered field is obtained:

$$\hat{U}_m(\mathbf{r}, w) \simeq \int_{\mathrm{V}} [\delta\rho(\mathbf{x}) w^2 \hat{u}_i^0(\mathbf{x}, w) G_{mi}^0(\mathbf{r}|\mathbf{x}, w) + \delta c_{ijkl}(\mathbf{x}) \hat{u}_{k,l}^0(\mathbf{x}, w) G_{mj,i}^0(\mathbf{r}|\mathbf{x}, w)] d\mathbf{x}. \quad \text{(A.21)}$$

The Born approximation is valid under the condition (Wu, 1989)

$$\frac{\delta p}{p^0} kR \ll 1, \quad \text{(A.22)}$$

where k is the wave field wavenumber, R denotes the size of the scattering inclusion (for example the diameter of a sphere), and $\delta p/p_0$ is the parameter perturbation ratio within the scattering inclusion,

$$\frac{\delta p}{p^0} = \frac{(\delta\rho)_{rms}}{\rho^0} + \frac{(\delta\lambda)_{rms} + 2(\delta\mu)_{rms}}{\lambda^0 + 2\mu^0}, \quad \text{(A.23)}$$

where $(\ )_{rms}$ stands for the root mean square value. According to Wu (1989), relation A.22 means that the total "phase fluctuation" caused by scattering must be roughly less than one radian. This condition is satisfied for two cases:

- When the volume of the scattering inclusion is very small in comparison with the wavelengths, i.e., $kR \ll 1$, in which case the scattering is called Rayleigh scattering;
- When the scatterers have a large spatial distribution but are weak so that A.23 is still satisfied, in which case the scattering is called Mie scattering.

For Rayleigh scattering, phase differences between the scattered far fields from the different parts of the scatterer can be neglected. The whole scattering inclusion can be treated as a point scatterer. The right-hand side of A.21 can be integrated out and Rayleigh-Born scattering radiation patterns for incident P-wave and S-waves (SV and SH) are obtained (see Wu, 1989). In this thesis work, the study of ${}^p\mathbf{U}^p$ was of the only interest, which is the P-wave response of a point scatterer initiated by the incident P-wave.

$${}^p\mathbf{U}^p = \mathrm{V} w^2 \left[\frac{\overline{\delta\rho}}{\rho^0} \cos\theta - \frac{\overline{\delta\lambda}}{\lambda^0 + 2\mu^0} - \frac{2\overline{\delta\mu}}{\lambda^0 + 2\mu^0} \right], \quad \text{(A.24)}$$

where θ is the angle between the incoming and scattered rays, V is the volume of the inclusion, and overline denotes average value.

For Mie scattering, when the wavelength is comparable to or smaller than the scattering inclusion, the phase differences of the incident and scattered fields caused by the size of the inclusion can no longer be ignored. The point scatterer approximation is no more valid. Nevertheless, the scattering response can still be calculated by representing the large scattering inclusion by many Rayleigh point scatterers and integrating the right-hand side of A.21. Integration over numerous point scatterers is a heavy load even for a very fast work station. To reduce the run time, analytic expressions for geometrical shapes such as a sphere, an ellipsoid and a cylinder, can be derived and used instead of numerical integrations. These analytic expressions are limited to homogeneous inclusions or heterogeneous inclusions where the heterogeneity can be analytically described (e.g., Gaussian heterogeneity). The study taken in this thesis could not accommodate such simplifications and the response of many Rayleigh scatterers representing the full volume of the inclusion was integrated numerically. The computer run-time was reduced by simplifying the elastic problem into an acoustic one ($\mu = 0$) and choosing the perturbations of the medium to be characterized only by changes in compressibility ($\delta\lambda \neq 0$ and $\delta\rho = 0$). Each of the Rayleigh scatterers becomes a simple secondary source.

A.3 Ray-Born Algorithm

The ray-Born algorithm applied to compute all of the modeled data in this thesis is given in a schematic form in Figure A.1. The most important components of the modeling algorithm (namely asymptotic ray theory and Born scattering approximation) are already treated in detail in the previous sections.

Here, only a brief explanation of other algorithm components, characteristics and options is given.

- Any type of acquisition geometry (2D, crooked line 2D and 3D) can be specified.
- Scattering inclusions can take arbitrary shapes and sizes. The user must specify coordinates of each Rayleigh scatterer the inclusion is composed of. The only automatic process for representing large inclusions with point scatterers that is embedded in the modeling algorithm, is done for the inclusions with a rectangular shape. Rectangles are specified by the coordinates of their four vertices. The modeling code divides the rectangles into numerous prisms of the desired size.
- Vertical component of displacement at the free surface is taken into account during

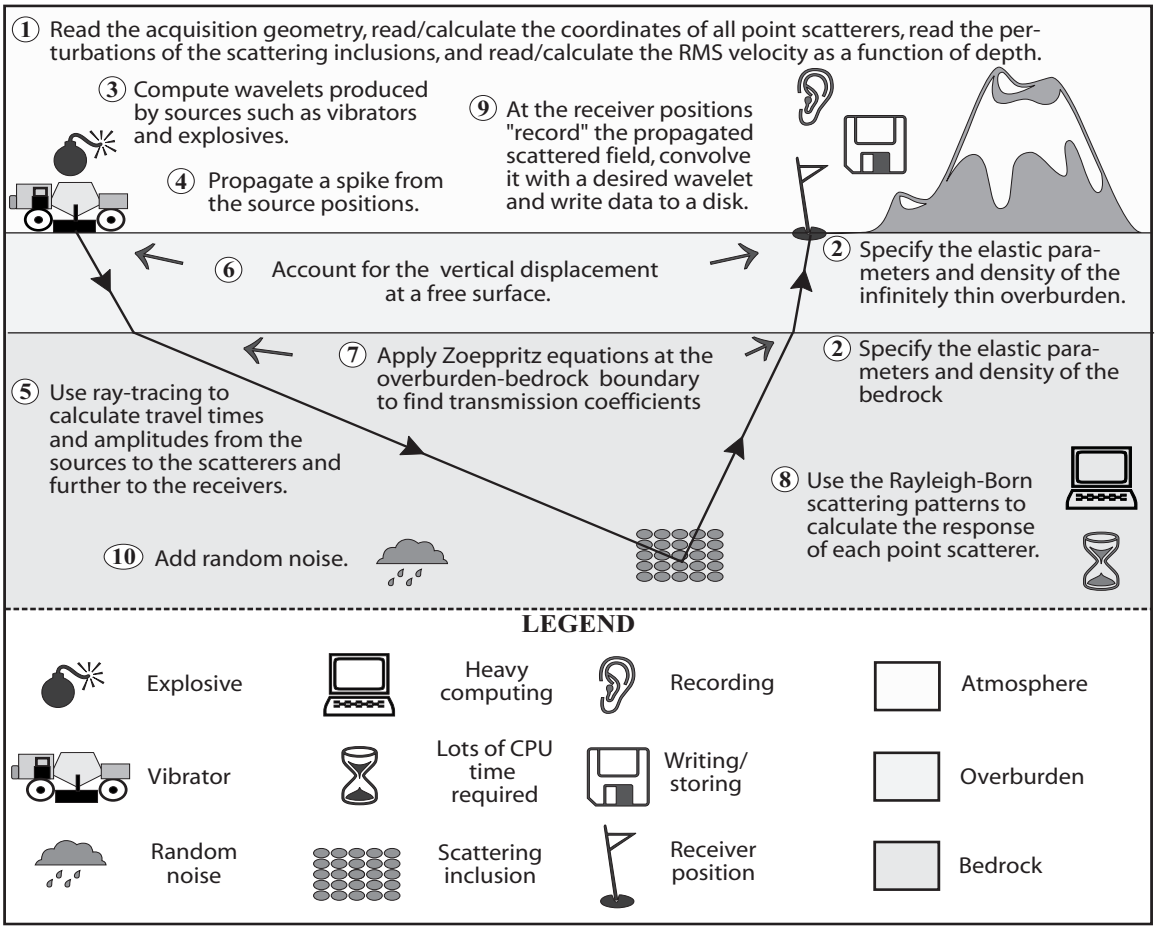

Figure A.1: Schematic diagram of the ray-Born algorithm used to model data in this thesis work. The processes numbered indicate the basic flow of the modeling process.

modeling. The vertical displacement at the free surface is calculated for a homogeneous and isotropic half space (see Ewing et. al., 1957).

- Directivity of the vibroseis source is accounted for by a cosine function.
- Transmission coefficients at the overburden/bedrock boundary are calculated using Zoeppritz equations (e.g., Richter, 1958, McCamy et. al., 1962, Jeffrey, 1959.)
- A 1D velocity model must be specified by the user.
- Computed data is convolved with the desired wavelet. Choices available in the modeling code are Klauder (see Ryan, 1994), Ormsby (see Ryan, 1994), and Ricker (see Ricker, 1944 and 1953, and Ryan, 1994) of the zero phase wavelets, and Butterworth (see Curtis, 1975) of the minimum phase wavelets.
- Adding Gaussian (random) noise is one of the options available.

Appendix B

Descriptions of the Models

B.1 Models 1 to 4

Table B.1:

GENERAL PARAMETERS	
Acquisition parameters	Same as for Sturgeon Lake Line (look in Appendix C)
Wavelet type and frequency content	Butterworth minimum phase wavelet, 20 to 300 Hz, (low gate slope = 18 dB/Oct, high gate slope = 24 dB/Oct)
Vp, Vs and density of the infinitely thin overburden	550 m/s, 318 m/s and 1.6 g/ccm
Vp, Vs and density of the bedrock	6000 m/s, 3464 m/s and 1.9 g/ccm
Random noise	Added to computed data
Recording time for models 1, 2, 3 and 4 respectively	2.0 s, 2.5 s, 3.0 s and 2.2 s
Sampling rate	1 ms
Number of reflectors imbedded in models 1, 2, 3 and 4 respectively	4, 6, 6 and 4

Table B.2:

PARAMETERS OF THE REFLECTORS							
Model	Reflec. No. in Model	Northing, Easting and Depth of the Reflector's Center	Shape and Size of the Reflector	True Dip and Azimuth of the Dip Line	Refl. Coef.	Number of Scatterers in Reflector	Length, Width and Thickness of Scatterers
Model 1	**1**	N=5527476.02m, E=649959.96m, D=1000.00m	Square 10x10 m	N/A	0.100	1	l=10m, w=10m, t=6m
	2	N=5527476.02m, E=649959.96m, D=3000.00m	Square 10x10 m	N/A	0.120	1	l=10m, w=10m, t=6m
	3	N=5527476.95m, E=652107.63m, D=1000.00m	Square 10x10 m	N/A	0.140	1	l=10m, w=10m, t=6m
	4	N=5527476.95m, E=652107.63m, D=3000.00m	Square 10x10 m	N/A	0.170	1	l=10m, w=10m, t=6m
Model 2	**1**	N=5528995.95m, E=651814.92m, D=1000.00m	Square 1.5x1.5 km	0.00 dgr, 46.77 dgr	0.100	22500	l=10m, w=10m, t=6m
	2	N=5528227.01m, E=651089.79m, D=1194.11m	Square 1.5x1.5 km	15.00 dgr, 46.77 dgr	0.120	22500	l=10m, w=10m, t=6m
	3	N=5527422.08m, E=650330.86m, D=1375.00m	Square 1.5x1.5 km	30.00 dgr, 46.77 dgr	0.140	22500	l=10m, w=10m, t=6m
	4	N=5526584.94m, E=649541.35m, D=1530.33m	Square 1.5x1.5 km	45.00 dgr, 46.77 dgr	0.170	22500	l=10m, w=10m, t=6m
	5	N=5525721.45m, E=648727.60m, D=1649.52m	Square 1.5x1.5 km	60.00 dgr, 46.77 dgr	0.200	22500	l=10m, w=10m, t=6m
	6	N=5524839.33m, E=647896.09m, D=1724.44m	Square 1.5x1.5 km	75.00 dgr, 46.77 dgr	0.240	22500	l=10m, w=10m, t=6m
Model 3	**1**	N=5525793.16m, E=648505.36m, D=1500.00m	Square 1.5x1.5 km	0.00 dgr, 133.32 dgr	0.100	22500	l=10m, w=10m, t=6m
	2	N=5529926.54m, E=651769.25m, D=1694.11m	Square 1.5x1.5 km	15.00 dgr, 133.32 dgr	0.120	22500	l=10m, w=10m, t=6m
	3	N=5527283.54m, E=648454.09m, D=1875.00m	Square 1.5x1.5 km	30.00 dgr, 133.32 dgr	0.140	22500	l=10m, w=10m, t=6m
	4	N=5530269.54m, E=649930.17m, D=2030.33m	Square 1.5x1.5 km	45.00 dgr, 133.32 dgr	0.170	22500	l=10m, w=10m, t=6m
	5	N=5530649.97m, E=647982.50m, D=2149.52m	Square 1.5x1.5 km	60.00 dgr, 133.32 dgr	0.200	22500	l=10m, w=10m, t=6m
	6	N=5531469.99m, E=645547.49m, D=2204.77m	Square 1.5x1.5 km	70.00 dgr, 133.32 dgr	0.240	22500	l=10m, w=10m, t=6m
Model 4	**1**	N=5527770.98m, E=650217.00m, D=500.00m	Square 2.0x2.0 km	15.00 dgr, 180.00 dgr	0.100	40000	l=10m, w=10m, t=6m
	2	N=5528070.01m, E=650217.00m, D=750.00m	Square 2.0x2.0 km	30.00 dgr, 180.00 dgr	0.120	40000	l=10m, w=10m, t=6m
	3	N=5528537.00m, E=650217.00m, D=900.00m	Square 2.0x2.0 km	45.00 dgr, 180.00 dgr	0.140	40000	l=10m, w=10m, t=6m
	4	N=5529369.05m, E=650217.00m, D=1000.00m	Square 2.0x2.0 km	60.00 dgr, 180.00 dgr	0.170	40000	l=10m, w=10m, t=6m

B.2 Models 5 to 7

Table B.3:

GENERAL PARAMETERS	
Acquisition parameters	Same as for Line 23, Abitibi-Grenville Transect, (look in Appendix C). For models 6 & 7 only northern third of Line 23 was used
Wavelet type, wavelet frequency content, wavelet length and sweep length	Klauder zero phase wavelet, 10 to 56 Hz, 200 ms, 14 s
Vp, Vs and density of the infinitely thin overburden	550 m/s, 318 m/s and 1.6 g/ccm
Vp, Vs and density of the bedrock	6000 m/s, 3464 m/s and 1.9 g/ccm
Random noise	Added to computed data
Recording time for models 5, 6 and 7 respectively	18.0 s, 9.0 s and 9.0 s
Sampling rate	8 ms
Number of reflectors imbedded in models 5, 6 and 7 respectively	15, 4 and 4

Table B.4:

PARAMETERS OF THE REFLECTORS							
Model	Reflec. No. in Model	Northing, Easting and Depth of the Reflector's Center	Shape and Size of the Reflector	True Dip and Azimuth of the Dip Line	Refl. Coef.	Number of Scatterers in Reflector	Length, Width and Thickness of Scatterers
Model 5	**1**	N=5324904.23m, E=600019.49m, D=3535.53m	Square 2.0x2.0 km	45.00 dgr, 270.00 dgr	0.120	6400	l=25m, w=25m, t=48m
	2	N=5324904.23m, E=603555.02m, D=7071.07m	Square 2.0x2.0 km	45.00 dgr, 270.00 dgr	0.145	6400	l=25m, w=25m, t=48m
	3	N=5324904.23m, E=607090.56m, D=10606.60m	Square 2.0x2.0 km	45.00 dgr, 270.00 dgr	0.170	6400	l=25m, w=25m, t=48m

TABLE B4 CONTINUES ON THE NEXT PAGE

TABLE B4 CONTINUED

PARAMETERS OF THE REFLECTORS

Model	Reflec. No. in Model	Northing, Easting and Depth of the Reflector's Center	Shape and Size of the Reflector	True Dip and Azimuth of the Dip Line	Refl. Coef.	Number of Scatterers in Reflector	Length, Width and Thickness of Scatterers
Model 5	**4**	N=5324904.23m, E=610626.09m, D=14142.14m	Square 2.0x2.0 km	45.00 dgr, 270.00 dgr	0.200	6400	l=25m, w=25m, t=48m
	5	N=5324904.23m, E=614161.63m, D=17677.67m	Square 2.0x2.0 km	45.00 dgr, 270.00 dgr	0.240	6400	l=25m, w=25m, t=48m
	6	N=5318729.31m, E=597822.22m, D=2500.00m	Square 2.0x2.0 km	0.00 dgr 315.00 dgr	0.100	6400	l=25m, w=25m, t=48m
	7	N=531781425m, E=598737.28m, D=4829.63m	Square 2.0x2.0 km	15.00 dgr 315.00 dgr	0.120	6400	l=25m, w=25m, t=48m
	8	N=5316077.66m, E=600473.87m, D=6495.19m	Square 2.0x2.0 km	30.00 dgr, 315.00 dgr	0.140	6400	l=25m, w=25m, t=48m
	9	N=5313729.31m, E=602822.22m, D=7071.07m	Square 2.0x2.0 km	45.00 dgr, 315.00 dgr	0.170	6400	l=25m, w=25m, t=48m
	10	N=5311074.66m, E=605476.87m, D=6250.00m	Square 2.0x2.0 km	60.00 dgr, 315.00 dgr	0.200	6400	l=25m, w=25m, t=48m
	11	N=5315859.34m, E=591857.07m, D=2500.00m	Square 4.0x4.0 km	0.00 dgr, 315.00 dgr	0.100	25600	l=25m, w=25m, t=48m
	12	N=5314944.28m, E=592772.13m, D=4829.63m	Square 4.0x4.0 km	15.00 dgr, 315.00 dgr	0.120	25600	l=25m, w=25m, t=48m
	13	N=5313207.69m, E=594508.72m, D=6495.19m	Square 4.0x4.0 km	30.00 dgr, 315.00 dgr	0.140	25600	l=25m, w=25m, t=48m
	14	N=5310859.34m, E=596857.06m, D=7071.07m	Square 4.0x4.0 km	45.00 dgr, 315.00 dgr	0.170	25600	l=25m, w=25m, t=48m
	15	N=5308204.69m, E=599511.72m, D=6250.00m	Square 4.0x4.0 km	60.00 dgr, 315.00 dgr	0.200	25600	l=25m, w=25m, t=48m
Model 6	**1**	N=5319936.00m, E=601512.00m, D=7071.07m	Square 3.0x3.0 km	45.00 dgr, 315.00 dgr	0.100	14400	l=25m, w=25m, t=48m
	2	N=5329936.00m, E=591512.00m, D=7071.07m	Square 3.0x3.0 km	45.00 dgr, 135.00 dgr	0.100	14400	l=25m, w=25m, t=48m
	3	N=5324936.00m, E=607118.60m, D=10606.0m	Square 3.0x3.0 km	45.00 dgr, 270.00 dgr	0.140	14400	l=25m, w=25m, t=48m
	4	N=5324936.00m, E=596512.00m, D=15000.00m	Square 3.0x3.0 km	0.00 dgr, N/A	0.140	14400	l=25m, w=25m, t=48m
Model 7	**1**	N=5319936.00m, E=601512.00m, D=7071.07m	Square 3.0x3.0 km	45.00 dgr, 315.00 dgr	0.100	14400	l=25m, w=25m, t=48m
	2	N=5329936.00m, E=591512.00m, D=7071.07m	Square 3.0x3.0 km	45.00 dgr, 135.00 dgr	0.200	14400	l=25m, w=25m, t=48m
	3	N=5324936.00m, E=607118.90m, D=10606.60m	Square 3.0x3.0 km	45.00 dgr, 270.00 dgr	0.280	14400	l=25m, w=25m, t=48m
	4	N=5324936.00m, E=596512.00m, D=15000.00m	Square 3.0x3.0 km	0.00 dgr, N/A	0.140	14400	l=25m, w=25m, t=48m

Appendix C

Acquisition Parameters

Table C.1: **High-Resolution Sturgeon Lake Line**

Acquisition company, party number and job number	JRS Exploration Co. Ltd, 504, 177-01
Client's name and date acquisition was carried out	Noranda Mining and Exploration, November 9th, 1997
Acquisition type and line length	2D crooked line data acquisition, 7.84 km
General direction of the line and prospect location	Northeast-southeast, Sturgeon Lake
Recording instrument	Sercel SN388 A.P.M. s/n 12
Filters (notch out)	Low out, high at 400 Hz
Preamplifier gain	12dB
Record length	3 s
Source type	Explosive
Source array type	Single holes
Charge size	500 g
Hole depth	4 to 9 m
Number of channels per recording spread	393
Number of geophones per channel	9 (3 in series x 3 in parallel)
Geophone spread type and geophone separation	9 in line, 37.5 cm
Geophone type and frequency	OYO 30-CT, 10 Hz
Type of base and damping	2" Spike, 68%
Receiver group interval	20 m
Source interval	40 m
Minimum and maximum offsets of the recording spread	0 m, 7840 m
Recording spread type	All stations fixed and alive, shots changing position
Number of channels in the gap	0
Sampling rate	1 ms
Subsurface coverage	120 fold
Station coordinates	Contact Lithoprobe Seismic Processing Facility

Table C.2: **Acquisition parameters of the regional lines 21, 23 and 24**

Acquisition company, party number and job number	JRS Geophysical Ltd, V-105, 107-02/03
Client's name and date done (lines 21, 23 and 24 respec.)	Lithoprobe, November 18th-23rd, 23rd-26th & 27th, 1990
Acquisition type and line length (21, 23 and 24 respec.)	2D crooked line data acquisition, 78.1, 41.4, 20.3 km
General direction and prospect location of Line 21	East-west, Noranda
General direction and prospect location of Line 23	North-south, Larder Lake
General direction and prospect location of Line 24	East-west, Larder Lake
Recording instrument	Sercel, model 368, serial number 135
Filters (notch out)	Low out, high at 8 9 Hz (with a slope of 72 dB/Oct)
Preamplifier gain	42dB
Record length	18 s
Stacker/Correlator	Calder, model ASAP, mode of operation CA
Noise rejection	Diversity stack
Source type	Vibroseis
Vibrators type and peak force	MERTZ model 18B, 40000 lbs
Drag length	100 m, weighted array
Number of vibrators and sweeps per vibrating point	4, 8
Source synchronizer	Pelton, model ADV. II
Sweep type	12-56 Hz, linear up-sweep, 0.5 tap
Sweep length	14 s
Spread type	Assymetric split spread
Spread diagram	8100 m - 150 m - VP - 150 m - 4100 m
Number of channels per recording spread	240
Number of geophones per channel	9
Geophone spread type and geophone separation	9 in line, 6.25 m
Geophone type, frequency and polarity	Mark L410, 14 Hz, SEG
Type of base and damping	2" Spike, 70%
Receiver group interval	50 m
Source interval	100 m
Minimum and maximum offsets of the recording spread	150 m and 8100/4100 m
Number of channels in the gap	5
Sampling rate	4 ms
Subsurface coverage	60 fold
Tape format, type and density	SEGY DEMUX, Memorex, 6250 bpi
Station coordinates	Contact Lithoprobe Seismic Processing Facility

Appendix D

Archean Cratons and the Superior Province

D.1 Plate Tectonics Through Time

Plate tectonics is widely accepted today as the principal process that controls the growth and destruction of the continental and oceanic crust (Condie, 1994a). When the history of plate tectonics begins, however, is still debatable. In a strict uniformitarain approach, it is speculated that plate tectonics starts from at least 4 Ga onwards. Apparent polar wonder paths obtained through paleomagnetic studies of several continental blocks provide strong evidence that continental drift existed as far back in time as Proterozoic (Windley, 1981). Recent studies of the Precambrian rocks support the existence of some form of plate tectonics in the latter part of the Archean (Condie, 1994a). There appears to be enough evidence for most geologists to shift the focus of the plate tectonics debate from: whether plate tectonics operated in the Archean to what form of plate tectonics took place during the Archean (Kröner, 1981, Condie, 1994a.)

Windley (1981) provides a tour of plate tectonics through eons, of which a concise version is presented here:

- The Archean (3.9–2.5 Ga) was characterized by extensive rifting, and vigorous growth (accretion) and destruction (subduction) of the oceanic lithosphere that eventually led to the formation of the continental crust. Few stable (i.e., persistent) cratons were formed until the end of the Archean ($\sim$ 2.7-2.6 Ga);
- The Archean–Proterozoic boundary represents a period during which the Archean

continental crust was thickened, uplifted, eroded, and injected by many intrusions and dykes;

- The Proterozoic (2.5–0.6 *Ga*) was a transitional period between the Archean and the Phanerozoic. Some greenstone mafic volcanic belts continued to form. Evidence indicates that the Wilson cycle may have been already established. Stable cratons were bordered by narrow fold belts and many abortive attempts at rifting these stabilized continental plates occur;

- The Phanerozoic (0.6 *Ga–present*) is a period characterized by a well understood Wilson cycle, in which the opening and closing of the oceanic basins is guided by the plate tectonics, but the process most likely occurs at a slower pace then in the earlier eons.

D.2 Archean Cratons and the Division of the Superior Province

Archean crust, though ancient and often heavily reworked, is still abundant as more than half of the present day continental crust was formed before the Proterozoic began (Green et al., 1990b, and references therein). High inhomogeneity of Archean cratons certainly imposes a great difficulty for their subdivision, or classification into different types of building blocks. The most general, and thus the most widely accepted classification divides Archean cratons into granite-greenstone (mainly) and granulite-gneiss (less common) rock associations, with these two types likely being formed in different tectonic environments (Windley, 1981). Subdivision of each Archean craton viewed in a singular form may include more than the two rock associations mentioned. The additionally distinguished rock associations are generally considered specific to the Archean craton studied.

The surveys considered in this study are both in the Archean Superior Province. It (figure D.1) covers an area of $1,572,000\ km^2$, or 23% of the Earth's exposed Archean crust (Thurston, 1991) and (represents a touchstone for many models of Archean accretion because it) is probably the most thoroughly and diversely studied Archean crust in the World. The geochronologic control is the best of any Archean province (Condie, 1994b), and it is comparably well mapped geophysically.

The Proterozoic orogenic belts surround the Superior Province; the Grenville Province

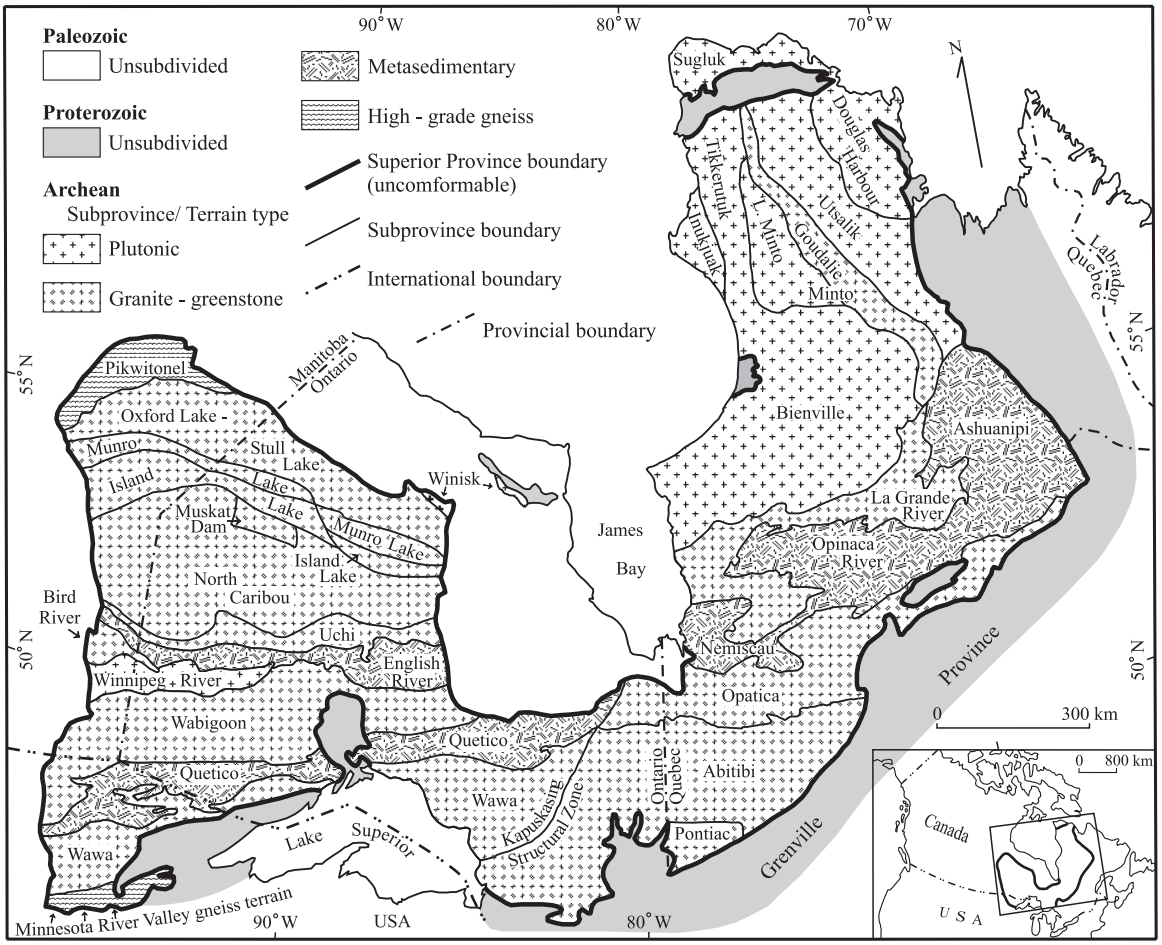

Figure D.1: Major tectonic subdivisions of the Superior Province. Slightly modified from Williams et al. (1992), which itself represents an improved version of the map presented by Card and Ciesielski (1986).

is on the east and southeast, the Churchill Province is on the east, north and west, and the Southern Province is on the south and west (Card and Ciesielski, 1986). Apart from its size, the outstanding feature of the Superior Province is an internal pattern of 100–200 km wide east-west trending lithotectonic belts formed by an array of geologically contrasting regions known as subprovinces (Clowes, R. M., (editor), 1993). This array of geologically different regions can be interpreted as a tectonic assemblage of successive arc terrains consistent with an accretionary plate tectonics model (Williams et al., 1992).

One of the recent and most often cited subdivisions of the Superior Province, the subdivision proposed by Card and Ciesielski (1986) and slightly modified by Williams et al. (1992), is presented in figure D.1. Card and Ciesielski (1986), and later Williams et al. (1992), base the subdivision of the Superior Province on all available geological, geochronological and geophysical data. This subdivision places subprovince boundaries

at structural discontinuities such as faults, and at lithologic, metamorphic and structural transition zones. Four types of lithotectonic domains are recognized:

- Volcano–plutonic (better known as granite–greenstone (see for example Condie, 1981, Windley, 1981, Williams, 1992));
- Metasedimentary (possibly unique to the Superior Province (Thurston, 1991));
- Plutonic;
- High–grade gneiss (or granulite–gneiss (Windley, 1981)).

These domains can be distinguished one from another because they differ in all or some of the following: (1) structural trend and style; (2) lithologic makeup; (3) metamorphic grade; (4) isotopic ages of rock units and events; (5) geophysical attributes, chiefly their aeromagnetic and gravity characteristics; and (6) metallogenic characteristics. Alternating granite–greenstone and metasedimentary domains that form the prominent striped pattern of the central Superior Province are closely associated spatially, and probably genetically. These domains are bounded in part on the north and south by high–grade gneiss domains.

The granite-greenstone subprovinces of the Superior Province are characterized by dominantly metavolcanic supracrustal sequences, the greenstone belts, and are bordered and intruded by voluminous felsic plutonic rocks, including early synvolcanic plutons and tonalitic gneisses, and younger foliated to massive plutons ranging from quartz diorite to granite and syenite. The structural patterns of the granite–greenstone subprovinces are a product of a polyphase deformation and are typically irregular. Metamorphic grade in the greenstone belts is generally subgreenschist or greenschist in the central parts and increases outward to low pressure amphibolite facies in the margins and in the surrounding plutonic gneisses.

Appendix E

Cross Dip Moveout

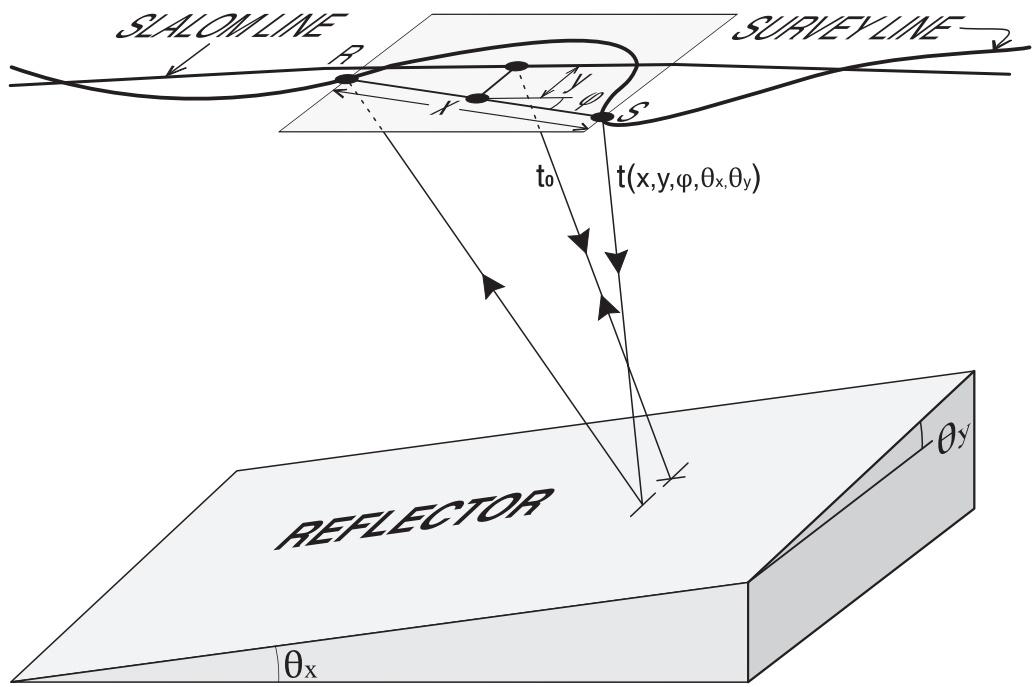

Figure E.1: Cross dip moveout. S and R are source and receiver respectively.

When the imaged structures have a 3D geometry and the data is acquired on crooked lines, source-reflector-receiver traveltime (t) can be expressed as (Wang and West, 1991b):

$$t^2 = (t_0 + \mathrm{p_y y})^2 + \mathrm{p_x^2 x^2}, \tag{E.1}$$

where t_0 is the zero offset traveltime, x is the source-receiver distance (x offset), y is the cross-line offset (y offset) and $\mathrm{p_y y}$ is the cross dip moveout (CDMO). $\mathrm{p_x}$ and $\mathrm{p_y}$ are

unknown and are dependent on the source-receiver azimuth (φ), reflector dip component along the slalom line (θ_x), reflector dip component orthogonal to the slalom line (θ_y), and root-mean-square velocity (V_{RMS}) to the reflector (see figure E.1).

$$p_x = \left[\frac{1 - \sin^2\theta_x + \sin^2\varphi(\sin^2\theta_x - \sin^2\theta_y) + \frac{1}{4}\sin 2\varphi \sin 2\theta_x \sin 2\theta_y}{V_{RMS}^2(1 - \sin^2\theta_x \sin^2\theta_y)}\right]^{\frac{1}{2}}, \tag{E.2}$$

and

$$p_y = \frac{-2\sin\theta_y \cos\theta_x}{V_{RMS}(1 - \sin^2\theta_x \sin^2\theta_y)^{\frac{1}{2}}}. \tag{E.3}$$

When $\sin^2\varphi \ll 1$ or when $x \ll x_{max}$, and $\sin^2\theta_x \sin^2\theta_y \ll 1$, p_x^2 may be adequately approximated as

$$p_x^2 = \frac{1}{V_{RMS}^2} - \frac{\sin^2\theta_x}{V_{RMS}^2}. \tag{E.4}$$

p_x and p_y are mainly dependent on the unknown dips θ_x and θ_y respectively, and must be found from seismic data.

Appendix F

Azimuth and Dip of a Reflector

When both the apparent in-line dip angle (ϕ) and the apparent cross-line dip angle (φ) of an imaged reflector can be estimated from the optimum cross dip section, the true dip (θ) of the reflector and the azimuth (ν) of the true dip line can be calculated. Employing a 3D Cartesian coordinate system with its x coordinate in the direction of the slalom line and z vertical, the angles ϕ and φ are related to the directional angles α and β between the unit normal vector to the reflector's plane and the x and y axes as follows:

For	0^0	$\leq \phi \leq$	90^0,	$\alpha = (90^0 - \phi)$,	(α and ϕ are complementary angles);
For	0^0	$\leq \varphi \leq$	90^0,	$\beta = (90^0 - \varphi)$,	(β and φ are complementary angles);
For	-90^0	$\leq \phi <$	0^0,	$\alpha = (180^0 + \phi)$,	(α and ϕ are supplementary angles);
For	-90^0	$\leq \varphi <$	0^0,	$\beta = (180^0 + \varphi)$,	(β and φ are supplementary angles).

The third directional angle γ that the unit normal vector to the reflector's plane forms with the z axis, is simply calculated as:

$$\cos\gamma = |\sqrt{1 - \cos^2\alpha - \cos^2\beta}|, \tag{F.1}$$

where $\gamma = \theta$, which is the true dip of the reflector.

Angle δ between the reflector's true dip line and the slalom line direction may then be expressed as:

$$\tan\delta = \frac{\cos\beta}{\cos\alpha}. \tag{F.2}$$

When calculating the angle δ, care must be taken about the signs of $\cos\alpha$ and $\cos\beta$ because they indicate the quadrant in which the normal to the reflector lies. Once δ is determined, it is simple to calculate the true azimuth ν of the reflector's dip line. This is done by adding angle δ to the azimuth of the slalom line[1].

[1] Angles measured clockwise are positive.

Glossary of terms and abbreviations

Terms

3D seismic data cube is an array $N_x \times N_y \times N_z$ pixels large where data values in the array are derived from seismic trace amplitudes.

CMP bin is a rectangle area used to "collect" data traces whose mid-points are scattered when data acquisition is carried out on crooked lines. Slalom line passes through the center of each CMP bin. Traces with mid-points that fall in CMP bins form CMP bin gathers.

Easting is the eastwards component of distance between a point and a reference point on the surface of the Earth.

Gather is a group of data traces. Seismic traces with a common shot form a **CSG (common shot gather)**; traces with a common receiver form a **CRG (common receiver gather)**; traces with a common offset form a **COG (common offset gather)**; and traces with a common mid-point form a **CMP gather**.

Migration is a mapping process that repositions the recorded reflectivity to its true subsurface location.

Muting is a procedure that sets parts of data traces to zero amplitude.

NMO stretch mute is done as a part of the NMO correction. It zeroes signal that was overly stretched (user specified) during the NMO correction.

CMP mute is a mute designed on CMP gathers after the NMO correction is applied. It is usually applied as a **top mute** (in which signal is zeroed from time zero to some selected time) or a **Surgical mute** (in which both start and end time for mute have arbitrary values).

Normal moveout correction is a time shift introduced to trace signals is order to align them before stack. **Normal moveout** is a consequence of non-coincidental sources and receivers.

Northing is the northwards component of distance between a point and a reference point on the surface of the Earth.

Source-receiver offset is the distance from the source to the receiver. **In-line offset**

has the same meaning as the source-receiver offset. **Mid-point offset** is the shortest distance from a mid-point to the slalom line. Cross-line offset has the same meaning as the mid-point offset.

Path length is the propagation distance of seismic wave energy along its source – scatterer/reflector – receiver path.

Prestack data processing encompasses all data manipulations that precede the CMP stack.

Poststack data processing encompasses all data manipulations that postdate the CMP stack.

RHO filter compensates for the slant stack's theoretical ω^{-1} spectral attenuation by multiplying the selected part of the amplitude spectra by the corresponding frequency taken to an arbitrary power.

Semblance is a measure of similarity of signals on a set of traces as a function of time.

Spread size is the length of the active acquisition line for a single source. **Cross spread size** is the maximum distance between mid-points in a CMP bin gather measured in the direction perpendicular to the slalom line.

Stacking: creating a data trace that is the point by point average of a group of traces.
CMP stack, section, or a profile is a 2D seismic reflection image $N_x \times N_y$ pixels large, obtained by stacking the data traces in CMP gathers after performance of the static, NMO, DMO and CDMO time corrections. This image is also called a **standard or phase CMP stack**.
Amplitude stack is formed by converting the data traces to absolute amplitudes, raising them to some power and stacking.
Cross dip stack is obtained by stacking the data traces at a desired cross slowness. When applied only to a part of a trace gather, it is called a **local slant stack**.
Partial stack is usually formed by stacking only parts of the data in CMP or CS gathers that are grouped in offset windows.

Seismic trace (data trace) is a digitally sampled time recording at one receiver station of seismic ground motion due to the impulsive source event. It is N_t pixels (samples) long and is usually the average signal recorded by a small array (group) of geophones.

Wavelet: a waveform that is bounded in both frequency content and time duration that

represents an idealized seismic source event.

Butterworth minimum phase wavelet is obtained from the realisable minimum phase band pass Butterworth filter.

Klauder wavelet is the source wavelet created by using a vibratory source:- the autocorrelation of the linearly swept sinusoidal signal used in vibroseis.

Abbreviations

AGC: Automatic gain control.

CDMO: Cross dip moveout.

CMP: Common mid-point.

COG: Common offset gather.

CPU: Central processing unit.

CRG: Common receiver gather.

CSG: Common shot gather. Also, common scatter-point gather.

CSP: Common offset gather.

COG: Common offset gather.

DMO: Dip moveout.

LCSZ: Larder-Cadillac Lake shear zone.

LPSF: Lincoln-Nipissing shear zone.

MP: Mid-point

NMO: Normal moveout.

RMS: Root mean square.

S/N: Signal to noise ratio.

SZOSTS: Synthetic zero offset seismic time section.

VMS: Volcanogenic massive sulphides.

VSP: Vertical seismic profiling.